# The Magellanic Clouds in VHE $\gamma$ rays as seen by H.E.S.S.

Dissertation

zur Erlangung des akademischen Grades
„doctor rerum naturalium“
(Dr. rer. nat.)
in der Wissenschaftsdisziplin „Astroteilchenphysik“

eingereicht an der
Mathematisch-Naturwissenschaftlichen Fakultät
der Universität Potsdam

angefertigt am
Deutschen Elektronen Synchrotron

vorgelegt von

Maria Haupt

Potsdam, den 28.04.2020

Disputation erfolgt am 08.06.2020

| | |
|---|---|
| Betreuer: | Prof. Dr. Christian Stegmann |
| 2. Gutachter: | Prof. Dr. Stephan Geier |
| 3. Gutachter: | Prof. Dr. Uli Katz |

Teile dieser Dissertation wurden veroeffentlicht:

H.E.S.S. Collaboration. Detection of variable VHE $\gamma$-ray emission from the extra-galactic $\gamma$-ray binary LMC P3. *Astronomy & Astrophysics*, 610:L17, Mar 2018. (**M. Haupt corresponding author**)

H.E.S.S. Collaboration. Systematic search for very-high-energy gamma-ray emission from bow shocks of runaway stars. *Astronomy & Astrophysics*, 612:A12, Apr 2018. (**M. Haupt corresponding author**)

# Zusammenfassung

Das Gebiet der Gammastrahlungsastronomie hat ein neues Fenster in das nicht-thermische Universum geöffnet, welches erlaubt, die Beschleunigungsorte der kosmischen Strahlung und ihrer Rolle in evolutionären Prozessen in Galaxien zu untersuchen. Der Nachweis von fast einhundert sehr hochenergetischen Gammastrahlungsquellen in unserer Milchstraße zeigt, dass Teilchenbeschleunigung bis in den zweistelligen TeV-Energiebereich ein häufiges Phänomen ist. Darüber hinaus hat der Nachweis von sehr hochenergetischer Gammastrahlung von anderen Galaxien bestätigt, dass die kosmische Strahlung nicht ausschließlich in der Milchstraße beschleunigt wird. Die rasante Entwicklung der Gammastrahlungsastronomie in den letzten zwei Jahrzehnten führte zu einem Übergang von der Detektion und Untersuchung einzelner Quellen hin zu Quellpopulationsstudien. Um die Frage zu beantworten, ob die Quellpopulationen hochenergetischer Gammastrahlung in der Milchstraße einzigartig sind, sind Beobachtungen von anderen Galaxien erforderlich, für die es möglich ist, trotz ihrer Entfernung, einzelne Quellen aufzulösen. Die Magellanschen Wolken, zwei Satellitengalaxien der Milchstraße, sind solche Galaxien, welche im letzten Jahrzehnt durch das H.E.S.S.-Experiment intensiv beobachtet wurden. In dieser Arbeit werden die Daten von insgesamt 450 Stunden H.E.S.S.-Beobachtungen der Großen Magellanschen Wolke und der Kleinen Magellanschen Wolke vorgestellt. Während der Analyse der Datensätze wird besonderer Wert auf die Evaluierung der systematischen Unsicherheiten des Experiments gelegt, um eine unverfälschte Flussabschätzung der potentiellen hochenergetischen Gammastrahlungsquellen der Magellanschen Wolken zu gewährleisten. Die detaillierte Analyse der Beobachtungen führte zur Detektion hochenergetischer Gammastrahlung des Binärsystems LMC P3 in der Großen Magellanschen Wolke und erhöht somit die Anzahl der detektierten Gammastrahlungsquellen in dieser Galaxie auf vier. Dieses neuentdeckte Binärsystem ist das bisher leuchtstärkste in der Quellklasse der Gammastrahlungsbinärsysteme. Für keine andere Quelle in den Magellanschen Wolken wird hochenergetische Gammastrahlung nachgewiesen und es werden Obergrenzen auf den integralen Fluss ermittelt. Diese Flussobergrenzen werden verwendet, um Populationsstudien auf der Grundlage bekannter hochenergetischer Quellklassen sowie bestehender Quellkataloge anderer Wellenlängen durchzuführen. Ein systematischer Vergleich zwischen den Quellpopulationen der Magellanschen Wolken und der Milchstraße ergab, dass keine andere Quelle der Magellanschen Wolken so leuchtstark ist wie die leuchtstärkste hochenergetische Gammastrahlungsquelle in der LMC: der Pulsarwindnebel N 157B. Des Weiteren ist ein Drittel der untersuchten Quellpopulation der Magellanschen Wolken weniger leuchtstark als die vier bekannten Gammastrahlungsquellen in der Großen Magellanschen Wolke. Für einige wenige Quellen kann gezeigt werden, dass sie weniger leuchtstark sind als die leuchtstärksten Objekte in der Milchstraße, deren Leuchtkraft um mehr als eine Größenordnung schwächer ist als die der detektierten Quellen in der Großen Magellanschen Wolke. Basierend auf den Flussobergrenzen werden Unterschiede in den Quellpopulationen der Magellanschen Wolken und der Milchstraße sowie die Bedeutung der Quellumgebungen diskutiert.

# Abstract

The field of $\gamma$-ray astronomy opened a new window into the non-thermal universe that allows studying the acceleration sites of cosmic rays and the role of cosmic rays on evolutionary processes in galaxies. The detection of almost one hundred Galactic very-high-energy (VHE: $0.1 - 100\,\text{TeV}$) $\gamma$-ray sources in the Milky Way demonstrates that particle acceleration up to tens of TeV energies is a common phenomenon. Furthermore, the detection of VHE $\gamma$ rays from other galaxies has confirmed that cosmic rays are not exclusively accelerated in the Milky Way. The rapid development of $\gamma$-ray astronomy in the past two decades has led to a transition from the detection and study of individual sources to source population studies. To answer the question, whether the VHE $\gamma$-ray source population of the Milky Way is unique, observations of galaxies, for which individual sources can be resolved, are required. Such galaxies are the Magellanic Clouds, two satellite galaxies of the Milky Way, which have been surveyed by the H.E.S.S. experiment in the last decade. In this thesis, data from a total of 450 hours of H.E.S.S. observations towards the Large Magellanic Cloud (LMC) and the Small Magellanic Cloud (SMC) are presented. During the analysis of the data sets, special emphasis is put on the evaluation of systematic uncertainties of the experiment in order to assure an unbiased flux estimation of the potential VHE $\gamma$-ray sources of the Magellanic Clouds. A detailed analysis of the survey data revealed the detection of the $\gamma$-ray binary LMC P3, the most powerful $\gamma$-ray binary known so far, that is located the LMC, and thus, increases the number of known VHE $\gamma$-ray sources in the LMC to four. No other VHE $\gamma$-ray source is detected in the Magellanic Clouds and integral flux upper limits are estimated. These flux upper limits are used to perform a source population study based on known VHE source classes and existing multi-wavelength catalogues. A comparison of the source populations of the Magellanic Clouds and the Milky Way revealed that no other source in the Magellanic Clouds is as bright as the most luminous VHE $\gamma$-ray source in the LMC: the pulsar wind nebula N 157B, and that one-third of the source population of the Magellanic Clouds is less luminous than the other known VHE $\gamma$-ray sources in the LMC. For only a couple of sources luminosity levels of Galactic VHE sources, that are more than one order of magnitude fainter than the detected sources in the LMC, are constrained. Based on the flux upper limits, differences on the TeV source populations in the Magellanic Clouds and the Milky Way as well as the importance of the source environments will be discussed.

# Contents

# Chapter 1

# Introduction

The thermal radiation in the universe has been explored by the field of classical astronomy for centuries. In contrast, studies of the non-thermal phenomena describing radiation originating from relativistic cosmic rays only started in the last century with the discovery of cosmic rays by Victor Hess in 1912 [1]. Observations of cosmic rays suggest that they are distributed throughout the Milky Way and that a significant fraction of the total energy content in the Galaxy is contained in non-thermal particles. Interactions of cosmic rays with the interstellar medium (ISM) lead to plasma instabilities as well as cosmic-ray feedback through magnetic field amplifications. Furthermore, cosmic rays add a significant pressure to the ISM and thus are believed to play a significant role in star and galaxy formation mechanisms [2, 3]. The origin of cosmic rays is a key question in the field of astroparticle physics. As cosmic rays consist of charged particles, i.e., 99% hadrons (protons, helium and heavier nuclei) and 1% leptons (electrons and positrons), they are deflected in the solar, Galactic and Extragalactic magnetic fields and hence they lose information about their origin when travelling through the Universe. To study Galactic acceleration sites, where particles are accelerated to energies of up to $\sim 10^{15}$ eV, non-charged messengers are required. When relativistic cosmic rays interact with the ambient medium — for instance with radiation fields, magnetic fields or surrounding matter of sources — they lose energy via non-thermal processes (e.g., synchrotron or inverse Compton radiation) that produce photons over a wide range of frequencies from the low radio to the VHE $\gamma$-ray regime. While non-thermal radio and X-ray emission carries information about the leptonic cosmic-ray population tracing the ambient radiation fields and magnetic fields[1], $\gamma$ rays can be used to determine whether predominantly leptonic or hadronic cosmic rays are accelerated in a certain source. Furthermore, $\gamma$ rays provide information on the maximum energy to which a source can accelerate particles. The differentiation between leptonic and hadronic cosmic rays as well as the determination of their maximum energy are of particular interest to solve the standard paradigm for the origin of

---

[1] Secondary electrons and positrons produced by hadronic cosmic rays can also radiate in X-rays. However, the emission level is typically lower than that from primary electrons as high particle densities are required.

Galactic cosmic rays that are believed to have energies of up to $\sim 10^{15}$ TeV ($1$ PeV).
High-energy (HE, $0.1 - 100$ GeV) $\gamma$-ray observations are performed with space-based experiments. The latest generation of satellites are *Fermi*, carrying two instruments: the *Fermi* Large Area Telescope (*Fermi*-LAT) [4] and the *Fermi* Gamma-ray Burst Monitor (*Fermi*-GBM) [5], and Astro-rivelatore Gamma a Immagini LEggero (AGILE) [6]. Due to the rapidly decreasing $\gamma$-ray flux with increasing energies and the limited size of space-based detection areas, very-high-energy (VHE, $0.1 - 100$ TeV) $\gamma$ rays are indirectly detected by ground-based telescopes using the atmosphere as a calorimeter. The development and implementation of technological concepts to first measure and extract the $\gamma$-ray signal of a source paid off in 1989 with the first detection of a source of VHE $\gamma$ rays, the Crab nebula [7].

The field of $\gamma$-ray astronomy has grown considerably in recent years. While the first and second generation of imaging atmospheric Cherenkov teleskope (IACT) arrays advanced the establishment of $\gamma$-ray astronomy as a new field, the third generation of IACT arrays has led to a transition from the detection and study of individual sources to source population studies, which are common in the classical fields of astrophysics. VHE $\gamma$-ray sources have been detected everywhere in the Milky Way and multiwavelength studies have revealed the versatility of TeV source classes. Between 2004 and 2013 the High Energy Stereoscopic System (H.E.S.S.) conducted a survey of the Galactic plane at very-high energies, the H.E.S.S. Galactic Plane Survey (HGPS), as shown in Figure 1.2. The HGPS catalogue contains 78 VHE $\gamma$-ray sources, including 16 (composite) supernova remnants (SNRs), 12 pulsar wind nebulae (PWNe), 3 $\gamma$-ray binaries and a number of associated but not firmly identified sources, as well as objects with still undetected counterparts at lower wavelengths (i.e., objects which are TeV bright, but radio/X-ray faint). These observations, complemented by observations of other IACTs, thus deliver an ideal basis for source population studies of Galactic particle accelerators. Comprehensive population studies of Galactic PWNe, SNRs and bow shocks of runaway stars have been performed over the last five years [8–10] leading to a deeper understanding of the similarities and differences of individual sources within a source class and the impact of the source environment on particle acceleration and radiative loss mechanisms. Furthermore, these population studies can reveal information about the contribution of individual source classes to the energy budget of Galactic cosmic rays.

The question of the uniqueness of the Milky Way and its source population has fascinated astrophysicists for centuries. While scientists in classical astrophysical fields have already proven the universality of physical laws in the entire visible Universe, astroparticle physicists have only started to explore the non-thermal Extragalactic Universe. The detection of VHE $\gamma$ rays from the starburst galaxies M 82 [12] and NGC 253 [13] confirmed that cosmic rays are not accelerated exclusively in the Milky Way. However, the connection between the Galactic population of VHE $\gamma$-ray sources and the "integrated" emission of individual sources, unresolved sources and interstellar diffuse emission, seen from these galaxies is missing. To answer questions like i) "Do particle acceleration and interaction mechanisms work in the same way for different

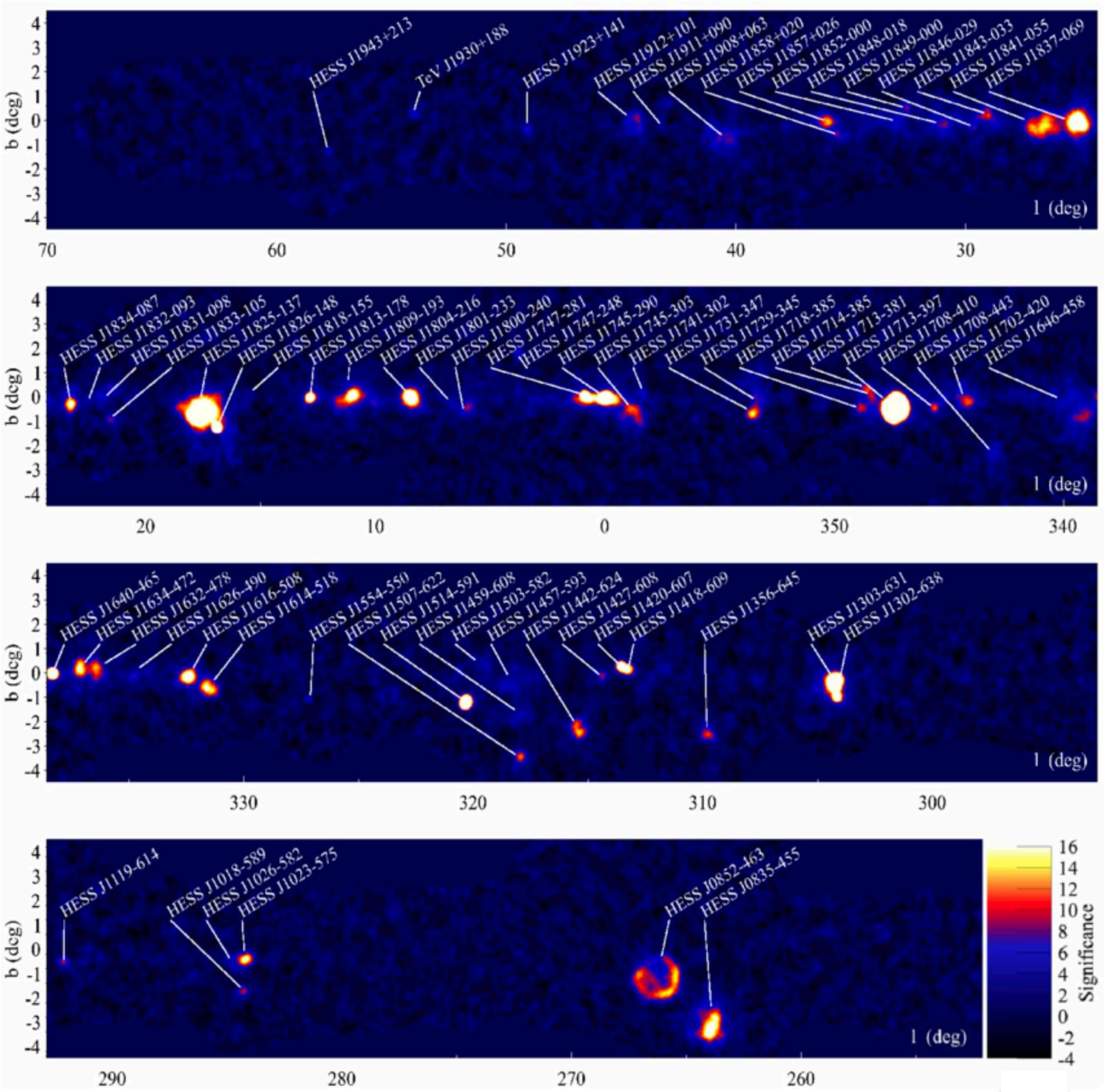

Figure 1.1: Significance sky map for the integrated VHE $\gamma$-ray flux above $1$ TeV showing the distribution of VHE $\gamma$-ray sources in the Galactic plane. Figure taken from H.E.S.S. collaboration (2018) [11].

galaxies?", ii) "How efficient are other galaxies in converting energy from stellar sources into VHE cosmic rays?" or iii) "How important is the environment within a galaxy for the efficiency of the VHE $\gamma$-ray production?" observations of galaxies that are at the same time close enough to resolve individual sources and distant enough to resolve the "integrated" large-scale emission are required. These criteria are fulfilled by two satellite galaxies of the Milky Way: the Small Magellanic Cloud (SMC) and the Large Magellanic Cloud (LMC). Both Magellanic Clouds are well-studied over the observable electromagnetic spectrum. Studies indicate that both galaxies underwent recent episodes of enhanced star formation [14–18] leading to the formation of young stellar populations, which are the progenitors of many identified VHE $\gamma$-ray sources. Surveys of non-thermal radio and X-ray emission revealed that cosmic rays are indeed accelerated to relativistic energies in individual sources of the Magellanic Clouds (e.g. [19–22]) and the detection of diffuse HE $\gamma$-ray emission as seen by *Fermi*-LAT confirmed that cosmic rays are at least accelerated to tens of GeV energies.

With its location in the Southern Hemisphere, the H.E.S.S. array is ideally suited to conduct a survey of the Magellanic Clouds. The first targeted observations of the Tarantula nebula region in the LMC, which were performed between 2005 and 2013, revealed significant VHE $\gamma$-ray emission from three sources: a SNR, a PWN and a superbubble [23]. To study the entire source populations of the Magellanic Clouds, H.E.S.S. performed a survey of the SMC and LMC between 2014 and 2019. In this thesis, data from a total of $450\,\mathrm{h}$ of H.E.S.S. observations towards the LMC and the SMC are presented. A detailed analysis of the survey data is performed to study the VHE $\gamma$-ray source populations of the Magellanic Clouds and how they compare to the VHE $\gamma$-ray source populations of the Milky Way. Differences between the VHE $\gamma$-ray source populations in the Magellanic Clouds and the Milky Way as well as the importance of the source environments will be discussed.

This thesis is structured as follows: In Chapter 2 the H.E.S.S. experiment and the general work principle of IACTs are introduced followed by the data analysis technique and a discussion of systematic uncertainties in the Magellanic Clouds data sets in Chapter 3. The theoretical background of the VHE $\gamma$-ray source classes that are investigated in this thesis is given in Chapter 4. The H.E.S.S. survey of the Magellanic Clouds including the analysis and results of the survey data is described in Chapter 5. Finally, in Chapter 6 the results of the different source populations in the LMC and SMC are compared to those of the Milky Way and the impact of physical properties of the source populations and the source environment are discussed.

---

[2] https://www.noao.edu/outreach/press/pr06/pr0601.html

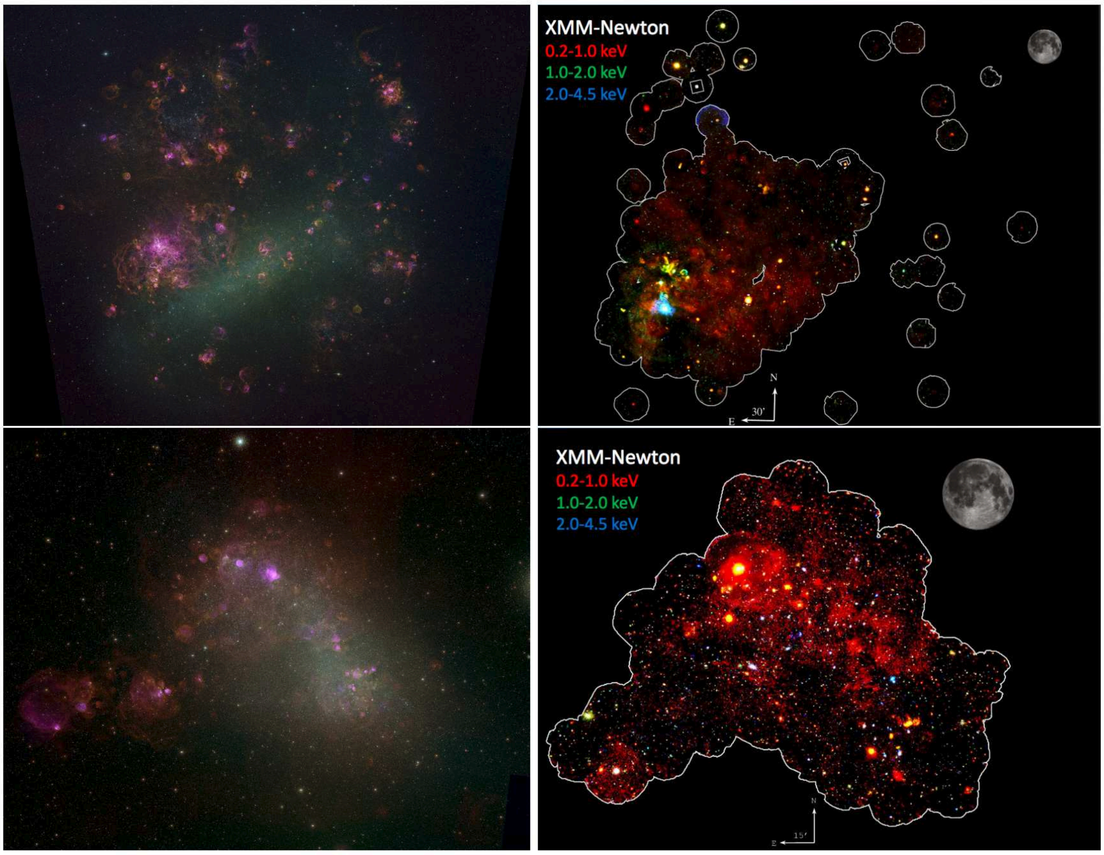

Figure 1.2: Optical and X-ray images of the Magellanic Clouds. *upper left*: LMC observed in five wavelength bands: emission lines of hydrogen ($\mathrm{H}\alpha$), double-ionized oxygen ([O III]), and single-ionized sulphur ([S II]), plus red and green continuum bands. Image Credit: C. Smith, S. Points, the MCELS Team and NOAO/AURA/NSF[2]. *upper right*: XMM-Newton survey of the LMC in three wavelength bands. Image Credit: [21]. *lower left*: Same as upper left figure, but for the SMC. Image Credit: F. Winkler/Middlebury College, the MCELS Team, and NOAO/AURA/NSF[2]. *lower right*: XMM-Newton survey of the SMC in three wavelength bands. Image Credit: [21].

# Chapter 2

# The H.E.S.S. Experiment

H.E.S.S.— the High Energy Stereoscopic System — is one of the current generation of ground-based IACTs which measure VHE $\gamma$ rays to search for the acceleration sites of cosmic rays in the Universe. Although the Earth's atmosphere is opaque to (very-)high energy $\gamma$ rays, interactions with atoms and molecules in the air induce electromagnetic particle cascades which emit Cherenkov light. Therefore, IACTs like H.E.S.S. detect $\gamma$ rays indirectly by making use of the imaging atmospheric Cherenkov technique. As interactions of cosmic rays with the atmosphere also lead to particle cascades that emit Cherenkov light, the sensitivity of IACTs is determined by their capability to reject the cosmic ray background. In this chapter, the main work principle of IACTs is described in Section 2.1 followed by an introduction to the H.E.S.S. experiment including the technological as well as the observational concept in Section 2.2.

## 2.1 Imaging Atmospheric Cherenkov Technique

The spectra of astronomical sources peak at energies far below the VHE regime, so the VHE $\gamma$-ray flux is often as low as $\sim 10^{-7}\,\mathrm{m}^{-2}\,\mathrm{s}^{-1}$ at energies above $1\,\mathrm{TeV}$; this requires detectors with very large collecting areas. In addition, at these high energies, the $\gamma$ rays have low interaction probabilities and therefore require large amounts of interacting material in order to be detected. For these reasons, ground-based IACTs detect VHE $\gamma$ rays indirectly, making use of the atmosphere as a calorimeter. Highly energetic photons enter the atmosphere and interact with the atmospheric material to produce a shower of secondary particles that emit Cherenkov light. When the Cherenkov photons reach the ground, these short flashes of photons get collected by large mirrors and are focussed onto a fast optical camera. The recorded images of the cameras are then used to reconstruct the information about the primary $\gamma$ ray and its cosmic origin. The detection principle of IACTs is described in more detail in the following subsections.

### 2.1.1 Air Showers

When a cosmic ray hits the Earth's atmosphere, it interacts with the atmospheric nuclei and produces a cascade of secondary particles called an *extensive air shower* (EAS). An electromagnetic EAS, induced by a VHE $\gamma$ ray, is driven by two alternating processes: pair production and Bremsstrahlung. An incident photon undergoes pair production in the Coulomb field of an atmospheric nucleus. The resultant electron-positron pair emits part of their energy as photons via Bremsstrahlung, which will again undergo pair production. The number of secondary particles grows exponentially as the shower develops in the atmosphere until the shower reaches its maximum, at which point the number of secondary particles is proportional to the energy of the primary $\gamma$ ray. The shower maximum is reached when the energy of the emitted photons becomes less than $1022$ MeV, which is the minimum energy needed to create an electron-positron pair with a rest energy of $511$ MeV each, and the energy loss of the secondary particles due to ionisation and excitation of the atmospheric nuclei is larger than their energy loss due to Bremsstrahlung.

Besides the highly energetic $\gamma$ rays, also other cosmic rays like electrons, hadrons or heavier nuclei reach Earth and develop air showers when entering the atmosphere. These cosmic-ray induced EAS occur $10^5$ times more frequently than $\gamma$-ray induced EAS. Whereas an electromagnetic EAS induced by an electron is difficult to distinguish from a $\gamma$-ray induced EAS, interactions of hadronic cosmic rays with atmospheric nuclei lead to a variety of secondary particles like pions, mesons, neutrinos, kaons and muons, which do not appear in non-hadronic EAS. If a neutral pion ($\pi^0$) is produced and decays into two energetic photons, a predominantly electromagnetic shower can develop. Due to the diverse shower development, hadronic showers often produce several branches of electromagnetic EAS which result in a more complex footprint when observed from the ground. However, hadronic cosmic rays that decay into $\pi^0$ during their first interactions with the atmospheric nuclei can produce a $\gamma$-ray like EAS and hence look like $\gamma$-ray induced showers. Figure 2.1 shows a comparison of the longitudinal and lateral extension of both the $\gamma$-ray and cosmic-ray induced EAS.

Because they travel through the atmosphere faster than the speed of light in air, the secondary particles produce Cherenkov light (Čerenkov 1934 [25]). This Cherenkov light is produced when the energy losses due to ionisation of the atmospheric molecules are approximately equal to the energy losses due to Bremsstrahlung or pair production. The opening angle of the Cherenkov light cone, $\theta$, is given by $cos(\theta) = 1/(\beta n_{\text{air}})$, with $\beta = \frac{v}{c}$ being the particle velocity with respect to the speed of light and $n_{\text{air}}$ being the refractive index of air. The refraction index of air at an altitude of $10$ km, where the number of particles in the shower reaches its maximum, can be calculated following the barometric formula:

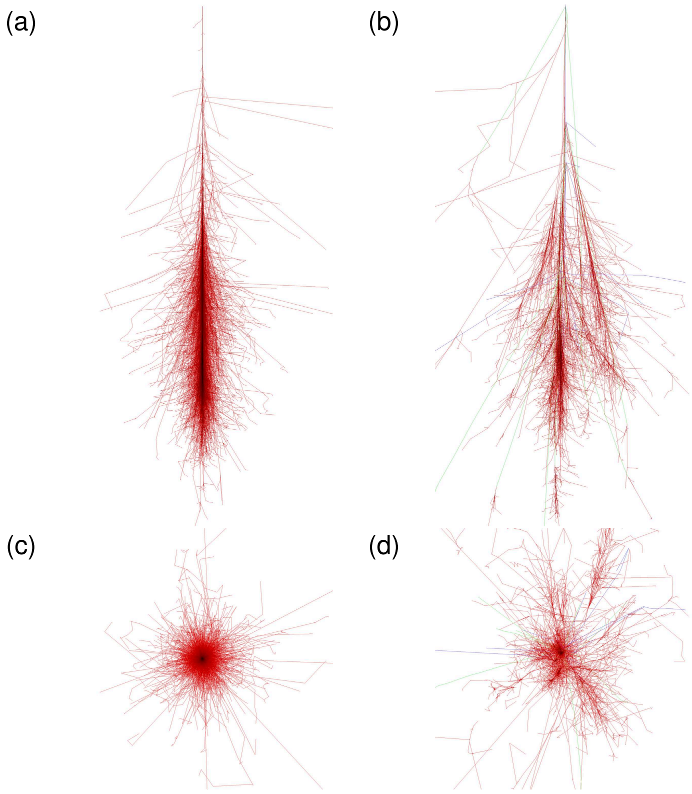

Figure 2.1: Shown are two simulations of a $\gamma$-ray induced (left) and proton induced (right) EAS with an initial energy of 100 GeV. The upper figures show the showers in the $x-z$ plane and the lower figures show the showers in the $x-y$ plane. For these diagrams, the z axis is along the shower propagation direction while the x and y axes are perpendicular to the shower direction. Image credit: Johannes Knapp [24].

$$n_{\mathrm{air}}(h) = 1 + \eta_0 \, \mathrm{e}^{-\frac{h}{h_0}}$$

where $\eta_0 = 2.9 \times 10^{-4}$ at an altitude of $h_0 = 7.1\,\mathrm{km}$. The resulting refraction index at an altitude of $h = 10\,\mathrm{km}$ is thus $n_{\mathrm{air,10\,km}} \sim 1,00007$. Assuming $\beta \sim 1$, the resulting opening angle of the Cherenkov light cone is roughly $0.7^\circ$. These Cherenkov light flashes have a typical duration of $10\,\mathrm{ns}$. The illuminated area on the ground at the mean altitude of IACTs of $2000\,\mathrm{m}$ above sea level has a diameter of roughly $100\,\mathrm{m}$ for a primary $\gamma$ ray of about $100\,\mathrm{GeV}$ and increases up to several hundred meters with increasing primary $\gamma$-ray energy. Cosmic-ray induced EAS lead in general to even broader footprints on the ground compared to a $\gamma$-ray induced EAS with the same energy.

### 2.1.2 Detection Principle

The weak and short flashes of Cherenkov light are detected by IACTs when they fall within the Cherenkov light pool. The telescopes are composed of large spherical or parabolic reflectors with areas of $\sim 10^2\,\mathrm{m}^2$ that are composed of tessellated mirrors, and a fast optical camera to read out the signal. The mirrors collect the Cherenkov photons which are then reflected to the focal plane of the telescope, where the camera is situated. In order to record the short light flashes the cameras of IACTs consist of an array of light amplifying photo multiplier tubes (PMTs) that provide the required resolution on a nanosecond time scale. Light collecting Winston cones are placed in front of the PMTs to reduce the loss of photons due to gaps between the individual PMTs and to reduce stray light in the camera. The mirrors and Winston cones are optimised to particularly reflect light in the wavelength range of $300-600\,\mathrm{nm}$, which is the typical wavelength range of Cherenkov light produced by VHE $\gamma$ rays interacting with the atmosphere.
The resulting image in the camera represents is a two-dimensional projection of the EAS. The imaging geometry is schematically illustrated in Figure 2.2. Whereas the length and the width of the ellipse are determined by the angle under which the shower is observed and the lateral extent of the EAS, respectively, the position of the shower image in the camera is mainly determined by the distance between the shower axis and the reflector axis. The orientation of the image depends on the inclination angle between the shower and the optical axis of the telescope. While $\gamma$-ray induced EAS typically lead to elliptical images in the camera due to their rather small lateral extent, most of the hadron-induced EAS exhibit a more irregular lateral shape resulting in a more complex shower image in the camera. By considering the geometry of the recorded shower images a large fraction of the hadron-induced EAS images can be rejected.

One end of the major axis of the camera image points to the origin of the primary $\gamma$ ray in the sky and the other end towards the impact position of the EAS on the ground. The energy of the

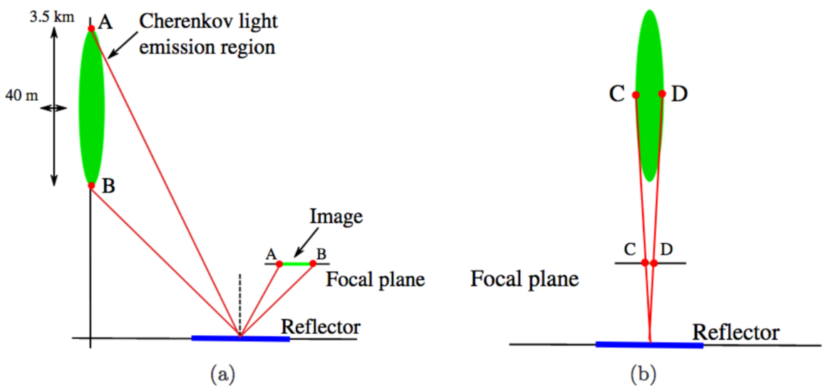

Figure 2.2: Schematic illustration of the imaging geometry in VHE $\gamma$-ray astronomy. (a) Mapping of the EAS into the camera located in the focal plane of the telescope. The image position in the camera is determined by the distance between shower axis and the reflector axis. (b) The EAS as seen from the telescope position. The lateral spread of the EAS as well as the distance between the shower and the telescope affect the width of the camera image. Image taken from [26].

primary $\gamma$ ray can be estimated based on the total intensity of the camera image in combination with the distance between the telescope and the reconstructed shower impact point. The presence of multiple telescopes within a Cherenkov light pool provides a stereoscopic view of the EAS, and significantly improves the geometric reconstruction of the primary photon.

Although the properties of the primary particles can be roughly reconstructed by fundamental geometric considerations, more advanced techniques are required to improve the reconstruction of the direction and the energy of the primary particles. The actual image that is produced by a given particle shower diverges from theoretical predictions due to environmental effects as well as the non-ideal nature of the detectors. Therefore, to reconstruct the energy of the primary particle based on the camera shower images, Monte Carlo (MC) simulations are used. The simulations track the air shower development in the atmosphere and the IACT array, whose components are simulated based on the real instrument including the mirrors and Winston cones as well as the camera [27]. A large number of $\gamma$-ray MC events are generated, covering a broad range in energy and direction. These MC events are then reconstructed in the same way as real $\gamma$ rays. Based on these simulations, *lookup tables* — which compare the properties of the simulated and reconstructed events — are generated and are used to reconstruct the properties of a real primary $\gamma$ ray by comparing the properties of the reconstructed event. Using these MC based lookup tables, the reconstruction of the energy and direction of the primary $\gamma$ ray is significantly improved compared to the basic reconstruction from geometrical considerations. The same MC simulations are also used to produce the instrument response functions (IRFs) of the IACT which are needed for the flux calculation of a $\gamma$-ray source.

### 2.1.3 Sources of Background Noise for IACTs

While $\gamma$ rays can be directly traced back to their source of origin, charged cosmic rays like electrons, protons or heavier nuclei are deflected in the Intergalactic and Galactic magnetic fields and therefore lose the information of their specific source location by the time they reach Earth. Nevertheless, they also produce Cherenkov light and trigger the telescopes, and hence contribute a significant diffuse background. To separate $\gamma$-ray induced EAS from the main source of background, namely, hadron induced EAS, the different shower image profiles as illustrated in the bottom panels of Figure 2.1 can be used.

In addition to the EASs, single muons or stars emit ultraviolet photons and can add a significant amount of background. While muons produce a ring-like image in the camera and can thus easily be identified, the night-sky background due to the low energy ultraviolet photons only triggers individual PMTs of individual telescopes. By requiring that an event must have been observed by at least two telescopes, the impact of the night-sky background can be greatly reduced.

## 2.2 The H.E.S.S. Experiment

The H.E.S.S. experiment, which is named after the pioneering cosmic-ray physicist and Nobel price winner Victor Hess (1883-1964), is one of three currently operating air Cherenkov $\gamma$-ray experiments. Its location in the Southern Hemisphere makes it particularly suitable for observations of the Galactic Plane and has led to a significant number of new sources detected in the VHE $\gamma$-ray regime, laying the foundation for population studies of Galactic sources in the VHE $\gamma$-ray regime. Apart from the Galactic centre, H.E.S.S. is also capable of observing and resolving sources outside of the Galaxy such as the Magellanic Clouds, two close-by satellite galaxies of the Milky Way. The analysis of the source populations of the Magellanic Clouds is presented in this work.

### 2.2.1 The H.E.S.S. Array

The H.E.S.S. array consists of five IACTs that are located in the Khomas Highland of Namibia at 1800 m above sea level. The four identical small-sized telescopes (also called CT1-4) were inaugurated in 2004; each telescope has a mirror diameter of $12$ m and the four are placed in a square with a side length of $120$ m. The telescope separation is chosen to be roughly the size of a typical Cherenkov light cone when it reaches the ground, $\gtrsim 100$ m, to guarantee a mostly stereoscopic view of the shower. A fifth, large-size telescope of $28$ m diameter (CT5) was inau-

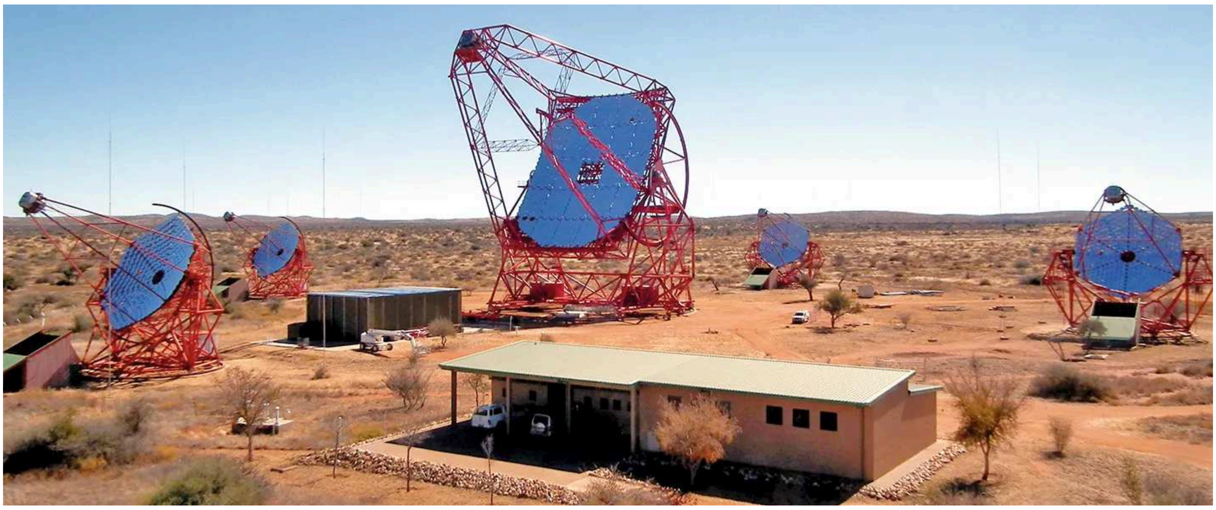

Figure 2.3: The large-size and four small-sized telescopes of the H.E.S.S. array located in the Khomas Highlands in Namibia. Figure taken from [28].

gurated in 2012 and is placed in the centre of the array. The array layout of H.E.S.S. is shown in Figure 2.3. The era between 2004 and 2012 is called H.E.S.S. phase I followed by the H.E.S.S. phase II starting with the operation of CT5 in 2012.

The small-sized telescopes are sensitive to VHE $\gamma$ rays with energies of $\sim 100\,$GeV - $100\,$TeV. Due to its larger size CT5 is more sensitive to low energy $\gamma$-ray events and is optimised for $\gamma$-ray energies of $\sim 30\,$GeV - $10\,$TeV.

To make full use of the stereoscopic view of the telescope array, an event that triggers CT1-4 is only read out, if at least two telescopes of the full CT1-5 hybrid array record the event simultaneously. In addition, due to the ability of CT5 to image showers from lower energy gamma rays on its own, monoscopic events (only seen by CT5) can be read out as well.

### 2.2.2 Technological Concept of the H.E.S.S. Telescopes

All five telescopes consist of two main components: light collecting mirrors that are mounted on a steel support structure and a camera that is installed at the focal plane of the telescope. The small-sized CT1-4 telescopes are equipped with 382 round mirror facets with a total mirror surface of $108\,\text{m}^2$ per telescope, while the larger CT5 consists of 875 mirror facets and has a light collecting mirror surface of $614\,\text{m}^2$. The mirrors are held by an Alt-Az mount that can point the telescope to any position in the sky. The collected Cherenkov light is focussed onto the camera situated in the focal plane at about $15\,$m ($36\,$m for CT5) above the mirror-holding dish [29]. Each camera is composed of 960 (2048 for CT5) light amplifying PMTs, and a light collecting Winston cone is placed in front of each PMT.

Some loss in performance is expected due to the non-ideal properties of the detector components, and must be quantified to properly reconstruct incoming $\gamma$ rays. The optical response describes the performance of the mirrors and the Winston cones. A regular mirror alignment guarantees that the reflected Cherenkov light is focussed into the camera [30]. The mirrors and Winston cones are optimised for reflecting blue and ultraviolet light, since, on the one hand, the Cherenkov light peaks at roughly $330$ nm on the ground [31] and, on the other hand, the night-sky background becomes more significant with increasing wavelengths, as shown in Figure 2.4a.

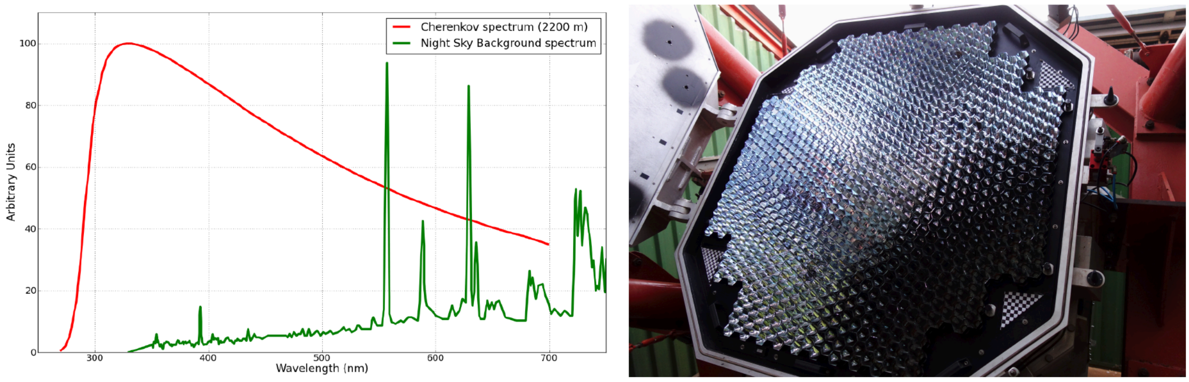

(a)

(b)

Figure 2.4: (a) Spectral energy distribution for the emitted Cherenkov light (red) at the altitude of the H.E.S.S. array and the night-sky background (green). The wavelength range for the optimal signal-to-background ratio is between $300$ nm and $600$ nm. Figure taken from [31]. (b) Design of the camera of the small-sized telescopes.

As the H.E.S.S. telescopes are located in the desert in Namibia, swirled dust settles on the surface of the mirrors and Winston cones leading to a decrease in their reflectivity over time. A recoating and exchange of the mirrors and Winston cones improves the reflectivity for a short time and slows down the degradation process. In addition shadowing effects due to the structural components of the telescopes have to be considered in the MC simulations of the telescopes.

The Cherenkov photons arriving in the PMTs of the camera, which are mapped to pixels, are converted to photo-electrons (p.e.) and the signal is amplified. The light pulses are integrated over the typical pulse duration of $16$ ns and are digitised. Figure 2.4b shows a camera of one of the small-sized telescopes.

The purpose of the H.E.S.S. trigger system is to detect $\gamma$ rays while rejecting as much noise as possible. It operates on two levels: i) on a single telescope level and ii) on a system-wide level. To reject the random low-energy background events due to the ultraviolet photons from stars, a minimum number of three neighbouring pixels with an intensity exceeding a pixel threshold of $5.5$ p.e. within $1.5$ ns is required. Once a telescope fulfils the first trigger criterion, a signal is sent to a central trigger system, where the multi-telescope coincidence decision is made. The second trigger level is passed when at least two telescopes are triggered by an event coincidentally within a trigger time window of $\sim 80$ ns [32]. However, to make full use of the lower energy threshold of CT5, the first trigger criterion is sufficient in the case that only CT5 is triggered by an event. Thus, the array operates simultaneously in stereoscopic and monoscopic modes. With a trigger rate of up to $5\,\mathrm{kHz}$ close to zenith [33], the typical participation fraction, which describes the fraction of events being triggered by a certain telescope, of CT5 is $> 0.8$ [34]. For CT1-4 the participation fraction is significantly lower ($\ll 1$) due to the lower stereoscopic trigger rates of $\sim 250\,\mathrm{Hz}$ close to zenith, hence most of the triggered events are monoscopic events. If an event passes both the individual and system-wide trigger criteria it is finally read out and saved to disk.

During the read-out process — consisting of the multi-telescope event coincidence inquiry, the PMT pulse integration time, the conversion of the PMT data and the data transfer itself — the telescopes are kept busy for a certain time and no further event can trigger the telescopes during this time, known as the deadtime. In the H.E.S.S. phase I era the deadtime for CT1-4 was as high as $\sim 460\,\mu\mathrm{s}$. After an upgrade of the CT1-4 cameras between 2016 and 2017, read-out buffers and new read-out hardware were installed, leading to a significant reduction of the deadtime of $7\,\mu\mathrm{s}$ [35]. The deadtime for CT5 is $15\,\mu\mathrm{s}$ [33].

### 2.2.3 Observations and Calibrations

With a field of view of $5^\circ$ (CT1-4) and $3.5^\circ$ (CT5) and a spatial resolution of $\sim 0.1^\circ$, the H.E.S.S. array is best suited for targeted observations of individual astrophysical sources. The telescopes point towards a selected source in the sky, which is tracked over the duration of the observation as it moves across the sky. Each observation, called an observation *run*, has a duration of $28$ min, which is chosen to balance the integration time over atmospheric variations and the minimum exposure needed for a detection of bright sources like the Crab nebula, which is the standard candle in VHE $\gamma$-ray astronomy. The observations are mainly performed during moonless nights[1]. To account for background inhomogeneities in the source environment, the sources are typically observed in wobble mode [36, 37], where the source is observed at four different camera pointing positions with an offset in Ra and Dec of $\pm 0.7^\circ$ ($\pm 0.5^\circ$) for CT1-4 (CT1-5 or CT5 mono) observations.

The "raw data" that comes from the cameras need to be calibrated to prepare them for the analysis. This step is necessary as variations in the optical response (e.g., mirror-by-mirror variations of the reflectivity) as well as in the camera response (e.g., variations in the single photo-electron response and relative quantum efficiency variations from PMT to PMT) of the instrument can lead to large uncertainties in the event reconstruction.

The overall optical response of the instrument is measured constantly by studying the Cherenkov light of single muons hitting the telescopes or the ground nearby. Muons arriving parallel to the optical axis of the telescope produce well defined ring-like images of Cherenkov light with a

---

[1] Recently, H.E.S.S. started to observe under moderate moonlight with a maximum moon fraction of $\sim$50%. The evaluation of the data is ongoing. However, this work only makes use of observations that were taken under moonless conditions.

radius, given by the angle of the Cherenkov light and the altitude of the IACTs, and a known relation between the measured intensity and the muon energy [38]. A change of the optical response affects directly the measured Cherenkov light intensity in each pixel of the camera and hence the energy reconstruction of the muon. To calibrate for nightly variations in the optical response, a correlation coefficient is estimated for each observation based on the continuously monitored muon rings in the camera.

The camera response is calibrated using two LED systems. A flashing LED in front of the camera is used to measure the single photo-electron response of each PMT. A second LED system, that provides a uniform illumination across the camera, is installed in the centre of each dish to monitor the relative quantum efficiency variations of the PMTs as well as different light collection efficiencies of the Winston cones, which cause an inhomogeneity in the camera. These *single-photo-electron* and *flat-fielding* observations are taken regularly under observation-run conditions.
In addition, each PMT produces an electronic pedestal due to thermal noise inside the PMTs. The electronic pedestal depends on environmental properties such as the atmospheric temperature and the level of night-sky background. Therefore, *electronic pedestal* runs are taken with closed camera lids to turn off the night-sky background to determine the electronic pedestal for each PMT.
The H.E.S.S. standard calibration procedure is summarised in this paper [39].

After the calibration of the data, an image cleaning procedure using a two-level filter is applied to all camera images containing a $\gamma$-like event to further exclude signals in the camera due to night-sky background photons. As the night-sky background photons typically lead to low intensity signals in the pixels, only those pixels that measured an intensity of more than $10$ p.e. and have a neighbouring pixel with an intensity of at least $5$ p.e. (and vice versa) are kept for the event reconstruction. In addition, isolated pixels with an intensity that is more than $3\sigma$ away from the rms of the pedestal value are rejected. In case of a template based event reconstruction (see Section 3.1.3) cleaning thresholds of $7$ p.e. and $4$ p.e. are used and two rows of pixels around the selected pixels are kept as well for an improved estimation of the electronic pedestal.

# Chapter 3

# H.E.S.S. Data Analysis and Systematic Uncertainties

This chapter focuses on the data analysis of H.E.S.S. observations (Section 3.1) followed by an investigation of systematic uncertainties in the data sets (Section 3.2). The systematic uncertainties are then evaluated for a sample of bow shocks of runaway stars in section 3.3.

## 3.1 Data Analysis

The H.E.S.S. data analysis includes multiple steps: a data quality selection, the parametrisation of the camera images, the event reconstruction and $\gamma$-hadron separation, the signal extraction including the estimation of a remaining background, and finally the significance and flux estimation of the measured $\gamma$-ray emission. All these steps are described in detail in the following sections.

### 3.1.1 Data Quality Selection

Varying observational conditions or malfunctioning hardware can affect the quality of the data and thus increase systematic uncertainties in the event reconstruction. On the one hand, hardware related problems like turned-off camera pixels or unusual trigger rates of single telescopes during an observation can affect the event reconstruction itself and lead to increased systematic uncertainties in the estimated source flux and hence in the detection probability. Atmospheric variations on the other hand affect only the energy reconstruction of the events and hence lead to increased uncertainties in the reconstructed flux normalisation. Therefore, the data have to

pass a data quality selection first, before the recorded events are reconstructed. A standardised quality selection is especially important for surveys and population studies with data sets consisting of several hundred or even more than thousand runs, requiring the same systematics over the whole data set.
The following set of hardware and atmosphere-related data quality selection criteria are applied to each data set:

- The live-time of an observation run is required to be $> 10\,\mathrm{min}$ to collect sufficient statistics for determining proper pedestal values of each camera pixel and exclude runs that were truncated due to hardware problems. Besides hardware problems, other reasons like the end of the night, an automated target-of-opportunity observation of a transient source or deteriorating weather conditions can cause a run to get stopped.

- The participation fraction of a small-size telescope has to be $> 0.4$ ($> 0.04$ for CT1-5 observations due to higher CT5 trigger rates) and for the large-size telescope $> 0.5$. A participation fraction of $0.4$ means that each telescope should have triggered on at least 40% of the total number of triggered events. This is equivalent to a mean event multiplicity of $1.6$ assuming that all telescopes have the same trigger rate. If this criterion is not met, it might be an indication of camera hardware problems.

- The allowed fraction of turned-off pixels due to hardware problems is 12.5% (7%) for CT1-4 (CT5) and the allowed fraction due to turned-off high voltage in the pixels is 5% (4%) for CT1-4 (CT5). A higher fraction of turned-off pixels significantly affects the event reconstruction leading to an increase in the systematic uncertainties [40].

- A maximum mean deviation of $1'$ and a maximum rms of $10''$ on the actual tracking position (in Azimuth and Altitude) with respect to the nominal tracking position are required to ensure a stable tracking and guarantee a small systematic uncertainty on the reconstructed source position [41].

∗ The relative fluctuation in the system trigger rate over the entire run is required to be less than $\pm$30% of the mean trigger rate. A rapidly decreasing trigger rate is an indicator for worsening atmospheric conditions caused by an increase of dust attenuation or in-moving haze during the run leading to increased systematic uncertainties on the energy reconstruction.

∗ The system trigger rate fluctuation is required to be less than 10% on the time-scale of minutes. This rejects runs in which, for example, small compact clouds move through the field of view leading to fluctuations in the trigger rate.

∗ The atmospheric transparency coefficient has to be in the range of [0.8,1.2] (arbitrary units, a value of 1 means average atmospheric transparency conditions). The atmospheric transparency coefficient is a combined quantity that is estimated based on the telescope trigger rates, the muon efficiency and the camera gains, and reflects the atmospheric transparency. A cut on this quantity ensures a data set with stable atmospheric conditions and hence moderate systematic uncertainties in the energy reconstruction [42].

The first set of criteria (*detection criteria*, listed with a circle) are typically applied for the purpose of the detection of a typically new source. If a source is already detected and a spectrum is to be derived, the *spectral criteria* (listed with stars) are applied in addition to the detection criteria to ensure stable $\gamma$-ray fluxes over the entire data set and hence constant flux normalisations from run to run. These standard spectral quality cuts are applied to all data sets that are used for this work unless otherwise stated.

### 3.1.2 Image Parametrisation

The pioneering method for the reconstruction of the primary $\gamma$ ray based on the camera image is described by Hillas (1985) [43]. The shower images are parametrised by the *Hillas parameters* that describe the first and second order moments of the ellipse, as shown in Figure 3.1:

- Length L (semi-major axis) and width W (semi-minor axis) of the ellipse.
- Size A (total image amplitude): sum of pixel amplitudes over shower image.
- Orientation of the ellipse
  - Centre of gravity: barycentre of the image amplitudes in the shower image.
  - Local distance d: angular distance between the centre of gravity and the camera centre.
  - Azimuthal angle $\varphi$ of the image main axis with respect to the camera x-axis.
  - Orientation angle $\alpha$ of the major axis with respect to the image main axis.

The geometry and image amplitude of the shower image are necessary to reconstruct the energy of the primary particle, while the orientation of the ellipse in the camera determines the origin in the sky.

Before reconstructing the direction and energy of the primary $\gamma$-ray event, a set of *pre-selection* cuts are applied to all events to guarantee that the showers can be properly reconstructed. The pre-selection level includes a cut on i) the event multiplicity (at least two telescopes are required to have recorded the same event) to guarantee a stereoscopic reconstruction of the event which leads to a significant improvement of the energy and direction reconstruction by

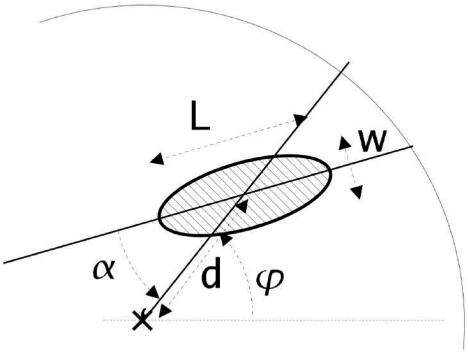

Figure 3.1: Schematic illustration of the Hillas parametrisation. The camera centre is marked with a cross. Figure taken from [44].

minimising uncertainties in the reconstruction, ii) a local distance cut that describes the distance between the centre of gravity of the shower image and the centre of the camera to avoid a reconstruction of truncated events at the camera edge that may result in a mis-reconstruction of the event energy and iii) and a cut on the telescope-wise image amplitude on the shower images to guarantee that the shower image can be properly parametrised. All events that pass the pre-selection cuts are further reconstructed.

### 3.1.3 Event Reconstruction

The well established image parametrisation method using the Hillas parameters delivers reliable results. However, the method is limited in how accurately it can reconstruct the event energy and direction. The use of MC simulations that are performed over a large range in the parameter space (i.e., the primary $\gamma$-ray quantities of energy, zenith angle and impact distance) significantly improves the event reconstruction. The momenta of the MC event camera-shower ellipses and their standard deviations can be inferred through the Hillas parametrisation and are related to the primary MC $\gamma$-ray quantities. By comparing these MC shower images to real shower images, the primary $\gamma$ rays can be reconstructed as the parameters of the corresponding MC primary $\gamma$ rays are known.
This reconstruction method yields an angular resolution of the event direction of $\sim 0.1^{\circ}$ and an energy resolution of 15% [45]. Both the angular and the energy resolution degrade with increasing zenith angles and increasing offsets between the event and the camera centre.

However, this work makes use of the more advanced template-based likelihood fitting method to reconstruct the energy of the primary $\gamma$-ray event [46]. The described analysis framework will be referred to as the ImPACT (Image Pixelwise fit for Atmospheric Cherenkov Telescopes) analysis. The templates are produced for several bins of a five dimensional parameter space of different zenith angles, azimuth angles, energy bands, impact distances and heights of shower maxima.

A large number of MC simulated $\gamma$-ray induced EASs get traced through the simulated telescope array and only those Cherenkov photons that would trigger the camera are kept and treated the same way (as for the Hillas parameter based analysis) as an actual $\gamma$-ray event. Instead of saving Hillas parameters in lookup tables, a complete bin averaged image of the shower is kept (called a template). An example for these templates is shown in Figure 3.2. For the primary $\gamma$-ray energy reconstruction, the Hillas reconstruction is used as a seed, and the corresponding set of templates with the closest parameters in the 4 dimensional parameter space is chosen to perform the likelihood fitting. This method yields an improvement of up to 50% at $500\,$GeV and 15% at $100\,$TeV in angular resolution, resulting in a point-spread function (PSF) with radius $0.07^\circ$ ($0.11^\circ$) for the CT1-4 (CT5) cameras, and a roughly 50% improvement in energy resolution compared to the classical Hillas analysis. Further, the energy threshold is reduced from $\gtrsim 1$ TeV (using the Hillas analysis) to $500\,$GeV at zenith angles of $60^\circ$ and source offsets of $\lesssim 2^\circ$ for CT1-4, with an even lower energy threshold of $100\,$GeV for lower zenith angles and smaller source offsets [45, 46]. (A more detailed description of the energy threshold estimation will be given is Section 3.1.6.) Some adaptations were required to make this template fitting framework suitable for an analysis of CT5 Mono events, since less information are available in a single telescope shower image leading to degeneracies in some of the fitted parameters [47]. For CT5 Mono events, the resulting angular resolution is about a factor of 2 worse than for CT1-4 stereo events of energies of $\lesssim 2\,$TeV, at which point shower images start to get truncated at the edge of the cameras. More importantly, however, the lower energy threshold is reduced to $\sim 30\,$GeV at zenith angles of $\lesssim 20^\circ$, increasing with increasing zenith angle. The improvement of the lower energy threshold will be relevant for this work.

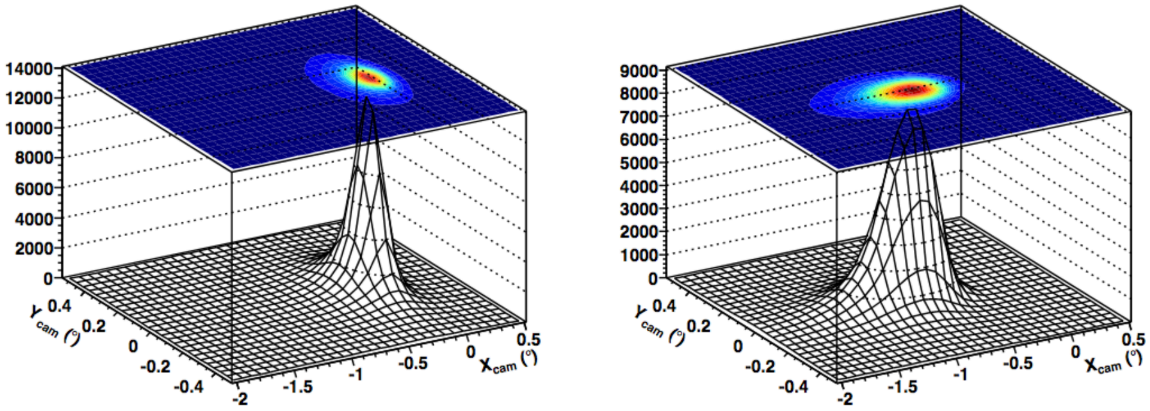

Figure 3.2: Shower image template for a $1\,$TeV primary $\gamma$ ray with an impact distance of $20\,$m (left) and $100\,$m (right) at an expected shower maximum of $300\,$g cm$^{-2}$. The z-axis units are given in p.e. per square degree. Figure taken from [46].

### 3.1.4 $\gamma$-Hadron Separation

After the events have been reconstructed, background rejection procedures select for the $\gamma$-like events for the analysis. Due to the more irregular lateral shape of hadron-induced EAS, the shower images in the camera have a more complex structure than $\gamma$-ray induced EAS, which typically exhibit well-defined elliptical shapes. Based on the classical Hillas parameters per telescope image, mean-scaled parameters of the width and length are calculated for each event by comparing them to the expected shape as determined from MC $\gamma$-ray simulations [45]. Cutting on these shape parameters yields a rejection of about 90% of all hadron induced EAS.

This work makes use of a more advanced $\gamma$-hadron separation framework [48]. The sensitivity of the H.E.S.S. array is improved by up to 45% using this framework, which makes use of the multivariate analysis technique of boosted decision trees for the $\gamma$-hadron separation [48]. The boosted decision trees are trained using the MC simulated $\gamma$ rays as signal and observed off-source events (*off*-Events) as background. The parameters that are used for the event classification are the mean reduced scaled width (MSCW) and mean reduced scaled length (MSCL), the mean reduced scaled width off (MSCWO) and mean reduced scaled length off (MSCLO), the depth of the shower maximum ($\mathrm{X}_{\max}$) and the telescope averaged spread in energy reconstruction ($\frac{dE}{E}$). Based on these parameters a signal-likeliness $\zeta$ is determined for every event splitting the sample of all events of an observation into two distributions, i.e. the $\gamma$-like events and the background events, which is shown in Figure 3.3. Depending on the $\gamma$-hadron separation cuts, the background rejection efficiency of all events that pass the pre-selection cuts can be close to 100% but at the expense of losing most of the $\gamma$ events. Typically a cut on 84% (90%) $\gamma$-ray efficiency is chosen with a background rejection of 98% (to be verified[1]) for the $\gamma$-hadron separation of CT1-4 (CT5 mono) events [49]. The applied cut on the $\gamma$-ray efficiency is part of the *post-selection* cuts to select $\gamma$-like events in the H.E.S.S. standard analysis.

The $\gamma$-ray spectra of observed sources vary strongly between different sources and therefore different sets of cut parameters are generated. This work mainly makes use of the *standard* cut parameter set, which is optimised for Crab-like sources with a flux-level of roughly 10% of the integrated Crab flux. These are suitable for most $\gamma$-ray sources and should be used if the $\gamma$-ray source type is not clearly known. A parameter set with *hard* cuts is used for weak sources (1% Crab flux) with spectra extending to $\gtrsim 10\,$TeV, and a set with *loose* cuts is optimised for strong sources (100% Crab) that mainly emit $\gamma$ rays at lower energies [45].

---

[1] A detailed study of the CT5 performance is ongoing and will be published soon.

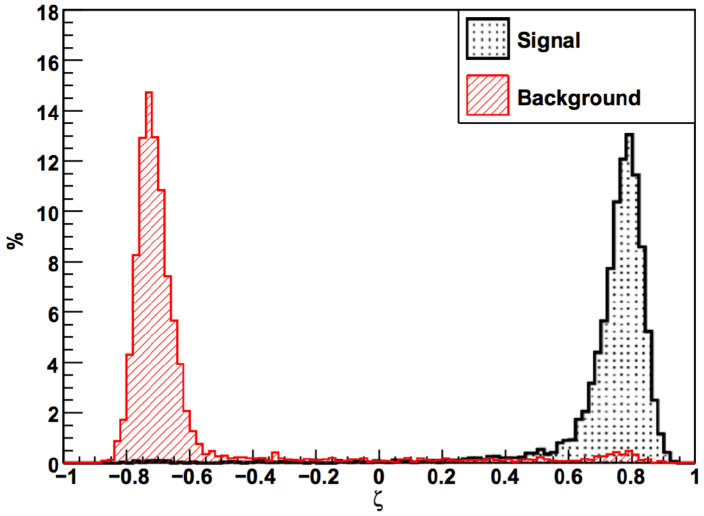

Figure 3.3: Output of the event classification based on the boosted decision tree method for event energies between $0.5 - 1.0$ TeV. The sample of events is separated into $\gamma$-like events and background events. Figure taken from [48].

### 3.1.5 Signal Extraction

$\sim$98% of the hadron-induced events are rejected by the boosted decision tree based $\gamma$-hadron separation. The remaining $\sim$2% of background events are most likely produced by hadronic cosmic rays, that look like $\gamma$-ray induced showers. To estimate the irreducible $\gamma$-like background, observations are taken "off-source" (i.e., not centred on the source position) and the background is estimated from the same observation run.

As a first step, when estimating the background, the reconstructed shower directions for all the $\gamma$-like events are filled into a two-dimensional histogram, called a *sky map*. All observation runs are processed separately during the analysis and the statistics are added to the final result. In a second step, *on* and *off* regions are defined, where the *on* region is a circle with radius $\Theta_{cut}$ centred on the source position. The *on* signal includes all events reconstructed within this *on* region. Depending on whether a sky map or a spectrum of the respective source is to be produced, the background level within the *on* region is either determined by the *Ring Background Model* or the *Reflected Regions Background Model*. As the instrument and reconstruction dependent acceptance for $\gamma$-like events in the camera strongly varies over the field of view, an accurate knowledge of the system acceptance is crucial for the background estimation and hence the estimation of the significance of the signal at the source position.

**Instrument Acceptance**

In general, the system acceptance for a given point in the camera field-of-view depends on

- its exact position with respect to the camera coordinate system and its radial distance to the camera centre. At larger radii, the triggering probability decreases, the $\gamma$-hadron separation cuts discard increasingly distorted shower images, and the background event reconstruction in the camera system becomes less accurate. Therefore, the radial acceptance decreases gradually with increasing radius to about 40% of the peak value at an offset of $2^\circ$ from the camera centre [45];
- the zenith and azimuth angle of the observation. EAS of $\gamma$-ray events observed at large zenith angles develop their shower maxima at larger distances to the telescope array and thus start to get truncated before they reach the focus of the telescopes at $\sim 10\,$km height. Therefore, the camera images of large zenith angle events are smaller compared to low zenith angle events with the same primary energy. This leads to a decreasing acceptance of low-energy events with increasing zenith angle. The Earth's magnetic field adds another asymmetry in the azimuth angle by deflecting the charged cosmic rays resulting in a shift of the reconstructed shower direction;
- the date, when the observation was performed. The increasing degradation of the detector components further decreases the system acceptance;
- variations of the night-sky background, causing inhomogeneities in the camera field of view.

For Extragalactic sources and most of the Galactic sources (in less populated sky regions), inhomogeneities due to the night-sky background can be neglected and zenith-angle effects (only) become important with increasing zenith angles. Therefore, a radially symmetric system acceptance is a good approximation. In addition, inhomogeneities in the background are accounted for by observing the target position in wobble mode in right-ascension and declination and then estimating the background for every observation position. The analysis framework used for this work generates one-dimensional acceptance profiles by estimating the number of background events as a function of the angular distance of the reconstructed event direction with respect to the camera centre. By rotating the one-dimensional radial acceptance profile, a two-dimensional acceptance sky map is generated and is used to scale the sky maps in the whole field of view. The acceptance can be determined either on a run-by-run basis from the observations themselves or from archival observations showing no significant $\gamma$-ray emission in the field of view (off-runs). Both methods have their advantages and disadvantages. In case of acceptance profiles determined from off-runs, lookup tables based on $\sim 2000$ runs divided in zenith angle bands and angular distance bins are produced. Since these off-runs are carefully selected based on their homogenous background distribution and residual inhomogeneities are averaged out over the large number of runs, the acceptance profiles are insensitive to run-by-run variations. On the other hand, although the lookups are available for a variety of combinations in the observational parameter space, they are integrated over time and hence changes in the detector response are averaged out, and the acceptance lookups may therefore not reflect the system acceptance of the data to be analysed. In addition, the event statistics decrease with increasing zenith angle to about 10% at a zenith angle of $50^\circ$ with respect to zenith. Both the limited coverage of the time space and the decreasing statistics at larger zenith angles lead to an increasing uncertainty if acceptance profiles from lookup tables are applied to observations performed at later times or at larger zenith angles. For these cases, it is usually more accurate to determine the system acceptance based on the observations themselves; exceptions are observations with a high night-sky-background level or large zenith angle observations of a well populated source region. Finally, the system acceptance is bound to a specific camera and hence a specific H.E.S.S. era. Since the installation of the HESSIU cameras in 2016, the number of collected off-runs for this era is very limited and thus the available statistics are insufficient to produce a robust set of lookups. Therefore, for all observations that have been taken after the camera upgrade the acceptance profiles are generated from the data itself.

When determined on a run-by-run basis, the acceptance profile reflects the detector response for this particular parameter space. Nevertheless, generating acceptance profiles based on a single run will be less accurate due to the lack of statistics. Another limiting factor is a possible contamination from another source in the field of view. In case of significant $\gamma$-ray emission outside the region of interest, the region with a significant excess of $\gamma$-ray events over background events is excluded from the acceptance determination, leading to a reduced number of background events in the corresponding angular distance bin. This effect is negligible at the edge of the field of view, but causes increasingly large biases towards the camera centre. If the observational offset becomes $\lesssim 0.4^\circ$, i.e., if a potential source were serendipitously observed and hence were not observed with a proper observational offset, determining the radial acceptance from the observations itself will lead to artefacts in the resulting sky maps and can even introduce a significant excess when no $\gamma$-ray excess is present.

For each analysis, an individual decision on whether to use acceptance profiles from the data itself or from lookup tables has to be made.

A common problem for all one-dimensional radial acceptance profiles is the already mentioned zenith angle dependence of the system acceptance. The increasing shower absorption at larger atmospheric depths and the large fields of view of H.E.S.S. of $5^\circ$ and $3.5^\circ$ translate into a zenith-angle dependent gradient in the system acceptance. As increasing absorption of the Cherenkov light causes an increased low energy threshold at larger zenith angles, an energy cut (rejection of all events with energies lower as a given energy threshold) can reduce inhomogeneities due to zenith-angle dependent gradients in the field of view. The importance of energy cuts is discussed in Section 3.1.6.

Depending on the background determination model, the rotated two dimensional acceptance profile is needed to correct the background for the radially decreasing background acceptance.

### Ring Background Model

In the case of the *ring background model* [50] the background is extracted from a ring centred at the *on* region as is shown on the left side of Figure 3.4. The normalisation factor $\alpha$ is approximately the ratio of the solid angle of the *on* region and the solid angle of the ring $\alpha = \frac{\Omega_{on}}{\Omega_{off}}$. To reduce fluctuations in the background estimation, $\alpha$ is typically chosen to be $\sim 1/7$ resulting in a ring radius of typically $0.5^{\circ}$. As the *on* region can be at any position in the field of view, the system acceptance is in general not constant across the ring. To determine the acceptance dependent $\alpha$, the background has to be corrected pixel-wise by the corresponding background acceptance value. In this way, the *ring background model* can be applied to any region in the field of view. Since the background correction is rather insensitive to large scale deviations between the actual and the determined acceptance profile due to the small ring extension compared to the entire field of view, and any linear gradients in the system acceptance are averaged out over the ring, this background model is best suited to generate sky maps showing the entire field of view of the data set. For determining a spectrum at the region of interest, a different background model has to be used.

### Reflected Regions Background Model

In the case of the *reflected regions background model* [50] the background is extracted from $N_{off}$ off regions arranged in a circle around the camera centre with all *off* regions having the same shape, size and offset to the camera centre as does the *on* region. This method can only be applied if the target source is observed in a wobble mode, with the optimised wobble offset being $0.5^{\circ}$ - $0.7^{\circ}$. As the *on* and *off* regions all have the same offsets to the observation position, their is no system acceptance correction necessary as it is radially symmetric, when determined as described in Section 3.1.5. The normalisation factor $\alpha$ is simply given by $\frac{1}{N_{off}}$. By observing the target source at equal offsets in RA and Dec and applying the *reflected regions background model* to every observation as is shown for two observation positions on the right hand-side of Figure 3.4, any large-scale, linear background gradients get averaged out. Due to its independence of the radially symmetric system acceptance and the *on* and *off* event offset distributions being identical, this method is best suited for a spectral analysis of the region of interest.

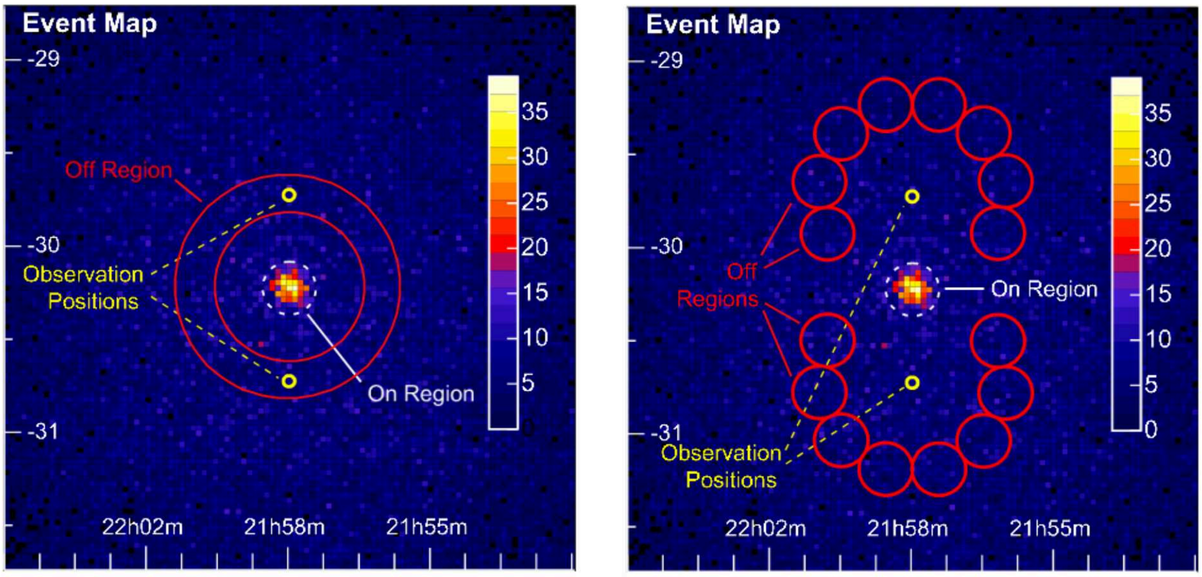

Figure 3.4: Schematic illustration of the *ring* (left) and *reflected region* (right) *background model*. The *on* region is indicated with a white dashed circle. The background in either case is estimated based on the events inside the *off* regions shown in red. Figure taken from [50].

### Significance Computation

Due to the typically low signal-to-background ratio and the detector sensitivity in $\gamma$-ray astronomy, the significance of a $\gamma$-ray signal needs to be carefully estimated to prove that an excess of $\gamma$ rays is due to a source rather than a fluctuation in the background. The significance of a VHE $\gamma$-ray signal is computed based on the number of *on* events ($N_{on}$) and *off* events ($N_{off}$) within the region of interest with radius $\Theta_{cut}$. The excess of events $N_{excess}$ in the signal region over the background events is given by:

$$N_{excess} = N_{on} - \alpha N_{off},$$

where $\alpha$ is the normalisation factor which depends on the exposure time, the zenith angle of the observation, the solid angle and acceptance differences between the *on* and *off* regions. Based on the number of events in the *on* and *off* regions and the normalisation factor $\alpha$, the statistical significance S of the excess in the *on* region can be derived by following the approach of Li & Ma (1983, Eq. 17) [51]:

$$S = \sqrt{2}\left\{N_{on}\, ln\left[\frac{1+\alpha}{\alpha}\left(\frac{N_{on}}{N_{on}+N_{off}}\right)\right] + N_{off}\, ln\left[(1+\alpha)\left(\frac{N_{off}}{N_{on}+N_{off}}\right)\right]\right\}^{1/2}. \tag{3.1}$$

A potential VHE $\gamma$-ray source is typically defined as a significant VHE $\gamma$-ray emitter when the significance $S$ exceeds $5\sigma$.

However, a blind search for significant VHE $\gamma$-ray emission over a wide field of view considerably increases the number of test positions (trials). As the probability of detecting a region with a certain significance increases with increasing trials, the measured significance should be corrected for the number of trials to get an estimate of the "true" significance of a potential source. Under the assumption that the significance distribution follows a normal distribution, the *post trial* significance can be computed via

$$1-\mathrm{erf}\left(\frac{\sigma_{\text{post}}}{\sqrt{2}}\right) = n_{\text{trials}}\left(1-\mathrm{erf}\left(\frac{\sigma_{\text{pre}}}{\sqrt{2}}\right)\right)$$

$$\Leftrightarrow$$

$$\sigma_{\text{post}} = \sqrt{2}\,erf^{-1}\left[1-n_{\text{trials}}\left(1-\mathrm{erf}\left(\frac{\sigma_{\text{pre}}}{\sqrt{2}}\right)\right)\right],$$

with erf being the Gauss error function.

### 3.1.6 Effective Area and Energy Threshold

To reconstruct the $\gamma$-ray flux from a source, the effective area of the instrument as well as the definition of the valid energy range are needed. The effective detection area is comparable to that of the Cherenkov light pool on the ground and is a function of the zenith angle, the azimuth angle, the offset between the source position and the observation position, the $\gamma$-ray energy and the selection cuts that are applied. By using MC simulations of $\gamma$-ray events with fixed parameters over the entire phase space, the effective area is modelled by counting the fraction of simulated events fulfilling the array trigger rate requirements and selection cuts as a function of the energy [52]. To cover the entire parameter space, the discrete instrument response functions are interpolated. In general, the effective areas can be determined either as a function of true ($E_{\text{true}}$) or reconstructed energy ($E_{\text{reco}}$). For H.E.S.S. analysis, the effective areas as a function of $E_{\text{true}}$ are used as they do not depend on the simulated energy spectrum, and it leads to more accurate results when determining an integrated effective area over the whole energy spectrum, as needed for the production of sky maps.

In addition, an accurate reconstruction of the event energy is crucial for the spectral reconstruction. The uncertainty of the spectral reconstruction increases at the lowest (and highest) end of the $\gamma$-ray spectrum caused by either an increasing bias in the event energy reconstruction or by the decreasing effective area with decreasing event energy. Both the energy bias as well as the effective area can be used to determine the safe energy threshold for the spectral reconstruction. The former method is typically used for the CT1-4 data. The energy bias $\Delta_E$ is defined as $\Delta_E = \frac{E_{\text{reco}}-E_{\text{true}}}{E_{\text{true}}}$, where $E_{\text{true}}$ is the simulated true $\gamma$-ray event energy and $E_{\text{reco}}$ is the reconstructed event energy. The left panel of Figure 3.5 shows the relative energy bias as a function of $E_{\text{true}}$ for zenith angles of $20^{\circ}$, $45^{\circ}$ and $55^{\circ}$ at an event offset of $2.0^{\circ}$ to the observation position. The safe energy threshold is defined at energy $E_{\text{true,min}}$, where the energy bias is $\Delta_E \leq 0.1$ [45]. The absorption of Cherenkov light in the atmosphere increases with increasing atmospheric depth at larger zenith angles. This effect increases with decreasing $\gamma$-ray energy, causing higher spectral energy thresholds at larger zenith angles. The energy threshold also increases with increasing event offset (not shown in the figure) due to selection cut effects. Events with offsets close to the edge of the field of view can be truncated and hence, for these events, a mis-reconstruction is more likely compared to events with lower offsets. This effect can be taken into account by applying cuts on the reconstructed primary photon direction.

When analysing CT5 data, it is better to use the effective area to determine the safe energy threshold as the event reconstruction of events seen by a single telescope becomes more uncertain. Especially at large zenith angles, the energy bias does not fall below the 10% threshold over the whole energy range. Effective areas as a function of $E_{\text{true}}$ are shown in the right panel of Figure 3.5 for zenith angles of $20^{\circ}$, $45^{\circ}$ and $55^{\circ}$ at an offset of $1.5^{\circ}$. The safe energy threshold is defined at energy $E_{\text{true,min}}$, where the effective area reaches 10% of its maximum.

The energy spectrum is only reconstructed above the safe spectral energy threshold to avoid large systematic uncertainties close to the analysis energy threshold.

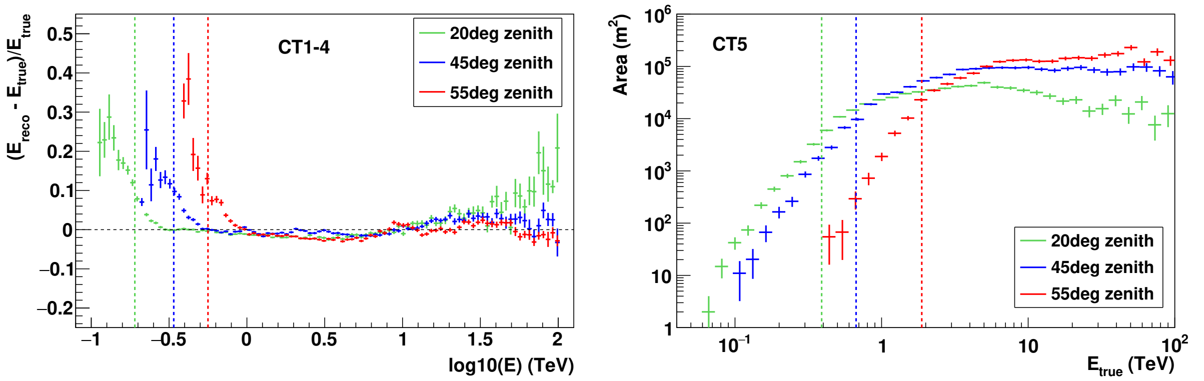

(a)

(b)

Figure 3.5: (a) Relative energy bias as a function of energy for zenith angles of $20^{\circ}$ (green), $45^{\circ}$ (blue) and $55^{\circ}$ (red). The respective energy thresholds at an energy bias of 10% are indicated with vertical lines. (b) Effective collection area for CT5 as a function of true energy for zenith angles of $20^{\circ}$ (green), $45^{\circ}$ (blue) and $55^{\circ}$ (red). The vertical lines denote the respective energy thresholds at 10% of the maximum of the effective area.

### 3.1.7 Spectral Energy Reconstruction and Flux Calculation

After applying the safe energy threshold cut to the reconstructed events, the $\gamma$-ray spectrum of a potential $\gamma$-ray source can be reconstructed. The differential energy spectrum that is estimated via

$$F(E_{\mathrm{true}}) = \frac{\mathrm{d}^3 N}{\mathrm{d}E_{\mathrm{true}}\,\mathrm{d}A\,\mathrm{d}t}$$

depicts the number $N$ of $\gamma$ rays per true energy $E_{\mathrm{true}}$, area $A$ and time interval $t$. However, the quantity measured by H.E.S.S. ($N_{excess}$) reflects the $\gamma$-ray rate after the $\gamma$-hadron separation and background rejection in dependence of the reconstructed energy $E_{\mathrm{reco}}$:

$$\frac{\mathrm{d}N}{\mathrm{d}E_{\mathrm{reco}}\,\mathrm{d}t} = \int_0^\infty P A_{\mathrm{eff}} F(E_{\mathrm{true}})\,\mathrm{d}E_{\mathrm{true}}. \tag{3.2}$$

$P$ is the probability density function describing the probability of an event with energy $E_{\mathrm{true}}$ being reconstructed with an energy $E_{\mathrm{reco}}$ and is directly related to the energy resolution and the energy reconstruction bias. $A_{\mathrm{eff}}$ is the effective collection area $\tilde{A}_{\mathrm{eff}} = \int 2\pi\, r\,\mathrm{d}r P_\gamma$, where $P_\gamma$ is the $\gamma$-ray detection probability, convolved with the $\gamma$-ray selection efficiency. Both quantities depend on the true primary $\gamma$-ray energy, the zenith angle, the azimuth angle and the event offset to the observation position of the instrument, while $P$ additionally depends on the reconstructed event energy. Equation 3.2 cannot be solved analytically for the differential energy spectrum $F(E_{\mathrm{true}})$. Instead, approaches such as $\chi^2$-fitting, unfolding or forward folding can be used. This work makes use of the forward folding approach, where an assumed spectral energy distribution with a predefined spectral shape is folded with the instrument response functions and compared to the measured energy distribution. Typically, the spectral energy distributions are assumed to follow a power law, an exponential cut-off power law, a curved power law or a broken power law.

The expected spectral energy distribution is determined on a run-by-run basis in $n$ reconstructed energy bins $[E_{\mathrm{reco},i}, E_{\mathrm{reco},i+1}]$ above the spectral energy threshold. In practise, the expected number of $\gamma$-ray and background events is determined for the given spectral energy shape by integrating Equation 3.2 over time and reconstructed energy within the bin edges and then summing up over all runs. The best estimate for the expected $\gamma$-ray and background events is obtained by maximising the probability to observe a specific number of $\gamma$-ray and background events, given that a certain number of $\gamma$-ray and background events is expected, in the regime of Poisson statistics. Finally, the best estimate for the differential spectral energy distribution is obtained by minimising the negative log-likelihood $-L = -log(P)$ while varying the spectral parameters (e.g. norm, index, cut-off) of the assumed spectral shape. As the expected source spectrum $\phi_{\mathrm{fit}}$ is determined directly from the $\gamma$-ray and background events, no flux points need to be calculated. However, this is done in a separate step by comparing the measured excess events per energy bin to the expected number of events $n_\gamma$:

$$F(\bar{E}) = \frac{(N_{\mathrm{on}} - \alpha N_{\mathrm{off}})\, \phi_{\mathrm{fit}}(E)}{n_\gamma}.$$

The flux value is given at a mean energy $\bar{E}_i$ of the respective energy bins, which is determined from the determined fit function and the effective area at the true energy. For more information the reader is referred to [26, 45, 53].

### 3.1.8 Upper Limit Estimation

Although a detection of significant $\gamma$-ray emission from a potential $\gamma$-ray source is desirable, most of the observations result in non-detections. However, even a non-detection can help to improve the understanding of acceleration and radiation mechanisms in the Universe. By estimating upper limits on the flux level of the investigated source and hence excluding a higher flux at a certain confidence level, models predicting a particular flux level can be constrained. In $\gamma$-ray astronomy the two most commonly used approaches to estimate upper limits are the frequentist and the bayesian approaches. Whereas a Bayesian makes statements about the true value of a measured parameter like "The confidence level $\alpha$ is my degree of belief that the true value is indeed within the calculated confidence interval,", a Frequentist makes statements about the limits of the confidence interval based on a large statistical sample like "When I calculate the confidence interval with a confidence level $\alpha$ for a repeating experiment, then $\alpha$% of the calculated confidence intervals should contain the true value." The analysis framework that is used for this work follows the frequentist approach that is described by Rolke, Lopez & Conrad (2005) [54]. This method allows for the treatment of problems with several not well-known nuisance parameters and is adapted to problems with small signals. Although this method has its limitations, due to an incorrect coverage in cases of small signals where parameters lie close to the physical boundaries, the main advantage of this method is the treatment of efficiencies of the experiment with a Binomial or Gaussian distribution. This allows for the inclusion of the systematic uncertainties of an experiment into the estimation of confidence intervals.

Upper limits on the flux can be reported as either differential or integral upper limits. While differential upper limits are the preferred option when comparing the excluded flux level for a certain source to its spectral energy distribution or model predictions for a differential flux, integral upper limits contain information about the total energy in $\gamma$ rays in a defined energy interval and thus reveal information about the total energy in cosmic rays in a certain energy range. In both cases assumptions about the spectral behaviour have to be made. Typically, a spectrum following a power law with spectral index $\Gamma$ is assumed:

$$\frac{dN}{dE} = N_0 \times \left(\frac{E}{E_0}\right)^{-\Gamma}, \tag{3.3}$$

where $N$ is the number of particles per area $A$ and time interval $t$. By comparing the expected number of $\gamma$ rays

$$dN_{\text{expected}} = \int_{E_{\min}}^{E^{\max}} A_{\text{eff}}(E) \times t \times \left(\frac{dN}{dE}\right) dE$$

to the actually measured excess of $\gamma$ rays and setting

$$dN_{\text{expected}} = dN_{\text{measured}} = dN_{\text{excesslimit}}$$

the upper limit on the number of particles at energy $E_0$ can be inferred via

$$N_0 = dN_{\text{excesslimit}} \times \left[\int_{E_{\min}}^{E_{\max}} A_{\text{eff}}(E)\, t\, \left(\frac{E}{E_0}\right)^{-\Gamma} dE\right]^{-1}.$$

The integral upper limit on the number of $\gamma$ rays $dN_{\text{ul}}$ is then calculated by integrating Equation 3.3 over a defined energy interval [$E_{\min}, E_{\max}$]

$$dN_{\text{ul}} = \int_{E_{\min}}^{E_{\max}} \frac{dN}{dE} dE \tag{3.4}$$

and the differential flux upper limit is calculated via

$$\frac{dN_{\text{ul}}}{dE} = \frac{1}{dE} \int_{E_{\min}}^{E_{\max}} \frac{dN}{dE} dE. \tag{3.5}$$

To infer information about the total energy content in $\gamma$ rays in a certain energy range, the upper limits are typically translated into upper limits on the energy flux through

$$E^2\, dN_{\text{ul}} = \int_{E_{\min}}^{E_{\max}} E \frac{dN}{dE} dE. \tag{3.6}$$

When comparing the results for various sources located at different distances, it is more convenient to estimate upper limits on the distance independent luminosity of the source:

$$L_{\text{ul}} = 4\pi d^2 \times \int_{E_{\min}}^{E_{\max}} E \frac{dN}{dE} dE. \tag{3.7}$$

These equations will be used in chapter 5.

## 3.2 Systematic Uncertainties

All physical measurements come with uncertainties limiting their accuracy. Apart from statistical uncertainties that cannot be reduced, systematic uncertainties are of great importance when experimental results are discussed. The latter lead to a (one-sided) bias in the experimental results and may lead to inaccurate interpretations of the data.

In the H.E.S.S. experiment systematic uncertainties are mainly related to the MC simulations (required for the event reconstruction), instrument components like the camera and the read-out process, variations in the data sets due to varying observational conditions, and the choice of the analysis framework. The data calibration and the data quality selection cuts, which are described in Section 2.2.3 and 3.1.1, respectively, significantly reduce potential systematic uncertainties in the event reconstruction. However, not all systematic uncertainties can be corrected for. In this section the remaining systematic uncertainties in a data set are investigated in more detail.

### 3.2.1 Monte Carlo Simulations

For real events, atmospheric monitoring devices help to monitor quantitative criteria of the sky quality like its transparency or the cloud coverage for every single observation. In contrast, the MC simulations are only performed for predefined observational periods by assuming a constant atmosphere (and a mean optical efficiency); for these, the atmospheric monitoring devices deliver quantitative criteria of the atmospheric properties for the MC simulations. However, due to its highly turbulent character — i.e., seasonal varying atmospheric profiles and changing content of aerosols — the atmosphere is the least well understood component of the Cherenkov detector. A precise simulation of the atmosphere is crucial, since the amount of Cherenkov light that reaches Earth strongly depends on variations in the atmosphere. Systematic deviations of the atmospheric model from the actual atmospheric conditions lead to a shift of the $\gamma$-ray event energy and hence to a systematic uncertainty on the energy scale. There are three main components contributing to the final systematic uncertainty of the energy scale related to the shower simulation in the atmosphere: the shower interactions, the modelling of the atmosphere and the detector simulation.

The systematic uncertainties due to the simulation of the shower interactions (which are well known) are small as only electromagnetic interactions are considered. Whereas the systematic uncertainty due to the applied shower interaction simulation is constant and estimated to be less than 1% [45], the systematic uncertainty due to variations in the atmosphere, i.e. a seasonal change of the atmospheric density profile or variations in the atmospheric transmission, depend on the underlying data set. The seasonal change of the atmospheric density profile at the H.E.S.S. site is illustrated in Figure 3.6. Changes in the density profile mainly influence the production of the Cherenkov light, thus leading to systematic uncertainties in the energy reconstruction of the primary $\gamma$ ray. Whereas observations are taken during the whole year and hence cover winter and summer periods, the MC simulations are done for an averaged density profile, leading to a systematic uncertainty on the energy scale of 1% for a dataset taken only during one season; this increases up to 4% for a dataset that covers summer and winter seasons [55]. Variations in the atmospheric transmission or extinction coefficient caused by variations in the density of aerosols and ozone lead to variations in molecular scattering and absorption of secondary particles. The systematic uncertainty due to atmospheric transmission variations is estimated to be $f \equiv \Delta E/E = 5\%$ at a zenith angle of $0^\circ$ [56] and increases with increasing zenith angle as

$$f(z) = \frac{f(0)}{cos(z)}. \tag{3.8}$$

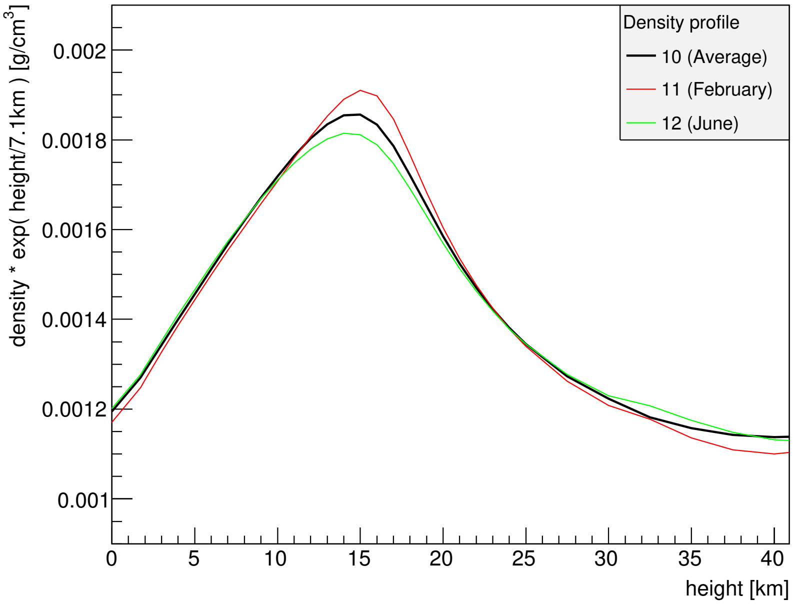

Figure 3.6: Density profiles for Windhoek. Shown are the yearly averaged density profile (black) as well as the density profile for February (red) and for June (green). The normalisation is based on the barometric formula. Image Credit: Heike Prokoph.

Systematic uncertainties due to the instrument simulations are rather small. Since the instrument parameters are well known, the systematic uncertainty on the flux is less than 1% over almost the entire energy range for a given simulated telescope type. The systematic uncertainties only increase at the energy threshold, where the trigger has to be understood very well, and at very high energies, where the shower images are truncated by the edges of the cameras; here they can be as high as 10% for CT5 [57].

### 3.2.2 Instrument Related Systematic Uncertainties

The two main components of instrument related systematic uncertainties are broken pixels in the camera and the dead time during the read-out process[2].

Since PMTs are sensitive to single photons, too many photons arriving at the same time can damage the PMTs. Bright stars in the field of view as well as meteorites, lightning, airplanes or satellites can trigger the over-current protection which turns the affected PMT off. In case of a transient event (i.e. a meteorite crossing the field of view), the pixels are turned on again after some minutes. Broken or turned-off pixels in the camera affect the $\gamma$-ray energy reconstruction as a broken pixel within a shower image leads to a slight mis-reconstruction of the total image amplitude, an important parameter for the primary $\gamma$-ray energy reconstruction, and hence causes a systematic uncertainty on the energy scale. A reconstruction is no longer possible when several broken or turned-off pixels lie within the shower image. For a standard Hillas analysis the systematic uncertainty on the flux due to individual broken / turned-off pixels is about 5%, whereas in the case of the more robust template fitting framework the systematic uncertainty is most likely less than 5%. For a more accurate estimate on the systematic uncertainty due to broken pixels, a data set dependent detailed study would be needed which is beyond the scope of this work. However, the systematic uncertainty due to broken pixels is only a subdominant contribution compared to the systematic uncertainty due to the atmosphere for example.

The camera trigger and read-out status information are stored for each event and each telescope, and is later used to precisely estimate the dead-time of the system. The systematic uncertainty on the flux estimate due to the dead-time estimation is therefore less than 1%. Nevertheless, software or hardware problems can increase the systematic uncertainty on the dead-time estimation as well as the so-called more relevant ghost events, caused by an increased electromagnetic noise in the camera when the data transfer starts, leading to a self-trigger of the camera. If a ghost event keeps the telescope busy, the dead-time increases, whereas the lifetime stays unchanged since no real event was recorded. Until June 2015, up to 5% of the events that triggered the CT5 camera were caused by ghost events, which directly translates to a $\lesssim$ 5% systematic uncertainty on the estimated flux for observations taken until Summer 2015. For observations taken after Summer 2015 a systematic uncertainty of 1% is assumed.

---

[2] There is one further instrument related systematic uncertainty, the pointing accuracy, which has no affect on the flux estimation. The pointing accuracy of the telescopes is mainly limited by the deformation of the support structure while pointing to the target position. These affects are well understood leading to a systematic pointing error of $\lesssim 20''$ [58].

### 3.2.3 Data Set Related Systematic Uncertainties

Variabilities in the observational conditions (e.g., short-term and long-term variations of the atmosphere) or the choice of the analysis framework lead to systematic uncertainties that are dependent on the data set and thus have to be investigated for every data set individually.

#### Run-by-Run Variability

The run-by-run variability is mainly caused by a variability of the atmospheric transparency coefficient leading to a variability in the measured flux [42]. For data sets taken over long time periods, the observational conditions and instrument responses may vary strongly. Variations in the measured flux between single observations are more likely to lead to increased systematic uncertainties in the final $\gamma$-ray flux measurement. The highest impact on the measured flux uncertainties originates from short time-scale variabilities in the atmospheric transparency, leading to a variation in the absorption of Cherenkov light and hence a systematic uncertainty on the energy reconstruction, which translates into a systematic uncertainty in the flux measurement. The systematic uncertainty due to a variability of the atmospheric transparency is estimated by taking the rms of the atmospheric transparency coefficient of all observations in a data set and has to be estimated for every data set individually.

#### Data Set Variability

When several data sets of the same source are taken, observational conditions can vary strongly between the data sets. In particular, if the observations are taken at different zenith angles, variations in the energy thresholds of the individual data sets can result in a systematic uncertainty in the spectral index [45]. A systematic uncertainty on the flux normalisation is covered by the systematic uncertainty estimation due to run-by-run variability.

#### Background Estimation

Systematic uncertainties in the background estimation mainly originate from a non radially symmetric system acceptance or systematic deviations of the background estimation at the edges of the camera. For both the *ring background model* and the *reflected region background model*, the systematic uncertainty on the background estimation has to be investigated separately.
When a sky map is produced and hence the *ring background model* is applied, for an observation without any significant $\gamma$-ray signal, the significance distribution of the background events follows a gaussian distribution centred at zero due to statistical fluctuations. Any deviation from

the normal distribution can be a hint of a systematic uncertainty in the background subtraction. For larger source extensions, for example, larger ring radii are needed and the background estimation therefore becomes more sensitive to acceptance deviations resulting in an increased systematic uncertainty. In the case of other $\gamma$-ray sources in the field of view, which have to be excluded from the background estimation, the exclusion region leads to reduced background statistics and hence higher systematic uncertainties, since the acceptance gradients would no longer cancel out. Another problem is caused by $\gamma$-ray sources in the field of view with fluxes just below the detection threshold resulting in an overestimation of the background; and these produce a shift or a broadening of the gaussian distribution. Without any significant $\gamma$-ray signal in the field of view, the systematic uncertainties are shown to be at a 1% level [45]. However, the exact systematic uncertainties may vary from data set to data set and thus should be estimated for every data set individually.

Deviations from a radially symmetric acceptance are mostly accounted for in the *reflected region background model* and edge effects in the camera field-of-view only become important in case for unusually large source offsets to the observation position. However, in the case of a source being serendipitously observed or being observed while performing a scan of the sky region, observations with different offsets contribute to the data set. In that case, relative system acceptance corrections between the single observations with different offsets have to be applied to the *on* and *off* regions to correct for deviating background acceptances. Nevertheless, this correction increases the systematic uncertainty of the background estimation, since background gradients cannot be properly averaged out anymore. The same is true for a background estimation with excluded $\gamma$-ray sources in the same field of view, preventing the model from finding enough suitable reflected background regions and thus lowering the available background statistics, or in the case of close-by source with a $\gamma$-ray emission just below the detection threshold as described for the *ring background model*. Like for the *ring background model* a study of the actual systematic uncertainties of the background estimation for the underlying data set has to be performed for each data set separately.

Systematic uncertainties in the background estimation lead to uncertainties in the reconstruction of the $\gamma$-ray spectrum and thus systematic uncertainties in the flux calculation as well as on the spectral index have to be investigated.

### Selection Cuts

The event reconstruction method and the selection cuts depend on the software that is chosen for an analysis and are typically optimised for sources with a particular VHE $\gamma$-ray spectrum. The choice of selection cuts is in most cases biased due to assumptions made about the source of interest. A comparison of the results based on different applied selection cuts and / or with results from using a completely different reconstruction framework leads to a data set dependent estimate on the systematic uncertainty in the flux measurement.

The two components of the systematic uncertainty due to data-set variability and the choice of selection cuts should only be considered in the case of a significant $\gamma$-ray emission. For a non-detection, statistical uncertainties dominate and would bias the estimation of systematic uncertainties due to the choice of selection cuts and data set variability only affects the spectral index of a $\gamma$-ray spectrum which can only be measured in the case of a significant $\gamma$-ray emission.

### 3.2.4 Summary of Systematic Uncertainties

All three main components that contribute to the total systematic uncertainty of a data set affect the measurement of the absolute $\gamma$-ray flux. Some of the components affect the flux estimation directly, while others affect the reconstruction of the energy scale and hence have an indirect impact on the flux calculation. The systematic uncertainties on the energy scale can be translated into systematic uncertainties in the flux estimation. It is shown, that the systematic uncertainty on the energy scale is mostly energy and impact distance independent and hence can be assumed to be constant. The systematic uncertainty on the energy scale directly translates into a systematic uncertainty in the flux measurement. If the $\gamma$-ray flux can be perfectly described by a power law (Equation 3.3), the systematic uncertainties on the flux are given by

$$\sigma_{F,\mathrm{syst}} = \left(\frac{dN}{dE}\right)_{meas} \times (1 \pm f(z))^{-\Gamma} \tag{3.9}$$

for a differential flux point or by

$$\sigma_{F,\mathrm{syst}} = \left(\frac{dN}{dE}\right)_{meas} \times \left((1 \pm f(z))^{-\Gamma-1} - 1\right) \tag{3.10}$$

for the integrated flux. The required spectral index is either taken from the spectral reconstruction of a $\gamma$-ray source or, in the case of a non-detection, an assumption about the spectral index of the potential $\gamma$-ray source.

A summary of all systematic uncertainties of a data set is given in the next section in Table 3.2, where the systematic uncertainties of data sets are studied based on a sample of bow shocks of runaway stars. For data set independent systematic uncertainties the fixed values are listed in the table. The data-set dependent systematic uncertainties are marked with a star.
The validation of all instrument component and data set related systematic uncertainties, described in the previous sections, is only given after a data quality selection is performed on the corresponding data set.

## 3.3 Study of Systematic Uncertainties of Bow Shocks of Runaway Stars

Based on the detection of non-thermal radio emission from the bow shock of the runaway star BD 43°3654 [59], confirming that at least electrons are accelerated to relativistic energies, models have been developed that predict VHE $\gamma$-ray emission at up to TeV energies from bow shocks of runaway stars [59–62]. A number of bow shocks of runaway stars listed in the second E-BOSS catalogue release were serendipitously observed by H.E.S.S. during the HGPS [63]. As surveys are typically performed with a systematic observation strategy, they deliver an ideal data set with which to perform mostly unbiased population studies for sources located in the core region of the survey. However, sources that are located at the edge of the field of view may suffer from increased systematic uncertainties. The data sets of the bow shocks of runaway stars observed by H.E.S.S. cover a large observational phase space (i.e. zenith angle, target offset to the observation position, exposure, coverage by different observation positions) and therefore deliver an ideal sample with which to study the systematic uncertainties of a source population with a large range of observational parameters. This section describes first the H.E.S.S. data analysis of a selected sample of bow shocks of runaway stars and second, investigates the systematic uncertainties and their impact on the flux upper limit estimation. The results and discussion of the analysis of the full sample of bow shocks of runaways stars that were observed by H.E.S.S. can be found in Appendix B.

### 3.3.1 Data Analysis of Selected Bow Shocks

A representative subsample of five bow shocks of runaway stars with the most extreme observational parameters in exposure, observation period, zenith angle and source offset to the observation position is chosen to study the range of systematic uncertainties in the data sets of this source population. All bow shocks are analysed with the ImPACT analysis method [46] as described in Section 3.1.3, and standard cuts are adopted. As the PSF of the H.E.S.S. instrument in combination with the ImPACT analysis method has a radius of $\sim 0.07^{\circ}$, the bow shocks in the selected sample, which all have an angular extent of $< 0.07^{\circ}$, are assumed to be point sources and are analysed at the position of the respective runaway star given in the second E-BOSS catalogue release. The background is estimated by using the *reflected regions background model*. The acceptance profile is determined from lookup tables as most of the sources were observed serendipitously without proper wobble observations and most of the bow shocks are located close to the Galactic plane, where contamination due to the presence of other sources in the field of view would significantly increase the systematic uncertainties in the background estimation. The significance of the $\gamma$-ray emission for each bow shock is estimated

Table 3.1: Observational parameters and results for the selected bow shocks of runaway stars from the second E-BOSS catalogue release.

| | HIP 38430 | HIP 44368 | HIP 72510 | HIP 98418 | J 111-6120 |
|---|---|---|---|---|---|
| Longitude [°] | 243.16 | 263.10 | 318.77 | 71.60 | 291.88 |
| Latitude [°] | 0.36 | 3.90 | 2.77 | 2.90 | $-0.50$ |
| Distance [pc] | 900 | $1900 \pm 200^a$ | 350 | 529.1 | 7600 |
| Live-time [h] | 1.75 | 7.85 | 12.76 | 4.05 | 52.91 |
| Mean (max) zenith angle [°] | 11.0 (18.0) | 27.8 (54.4) | 34.7 (44.0) | 59.0 (60.4) | 40.0 (54.0) |
| Mean offset to camera centre [°] | 2.41 | 0.70 | 2.18 | 0.77 | 1.12 |
| Significance [$\sigma$] | -0.03 | 1.92 | 2.13 | 0.93 | -0.23 |
| Integral flux upper limit $[10^{-12}\,\mathrm{TeV\,cm^{-2}\,s^{-1}}]$ | 34.06 | 7.95 | 19.08 | 30.34 | 2.27 |

Coordinates and distance are taken from the second E-BOSS catalogue release [65]. Observational parameters correspond to the H.E.S.S. data sets.

[a] The distance uncertainty is wrong in the second E-BOSS catalogue release ($1900 \pm 0.1$ pc), the correct value is $1.9 \pm 0.2$ kpc [66].

Integral flux upper limits are estimated at a 95% confidence level by assuming a spectrum following a power law with a spectral index of $\Gamma = 2.5$.

based on the *on* and *off* events using Equation 3.1.

None of the analysed bow shocks of runaway stars show significant VHE $\gamma$-ray emission in the energy range of $\sim 300$ GeV to $\sim 50$ TeV and, thus flux upper limits are estimated using the method by Rolke et al. (2001) [64]. Integral flux upper limits in the energy range of $0.1 - 10$ TeV are estimated at a confidence level of 95% assuming a spectrum following a power law with spectral index $\Gamma = 2.5$. Assuming different indices of $\Gamma = 2.0$ and $\Gamma = 3.0$ leads to marginal changes in the upper limits of the order of 10% or less. The results are summarised in Table 3.1.

### 3.3.2 Evaluation of the Systematic Uncertainties

To guarantee that the estimated flux upper limits are comparable and do not suffer from systematic biases within the sample, the systematic uncertainties are investigated and included in the flux upper limit calculation. The systematic uncertainties are estimated following the description in Section 3.2.

The systematic uncertainty due to atmospheric density profile changes is determined as follows: For observations performed within a single month, the atmospheric density profile can be assumed to be constant and the systematic uncertainty on the energy scale is at a 1% level. Observations covering a full season lead to an uncertainty of 2% on the energy scale. A coverage of two seasons will lead to a 3% systematic uncertainty on the energy scale and a coverage of three or four seasons will have a systematic uncertainty on the energy scale of 4%. These numbers are converted to systematic uncertainties on the flux via Equation 3.10.

The systematic uncertainty on the energy scale due to the zenith angle dependent atmospheric transmission is estimated based on Equation 3.8 and translated into a systematic uncertainty on the flux by using Equation 3.10.

The run-by-run variability is mainly caused by a variability in the atmospheric transparency coefficient leading to a variability in the measured flux. The uncertainties are calculated using the rms of the run-by-run atmospheric transparency coefficients for each data set.

Finally, the systematic uncertainty in the background estimation due to applying the *reflected region background model* is determined based on the difference in the one dimensional radial profile of the *on*-event sky map and the *on*-exposure sky map. The *on*-exposure sky map is produced by determining the radially symmetric two-dimensional acceptance sky map (based on lookups) and is scaled by the acceptance corrected total number of *on* events in the field of view. As the background level at the source position is estimated by $B = \alpha n_{off}$, where $n_{off}$ is the number of *off* events in $n$ reflected regions and $\alpha$ is given by $\alpha = \mathrm{exposure}_{on}/\mathrm{exposure}_{off}$, with $\mathrm{exposure}_{off} = n_{off}$, the systematic uncertainty in the background estimation is simply given by the systematic uncertainty in the acceptance determination. Thus, the systematic uncertainty on the background estimation is determined by the standard deviation of the ratio of the one-dimensional *on* and *on*-exposure sky maps for single pointing positions.

As none of the bow shocks show significant $\gamma$-ray emission, no systematic uncertainties on the flux measurement due to the choice of selection cuts can be estimated because the measured flux with different cut configurations is directly correlated to the sensitivity of the respective analysis configuration that was used. A comparison of the measured fluxes with different cut configurations would result in a comparison of the different cut sensitivities. Additionally, there is no estimate of the systematic uncertainty on the spectral index as no spectrum can be reconstructed based on flux upper limits.

Table 3.2 summarises the systematic uncertainties for the chosen bow shock sample. The total systematic uncertainties given at the bottom of the table range between 14% and 19% and are dominated by uncertainties in the atmospheric transmission and the background estimation. As the sample of bow shocks is chosen to cover a broad range of observational parameters, it can be assumed that the estimated systematic uncertainties apply for the whole sample of bow shocks of runaway stars. Since the systematic uncertainties are similar for all bow shocks in the sub sample, and to make sure that the systematic uncertainties are not underestimated for single bow shocks, a conservative maximum of 20% is assumed for all bow shocks. Using this conservative value, the final integral flux upper limits are then calculated as explained in Section 3.1.8. These flux upper limits deliver the basis for a population study of bow shocks of runaway stars with flux estimations that are as unbiased as possible, which led to the conclusion that a potential VHE $\gamma$-ray emission from this source class is below the flux level that is detectable by the current generation of IACTs (see Appendix B for more details).

Table 3.2: Systematic uncertainties on the flux measurement for the selected bow shocks of runaway stars.

| | HIP 38430 | HIP 44368 | HIP 72510 | HIP 98418 | J 111-6120 |
|---|---|---|---|---|---|
| MC Shower interactions | 1% | 1% | 1% | 1% | 1% |
| MC Atm. density profile* | 1% | 5% | 3% | 1% | 6% |
| Atmospheric transmission* | 8% (9%) | 9% (14%) | 9% (11%) | 15% (15%) | 11% (12%) |
| Broken pixels | 5% | 5% | 5% | 5% | 5% |
| Dead time | 1% | 1% | 1% | 1% | 1% |
| Background estimation* | 11% | 4% | 9% | 9% | 8% |
| Run-by-Run variability* | 2% | 6% | 5% | 5% | 6% |
| Total** | 15% | 14% | 15% | 19% | 17% |
| Integral flux upper limit**<br>$[10^{-12}\,\mathrm{TeV\,cm^{-2}\,s^{-1}}]$ | 37.65 | 10.41 | 24.94 | 37.15 | 2.64 |

[*] Uncertainties marked with a star are data set dependent and estimated separately for the listed bow shocks. The uncertainties due to atmospheric transmission variations are given for the mean zenith angle of the data set and in brackets for the maximum zenith angle of the data set.

[**] The total systematic uncertainty is calculated by adding the individual values in quadrature.

[***] Integral flux upper limits including a systematic uncertainty of 20% (see text for details). The flux upper limits are estimated at a 95% confidence level by assuming a spectrum following a power law with spectral index $\Gamma = 2.5$.

# Chapter 4

# The Magellanic Clouds

The Magellanic Clouds (shown in Figure 4.1) are two star forming galaxies in the neighbourhood of the Milky Way. The nearly face-on orientation — which gives access to the source distribution of the entire galaxy — combined with the given spatial resolution of $0.1^\circ$ of the H.E.S.S. experiment means that the Magellanic Clouds are nearby enough to have resolvable individual sources. At the same time, they are far away enough that the large-scale emission as seen by the Energetic Gamma Ray Experiment Telescope (EGRET) and *Fermi* at MeV-GeV energies [67–69] is distinguishable. Thus, they deliver the unique opportunity to study the connection between the Galactic VHE $\gamma$-ray source population and the integrated diffuse emission as seen in star forming galaxies. Furthermore, due to their different star formation histories the Magellanic Clouds provide an interesting laboratory for a comparison of the TeV source populations in the Magellanic Clouds to those discovered in the Milky Way and a study of the importance of the environment for the efficiency of the $\gamma$-ray production.

In the last decade H.E.S.S. performed a survey of the Magellanic Clouds that amounts in total to $\sim 450$ h of observations. The survey of the Magellanic Clouds is presented in this chapter. After a short introduction to both Magellanic Clouds in Section 4.1, an introduction into particle acceleration mechanisms and non-thermal radiative losses will be given in Section 4.2 followed by an overview of the theoretical background of potential source classes in the Magellanic Clouds in Section 4.3.

## 4.1 Introduction

The Magellanic Clouds are two intensively studied star forming galaxies. Belonging to the Local Group, their moderate distances of $150 - 200$ ly allowed inhabitants of the Southern Hemisphere to observe these bright cloudy objects already centuries ago. More than 1000 years ago, they were first mentioned by the Persian polymath Ibn Qutaybah (828 - 889) [70] and the Persian astronomer Al Sufi (903 - 986) [71], whose accounts are probably based on travellers stories. In Europe the Magellanic Clouds were first reported in a letter dated January 6th, 1515 by Andrea Corsali [72], an Italian author on a Portuguese voyage. A couple of years later the Crew of Ferdinand Magellan (1480 - 1521) discovered and described the galaxies during their circumnavigation of the world (1519 - 1522) [73]. However, the name *Magellanic Clouds* only became popular in the 18th century in honour of Ferdinand Magellan. The naming still describes the apparent shape of the objects and reflects the lack of knowledge about their true nature at that time.

In the early 19th century astronomers became increasingly interested in the Magellanic Clouds. After the publication of the rather detailed sketches of the Magellanic Clouds by James Dunlop in 1828 [74], it was John Herschel who first catalogued star clusters and nebulae in his "General Catalog" [75], which was later incorporated in the well known "New General Catalogue" [76]. Since the beginning of the 20th century the Magellanic Clouds have played a major role in our understanding of the scales of our Universe. They were previously assumed to be nebulae enclosed in our own Galaxy, the Milky Way, and it was Henrietta Swan Leavitt who discovered the Cepheid period-luminosity relation based on Cepheids located in the Magellanic Clouds [77, 78] and thus laid the foundation for distance estimations far beyond the natural limits of $\sim 100\,$pc of established methods like the trigonometric parallax. The calibration of the relation through distance measurements of close-by Cepheids [79, 80] finally led to the conclusion that the Magellanic Clouds are two individual separated galaxies outside the Milky Way, called the Small Magellanic Cloud (SMC) and the Large Magellanic Cloud (LMC). A proposal by Mathewson et al. suggested that the SMC is in fact split into two galaxies with the smaller part, called the *Mini Magellanic Cloud*, being located behind the SMC with a separation of $\sim 12\,$kpc [81]; however, it was never shown to be true and more recent studies reveal somewhat contradicting results [82, 83]. Hence, the SMC is still regarded as a single galaxy.

The discovery of the Magellanic Bridge connecting the two Magellanic Clouds [84] as well as the Magellanic Stream, a trail of gas following the Magellanic Clouds [85], strongly suggests that the two satellite galaxies are interacting. Simulations of tidal encounters between the two Magellanic Clouds [86, 87], proper motion studies of the stellar populations [88] as well as star-formation (history) studies [14–16, 18, 89] support this picture. Recent close encounters between the Magellanic Clouds led to an increased star formation rate in both galaxies and hence resulted in an increased number of young ($\lesssim 10^7\,$yr) stellar populations. These are of special interest for astroparticle physics as they are the progenitors of the most promising source candidates for particle acceleration up to $\sim$TeV energies.

Figure 4.1: The Magellanic Clouds visible over the Paranal Observatory in Chile. Image Credit: ESO/J. Colosimo

### 4.1.1 The Large Magellanic Cloud

Among the four closest neighbouring galaxies, the Large Magellanic Cloud (LMC) is the closest star forming galaxy to the Milky Way at a distance of $\sim 50$ kpc [90]. Although its stellar mass is only approximately 4% of the Milky Way stellar mass [91, 92], the LMC has a star formation rate per unit solar mass that is on average five times larger than that of the Milky Way [15, 93], and studies show that the galaxy even underwent recent star formation periods at 2 Gyr, 500 Myr, 100 Myr and 12 Myr ago [15]. The LMC still shows higher star formation rates in the last 10 Myr [16], indicating a large number of young stellar populations. Tracers of the latter are the numerous HII regions [94, 95], stellar clusters [96], SNRs [97] and high-mass X-ray binaries (HMXBs) [98, 99]. One of the most prominent regions in the LMC is the Tarantula Nebula (also known as 30 Doradus) — the most massive and most active starburst region of all Local Group galaxies. The many luminous and massive O3 and Wolf-Rayet stars with strong winds provide a significant amount of target material for VHE $\gamma$-ray production. Furthermore, the Tarantula Nebula contains many SNRs of various ages, making this region a promising place to search for VHE $\gamma$-ray emission. The detection of diffuse HE $\gamma$-ray emission from the LMC with EGRET in 1992 led to the assumption that the cosmic-ray density in the LMC is comparable to the Milky Way [67]. Between 2007 and 2013 H.E.S.S. performed observations of the Tarantula Nebula and found three individual, exceptionally powerful sources, which are identified as the SNR N 132D, the PWN N 157B and the superbubble 30 DorC, all of which are shown in Figure 4.2 [23]. While conducting the analysis for this work, another $\gamma$-ray emitter has been found and identified as the $\gamma$-ray binary LMC P3 [100], which will be described in more detail in Section 6.6.1. As the data set taken until the last H.E.S.S. publication was limited in spatial extent as well as in sensitivity, subsequent observations covering the entire LMC were performed by H.E.S.S., for which the analysis is presented in this work (Section 5.2).

In addition to the point-like sources, diffuse emission consisting of several components from degree-scale up to the extent of the entire galaxy was detected with the *Fermi*-LAT at up to $\sim 10$ GeV (see Figure 4.3a) [69], implying a large-scale population of cosmic rays with energies of up to at least $\sim 100$ GeV and the existence of significant amounts of target material for the $\gamma$-ray production.

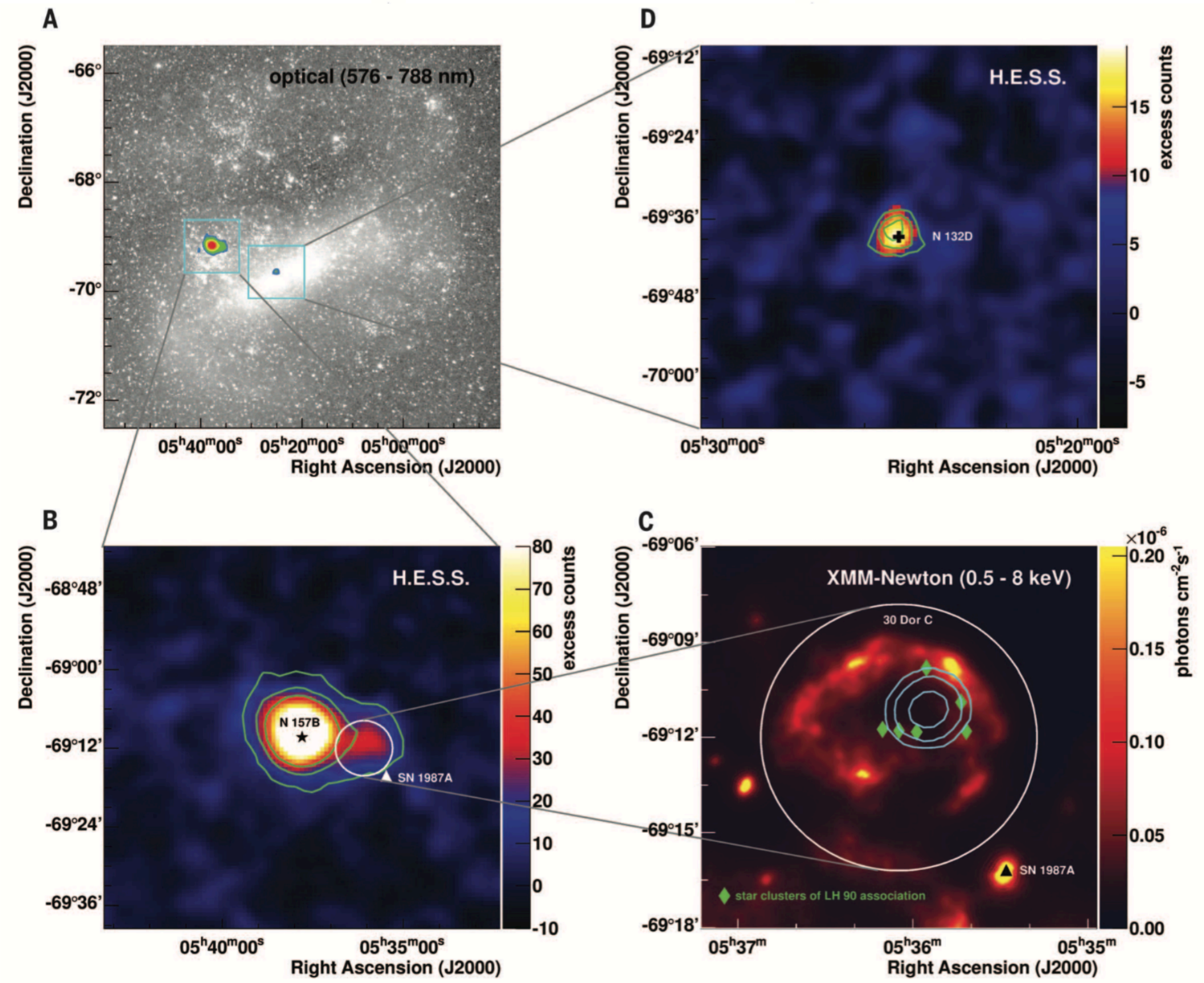

Figure 4.2: The three known VHE $\gamma$-ray sources in the Magellanic Clouds. *Upper left*: the VHE $\gamma$-ray emission of all three sources overlaid on an optical image of the LMC. *Upper right*: The VHE $\gamma$-ray excess of the SNR N 132D. *Lower left*: VHE $\gamma$-ray excess map of the PWN N 157B and the superbubble 30 DorC. *Lower right*: X-ray image of the superbubble 30 DorC. Figure taken from [23].

### 4.1.2 The Small Magellanic Cloud

At a distance of $\sim 60$ kpc [101] the Small Magellanic Cloud (SMC) is the second nearest star forming galaxy to the Milky Way. With a stellar mass of only 0.5% of the Milky Way mass [91, 92], the SMC nevertheless exhibits a star formation rate per unit solar mass that is 20 times higher than that of the Milky Way [93] with several recent star-formation peaks in the last $\sim 500$ Myr [14, 16–18], probably triggered by tidal interactions with the LMC or Milky Way [14]. The SMC shows evidence for ongoing star formation at a higher rate towards the SMC *Bar* starting $\sim 10$ Myr ago [16, 18]. The large population of young X-ray binaries, predominantly HMXBs with OBe star companions [102, 103], is most likely linked to the recent star formation episode. Next to the HMXBs, the SMC also hosts many SNRs [104] and HII regions accumulated in star forming regions (SFRs) [105], making the SMC an ideal target for studying young stellar populations over a wide range of age. With a high gas content and a low metallicity ($\sim 0.2\times$ solar [106, 107]), the SMC offers a laboratory significantly different from those of the Milky Way and the LMC and hence makes a comparison of the source populations in these three galaxies particularly interesting for the study of particle acceleration mechanisms and the importance of the environment.

The diffuse emission detected by *Fermi*-LAT in the HE range (as shown in Figure 4.3b) proves that particles are accelerated to at least $\sim$ GeV energies [68, 108]. In addition, although emission from star formation tracers such as far-infrared or radio emission is about an order of magnitude lower than in the LMC, the efficiency with which $\gamma$ rays are produced, the *calorimetric* fraction, is significantly higher in the SMC than in the LMC [109].

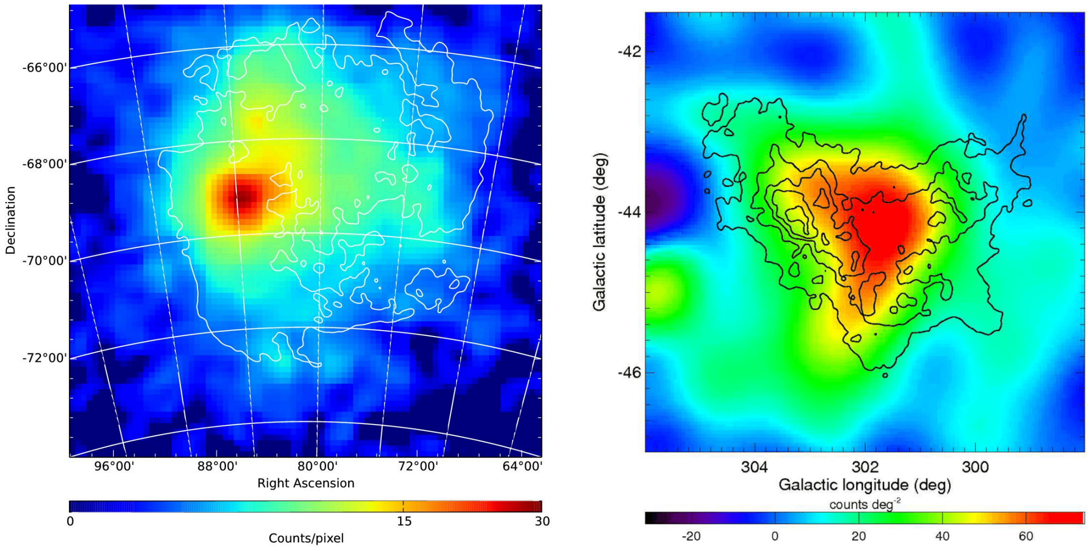

(a)

(b)

Figure 4.3: Diffuse HE $\gamma$-ray emission of the (a) LMC and (b) SMC as seen by *Fermi*-LAT [68, 69].

## 4.2 Particle Acceleration and Non-Thermal Radiative Losses

Observations of Galactic source classes emitting non-thermal radiation reveal that a variety of mechanisms are required to accelerate particles in different astrophysical environments to PeV energies. Shocks of SNRs and PWNe provide perfect conditions for particle acceleration up to $\sim 10^{15}$ eV resulting in $\gamma$-ray emission up to multi-TeV energies [7, 63, 110]. On the other hand, TeV $\gamma$-ray emission is also observed from pulsars, where no shocks are formed, and hence a different acceleration mechanism is assumed to be responsible for the particle acceleration. The acceleration mechanisms discussed in the literature include stochastic processes in turbulent environments, acceleration behind shocks, varying magnetic fields in compact sources and magnetic reconnection. Independent of the acceleration mechanism, the relativistic particles lose energy via non-thermal radiative losses leading to non-thermal emission that is observed from radio to $\gamma$-ray energies.

The following sections give an introduction to the most accepted acceleration mechanisms in the literature followed by a description of the relevant radiative losses for the production of non-thermal emission.

### 4.2.1 Second Order Fermi Acceleration

In 1949 Enrico Fermi proposed the first mechanism to explain how cosmic rays can be accelerated [111]. Charged particles are deflected by magnetic clouds randomly moving through the ISM. Deflected particles only gain energy in head-on collisions which invert the momentum of the particle from $\vec{p}$ to $-\vec{p}$, but as head-on collisions are expected to be more likely, particle gain energy on average. By assuming the mass of the cloud to be much larger than the mass of the particle ($M_{\mathrm{cloud}} \gg M_{\mathrm{p}}$), and the cloud to be moving slowly compared to the speed of light ($v_{\mathrm{c}} \ll c$), the energy gain for a particle of energy $E$ after a collision is given by:

$$\frac{\Delta E}{E} \propto \left(\frac{v_{\mathrm{c}}}{c}\right)^2 .$$

As the energy gain is proportional to $(v_c/c)^2$, this acceleration mechanism is also referred to as *second order Fermi acceleration*. Fermi showed that in the case of an energy independent particle escape time, the second-order Fermi acceleration mechanism leads to a particle spectrum with a power law when observed from Earth. However, this mechanism has its limitations as the acceleration times are on average $\tau_{\mathrm{acc}} \gtrsim 10^8$ yr $\gg t_{\mathrm{CR}}$, with $t_{\mathrm{CR}}$ being the age of the cosmic rays, which is much longer than the typical lifetime of $\lesssim 10^5$ yr of a Galactic accelerator. Furthermore, this acceleration mechanism only becomes efficient if particles are preaccelerated to $100\,\mathrm{MeV}$ and the power law distribution of the cosmic-ray spectrum is not universal as it depends on the

density and velocity of the clouds.
However, second order Fermi acceleration is still considered to be an active particle acceleration mechanisms in some source classes and helps to explain the flattening of the cosmic-ray spectrum at lower energies [112].

### 4.2.2 Diffusive Shock Acceleration

The idea of accelerating particles at discontinuities, like in the second order Fermi acceleration mechanism, is still present in the nowadays more commonly accepted mechanism, the *diffusive shock acceleration* [113–116]. Particles gain energy while crossing a shock front with small-scale magnetic inhomogeneities generated by high velocity particles colliding with the ISM. By experiencing head-on collisions while crossing the shock front upstream (ahead of the shock) and downstream (behind the shock) and under the assumption that the particles are isotropically distributed, the energy gain per cycle (upstream - downstream - upstream) of a particle with energy $E_0$ crossing a shock front with a velocity of $v_s$ is given by:

$$\frac{\Delta E}{E_0} \propto \left(\frac{v_\mathrm{s}}{c}\right).$$

Due to the energy gain being proportional to $(v_\mathrm{s}/c)$, this acceleration mechanism is also called *first-order Fermi acceleration*. As the upstream medium is approaching towards the shock front, the probability of a particle in the upstream region crossing the shock front is $P = 1$. On the other hand, downstream particles moving away from the shock front can get advected away and hence can leave the shock system with a probability $P_\mathrm{esc} \neq 0$, which naturally leads to a particle energy spectrum with a power law shape. In the limit of strong shocks, the compression factor $r$, which denotes the ratio between the upstream and downstream bulk velocity, is $r = v_1/v_2 \sim 4$, leading to a power law index of $\sim 2$.
The maximum acceleration rate is reached in the regime of *Bohm diffusion* denoting the slowest possible diffusion. In the Bohm regime the mean free path of the particles is equal to the gyroradius $r_g = E/(eB)$, with $E$ being the energy of the particle and $B$ the magnetic field. Assuming identical magnetic fields in both regions, upstream and downstream, the acceleration time for a particle is given by:

$$t_\mathrm{acc} \propto \eta \frac{r_g}{c} \quad \text{with} \quad \eta \propto 20 \frac{D}{r_g c} \left(\frac{c}{v_s}\right)^2,$$

with $\eta = 1$ in the Bohm limit. $D = \frac{r_g c}{3}$ is the diffusion coefficient.
The particle acceleration becomes more efficient with larger shock velocities or magnetic field strengths. The acceleration times increase with increasing particle energies.

A direct evidence for diffusive shock acceleration is provided by Kis et al. by showing that upstream particles undergo diffusive transport into the upstream region in the Earth bow shock [117].

### 4.2.3 Magnetic Reconnection

Magnetic reconnection occurs when two magnetic fluxes of opposite polarity encounter each other. If the magnetic resistance is finite, the converging magnetic field lines annihilate at the discontinuity surface and form a *current sheet*. It is assumed that particles are accelerated in a way similar to the first-order Fermi process [118]. Cosmic rays gain energy in head-on collisions with the two converging magnetic fluxes while bouncing back and forth several times[1]. The energy gain in each cycle is

$$\frac{\Delta E}{E_0} \sim \left(\frac{v_\mathrm{r}}{c}\right),$$

where $v_r$ is the reconnection velocity at which the two converging magnetic fluxes approach each other.

The accelerated particles are shown to have a power-law distribution, which is in agreement with radio observations of flares of Galactic microquasars [118]. A review of the recent developments in the theory of magnetic reconnection is given by de Gouveia Dal Pino & Kowal [120].

### 4.2.4 Non-Thermal Radiative Losses

Relativistic cosmic rays — i.e., electrons and positrons (both of which are in the following summarised as electrons), protons and heavier nuclei — can lose energy via non-thermal radiation through interactions with ambient matter, radiation fields and magnetic fields. The kinetic energy that is transferred to non-thermal particles through cosmic-ray acceleration is released via non-thermal photons over the entire electromagnetic spectrum. The resulting spectral energy distribution depends on the dominating radiative losses. Whereas leptons mainly lose energy by inverse Compton scattering, synchrotron radiation or relativistic Bremsstrahlung, hadrons lose energy via proton-proton inelastic collisions. Depending on whether the hadronic or the leptonic energy losses dominate in a source, the acceleration efficiency and maximum energy have different dependencies on the acceleration timescales. The different processes are described in more detail in the following.

---

[1] A similar process within a collisionless reconnection scenario is discussed in the literature as well [119].

### Synchrotron Radiation

Synchrotron radiation is the emission of photons by charged relativistic particles due to their deflection while gyrating in a magnetic field. The emitted energy spectrum covers a broad energy range from $\sim 10^{-10}$ - $\sim 10^{5}$ eV with a peak at $\sim 1$ eV. As the energy-loss rate $(\mathrm{d}E/\mathrm{d}t)_{\mathrm{sy}}$ is proportional to $m^{-4}$, with $m$ being the mass of the relativistic particle, the energy-loss rate for electrons appears $m_{\mathrm{p}}/m_{\mathrm{e}} = 10^{13}$ times faster than for protons with the same energy and hence leads to a significantly higher non-thermal photon flux. The average energy-loss rate due to synchrotron radiation of a relativistic electron only depends on its energy $E$ and the magnetic field strength $B$:

$$(\mathrm{d}E/\mathrm{d}t)_{\mathrm{sy}} \propto E^2 B^2. \tag{4.1}$$

Thus, the flux of the emitted non-thermal photons increases with increasing magnetic field. The energy-loss timescale, also called the cooling time, for synchrotron radiation is proportional to the energy of the particles (assuming a fixed magnetic field). This means that particles with higher energies cool (lose energy) faster than particles with lower energies. Therefore synchrotron radiation is the dominating mechanism for non-thermal radiative losses at energies in the radio or X-ray regime. A comprehensive description of the theory is given by, e.g., Ginzburg & Syrovatskii [121].

### Inverse Compton Scattering

The same electron population that is cooling by releasing energy via synchrotron radiation also interacts with the ambient photon field. The relativistic electrons lose kinetic energy by up-scattering low energy photons. This process is called *inverse Compton* scattering as energy is transferred from electrons to photons rather than the other way around as is described by the original Compton scattering process [122]. The cooling time can be determined based on the calculation for the energy-loss rate by Blumenthal & Gould [123]:

$$t_{\mathrm{IC}}^{-1} = \frac{1}{E} \int_{\varepsilon_{\min}}^{\varepsilon_{\max}} \int_{\varepsilon}^{\frac{bE}{1+b}} (\varepsilon_1 - \varepsilon) \frac{\mathrm{d}N}{\mathrm{d}t\,\mathrm{d}\varepsilon_1} \mathrm{d}\varepsilon_1, \tag{4.2}$$

with $\varepsilon$ and $\varepsilon_1$ being the incident and scattered photon energy, respectively, and

$$\frac{\mathrm{d}N}{\mathrm{d}t\,\mathrm{d}E_1} = \frac{2\pi r_{\mathrm{e}}^2 m c^3}{\gamma} \frac{n_{\mathrm{ph}}(\varepsilon)\mathrm{d}\varepsilon}{\varepsilon} \left[ 2q \ln q + (1+2q)(1-q) + \frac{1}{2} \frac{(\Gamma_\varepsilon q)^2}{1+\Gamma_\varepsilon q}(1-q) \right]$$

with

$$E_1 = \frac{\varepsilon_1}{\gamma m_\mathrm{e} c^2}, \qquad \Gamma_\varepsilon = \frac{4\varepsilon\gamma}{m_\mathrm{e} c^2} \qquad \text{and} \qquad q = \frac{E_1}{\Gamma_\varepsilon (1 - E_1)}.$$

$n_\mathrm{ph}(\varepsilon)$ is the ambient radiation field density. The dimensionless parameter $\Gamma_\varepsilon$ determines whether the scattering can be described in the Thomson regime $(\Gamma_\varepsilon \ll 1)$, in which the cross-section for the interaction of a lepton and a photon can be approximated by the Thomson cross-section [124], or in the Klein-Nishina regime $(\Gamma_\varepsilon \gg 1)$, which prescribes a decrease of the electron-photon cross-section with increasing centre-of-mass energy [125].

The target photon field is characterised either by the VHE $\gamma$-ray source itself or by accumulated photon fields of the environment. The relevance of the target photon fields for the $\gamma$-ray emission depends on the electron spectrum and on the energy of the $\gamma$ rays.

### Relativistic Bremsstrahlung

Bremsstrahlung radiation is released when a relativistic charged particle is deflected and hence decelerated in the Coulomb field of another charged particle [123]. In astroparticle physics the most efficient energy-loss occurs when relativistic electrons are deflected in the Coulomb fields of protons and ionised nuclei. The cooling time for neutral hydrogen atoms with a density $n$ is given by:

$$t_\mathrm{Br}^{-1} = \frac{1}{E_e}\left(\frac{dE_e}{dt}\right) \approx 2.6 \times 10^{-6} \frac{n}{\mathrm{cm}^3}. \tag{4.3}$$

The $\gamma$-ray spectrum resulting from Bremsstrahlung of an electron population following a power law distribution also follow a power law with the same spectral index.

### Proton-Proton Inelastic Collisions

Protons mainly lose energy through inelastic proton-proton collisions by producing neutral and charged pions. Whereas neutral pions directly decay into two photons after a lifetime of $\approx 10^{-16}$ s, charged pions decay into secondary electrons and positrons (and neutrinos) that can again cool via synchrotron or inverse Compton emission. The target material is provided by protons in the ambient material. The cooling time for proton-proton collisions only depends on the density of the target protons $n$, which is proportional to the density of the ambient material and the cross-section $\sigma_\mathrm{pp}$

$$t_\mathrm{pp}^{-1} \propto n\sigma_\mathrm{pp}. \tag{4.4}$$

More details on the estimation of the cross-section can be found in Kelner et al. [126].

### Absorption through $\gamma$-$\gamma$ Annihilation via Pair Creation

The $\gamma$ rays emitted via radiative losses of relativistic particles can be absorbed in the acceleration region immediately after being created due to photon-photon annihilation via pair production with thermal and non-thermal photons in the acceleration region. The absorption depends on the line of sight and hence on the orientation and dimension of the system. The threshold energy is given by

$$E\varepsilon = \frac{2(m_\mathrm{e}c^2)^2}{1 - e_\gamma e_\mathrm{ph}}, \tag{4.5}$$

with $e_\gamma$ and $e_\mathrm{ph}$ being the directions of the travelling $\gamma$ ray and photon, respectively.
The $\gamma$-ray absorption leads to a reduction of the $\gamma$-ray flux finally reaching Earth.

### Estimation of Maximum Particle Energy

Particles start to cool via non-thermal radiative losses as soon as the accelerated relativistic particles exceed a minimum energy $E_\mathrm{min} \gtrsim m_\mathrm{e}c^2$. The maximum energy of the electrons and protons is reached when the energy losses dominate over the particle acceleration. Thus, the maximum energy can be estimated, by equating the acceleration timescale $t_\mathrm{acc}$ with the smallest cooling rate $t_\mathrm{cool,min}$. As the gyroradius of the particles increases with increasing energy, particles will only stay in the acceleration region when in addition the Hillas criterion is also fulfilled:

$$E_\mathrm{max} < 300 \frac{r_\mathrm{g}}{(1\mathrm{cm})} \frac{B}{(1\,\mu\mathrm{G})}\,\mathrm{eV}. \tag{4.6}$$

$r_\mathrm{g}$ is the maximum gyroradius a particle can have and still stay in the acceleration region.

## 4.3 Particle acceleration in the Magellanic Clouds

The large number and variety of Galactic and Extragalactic VHE $\gamma$-ray sources [127] demonstrates that particle acceleration up to multi-TeV energies is the rule rather than the exception. Whereas some source classes are already well established as VHE $\gamma$-ray emitters, for other source classes only single representatives have been detected. In the following, the particle acceleration and $\gamma$-ray emission mechanisms will be described for the most common VHE $\gamma$-ray source classes — the SNRs and PWNe — as well as for $\gamma$-ray binaries and pulsars. Furthermore, an introduction to the promising source class of SFRs as well as to particle acceleration mechanisms leading to diffuse $\gamma$-ray emission will be given.

### 4.3.1 Supernova Remnants

SNRs are the remnants of stars that exploded at the end of their lifetimes. The ejected material propagates through the ISM in a shell and is typically seen in radio [128] or X rays (recent review by [129]). There are two main classes of supernovae — core-collapse supernovae and thermonuclear supernovae. Thermonuclear or Type Ia supernovae occur when low-mass white dwarfs in binary systems accrete matter from their companions until the Chandrasekhar limit of $M_\star \sim 1.4 M_\odot$ is reached causing a thermonuclear explosion. Core-collapse or Type II supernovae are caused by massive stars ($M_\star \gtrsim 8 M_\odot$) that have burned their central material up to the most stable element iron until the Chandrasekhar limit is reached. This leads to a collapse until a proto-neutron star is formed on which the outer layers of the star bounce back resulting in the supernova explosion. In the case of the most massive stars, the proto-neutron star will further collapse to a black hole. More details on the processes for Type Ia and Type II supernovae are given by [130–133]. Independent of the type of the supernova an average energy of $\sim 10^{51}$ erg is released in the form of kinetic energy of the ejected material.

The evolution of SNRs resulting from core-collapse supernovae can be roughly described by four main phases:

1. Free expansion (blast wave)
2. Adiabatic phase (Sedov-Taylor phase)
3. Radiative phase (snow-plow phase)
4. Dilution phase (merging into ISM).

The characteristics of the different phases are illustrated in Figure 4.4b. After the turbulences caused by the acceleration of the envelopes through the supernova explosion have settled [135],

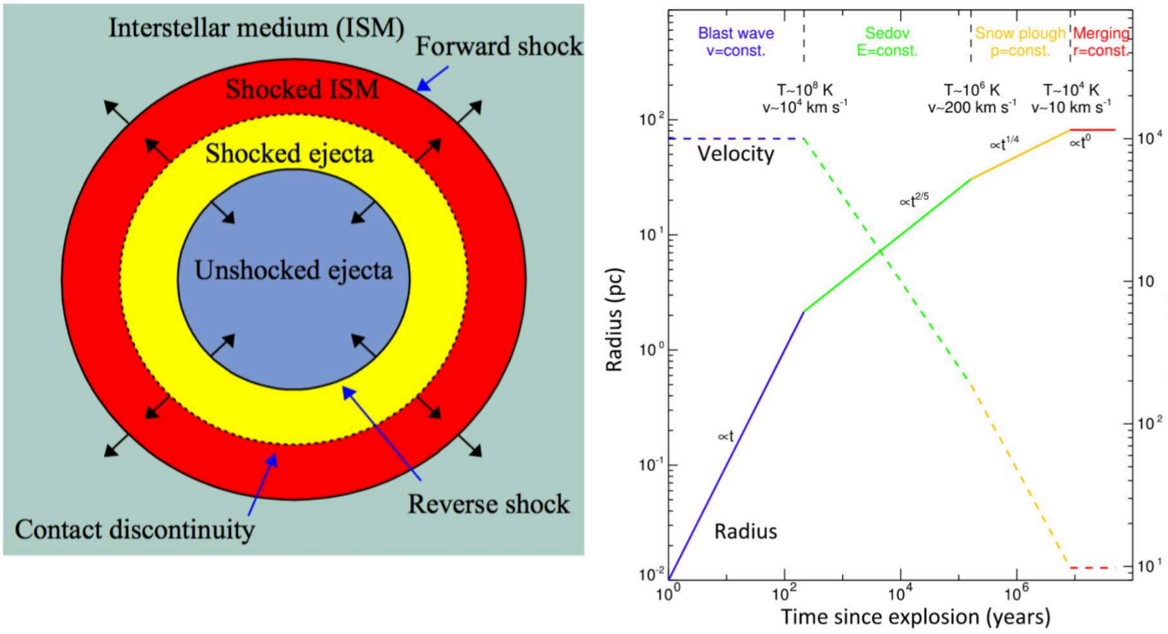

(a)

(b)

Figure 4.4: *Left*: Schematic structure of a SNR that is expanding into a uniform low density medium [53]. *Right*: Evolution phases of SNRs resulting from core-collapse supernovae [134], which are described in the text.

the ejecta expands freely into the ISM with a nearly constant velocity of $\sim 10^4$ km s$^{-1}$. While supersonically expanding into the ISM, the ambient matter is compressed resulting in a shell-like system of two shocks as is shown in Figure 4.4a. The swept-up medium rebounds of the ISM forming a second *reverse shock* propagating inwards while decelerating, compressing and heating the unshocked ejecta. The two shock regions, the expanding shell of shocked ISM and the inward moving shell of the shocked ejecta, are separated by the *contact discontinuity*. The free expansion phase ends after $\sim 10^2$ yr when the total mass of the swept-up material equals the mass of the original supernova ejecta. The only known SNR that is currently in the free expansion phase is SN 1987A.

When the swept-up mass starts to dominate over the ejected mass, the remnant enters the *adiabatic phase*. At this point, the shock slows down. The supernova ejecta mixes with the shocked gas causing an enhancement of the magnetic field inside the shell of the SNR. Prominent SNRs in this phase are Tycho, Cas A and SN 1006. After $\sim 10^4$ yr radiative losses of the hot shocked gas become increasingly important and the remnant enters the *radiative phase*. The temperature of the shock wave decreases to $< 10^6$ K, at which point radiative processes start to cool the medium efficiently. Most of this energy is radiated as optical light. Known SNRs in this phase are IC 443 and W 44. Continuous sweeping-up of the ambient medium further increases the mass of the dense shell while further slowing down the shock until the latter reaches the speed of the surrounding ISM. At this point, the shock is finally absorbed into the ISM (*dilution phase*). Further details can be found in [136–139]. However, as the case of RCW 86 shows, the evolution of SNRs is often much more complex [140].

Cosmic rays are assumed to be accelerated via diffusive shock acceleration while crossing the shock fronts of the SNR [113, 141–143] (more details are given in Section 4.2.2). Simple power considerations led to the consideration of SNRs as the prime candidate sources for cosmic rays with energies up to the "knee" ($E \sim 3 \times 10^{15}$ eV) of the cosmic ray spectrum [144, 145]. Assuming the cosmic rays have a mean energy density of $1-2\,\mathrm{eV\,cm^{-3}}$ [146] and a mean escape time from the Galaxy of $\tau_{\mathrm{esc}} \sim 10^7$ yr [147, 148], the total power in Galactic cosmic rays is about $10^{41}\,\mathrm{erg\,s^{-1}}$. With an average explosion energy of $\sim 10^{51}\,\mathrm{erg\,s^{-1}}$ and a rate of approximately 3 per century, supernovae provide a total power of $\sim 10^{42}\,\mathrm{erg\,s^{-1}}$. If on average 10% of the kinetic power is used for accelerating cosmic rays, then supernovae can provide the measured power in cosmic rays. However, the exact fraction of energy transformed into cosmic-ray energy is highly uncertain.

$\gamma$-ray experiments have shown that SNRs are indeed $\gamma$-ray sources that emit photons up to multi-TeV energies [63]. If SNRs are the main source of the measured hadronic cosmic-ray flux, they would have to be predominantly hadronic accelerators producing $\gamma$-rays via cosmic-ray interactions with the ambient matter. Detailed MC studies showed that protons with energy $E_p$ produce $\gamma$-rays with mean energies of $\sim 0.1E_p$ [149]. Based on the integrated $\gamma$-ray luminosity above 1 TeV $L_\gamma(>1\,\mathrm{TeV})$, which is the energy range this work is focussed on, the total energy in protons $W_p(>10\,\mathrm{TeV})$ can be inferred via:

$$L_\gamma(>1\,\mathrm{TeV}) = \frac{W_p(>10\,\mathrm{TeV})}{t_{\pi^0}} \tag{4.7}$$

$$\approx 2.5 \times 10^{-16} \left(\frac{n}{1\,\mathrm{cm}^{-3}}\right) \times W_p(>10\,\mathrm{TeV})\, s^{-1}, \tag{4.8}$$

where $n$ is the number density of the target protons with $n \approx 1\,\mathrm{cm}^{-3}$ for the interstellar gas and $t_{\pi^0}$ is the cooling time of neutral pions given by

$$t_{\pi^0} = \frac{1}{n\sigma_{pp}cf} \approx 4 \times 10^{15} \left(\frac{n}{1\,\mathrm{cm}^{-3}}\right)^{-1} \mathrm{s}. \tag{4.9}$$

The cross-section for proton-proton interaction with energies above 1 TeV is assumed to be constant with $\sigma_{pp} \approx 50\,\mathrm{mb}$ [150] and the scaling factor $f \approx 1/6$ comes from the assumption that protons transfer on average 1/2 of their energy into pions, of which 1/3 are neutral pions. These power estimations will be used in Section 5.2.4.

It is still under debate whether the observed $\gamma$-ray emission from SNRs is due to hadronic cosmic-ray interactions with the ambient matter or due to leptonic interactions with the ambient photon and magnetic fields. Depending on the environment of the SNR (i.e., the density of the ambient photon fields, the magnetic field strength or the available target material) either the hadronic or the leptonic energy losses dominate the resulting $\gamma$-ray spectrum. More details on non-thermal radiative losses are given in Section 4.2.4. For old ($> 10$ kyr) SNRs interacting with molecular clouds, which provide high densities of target material of up to $10^3 - 10^4$ cm$^{-3}$ [151, 152], the $\gamma$-ray emission is clearly associated with the acceleration of hadronic cosmic rays. The spectra of the SNRs W 28, W 44 or IC 443 show a clear feature ("pion bump") below GeV energies as predicted by hadronic models [153–158]. However, these old SNRs typically show a high-energy $\gamma$-ray cutoff at $\sim$ 10 GeV and hence cannot explain the cosmic ray flux up to $10^{15}$ eV. For young SNRs the interpretations are more controversial. The detections of numerous SNRs in non-thermal radio and X-ray synchrotron radiation confirm that electrons are accelerated in the remnants. Indeed studies of the SNR RCW 86 favour a leptonic model [159]. On the other hand, observations of the historical SNR Tycho [160–162], a Type Ia supernova that exploded in a roughly homogeneous ISM, reveal that the spectrum is only consistent with a hadronic acceleration scenario [163]. For other SNRs like SN 1006 [164], Cassiopeia A [110, 165–169] or RX J1713.7-3946 [170–173] none of the models can be ruled out, leading to the conclusion that leptons and hadrons may equally contribute to the $\gamma$-ray flux [174]. Studies of RX J1713.7-3946 indicate that the complexity of the environment around the remnant (strength of ambient photon field, strength of magnetic field and density of ambient material) plays a crucial role in identifying the dominant acceleration mechanism [165, 175–177].

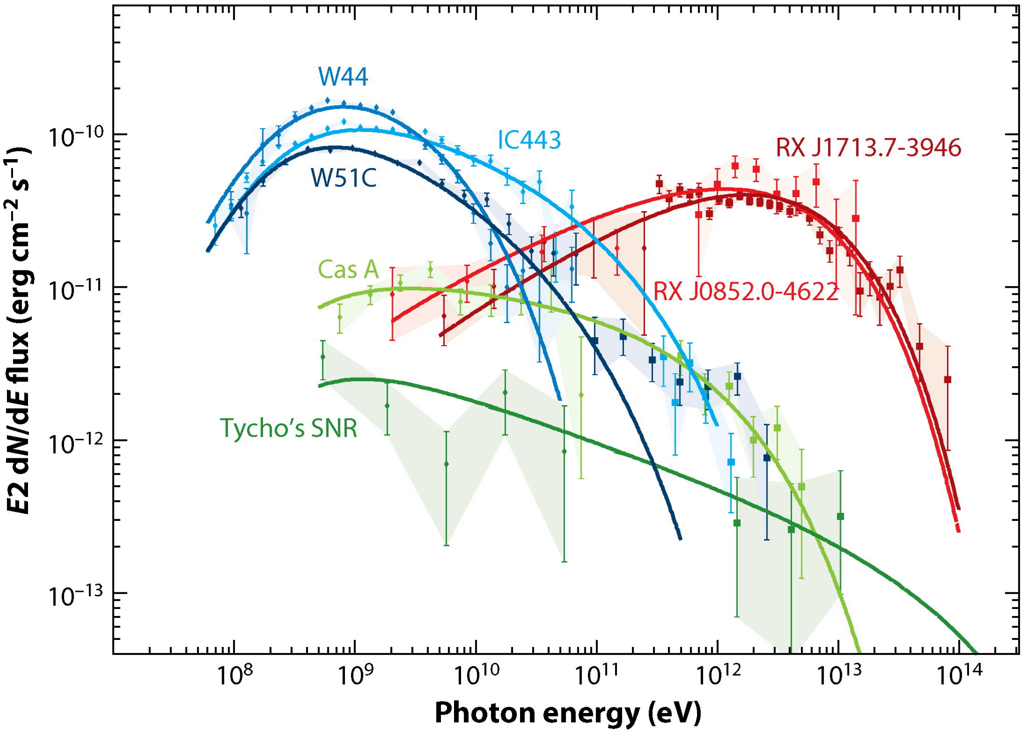

Figure 4.5: Spectral energy distributions of SNRs in different evolutionary stages [178].

While young ($\sim 10^2 - 10^3$ yr) SNRs are detected at up to $\sim$ TeV energies and have harder $\gamma$-ray spectra compared to the older population of SNRs, none of the detected SNRs shows evidence for particle acceleration up to the "knee" of the cosmic ray spectrum. Figure 4.5 shows spectral energy distributions in the energy range of $\sim$ 100 MeV to 100 TeV for seven SNRs. The evolution of the SNRs is clearly reflected in their $\gamma$-ray spectra. Whereas old ($\gtrsim 10$ kyr) SNRs like W 44, W 51C and IC 443 are bright at $\sim$MeV-GeV energies with cutoffs at $\sim 10$ GeV, middle-aged SNRs such as RX J1713.7-3946 and RX J0852.0-4622 show a peak in their emission at $\sim$TeV energies with cutoffs at $\sim 10$ TeV. Young SNRs have significantly lower $\gamma$-ray luminosities, although there is an indication of higher maximum energy cutoffs. It has been suggested that very young SNRs evolving into dense environments provided by the winds of their progenitors reach the maximum cosmic-ray energies of up to $10^{15}$ eV in the early phase of their evolution within days to months after the supernova explosion [179–181] through magnetic field amplifications [129, 182, 183]. The typical acceleration time for a particle of energy $E$ in a shock with velocity $v_{\mathrm{sh}}$ and a magnetic field $B$ can be approximated via:

$$
\begin{aligned}
t_{\mathrm{acc}} = \eta_{\mathrm{acc}} \frac{D}{v_{\mathrm{sh}}^2} \quad &= \eta_{\mathrm{acc}} \eta_{\mathrm{g}} \frac{cE}{3eBv_{\mathrm{sh}}^2} \\
&\approx 1.0 \times 10^4 \left(\frac{\eta_{\mathrm{acc}}\eta_{\mathrm{g}}}{30}\right) \left(\frac{v_{\mathrm{sh}}}{10{,}000\,\mathrm{km s^{-1}}}\right)^{-2} \left(\frac{B}{10\,\mathrm{G}}\right)^{-1} \left(\frac{E}{100\,\mathrm{TeV}}\right) \mathrm{s},
\end{aligned}
$$

where $D$ is the diffusion coefficient, $\eta_{\mathrm{acc}}$ is a numerical factor which depends on the shock compression ratio and $\eta_{\mathrm{g}}$ is the gyro factor. Provided that young SNRs exhibit magnetic fields of $\sim 10$ G and shock velocities of $\sim 10^4$ km s$^{-1}$, maximum energies of $100$ TeV can be reached within an acceleration time of a few hours and cosmic-ray energies up to the "knee" at $3 \times 10^{15}$ eV can be achieved within days to weeks. These extreme conditions can be provided by supernova events of type IIP, IIL, IIb and IIn (a review is given by [184]). However, no $\gamma$-ray emission from very young SNRs of these types has been detected so far and upper limits have been established [185]. Currently the most promising candidate is the youngest SNR SN 1987A located in the LMC and resulting from a type IIP supernova event in 1987. The analysis of SN 1987A in VHE $\gamma$ rays and the results are described in Section 6.6.2.

As there is no evidence so far that Galactic SNRs accelerate cosmic rays up to $\sim$PeV energies, the questions arise of whether the population of SNRs in the Milky Way is unique and how the Galactic population of SNRs compares to populations in other galaxies. Thus, studying the SNR populations in other galaxies may shed light on the question of what conditions are needed to accelerate cosmic rays up to PeV energies or if the cosmic-ray flux is produced by other source classes.

### 4.3.2 Pulsars and Pulsar Wind Nebulae

Pulsars are rapidly rotating ($P_\mathrm{s} \sim 10^{-3} - 10\,\mathrm{s}$ [2] [186]), highly magnetised ($B \sim 10^{11-15}\,\mathrm{G}$ [187]) neutron stars resulting from core-collapse supernovae of progenitors with masses of $8M_\odot \lesssim M \lesssim 20 - 50M_\odot$ [188, 189]. Typically detected in radio wavelength and HE $\gamma$ rays, pulsars emit periodically pulsed non-thermal emission at all wavelengths. Only recently has pulsed $\gamma$-ray emission up to $\sim$TeV energies been found from the Crab pulsar [190], the Vela pulsar [191] and Geminga [192]. These findings challenged particle acceleration models. Pulsars are surrounded by a dipolar field that co-rotates with the neutron star. The so called light-cylinder radius — $R_\mathrm{L} = \frac{cP}{2\pi} = 5 \times 10^9 \left(\frac{P}{1\,\mathrm{s}}\right)$ cm, with $P$ being the spin period — is defined as the distance at which the magnetic field lines would be rotating at the speed of light, and is therefore the radius at which the dipolar field lines open. In general, charged particles (mainly electrons and positrons) are believed to be accelerated in the *gaps* of the rotating magnetosphere, where the electric field has a component that is parallel to the magnetic field lines. The non-thermal emission up to $\sim$GeV energies is produced via synchrotron and curvature radiation, whereas the TeV emission seems to originate from inverse Compton scattering of ambient photons [193]. The detection of $\gamma$ rays beyond a few GeV indicates that $\gamma$ rays are likely produced in the outer magnetosphere as $\gamma$ rays produced closer to the surface of the neutron star would undergo severe pair production in the strong magnetic field. The exact location of these *gaps* is still under debate [194–196]. Other approaches suggest that particles might be accelerated in the ultrarelativistic particle wind (striped wind topology) [197–199] or in a magnetosphere with a force-free structure [200, 201]. Reviews on the current status of different models as well as particle-in-cell (PIC) simulations or magnetohydrodynamic (MHD) models can be found in [202–205].
Pulsars slow down as they age causing a decrease in the spin-down power — which describes the rotational energy-loss rate — of $-\dot{E}(t) \propto \frac{\dot{P}(t)}{P(t)^3}$, with $P$ being the spin period and $\dot{P}$ being the spin period derivative. Eventually the magnetic field strength also decreases with increasing age [206], though the magnetic field also depends on the exact nature of the pulsar's evolution. The *Fermi*-LAT results indicate that only pulsars with a spin-down power of $> 10^{33}\,\mathrm{erg\,s^{-1}}$ produce HE $\gamma$-ray emission at a level that is detectable with the current generation of HE $\gamma$-ray experiments [207]. In the case of VHE $\gamma$ rays observations suggest that a spin-down power of $> 10^{34}\,\mathrm{erg\,s^{-1}}$ is required to produce VHE $\gamma$-ray emission at a detectable level for the current generation of IACTs [190–192].

Young pulsars ($\lesssim 10^5$ yr) with a spin-down power exceeding $\dot{E} \sim 10^{33}$ erg s$^{-1}$ are able to power PWNe that are detectable with the current generation of IACTs [208, 209]. PWNe are a class of SNRs whose broadband emission due to the conversion of the rotational energy into electromagnetic radiation is mostly non-thermal. Hosting the most relativistic shocks of all Galactic sources, PWNe are the only Galactic source class showing evidence for particle acceleration at

---

[2] http://www.atnf.csiro.au/research/pulsar/psrcat

up to PeV energies (e.g., [210, 211])[3]. The cold ultrarelativistic particle wind of electrons and positrons released by the pulsar, which is assumed to carry most of the rotational power of the pulsar, is abruptly slowed down when it first impacts on the slow nonrelativistic ejecta of the SNR surrounding the pulsar. This interaction causes a reverse shock towards the pulsar (also called the termination shock). The highly magnetised pulsar wind close to the pulsar becomes matter dominated when approaching the shock. At this point the pressure of the pulsar wind equals the pressure of the plasma. Particles and magnetic field lines are randomised and the magnetic field decreases to $\sim 1-100\,\mu$G [213, 214]. The most commonly invoked acceleration process, the diffusive shock acceleration, does not work at highly relativistic shocks, unless the shocks are weakly magnetised or quasiparallel [215]. The current understanding of particle acceleration mechanisms in PWNe is that particles are accelerated through magnetic reconnection in the wind, at the termination shock and in the nebula [216, 217]. The exact shock structure and acceleration properties of highly magnetised shocks strongly depend on the inclination angle between the upstream field and the propagation direction of the shock [215, 218]. As the conversion from magnetic to kinetic energy through magnetic reconnection is very efficient, the magnetic energy decreases rapidly behind the termination shock leading to a particle dominated wind and the low magnetic field strengths mentioned before. However, the exact mechanisms of the particle acceleration in PWNe are still under debate. Although multidimensional magnetohydrodynamic models of PWNe have been able to reproduce the nebula morphology in detail, the problem of the transition from a highly magnetised wind to a matter dominated wind is still not fully solved. Further details on the current understanding of particle acceleration in PWNe and caveats of the different approaches can be found in [217, 219–222].

The accelerated electrons and positrons exhibit an energy distribution that follows a power law with spectral index $\Gamma \approx 2.2$ with an exponential cutoff at $\sim$ PeV [220]. However, at low energies the structure of the spectral energy distribution is more complex and thus a second population of relic electrons is used to explain the radio emission [223]. When the energetic particles leave the shock, they interact with the ambient magnetic and radiation fields. With high particle energy conversion efficiencies of up to 30% [224] of the pulsar's spin-down power, non-thermal radiation is produced via synchrotron emission and inverse Compton scattering, where a main contribution comes from up-scattering the synchrotron photons from the same electron population (synchrotron self-Compton) [223, 225]. The energetically subdominant inverse Compton emission strongly depends on the spin-down power of the pulsar as well as the strength of the magnetic field and ambient photon field. One example is the Crab nebula, which is very inefficient at producing VHE $\gamma$-ray emission through inverse Compton scattering due to high synchrotron losses in the strong magnetic field that exceeds the radiation energy density by two orders of magnitude. However, the high spin-down power can compensate for this. PWNe with magnetic fields

---

[3] There is one other location in the Milky Way where particles seem to be accelerated to up to PeV energies: in the vicinity of the Galactic centre [212]. However, the origin of the relativistic particles here is not firmly identified yet.

of $10\,\mu$G or less are more efficient at converting kinetic energy into inverse Compton emission (and less efficient at converting energy into synchrotron emission) and hence can compensate for the lower spin-down power. Observations show that only PWNe with a spin-down power of $> 10^{35}$ erg s$^{-1}$ lead to firm identifications at TeV energies [8] as was previously predicted [208]. The fact that the synchrotron emission reaches energies with a cutoff at a few tens of MeV — requiring particle energies of up to $10^{16}$ eV — despite the rapid synchrotron cooling time at high energies implies that leptonic particle acceleration in PWNe seems to be an extremely fast process [226]. On the other side, TeV emission is most likely caused by inverse Compton emission tracing homogeneous, time-constant photon fields like the cosmic microwave background (CMB) or IR photon fields and hence probe different acceleration timescales as the synchrotron emission. Figure 4.6 shows simulations of the evolution of the spectral energy distribution of the Crab nebula, demonstrating that the VHE $\gamma$-ray emission does not change significantly over one order of magnitude in time $10^3 - 10^4$ yr. This fact probably leads to the high fraction of sources associated with PWNe in the VHE regime [63]. As PWNe are detectable over a large range of ages from very young PWNe (e.g., the Crab nebula, MSH 15-52 or SHR G 0.9+0.1) to evolved stages of there lifetime (e.g., Vela X, HESS J1825-137 or J1718-385), population studies may reveal insights into the evolution of the population of PWNe. A comparison to the PWN population of another galaxy may reveal the importance of the environment on the non-thermal emission of PWNe.

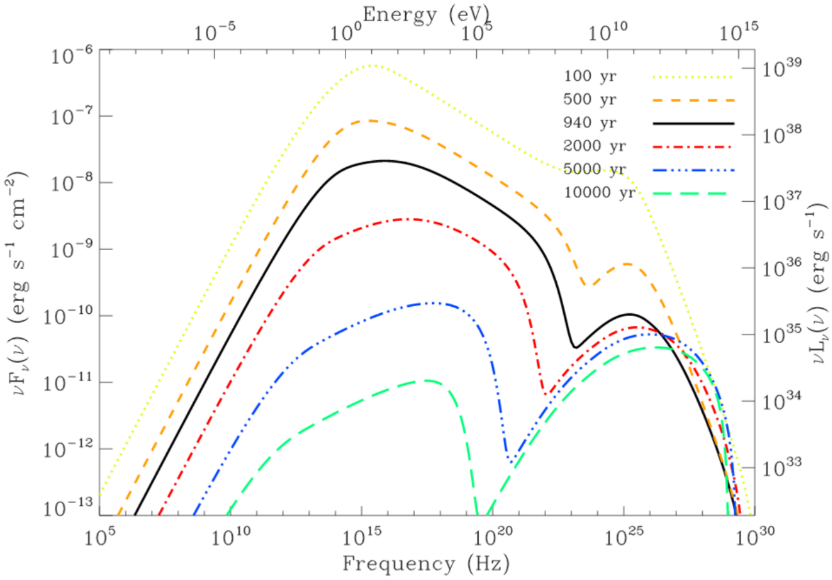

Figure 4.6: Simulated evolution of the spectral energy distribution of the Crab nebula [227].

### 4.3.3 $\gamma$-Ray Binaries

The name *$\gamma$-ray binary* covers three types of binary systems: binary systems consisting of a massive star and a pulsar or black hole (e.g. PSR B1259-63 or HESS J0632+057), colliding wind binaries (e.g., $\eta$ Carinae) and microquasars, for which $\gamma$-ray emission is expected but not yet detected [228]. As $\eta$ Carinae is the only detected representative of the class of colliding wind binaries [229, 230] and no microquasars have been detected in VHE $\gamma$-ray rays so far, this section focusses on those binary systems consisting of a massive star and a pulsar or black hole for which seven representatives have been detected at VHEs so far (PSR B1259-63 [231], LS 5039 [232], LS I +61°303 [233], HESS J0632+057 [234], 1 FGL J1018.6-5856 [235], PSR J2032+4127 [236] and LMC P3 [100], the only Extragalactic binary). These systems consist of a compact object (neutron star or a black hole) orbiting a massive early-type (O or Be type) star. They all show orbitally modulated non-thermal emission over a wide range of the electromagnetic spectrum from radio to VHE $\gamma$ rays. The spectral energy distributions are clearly dominated by $\gamma$ rays, while the X-ray fluxes are modest with hard spectra up to HE $\gamma$ rays. These characteristics indicate that $\gamma$-ray binaries are a distinct class of HMXBs, which are a class of binaries with the same type of objects as in $\gamma$-ray binaries but which are typically detected in X rays.

There are two favoured scenarios that explain the $\gamma$-ray emission in binaries: the *pulsar scenario* and the *microquasar scenario* (see Figure 4.7 left and right, respectively).

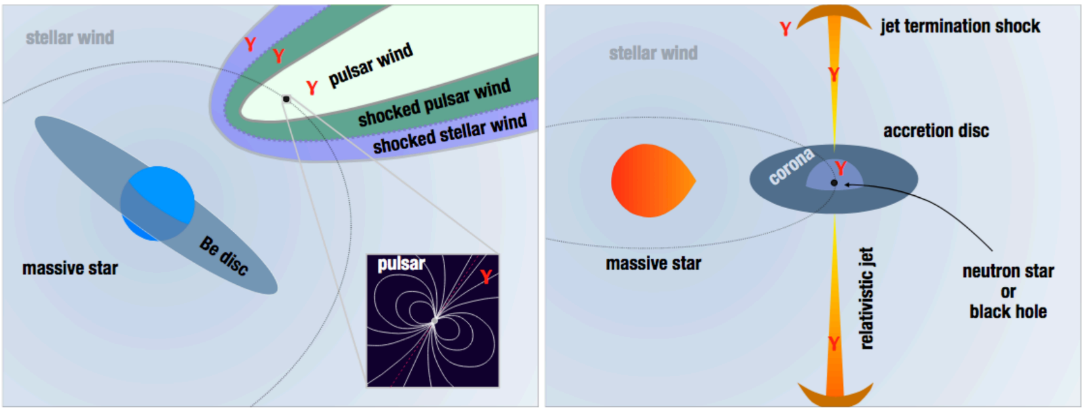

Figure 4.7: Two scenarios for $\gamma$-ray emission from binaries. Left: the relativistic wind of a rotation-powered pulsar orbiting a massive (Be-type) star interacts with the stellar wind and, if present, with the Be disc. $\gamma$-ray emission can be produced close to the pulsar, in the pulsar wind (see Section 4.3.2) or at the termination shocks of the stellar wind and the pulsar wind, as is indicated in the figure. Right: the compact object (either a neutron star or a black hole) accretes matter from the massive companion (O or Be type star) through its stellar wind or Be disc or through Roche-lobe overflow in supergiant systems. A relativistic jet may be launched. The $\gamma$-ray emission is assumed to originate from the corona of the accretion disc, within the jet or at the termination shock from the jet colliding with the ISM. Credit: [237]

In the *pulsar scenario*, in which the compact object is a pulsar, particle acceleration is assumed to arise from the pulsar or from interactions of the pulsar wind with the stellar wind. Similarly to isolated pulsars, particles might be accelerated in *gaps* with a non-zero electric field, or in the ultrarelativistic pulsar wind (more details are given in Section 4.3.2). The energy carried by the leptonic pulsar wind is released when the pulsar wind starts to interact with the stellar wind or the stellar disc of Be-type stars. The supersonic interaction of the winds results in a double shock structure with a contact discontinuity separating the shocked stellar and the shocked pulsar wind material resulting in a bow shaped interaction region, where the bulk kinetic energy is transferred to random motion of the positrons and electrons (see left hand-side of Figure 4.7). Like in PWNe, particles are thought to be accelerated at magnetic reconnection sites, which can be best described by striped wind models [197–199]. Striped *current sheets* originating from the separation of oscillating opposed magnetic poles of open field lines with different polarities compress the magnetic field of the shock triggering magnetic reconnection at the shock [216]. This scenario is more likely in binary systems as the termination shock is closer to the pulsar reducing the probability of dissipation of the current sheet before arriving at the termination shock. Further particle acceleration by "Fermi-like" processes finally yields a power-law distribution in energy for the electrons and positrons [238]. Non-thermal emission is then radiated downstream of the termination shock via synchrotron cooling and inverse Compton scattering at the photon field of the luminous star. The $\gamma$-ray binaries PSR B1259-63 and PSR J2032$+$4127 are the only systems so far for which the pulsar wind scenario, initially introduced by [239, 240], is confirmed [241]. A hadronic scenario seems to be unlikely for multiple reasons: as the energy loss is too inefficient before the cosmic rays leave the system, the maximum energy that can be reached is too low for proton-proton or proton-$\gamma$ interactions, and it is difficult to explain the observed $\gamma$-ray orbital modulations.

On the other hand, elongated radio emission at the position of the binaries has been interpreted as evidence of relativistic jets. Due to the analogy of the particle acceleration processes of microquasars and active Galactic nuclei, the *microquasar scenario* was developed. The compact object, either a neutron star or a black hole, accretes matter from the stellar wind, the Be disc, or through Roche-lobe overflow causing the launch of a relativistic jet. The mechanisms by which particles in (ultra)relativistic jets are accelerated is still not clear, as the complexity of collimated jet formation and particle acceleration inside jets still challenges theoretical simulations. Models that are currently discussed in the literature include diffusive shock acceleration, relativistic reconnection including current sheets, stochastic acceleration and magnetoluminescence. Non-thermal emission is believed to originate from synchrotron radiation and inverse Compton scattering photons of the ambient photon fields, but curvature radiation or proton synchrotron radiation are also discussed. For more details on the current status on physics of relativistic jets from active Galactic nuclei, the reader is referred to [242] and [243, 244] for the connections to microquasars. The *microquasar scenario* is the preferred particle acceleration scenario for two $\gamma$-ray binaries: LS 5039 [245] and LS I $+61^{\circ}303$ [246]. However, there is observational evidence that these elongated structures can be attributed to a cometary tail of the shocked pulsar wind. In that case, the observed VHE $\gamma$-ray emission can also be explained within the *pulsar scenario* [247, 248]. The detection of pulsed non-thermal emission in the known $\gamma$-ray binaries would confirm the *pulsar scenario*, whereas detections of pulsed non-thermal radio emission would favour the *microquasar scenario* as the pulsar wind pressure of radio pulsars is large enough to prevent accretion onto the neutron star. Measurements of the mass of the compact object could also rule out a pulsar if $M < 3M_{\odot}$. For a comprehensive overview of $\gamma$-ray binaries, the reader is referred to [237, 249].

The orbital modulation of the non-thermal emission (see Figure 4.8a) can be explained by $\gamma$-$\gamma$ absorption, cascade emission, anisotropic inverse Compton scattering and/or the eccentricity of the orbit.

- The strength of $\gamma$-$\gamma$ absorption of VHE photons through pair creation of electrons and positrons with ultraviolet photons from the star depends on the geometry and the orbital phase of the system. Head-on collisions are most efficient leading to a maximum of the VHE $\gamma$-ray absorption at inferior conjunction, when the compact object is between the star and the observer, whereas a minimum is reached at superior conjunction, when the compact object passes behind the star. The intensity distribution of the resulting $\gamma$-ray emission is sketched in Figure 4.8b. However, pair production is insufficient on its own to fully explain the VHE $\gamma$-ray emission that is observed for LS 5039, where the VHE extrema are inconsistent with the $\gamma$-$\gamma$ absorption [250].
- Cascade emission, which occurs when one of the particles created through $\gamma$-$\gamma$ absorption carries most of the energy triggering a cascade of inverse Compton scattering ultraviolet photons and electron-positron pair creation, reduces the effective opacity by redistributing the absorbed flux (see Figure 4.8c). Cascade emission thus leads to an additional shaping of the lightcurves after $\gamma$-$\gamma$ absorption [251, 252].
- Anisotropic inverse Compton scattering is caused by the dependency of the Compton cross-section on the angle between incoming and outgoing photons, being most efficient in head-on collisions. Thus, inverse Compton scattering is most efficient at inferior conjunction and minimum at superior conjunction. Furthermore, relativistic aberrations focus the emission from HE electrons along its direction of motion, wherefore the observer only sees emission from particles moving along the line of sight, and the spectral shape varies as scattering occurring in the Klein-Nishina regime (which dominates close to the stellar surface due to high stellar photon field energy densities) softens the spectrum, while scattering in the Thomson regime (that dominates at larger distances to the star) leads to a harder spectrum [253]. Furthermore, the orientation of the system to the observer has an impact on the observed $\gamma$-ray emission as shown in Figure 4.8d.
- If taking the orbital parameters into account and hence accounting for the changing photon field energy densities during one orbit due to the eccentricity of the orbit, the orbital modulation of the lightcurves only depends on the geometry of the system. The inclination

of the binary system affects the intensity of pair production and anisotropic inverse Compton scattering and thus may explain the amplitude of the modulated $\gamma$-ray emission. This approach successfully predicts an anticorrelation between the HE and VHE modulations in LS 5039 caused by the fact that only VHE photons are affected by $\gamma$-$\gamma$ absorption while the inverse Compton light curve is the same for both energy bands; however, it cannot explain the observed modulations in other $\gamma$-ray binaries.

The exact combination of these processes varies between the individual $\gamma$-ray binaries and has to be investigated for every $\gamma$-ray binary individually. The relevance of these processes for the $\gamma$-ray binary LMC P3 is discussed in Section 6.6.1.
Next to the orbital modulation of the $\gamma$-ray emission, an anticorrelation of the HE and VHE $\gamma$-ray emission is observed for some $\gamma$-ray binaries, e.g., LS 5039 and LMC P3, as is shown in Figure 4.8a for LS 5039. As mentioned before, this anticorrelation may be explained through the geometry of the system. Another approach explains the anti-correlation of the HE and VHE modulations with two different particle populations as the spectral components of the HE and VHE $\gamma$-ray emission seem to be independent from each other: HE $\gamma$-ray emission is not detected in all $\gamma$-ray binaries (e.g. HESS J0632+057), the lightcurves behave differently (i.e., in LS I $+61^{\circ}303$ and PSR B1259) and an exponential cutoff separates the HE $\gamma$-ray component from the VHE $\gamma$-ray component. As the HE $\gamma$-ray spectrum resembles the spectral energy distribution of pulsars, the emission may originate from particles accelerated in the vicinity of the pulsar, whereas the rest of the spectrum resembles that of a PWN leading to the assumption that VHE $\gamma$-ray emission originates from the termination of the winds in the *pulsar scenario* [255, 256]. Zabalza et al. propose that the HE $\gamma$-ray emission may originate from the apex of the contact discontinuity between the compact object and the star, while the VHE $\gamma$-ray emission is produced in the termination shock on the opposite side. Combined with the geometrical properties of the binary system, these different emission sites can explain the phase-shift of the HE and VHE $\gamma$-ray lightcurves [254]. Further information on models to explain the orbital modulations can be found in [249].

$\gamma$-ray binaries are assumed to be the progenitors of HMXBs [239]. After a lifetime of $\sim 10^5$ yr, corresponding to the spin-down timescale, the power in the pulsar wind decreases sufficiently, so that the pressure becomes too weak to prevent accretion of the stellar wind onto the compact object thereby suppressing the radio pulses. The pulsar wind and hence the associated non-thermal emission is also suppressed. The resulting HMXB is characterised by higher X-ray luminosities with curved spectra as well as X-ray pulsations indicating the spin period of the neutron star as compact object, and they are typically not detected in radio. With a lifetime of a few $10^6$ yr, corresponding to the maximum lifetime of the massive companion, many more HMXBs are detected than $\gamma$-ray binaries. However, out of the estimated $\sim 100$ existing $\gamma$-ray binaries in the Milky Way [257] only six have been detected so far. Missing radio observations,

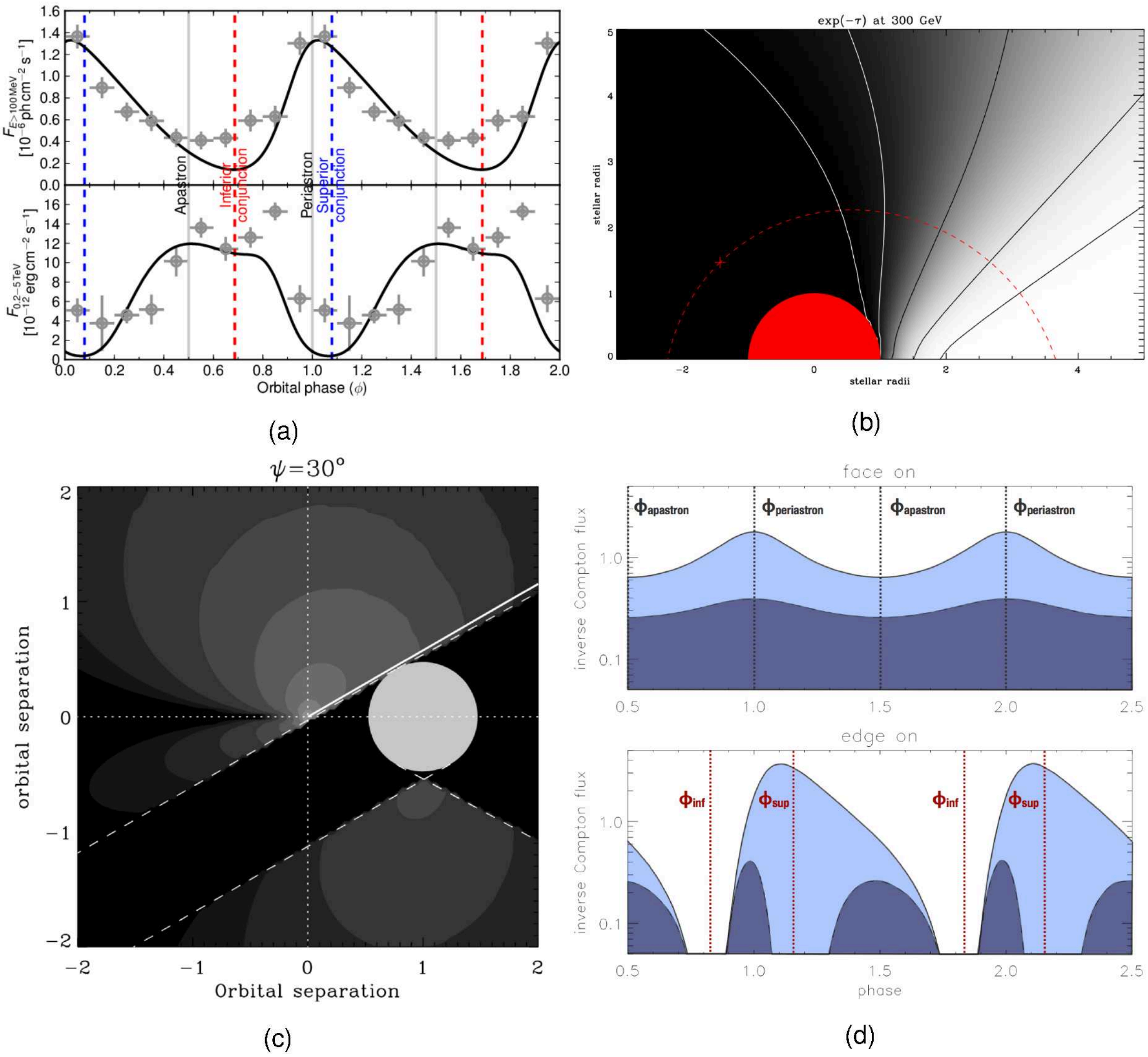

(a) (b) (c) (d)

Figure 4.8: Different processes that may explain the orbital $\gamma$-ray modulation. (a) HE (*Fermi*-LAT) and VHE (H.E.S.S.) lightcurves of the $\gamma$-ray binary LS 5039 demonstrating the orbital modulation of the $\gamma$-ray emission as well as the anticorrelation between the HE and VHE $\gamma$-ray lightcurve. Figure taken from [254]. (b) Intensity of $300\,$GeV $\gamma$ rays of LS 5039 after $\gamma$-$\gamma$ absorption due to pair creation with photons from the star. The intensity of the $\gamma$-ray emission increases towards brighter colours. The lines denote an absorption of 99%, 90%, 50%, 10%, and 1% (from left to right). The red dashed lines indicate the orbit. Figure taken from [249]. (c) Spatial distribution of the VHE $\gamma$-ray emission from the first generation of pair production in the case of cascade emission in LS 5039 when the system is at superior conjunction. The intensity increases towards brighter colours. Figure taken from [249]. (d) Orbital modulation of the anisotropic inverse Compton emission without absorption due to pair production with stellar photons (light blue) and after those absorption effects (dark blue). Top panel: The system is seen face-on; bottom panel: the system is seen edge-on. Figure taken from [249].

unknown physical parameters of the systems as well as the challenge of detecting weak $\gamma$-ray binaries in the HE and VHE regimes with the current generation of instruments may lead to a misclassification of $\gamma$-ray binaries as HMXBs. More multiwavelength observations of HMXBs and $\gamma$-ray binaries are required to get a better understanding of their evolutionary stages as well as their orbital parameters. The latter is especially important to resolve the orbital modulation of the binary that may eventually lead to a detection of $\gamma$-ray emission in a certain part of the orbit as the orbit-averaged $\gamma$-ray flux may not be detectable given the sensitivity of the current generation of $\gamma$-ray experiments.

### 4.3.4 Stellar Clusters inside Star Forming Regions

The current paradigm that Galactic cosmic rays up to the *knee* of the cosmic-ray energy distribution originate from SNRs is still not proven. Although VHE $\gamma$-ray observations confirm the presence of effective cosmic-ray acceleration in SNRs, the observed $\gamma$-ray spectra indicate that there are cutoffs in the cosmic-ray spectra below $\sim 100$ TeV (see Figure 4.5). In the last decade, stellar clusters of young massive stars have gained popularity as an alternative source class to explain the cosmic-ray flux up to $\sim$ PeV energies. Most massive stars form in groups like gravitationally bound stellar clusters or loosely bound associations and remain concentrated in these relative compact regions until they die as a supernova at their birthplaces. Massive ($> 20M_{\odot}$) O, B or Wolf-Rayet stars typically have high mass-loss rates ($10^{-7} - 10^{-5}M_{\odot}\,\mathrm{yr}^{-1}$) with supersonic velocities ($2000 - 3500\,\mathrm{km\,s^{-1}}$) [258] and typical kinetic luminosities of ($10^{36} - 10^{37}\,\mathrm{erg\,s^{-1}}$). Integrated over time, each star releases kinetic energy into the OB association of the same order of magnitude as that of a supernova explosion. As the first supernova events are only expected after $\gtrsim 10^6$ yr, the first period in the lifetime of a stellar cluster is dominated by stellar wind interactions while supernova events become increasingly important in the second period after the first supernova explosions inside the stellar cluster.

Figure 4.9 shows a schematic model for the acceleration and radiation processes of cosmic rays. Simple geometric and kinetic calculations (see, e.g., Parizot et al. [259]) lead to the conclusion that individual wind bubbles merge to form a superbubble within $\sim 10^6$ yr. Inside the superbubble a hot, low-density medium with isolated dense clumps remains. Collisions of continuous stellar winds in single, binary or collective processes lead to a turbulent medium with turbulent magnetic fields. Shock fronts of supernovae exploding inside the stellar cluster propagate through the turbulent medium, colliding with stellar winds as well as with the dense clumps to generate reflected shocks, and part of the explosion energy is converted into additional amplifications of existing magnetohydrodynamic fluctuations. SNRs inside stellar clusters are thought to become sub-

---

[4] https://astronomycommunity.nature.com/users/210810-ruizhi-yang/posts/45984-massive-stars-as-major-factories-of-galactic-cosmic-rays

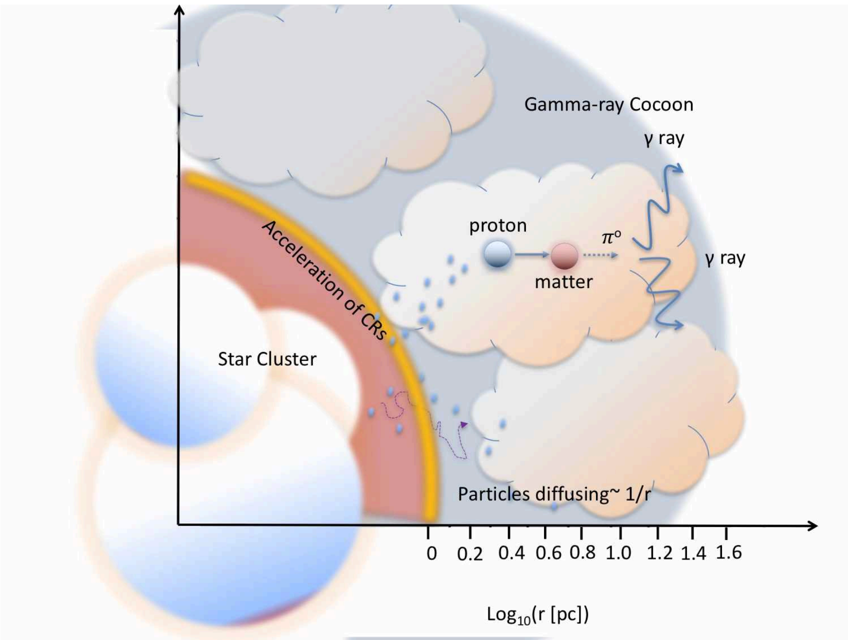

Figure 4.9: Schematic model for particle acceleration sites and radiation processes of cosmic rays in stellar clusters. Cosmic rays are assumed to be accelerated inside the stellar cluster. Protons diffuse away and lose their energy through interactions with the ISM, giving rise to VHE $\gamma$-ray emission. Image Credit$^4$.

sonic before they reach the supershell and never enter the radiative phase. Therefore, most of the explosion energy is turned into internal energy inside the cluster, by transferring a substantial fraction of the shock energy into additional turbulences, before the shell reaches the supershell and is thus available for particle acceleration. Cosmic rays are assumed to be mainly accelerated through (repeated) diffusive shock acceleration via turbulence and magnetohydrodynamic waves in the superbubble interior [259–261] as the expansion velocity of the superbubble shell seems to be too small for effective particle acceleration [260–262]. The maximum energy that can be reached is assumed to be $E_{\rm max} \sim 10^{17}$ eV (corresponding to the ankle of the cosmic-ray energy distribution) [259]. This maximum energy is naturally higher (roughly one order of magnitude) compared to that of isolated SNRs as the free expansion phase lasts longer and extends to larger radii, as well as due to the presence of pre-existing turbulent magnetic fields ahead of the shock front. However, the maximum energy crucially depends on the level of turbulence, the magnetic field strengths and the diffusion coefficient inside the superbubble [259, 263]. Some authors suggest in addition a continuous acceleration of injected low-energy particles through stochastic acceleration (second-order Fermi mechanism) up to very high energies [263]. The efficiency of converting the kinetic energy into relativistic particle acceleration is estimated to be as high as 30% of the energy injected by stellar winds and supernovae, making stellar clusters / associations a promising source class for particle acceleration up to the *knee* of the cosmic ray spectrum.

The question of whether the observed non-thermal emission is hadronic or leptonic in origin is not yet solved. The diffusion length is highly energy- and diffusion-coefficient dependent. The diffusion length of multi-TeV electrons cannot easily exceed $100$ pc [264, 265]. Additionally, the stellar photon field energy density inside a cluster with radius $\leq 3$ pc is $\sim 100$ erg cm$^{-3}$ and only decreases outside the cluster, thus delivering a dense target photon field, where electrons lose their energy through inverse Compton scattering while interacting with these ambient photons. Therefore, an increased $\gamma$-ray intensity towards the dense subclusters inside the superbubble would be expected in the case of an inverse Compton origin of the $\gamma$-ray emission. This scenario seems to be confirmed by X-ray observations (for a review see [266] and references therein). On the other hand, observations of VHE $\gamma$ rays indicate that the emission is most likely hadronic in origin as the emission seems to trace the interstellar gas surrounding the stellar cluster [267, 268]. However, Kavanagh et al. argue that the TeV $\gamma$-ray emission of the LMC superbubble 30 DorC is most likely caused by the leptonic acceleration mechanism based on the synchrotron radial profiles and their magnetic field estimates for the superbubble [269]. More in-depth multiwavelengths studies of individual targets are required to answer the question of the origin of the non-thermal emission. For further details the reader is referred to the reviews by Cesarsky & Montmerle [270], Parizot et al. [259] or Kavanagh [266].

SFRs are ideal targets to search for VHE $\gamma$-ray emission caused by collective wind interaction processes as they typically host several stellar clusters and/or associations and eventually up to a few SNRs, depending on the age of the SFR. Furthermore, as star formation is still ongoing, they typically contain molecular clouds, which would deliver the target material for accelerated cosmic rays to produce VHE $\gamma$-ray emission.

### 4.3.5 Diffuse $\gamma$-ray Emission

Aside from the VHE $\gamma$-ray emission that can be directly linked to individual sources, a diffuse $\gamma$-ray emission is also observed in several galaxies. While diffuse emission from the central molecular zone is detected in the Milky Way [271, 272], the diffuse emission that is seen in the starburst galaxies M 82 and NGC 253 seems to originate from their Galactic centres [12]. In the case of the LMC [69], SMC [68, 108] and M 31 [273] the origin of the diffuse emission is not fully understood, yet. Diffuse $\gamma$-ray emission of the galactic disks carries unique information about the production sites and propagation of accelerated charged particles in the galaxy, and is believed to be the key to answer the long standing question of the origin of cosmic rays. Accelerated electrons and hadrons can escape from their acceleration region and subsequently diffuse into the ISM. The energy dependence of the cosmic-ray diffusion alters the cosmic-ray spectrum from the source to the interaction region, where cosmic rays lose their energy via radiative processes, and thus also affects the shape of the spectrum of the non-thermal emission. Whereas the dominating radiative losses below $\sim 100$ MeV seem to be bremsstrahlung and inverse Compton scattering (and Coulomb losses at even lower energies) due to relativistic electrons interacting with the ambient radiation fields and magnetic fields, the dominating processes at energies above $\sim 100$ MeV are assumed to be the inverse Compton scattering of relativistic electrons, synchrotron emission in the magnetic field of the ISM as well as $\pi^0$-decay into $\gamma$ rays due to relativistic hadrons interacting with the ISM [12, 150]. At multi-TeV energies the diffuse emission is thought to be dominated by cosmic-ray interactions with the ISM as the inverse Compton flux from diffuse cosmic-ray electrons is suppressed by the softening of the electron spectrum in the multi-TeV range as well as the onset of Klein-Nishina suppression of the Compton-scattering cross-section. However, observations of the diffuse emission from the Galactic plane of the Milky Way by H.E.S.S. indicate that at $\sim$ TeV energies both neutral pion decay induced $\gamma$-ray emission and inverse Compton scattering are still relevant [271]. In addition, unresolved sources seem to contribute a non-negligible fraction of the total diffuse VHE $\gamma$-ray emission [68, 271].

The distribution of the parent particle population is expected to vary strongly over the galaxy (see, e.g., [69]). On the one hand, relativistic electrons undergo severe radiative energy losses through inverse Compton scattering of the interstellar radiation field and synchrotron radiation in the Galactic magnetic field. Thus, the most energetic electrons do not travel far from their acceleration sites before they lose most of their energy. Relativistic hadrons above $\sim 1$ GeV usually escape from the host galaxy and hence can travel much larger distances before they lose their energy through interactions with the ISM. On the other hand, regions with active star formation, where an enhanced rate of supernova explosions is expected leading to an enhanced cosmic-ray density, can cause small-scale variations of the (V)HE $\gamma$-ray emission. Whereas in these regions a fresh relativistic particle population is traced through the observed $\gamma$-ray spectrum, the older particle population is instead traced via a diffuse $\gamma$-ray emission on larger scales.

Of particular interest is the diffuse $\gamma$-ray emission at $\gtrsim$ TeV energies. As there is no reason to assume the diffusive shock acceleration mechanism to be different among the host galaxies, the cosmic-ray spectrum is very likely shaped primarily by the source population of the respective host galaxy as well as the cosmic-ray transport. Hence, a potential cutoff in the VHE $\gamma$-ray spectrum traces the maximum energy of the relativistic cosmic rays accelerated by a distinct source population and the spectral shape carries informations about the composition of the cosmic rays as well as the particle diffusion in the environment of the host galaxy. However, particle acceleration mechanisms may differ on short distance scales in a galaxy, as is the case in superbubbles and may have an additional impact on the cosmic-ray spectrum. Thus, observations of diffuse VHE $\gamma$-ray emission of galaxies can help to answer the question of the origin of the cosmic rays and how the environment affects the cosmic-ray transport.

# Chapter 5

# H.E.S.S. Survey of the Magellanic Clouds

The Magellanic Clouds provide an ideal test laboratory for comparing the VHE $\gamma$-ray source populations of the Milky Way to source populations of other galaxies and studying the importance of the source environments. The Magellanic Clouds contain a variety of known VHE $\gamma$-ray emitting source classes in a rather different environment compared to the Milky Way. The H.E.S.S. collaboration performed a survey of the Magellanic Clouds to search for potential VHE $\gamma$-ray sources and to compare the results of the source populations in the Magellanic Clouds with the Galactic source population. The survey of the Magellanic Clouds, the general analysis procedure as well as the systematic uncertainties of the data sets are described in detail in Section 5.1. The dedicated analysis of the LMC and SMC as well as the results are presented in Section 5.2 and 5.3, respectively.

## 5.1 H.E.S.S. Observations of the Magellanic Clouds

As both Magellanic Clouds are very extended sources with dimensions of $10.8^{\circ} \times 9.2^{\circ}$ in the case of the LMC[1] and $5.3^{\circ} \times 3.1^{\circ}$ in the case of the SMC[2]. Since both of these exceed or are equal to the field of view of $\sim 5^{\circ}$ ($\sim 3.5^{\circ}$) of the small-size (large-size) H.E.S.S. telescopes, the galaxies cannot be observed with the usual wobble mode. Instead, an observation pattern is chosen that provides a mostly homogeneous exposure over the entire galaxy. Figures 5.1 and 5.2 show infrared images [274] of the LMC and SMC with the observation pattern overlaid in white circles. The observation time per observation position is adjusted to guarantee a minimum exposure of $20\,$h over the entire galaxy.

---

[1] http://ned.ipac.caltech.edu/cgi-bin/nph-objsearch?objname=LMC&img_stamp=YES&list_limit=9&extend=no

[2] http://ned.ipac.caltech.edu/cgi-bin/objsearch?objname=Small+Magellanic+Cloud&extend=no&hconst=73&omegam=0.27&omegav=0.73&corr_z=1&out_csys=Equatorial&out_equinox=J2000.0&obj_sort=RA+or+Longitude&of=pre_text&zv_breaker=30000.0&list_limit=5&img_stamp=YES

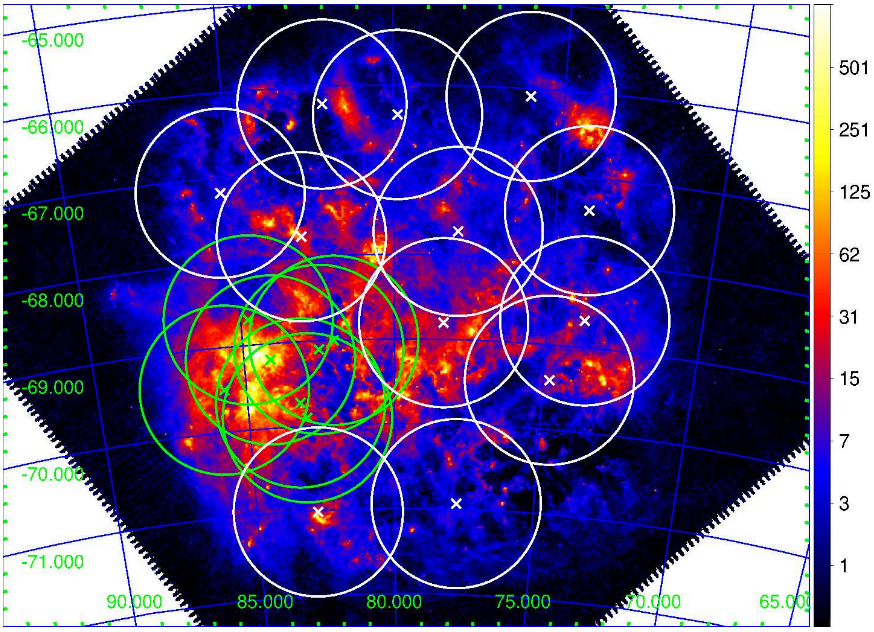

Figure 5.1: Observation positions (white crosses) for the survey of the LMC (white circles) overlaid on an infrared image [274] with units MJy sr$^{-1}$. The radius of the circles is $1^\circ$ corresponding to a $2^\circ$ field of view. Green circles belong to observations with a much deeper exposure taken previously to the H.E.S.S. survey of the LMC. The bright Tarantula nebula is located in the south-east of the LMC. Sky maps are shown in a Cartesian projection. North is up, east is right.

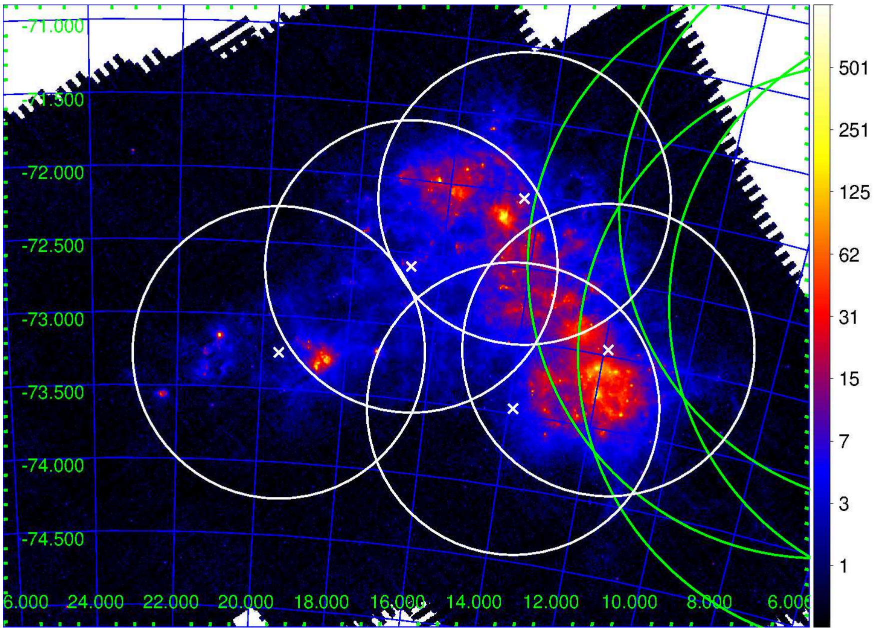

Figure 5.2: Observation positions (white crosses) for the survey of the SMC overlaid on an infrared image [274] with units MJy sr$^{-1}$. The radius of the circles is $1^\circ$. Further observations towards 47 Tucanae are shown in green with a radius of $2^\circ$ to visualise the overlap. The SMC *Bar* extends from the north to the south-west of the SMC, while the *Wing* is located in the east of the galaxy. Sky maps are shown in a Cartesian projection. North is up, east is right.

Certain regions of the LMC had already been observed between 2005 and 2013, prior to the combined survey of both Magellanic Clouds, leading to a deep exposure of $\sim 180$ h towards the exceptionally bright PWN N 157B. In order to cover the remaining galaxy with a homogeneous exposure, the observation positions are spread towards the outskirts of the galaxy. Each telescope pointing has an assigned priority, where the highest priority is given to observation positions complementing the LMC core with decreasing priority towards the outskirts with lower source densities. The LMC survey observations started in 2015 and are still ongoing. So far a homogeneous exposure of at least $20$ h has only been achieved for observation positions with higher priorities while the outskirts at the northwest of the galaxy only gained exposure from neighbouring observation positions with resulting exposures of as low as $0.5$ h. Therefore only a biased population study and comparison between the source populations of the LMC, the SMC and the Milky Way can be performed. The survey will be continued in the upcoming 2-3 years. The data set presented here was only taken with the HESSI array configuration (CT1-4). A full coverage with a deep exposure of the LMC with CT5 was out of reach due to the smaller field of view of CT5 and missing exposure towards the LMC core, as the first data sets towards N 157B were taken before CT5 was incorporated into the H.E.S.S. array.

For the SMC, each observation position is observed for $20$ h. Due to overlapping fields of view of the observation positions the deepest exposure is reached towards the SMC *Bar*, where most of the young stellar populations are located due to the increased star formation rate in the last Myrs. One observation position covers the *Wing*, where major star formation episodes occurred in the recent past. The SMC survey by H.E.S.S. was performed between 2014 and 2015 and the data were mainly taken in the hybrid array configuration (CT1-5) with the HESSI and HESSII cameras. Due to the HESSIU camera upgrade that started in 2015, CT1 was not available during the observations taken in 2015. The data set is complemented by a few observations performed in subarrays of CT5 mono, CT1-4 and a set of archival CT1-4 data taken between 2005 and 2012. Additionally, the SMC data set profits from observations taken of the globular cluster 47 Tucanae located inside the Milky Way, which has an angular separation of only $2.3^\circ$ to the SMC centre. Those observations are indicated in Figure 5.2 with green circles with a radius of $2^\circ$.

### 5.1.1 Introduction to the Data Sets

Large variations in atmospheric conditions as well as optical efficiencies of the telescopes in the data sets, taken over a long period of time, were addressed through the data quality selection (see Section 3.1.3) and a muon based calibration (see Section 2.2.3), respectively. The more stringent spectral quality selection criteria are applied to ensure a high quality of the large-zenith-angle data sets mostly taken under moderate weather conditions (cloudy sky and partly raining season in Namibia) and hence reduce the data set related systematic uncertainties. The cut on the run duration is reduced to $> 5$ min to include truncated runs due to the end of the night, or

due to the interruption of a run to observe a transient source with a higher priority.
In the case of the CT1-4 data sets, only those observations with at least three operational telescopes are included to improve the reconstruction of the event arrival direction.
In the case of the CT5 data set, the cut on the atmospheric transparency coefficient has to be excluded from the run selection, as it was not available for the data set presented in this thesis when the analysis was conducted. Only recently have preliminary atmospheric transparency coefficients for the data set become available and thus they are used to estimate the systematic uncertainty on the flux due to increased atmospheric variations within the CT5 data set (for more details see Section 5.1.3).

The final exposure of the data sets, for which the analysis is presented in this work, is shown in Figure 5.3. SMC and LMC contours based on IR images from the Multiband Imaging Photometer (MIPS) on the Spitzer Space Telescope [274] are overlaid in green. Due to non-equal exposures for the CT1-4 and CT5 observations towards the SMC and increasing systematics for the combined (CT1-5) data set (as explained in Section 5.1.3), the data set on the SMC is split and presented separately for CT1-4 and CT5; this gives the advantage of a lower energy threshold for the CT5 data set.
The LMC has a deep exposure of up to $\sim 200$ h towards PWN N 157B located in the LMC core. However, as the LMC survey is not concluded yet, the minimum exposure towards the outskirts gradually decreases down to $\sim 0.5$ h for the outermost sources that are covered by the survey.
In the case of the SMC, the deepest exposure is achieved towards the east of the SMC Bar which profits from the data set taken on 47 Tucanae. The SMC Bar has a minimum exposure of $\sim 40$ h ($\sim 20$ h) with a maximum of up to $\sim 60$ h ($\sim 40$ h) while the entire SMC has a minimum exposure of $\sim 15$ h ($\sim 7$ h) for the CT1-4 (CT5) data set.
The extend to which the results can be compared between the Magellanic Clouds and to the Milky Way will be discussed in Chapter 6.

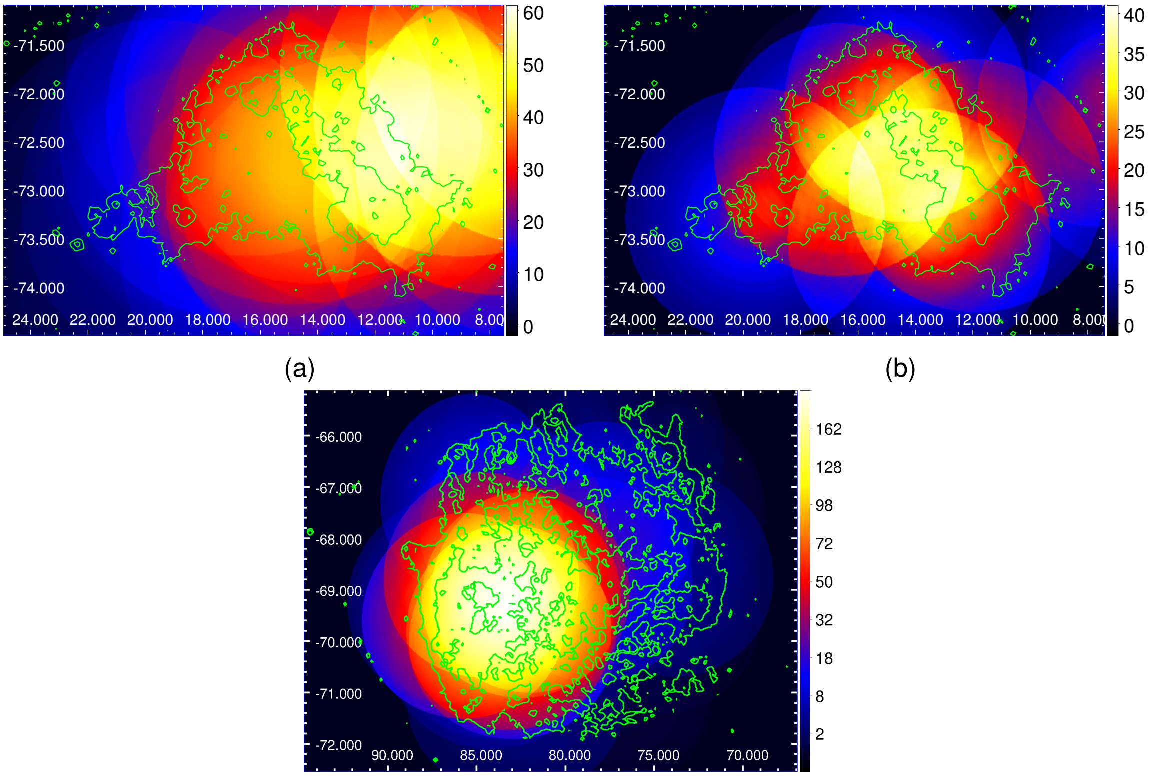

(a)

(b)

(c)

Figure 5.3: Acceptance corrected live-time (in units of [h]) maps for the presented data sets of the SMC and LMC: (a) SMC: CT1-4, (b) SMC CT5, (c) LMC. Overlaid in green are $70\mu\mathrm{m}$ IR contours $(1, 10, 100$ MJy sr$^{-1})$ [274]. Sky maps are shown in a Cartesian projection.

### 5.1.2 General Analysis of the Data Sets

Data sets of observations taken in a survey mode require a different analysis strategy from data sets of an individual source taken in a wobble mode. Whereas for individual objects mainly the source itself is of interest, for a survey data set the entire observed field must be investigated as potential VHE $\gamma$-ray sources may be located anywhere in the observed field. Therefore, a few adaptations are made to the analysis that are described in more detail in the following section. In order to guarantee a mostly unbiased comparison of the different source populations among the Magellanic Clouds, the same analysis is applied to the data sets of both galaxies, if not otherwise stated.

This work makes use of a multivariate analysis technique of boosted decision trees for the $\gamma$-hadron separation in combination with the template-based likelihood fitting method ImPACT for the event reconstruction (described in more detail in Section 3.1.4). Standard cuts are applied during the analysis as they were optimised to yield unbiased results for most of the known VHE $\gamma$-ray sources.

An energy reconstruction accuracy of $\sim 15\%$ and a direction reconstruction accuracy (radius of PSF) of $\sim 0.08^\circ \pm 0.004^\circ$ ($\sim 0.15^\circ \pm 0.02^\circ$) for the CT1-4 (CT5) data set is achieved. The PSF is slightly worse compared to the nominal values of $0.07^\circ$ ($0.13^\circ$) due to the large zenith angles of the observations and the large offset distribution between observation position and test position in the data sets.

Survey sky maps are produced on a run-by-run basis; each observation run is analysed individually, and all the individual sky maps are then summed up to produce the total survey sky maps, which are presented in a Cartesian projection in equatorial coordinates (J2000). As systematic effects in the event reconstruction increase with increasing offset to the camera centre, only those events with a reconstructed primary photon direction within a radius of $2^\circ$ ($1.3^\circ$) of the camera centre are included in the final event maps, resulting in an effective field of view of $4^\circ$ ($2.6^\circ$) diameter for the CT1-4 (CT5) data set (more details are given in Section 5.1.3). In addition, energy cuts have been applied to the reconstructed event energies to reduce systematic uncertainties in the energy reconstruction from an increasing bias towards the lower energy threshold of the observations. To guarantee a mostly unbiased flux estimation, additional energy cuts have been applied to obtain a uniform energy threshold over the entire field of view. The resulting energy thresholds are $1$ TeV and $400$ GeV for the CT1-4 and CT5 data set, respectively. For further details on the computation of the energy thresholds, the reader is referred to Section 3.1.6.

The $\gamma$-ray like background is estimated via the *ring background model* as it is best suited for the computation of sky maps (see Section 3.1.5). For each position in the field of view, the background is estimated in a ring with constant ring radius of $0.7^\circ$ around this position. Exclusion regions are defined iteratively to exclude significant $\gamma$-ray emission from the background estimation to avoid an overestimation of the background level. After a first analysis, in which only known sources are excluded from the background estimation, exclusion regions are defined for regions exceeding a significance threshold of $4.5\,\sigma$. This procedure results in an exclusion region of $0.35^\circ$ around the globular cluster 47 Tucanae in the case of the SMC as well as two additional exclusion regions (besides the three known sources N 157B, 30 DorC and N 132D) in the case of the LMC: i) an exclusion region of $0.25^\circ$ around a newly discovered source, spatially consistent with the $\gamma$-ray binary LMC P3 (more details are given in Section 6.6.1) and ii) an exclusion region of $0.25^\circ$ around an unidentified "hot spot" at RA = $80.146^\circ$ and Dec = $-68.889^\circ$.

The run-wise instrument acceptance maps are generated based on the data itself for the same energy thresholds as were used for the event sky maps. Deviations from a radially symmetric acceptance profile are negligible due to a low level of night-sky background and a low number of exclusion regions (more details are given in Section 5.1.3).

Sky maps (e.g., significance or flux upper limit maps) are computed based on the total survey sky maps, where, for each pixel in the field of view, all *on* and *off* events in the region of interest from all individual sky maps are summed. The background normalisation factor $\alpha$ is computed accordingly with $\alpha = \frac{\sum_0^n \Omega_{on}}{\sum_0^n \Omega_{off}}$, with $\sum_0^n \Omega_{on}$ being the sum of all solid angles of the *on* region and $\sum_0^n \Omega_{off}$ being the sum of all solid angles in the respective *off* regions. Significance and flux (upper limit) maps are then computed pixel-wise for a correlation radius $\Theta_{cut} = 0.071^\circ$ $(0.126^\circ)$ for the CT1-4 (CT5) data set following the descriptions of Section 3.1.7 and 3.1.8.

### 5.1.3 Systematic Uncertainties of the Magellanic Cloud Data Sets

The LMC and SMC data sets cover a large observational phase-space (e.g., atmospheric conditions, instrument response or zenith angles), which may lead to significant variations in the parameter phase-space between sources (e.g., zenith angles, source offsets to the telescope pointing). To guarantee a mostly unbiased flux comparison of intra- and inter-Galactic populations, the systematic uncertainties of the data sets are investigated in this section while mainly following the descriptions in Section 3.2.

In Section 3.3 it was shown that the systematic uncertainties only marginally vary for a wide range of observational parameters such as the exposure, the mean zenith angle and the mean offset of the source to the observation position. Therefore, the systematic uncertainties for the data sets of the Magellanic Clouds are estimated for the total data sets and are assumed to be valid for all positions in the field of view even though they cover a wide range in exposure or offsets to the observation position.

As the observational conditions (e.g., the observation strategy, minimum exposure or zenith angle distribution) for the SMC and the LMC are roughly comparable, the systematic uncertainties are investigated using the SMC data sets (for both the CT1-4 and CT5 data sets). The resulting cuts and systematic uncertainties of the CT1-4 data set are then applied to the LMC data set as well, to guarantee a mostly unbiased comparison of the fluxes between the SMC and LMC source populations.

#### Systematic Uncertainties in the Background Estimation

Systematic uncertainties in the background estimation mainly originate from increasingly large uncertainties in the event reconstruction at low energies. These uncertainties also increase with increasing zenith angles of the observations as well as increasing event offsets to the camera center.

The mean zenith angle for both SMC data sets is $50^\circ$. As the amount of available off-data decreases with increasing zenith angle, the available statistics of those off-runs may not be sufficient to determine a representative acceptance profile for the underlying data set. This fact is even more relevant for the CT5 data set as CT5 has only been operational since 2012 and even

Table 5.1: Background estimation with different acceptance modelling.

| Acceptance model | CT1-4 | | CT5 | |
|---|---|---|---|---|
| | mean | $\sigma$ | mean | $\sigma$ |
| data itself | -0.047 | 0.99 | -0.054 | 1.03 |
| off-data | -0.028 | 1.00 | -0.043 | 1.14 |

mean and $\sigma$ are the mean and the width of a Gaussian distribution fitted to the significance distribution.

less off-data are available for CT5 data sets at large zenith angles. A comparison of the background estimation — computed by using acceptance profiles from off-data and by determining the acceptance profile from the data itself — is summarised in Table 5.1 for both the CT1-4 and CT5 data sets. If the background estimation is purely dominated by statistical fluctuations, the significance distribution of the background events is expected to follow a Gaussian distribution with a mean of $0$ and a standard deviation of $1$. Any deviation from a Gaussian distribution is a potential indicator of systematic uncertainties during the background estimation that can be caused by, amongst other reasons, one dimensional acceptance profiles deviating from the actual two dimensional acceptance of the underlying data set and hence will lead to an over- or underestimation of the $\gamma$-ray background. Whereas for the CT1-4 data set, there is almost no difference in the background estimation using the two methods, the CT5 data set shows a clear preference for the acceptance determination from the data itself; this may be due to the lack of statistics for large zenith angle off-data, the interpolation of the off-data to match the observational zenith angle, or differences in the shapes of the instrument acceptance.

A further check of the significance sky maps in different energy bins showed hotspots at higher energies ($2.5 - 6.3$ TeV) when using acceptance from lookups for the CT5 data set. These hotspots are caused by strongly deviating acceptance profiles towards the observation position, between the acceptance determination from lookups and based on real data. When using acceptance from lookups for energy ranges above $\sim 1$ TeV for the CT5 mono data, the acceptance is underestimated for regions close to the observation position; this leads to an underestimation of the background close to the observation position (or an overestimation of the background in the surrounding ring) and hence an overestimated $\gamma$-ray flux towards the centre of the field of view which can even lead to a significant fake $\gamma$-ray emission.

Both tests show a clear preference for acceptance determination from the data itself for the CT5 data set and hence acceptance profiles from data are used for all analyses results presented in the following. For consistency reasons the acceptance profile is determined from the data itself for both the CT5 and CT1-4 data sets.

In addition, the one dimensional acceptance profile is smoothed by a polynomial of sixth degree over 150 bins or a polynomial of third degree over 40 bins for the CT1-4 and CT5 data set, respectively, to eliminate ring-like features in the acceptance due to low statistics.

Another systematic uncertainty is caused by a combination of the changing atmospheric depth — which varies significantly over the field of view of $5^\circ$ $(3.5^\circ)$ of the CT1-4 (CT5) telescopes for observations at zenith angles of $\geq 50^\circ$ — and the presence of truncated events arriving at the edge of the field of view. The absorption of Cherenkov light in the atmosphere $\tau_{\mathrm{abs}}$ increases with increasing atmospheric depth at increasing zenith angles $z$ as $\tau_{\mathrm{abs}} \propto \cos(z)$. The effect increases with decreasing $\gamma$-ray energy, causing an increased energy threshold with increasing zenith angles. On the other hand, truncated events at the edge of the field of view are more likely to be misreconstructed (towards lower energies) leading to an increased systematic uncertainty with increasing event offsets to the camera center at the lower end of the energy scale (see Section 3.1.6). If no cut on the energy threshold is applied to the data sets of the Magellanic Clouds, the significance distribution of CT5 broadens significantly ($\sigma = 1.58$) indicating increased systematic uncertainties in the background estimation. For the CT1-4 data set the systematic uncertainties are negligible ($\sigma = 1.027$), which is most likely due to the improved event reconstruction in a stereo mode. The gaussian width can be estimated by $\sigma = \sqrt{\sigma_{\mathrm{stat}}^2 + \sigma_{\mathrm{syst}}^2}$, where $\sigma_{\mathrm{stat}} = 1.$ A width of $\sigma = 1.58$ results in $\sigma_{\mathrm{syst}} = 1.22.$ In this case, the systematic uncertainties are more significant than the statistical uncertainties. Therefore, two cuts are applied to the data sets: first, a cut on the reconstructed primary photon direction at $2^\circ$ $(1.3^\circ)$ for the CT1-4 (CT5) data set and second, a cut on the energy threshold. As the Magellanic Clouds are observed in a survey mode, potential $\gamma$-ray sources are spread over a range of offsets to the camera centre. As the energy threshold increases with increasing offset to the camera center, a conservative energy threshold at the maximum event offset of $2^\circ$ $(1.3^\circ)$ from the observation position is applied to each individual run of the CT1-4 (CT5) data set. These cuts reduce the systematic uncertainties in the background estimation of the CT5 data set significantly, resulting in a gaussian distribution with a width of $\sigma = 1.15$ and hence a systematic uncertainty with $\sigma_{\mathrm{syst}} = 0.57$.

However, these energy thresholds vary from run to run due to the variation of the zenith angles which range between $48^\circ$ and $57^\circ$ within the data sets. Figure 5.4 shows the distribution of energy thresholds for both data sets of the SMC. The energy thresholds of the observations mainly range between $\sim 700$ GeV and $\sim 1$ TeV ($300$ GeV and $400$ GeV) for the CT1-4 (CT5) data set. Due to overlapping observation positions, the energy thresholds of the single observation positions average out to give a more homogeneous data set energy threshold. However, the $\gamma$-ray statistics close to the energy threshold vary strongly depending on the potential source location in the field-of-view and the number of observations contributing statistics in a certain energy range. To ensure that the population study is not biased by low statistics close to the energy threshold, a conservative energy threshold of $1$ TeV and $400$ GeV is chosen for the CT1-4 and CT5 data set, respectively. An inspection of the energy threshold distribution of the LMC data set with energy thresholds ranging between $\sim 500$ GeV and $\sim 1$ TeV confirmed the validation of applying an energy threshold of $1$ TeV to the LMC data set as well.

A summary of the quality of the background estimation after applying the different energy cuts is given in Table 5.2. The mean and width of the Gaussian distribution that best describes the

Table 5.2: Background systematics after application of energy cuts.

| Energy cuts | CT1-4 | | CT5 | |
|---|---|---|---|---|
| | mean | sigma | mean | sigma |
| None | 0.041 | 1.027 | 0.267 | 1.577 |
| Safe Energy Threshold | 0.024 | 1.008 | 0.324 | 1.153 |
| 1 TeV / 400 GeV | -0.054 | 0.992 | 0.298 | 1.105 |

significance distribution of the background are given for the background estimation under three scenarios: 1) without applying any energy cuts, 2) after applying the safe energy threshold cut, and 3) after applying the energy cut of $1$ TeV and $400$ GeV for the CT1-4 and CT5 data set, respectively. While the effect of applying different energy cuts is less significant for the CT1-4 data set, the background estimation is significantly improved for the CT5 data set after applying all cuts, due to the lower energy threshold of the telescope.

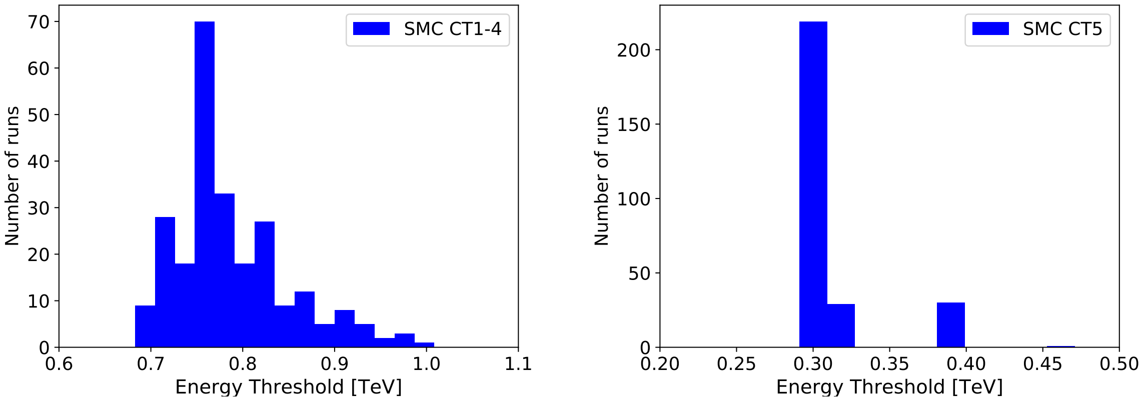

(a) (b)

Figure 5.4: Energy threshold distribution for all runs of the (a) CT1-4 and (b) CT5 data sets.

### Instrument Related Systematic Uncertainties

Instrument related uncertainties are mainly caused by the atmosphere, the camera and the read-out. Following the description in Section 3.2, the data set related systematic uncertainties are summarised here.

To estimate the systematic uncertainties caused by seasonal variations in the atmospheric density profile, the same approach as for the bow shocks is applied (see Section 3.3.2). The observations of both data sets (CT1-4 and CT5) are taken between the months of July (Namibian winter) and December (Namibian summer), covering the most extreme variations in atmospheric density profiles. Therefore, the maximum systematic uncertainty on the energy scale of 4% is assumed for both data sets, which is converted into a systematic uncertainty on the flux of 5% via Equation 3.10 by assuming a spectral index of $\Gamma = 2.3$.

The systematic uncertainty due to the zenith angle dependent atmospheric transmission is estimated using Equation 3.8 and Equation 3.10. In Section 3.3.2 it is shown using the sample of bow shocks that the systematic uncertainties are consistent for zenith angle variations of $\sim 5^{\circ}$. Thus, the mean observational zenith angle of $50^{\circ}$ is used to estimate the systematic uncertainties due to the zenith angle dependent atmospheric transmission, which is estimated to contribute a systematic uncertainty on the flux of 11%.
The systematic uncertainties due to broken pixels is conservatively assumed to be 5% for both data sets and the systematic uncertainties due to dead time estimations are estimated to be less than 1% for the CT1-4 data set and 5% for the CT5 data set, as detailed in Section 3.2.2.

**Data Set and Analysis Related Systematic Uncertainties**

The Magellanic Clouds data sets are gathered over a long period of time and hence observational conditions and instrument responses may vary strongly. Variations in the atmospheric transmission between individual observations can significantly increase the systematic uncertainties of the data set. Furthermore, systematic uncertainties in the background estimation may increase due to varying statistics in data sets covering a large region in the sky. These data set as well as analysis dependent systematic uncertainties are estimated in the following.
The systematic uncertainty on the flux due to short-term variations in the atmospheric transmission is estimated based on the rms of the atmospheric transparency coefficients of every individual run in the data set, for both data sets separately, and is estimated to 8% and 28% for the CT1-4 and CT5 data set, respectively. The significantly higher systematic uncertainty in the CT5 data set compared to the CT1-4 data set originates from the fact that the data quality selection of the CT5 data set was done without taking the atmospheric transparency coefficients into account (see Section 5.1.1) leading to a larger variation in the atmospheric transparency coefficients in the CT5 data set.
Another systematic uncertainty on the measured flux originates from the systematic uncertainty in the background estimation. Unlike for individual sources with significant $\gamma$-ray emission, a common systematic uncertainty for the entire data set is estimated here. As the iterative approach to find exclusion regions revealed no significant $\gamma$-ray emission in the SMC (and only 4 point-like sources in the LMC) it can be assumed that the sky maps mainly show statistical fluctuations. Thus, established methods like variations in the signal-to-noise ratio for different observation positions cannot be used for the data sets of the Magellanic Clouds. However, the widths of the background significance distributions for both data sets (see Table 5.2) indicate that the systematic uncertainties are subdominant over the field of view compared to the statistical uncertainties, with $\sigma_{\mathrm{syst}} \lesssim 0.5\sigma_{\mathrm{stat}}$. Therefore, a systematic uncertainty of 1% on the background estimation is assumed for the entire data set, in agreement with the findings by H.E.S.S. Collaboration (2006) [275]. As the background estimation for the sky map production is done with the

*ring background model*, the radially decreasing $\gamma$-ray acceptance as well as edge effects (due to regions for which the background can only be estimated based on truncated rings) may cause systematic effects over the field of view of a telescope pointing. Therefore, the individual *on* and *off* event sky maps are used to identify such systematic effects. For every observation position, all available individual *on* and *off* event sky maps are summed up to increase the statistics. The *on* and *off* events are summed divided into 20 right ascension bins and 30 declination bins in a grid centred on the observation position. By using Equation 3.1, a significance distribution along the slices is estimated and fitted with a straight line. Figure 5.5 shows the significance distribution for one observation position for both data sets along the right ascension and declination axis as an example. Although there is no evidence for increased systematic effects towards the edge of the field of view, a gradient of $\sim 0.2\sigma$ per degree is found over the field of view, resulting in a dependence of the systematic uncertainties on the position in the field of view. This systematic uncertainty is not included in the total systematic uncertainty of the data set, but shows that the results of the analysis should be taken with a grain of salt.

Finally, the systematic uncertainties of the background estimation are validated in several energy bins, confirming the increasing systematic uncertainties towards the lower energy threshold and thus the need for the energy cuts determined in Section 5.1.3.

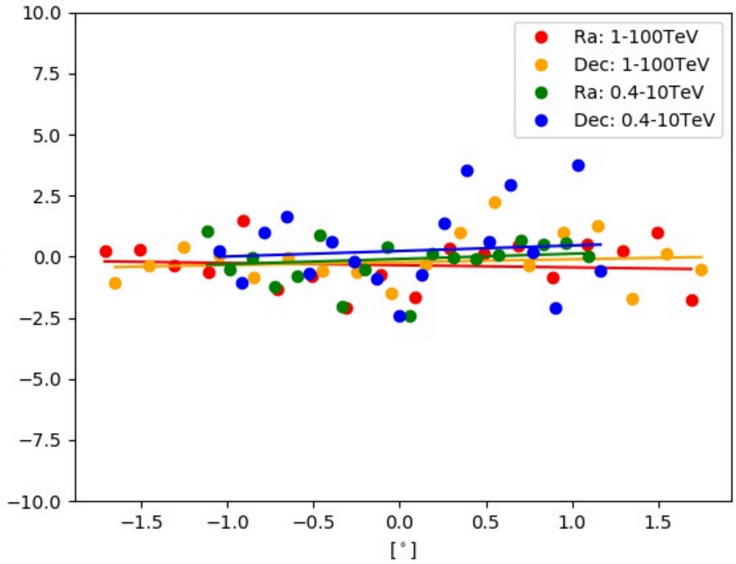

Figure 5.5: Significance distribution along the right ascension and declination axis (in camera coordinates) for the CT1-4 and CT5 data set. A significance gradient of $\sim 0.2\sigma$ per degree is found over the field-of-view.

All relevant systematic uncertainties are summarised in Table 5.3. The total systematic uncertainties add up to 16% and 31% for the CT1-4 and CT5 data set, respectively. Thus, a systematic uncertainty of 16% is also applied to the LMC data set. Unless otherwise stated, these systematic uncertainties are taken into account when estimating any fluxes or flux upper limits, as

Table 5.3: Systematic uncertainties on the flux measurement for the SMC data sets.

| Uncertainty | CT1-4 | CT5 |
|---|---|---|
| MC Shower interactions | 1% | 1% |
| MC Atm. density profile | 5% | 5% |
| Atmospheric transmission | 11% | 11% |
| Broken pixels | 5% | 5% |
| Dead time | 1% | 5% |
| Background estimation | 1% | 1% |
| Run-by-Run variability | 8% | 28% |
| Total | 16% | 31% |

described in the following sections.

## 5.2 Analysis of the Large Magellanic Cloud

This section focusses on the analysis and results of the LMC survey data sets. The H.E.S.S. survey data set together with the results will be described in Section 5.2.1. Section 5.2.2 concentrates on the upper limit estimation. In Section 5.2.3 the selected H.E.S.S. source candidate catalogues are presented, followed by the description of the flux upper limit catalogues in Section 5.2.4. A comparison of the source populations in the Magellanic Clouds and in the Milky Way are given in Chapter 6.

### 5.2.1 Characterisation of the LMC Data Set

At the distance of the Magellanic Clouds all known Galactic $\gamma$-ray source classes, such as SNRs, PWNe, pulsars or $\gamma$-ray binaries, can be assumed to be point sources for the H.E.S.S. telescopes. Therefore, a point-source analysis with a $\Theta^2$ cut of $0.005\,\mathrm{deg}^2$, which corresponds to a PSF with radius of $\sim 0.07^\circ$, is performed and all sky maps described in the following are correlated with this radius. For all analyses a lower energy threshold of $1\,$TeV is applied. In the case of the upper energy threshold, the value chosen depends on the purpose. When estimating the significance of the $\gamma$-ray emission for a certain location, all reconstructed events above the energy threshold are considered. The maximum energy is given by the maximum reconstructed event energy for each location in the field of view. If a flux, sensitivity or flux upper limit is derived, only events with reconstructed energies between $1-10\,$TeV are considered to ensure that a lack of instrument sensitivity at higher energies does not influence the flux estimations; note that this may result in too optimistic estimates. The derived flux is then extrapolated to an energy range of $1-100\,$TeV. More details will be given in Section 5.2.2.

Figure 5.6a shows a map of the integrated sensitivity in the energy range $1-100\,$TeV for a point-like $\gamma$-ray excess that refers to the nominal $5\sigma$ threshold, that is used as a definition for a significant $\gamma$-ray emission. Towards the Tarantula nebula, in the region with the deepest exposure, a point-source flux sensitivity of as low as $\sim 8 \times 10^{-10}\,\mathrm{m}^{-2}\mathrm{s}^{-1}$ is reached, which corresponds to an integrated luminosity of $L \sim 1.2 \times 10^{35}$ erg s$^{-1}$. Towards the outskirts of the LMC a significantly reduced point-source flux sensitivity level of $\gtrsim 10^{-8}\,\mathrm{m}^{-2}\,\mathrm{s}^{-1}$ ($L \gtrsim 1.5 \times 10^{36}$ erg s$^{-1}$) is reached.

A sky map of the significance of the measured $\gamma$-ray excess is shown in Figure 5.6b. Significant emission is found for the known sources: the PWN N 157B and the superbubble 30 DorC. A hint of an increased $\gamma$-ray excess is found at the positions (RA $= 80.15°$, Dec $= -68.89°$) and (RA $= 84.00°$, Dec $= -67.59°$). While no counterpart at other wavelengths is found for the former position, the latter position is coincident with the recently detected $\gamma$-ray binary LMC P3 [276]. This position is investigated in more detail in Section 6.6.1. For the rest of the field of view no significant $\gamma$-ray emission is seen and the significance distribution is compatible with background only. When comparing the integrated flux in the energy range of $1-100$ TeV of PWN N 157B of $7.2 \times 10^{-9}\,\mathrm{m}^{-2}\,\mathrm{s}^{-1}$ with the sensitivity sky map shown in Figure 5.6a it can be concluded that it is unlikely that the LMC contains another $\gamma$-ray source as powerful as PWN N 157B. However, due to the limited exposure towards the outskirts of the LMC, another powerful $\gamma$-ray emitter in the LMC cannot be ruled out until the LMC survey has been completed.

Based on the derived $\gamma$-ray excess, upper limits on the integrated flux for selected potential $\gamma$-ray sources are estimated (see Section 5.2.2). These upper limits are used as the basis for a comparison of the $\gamma$-ray source population in the SMC, the LMC and the Milky Way in Chapter 6.

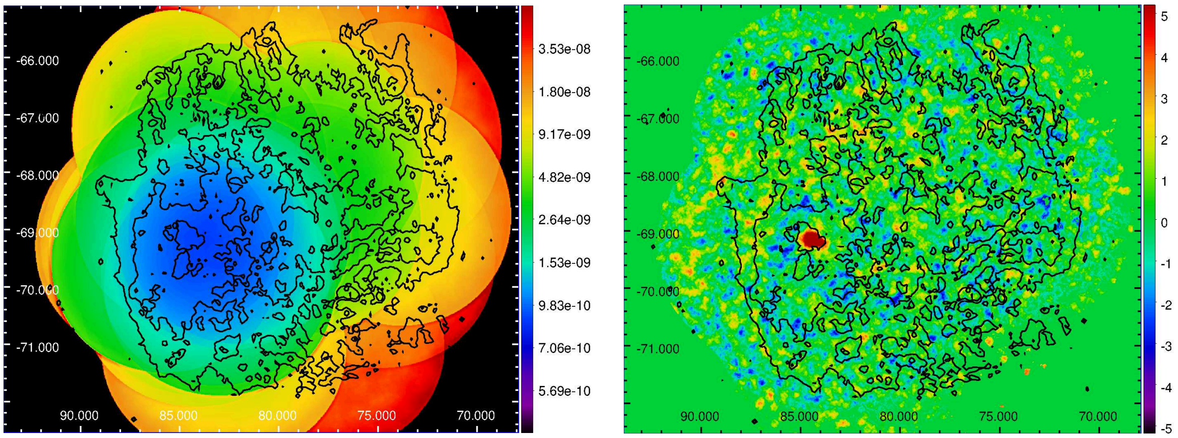

(a) (b)

Figure 5.6: (a) Integrated sensitivity (in units of m$^{-2}$ s$^{-1}$) in the energy range of $1-100$ TeV for a point-like $\gamma$-ray excess with a significance of $> 5\sigma$. (b) Significance (in units of $\sigma$) for point-like $\gamma$-ray emission above an energy threshold of 1 TeV. The sky maps are correlated with a radius of $\Theta = 0.07°$ and are shown in a Cartesian projection. Contours are the same as in Figure 5.3.

### 5.2.2 Estimation of Integral Flux Upper Limits

Significant $\gamma$-ray emission is only found for four sources in the LMC, while the rest of the data set is background dominated. As potential sources of $\gamma$-ray emission below the sensitivity of the H.E.S.S. instrument may be distributed over the entire galaxy, integrated flux upper limits are estimated for the whole field of view to constrain the potential $\gamma$-ray flux for the entire population in the LMC. The integrated flux upper limits are estimated following the approach by Rolke et al., as described in Section 3.1.8. The lack of statistics above $10\,$TeV due to a decreasing instrumental sensitivity with increasing $\gamma$-ray energies may lead to an underestimation of the integral flux. Therefore, the integral flux upper limits are derived based on the reconstructed events within an energy range of $1-10\,$TeV and are then extrapolated to an energy range of $1-100\,$TeV. A $\gamma$-ray spectrum following a power law with index $\Gamma = 2.3$ is assumed. The upper limits are estimated for a confidence level of 95% while taking into account the systematic uncertainties obtained for the CT1-4 data set of the SMC.

For individual $\gamma$-ray source candidates, the more accurate *reflected region background model* is usually applied for the flux reconstruction and hence the integral flux upper limit calculation (for more details see Section 3.1.5). However, analysing every potential $\gamma$-ray source separately would result in a huge computational effort for a survey with a large field of view. Therefore, the integral flux upper limit estimation is based on the *ring background model*. To ensure that the upper limits estimated using the *ring background model* are not biased compared to the upper limits obtained from dedicated analyses for point-like $\gamma$-ray sources, integral flux upper limits are estimated based on both background rejection approaches for a representative sample of test positions in the field of view, and the results are compared. This comparison is also done for the SMC CT5 data set.

The comparison of the integral flux upper limits for a range of mean offsets between test position and observation position is shown in Figure 5.7. No systematic bias between the integral flux upper limits is found. For more than 95% (84%) of the test positions in the CT1-4 (CT5) data set the ratio of the integral flux upper limits is less than a factor of $2$, which is less than the variation caused by statistical fluctuations. The difference in the integral flux upper limits is caused by the difference of the background levels estimated with either the *ring background* or the *reflected region background model*. Thus, estimating integral flux upper limits based on the *ring background model* is a valid approach for large data sets.

The resulting sky map containing the estimated integral flux upper limits for VHE $\gamma$-ray emission from sources that appear point-like for the H.E.S.S. instrument is shown in Figure 5.8. All integral flux upper limits that are listed in the following sections are extracted from these upper limit sky maps, if not otherwise specified.

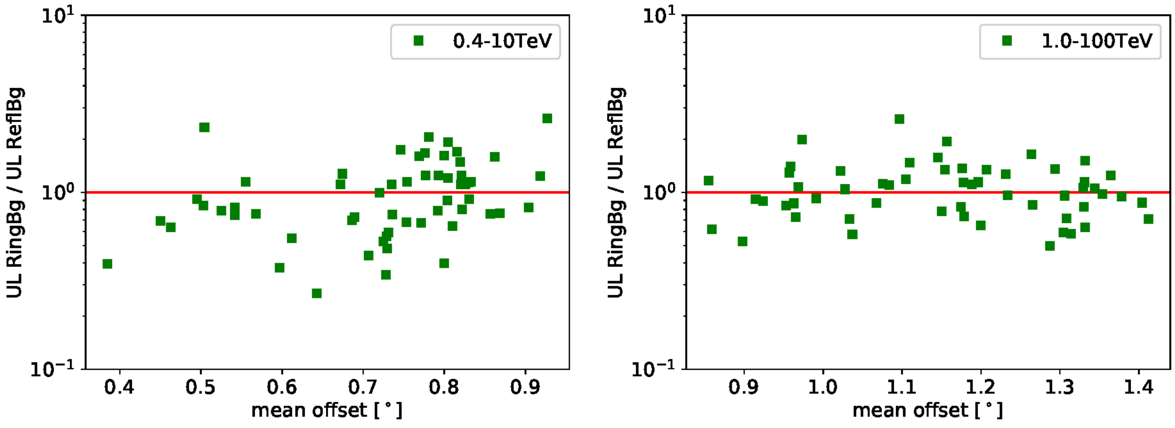

(a) (b)

Figure 5.7: Ratio of the integral flux upper limits, estimated by applying the *ring background model* and the *reflected region background model* for the background rejection as a function of the mean offset between the test position and the observation position for both data sets: (a) CT5, (b) CT1-4.

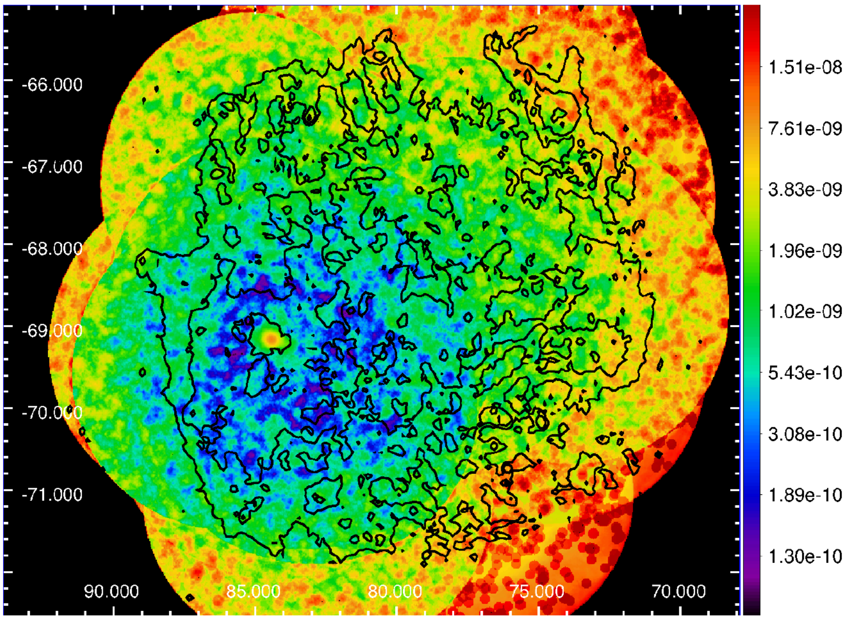

Figure 5.8: LMC sky map of the integral flux upper limits (in units of $\mathrm{m}^{-2}\,\mathrm{s}^{-1}$) within an energy range of $1-100$ TeV. Upper limits are given for a 95% confidence level with an assumed spectral index of $\Gamma = 2.3$. Systematic uncertainties of $16\%$ are taken into account. Correlation radii and coordinate system are the same as in Figure 5.6. Contours are the same as in Figure 5.3.

### 5.2.3 The H.E.S.S. Source Candidate Catalogue of Potential VHE $\gamma$-Ray Sources in the LMC

For a number of potential VHE $\gamma$-ray sources non-thermal emission has been detected in other wavelengths (mainly in radio oder X rays), indicating that their VHE $\gamma$-ray flux may be just below the sensitivity threshold of the H.E.S.S. instrument. Some of these sources were indeed thought to be powerful VHE $\gamma$-ray emitters similar to PWN N 158A [277]. Flux measurements as well as flux upper limits in the VHE regime can thus help to constrain models for the $\gamma$-ray production mechanisms in sources located in environments such as those found in the Magellanic Clouds. H.E.S.S. source candidate catalogues of confirmed non-thermal radiation emitting sources are compiled and the results for these sources are extracted from the sky maps at the respective source location. For all sources that do not show significant VHE $\gamma$-ray emission, integral flux upper limits are reported. Only catalogues with established $\gamma$-ray source classes are used, as the expectation to find a new $\gamma$-ray source class is rather low due to the lower $\gamma$-ray flux that is expected from the LMC compared to the Milky Way. Therefore, no HII regions — containing potential young stellar objects, young massive stellar clusters or globular clusters — are considered here. The following confirmed $\gamma$-ray source classes are considered in this work: SNRs, PWNe, HMXB (as potential $\gamma$-ray binaries) and pulsars.

The list of SNRs is taken from Maggi et al. [97], which contains the first comprehensive catalogue of SNRs detected in non-thermal X rays in the LMC. This catalogue contains 59 confirmed SNRs including N 132D, for which VHE emission has already been detected by H.E.S.S. [23]. For three SNRs in the sample, a PWN is either detected in their centre or there is strong evidence for an embedded PWN; thus, these objects are listed twice — in the H.E.S.S. source candidate catalogue of SNRs as well as in the H.E.S.S. source candidate catalogue of PWNe.

One of these three PWNe is N 157B [278], the most powerful VHE $\gamma$-ray emitting PWN detected so far [23]. Among the other two PWNe is the promising PWN N 158A [279], for which VHE $\gamma$-ray emission at a level detectable by H.E.S.S. was predicted [277], and J0531-7100 [280]. Together with the PWN J0453-6829, which was detected in X rays [281], the resulting H.E.S.S. source candidate catalogue for PWNe comprises four sources. Additional information that is not provided in the respective detection paper is taken from the ATNF catalogue[3] [282]. An additional SNR (DEM L241) is discussed to be a composite SNR [283] in the literature, but more recent studies disfavour a PWN morphology inside the remnant [284]; therefore, this source will not be included in the H.E.S.S. source candidate catalogue of PWNe.

In the case of the $\gamma$-ray binaries, only one source (LMC P3) has been firmly detected in HE $\gamma$-rays with *Fermi*-LAT [276]. As this source has been previously classified as a HMXB [285], (V)HE $\gamma$-ray emission from sources classified as HMXB should not be ruled out. Apart from LMC P3, pulsed radio emission has also been detected for one other HMXB (1A0535-668) [286], making

---

[3] An updated version of this catalogue can be found here: http://www.atnf.csiro.au/research/pulsar/psrcat.

this source a potential candidate $\gamma$-ray binary. The H.E.S.S. source candidate catalogue of $\gamma$-ray binaries is complemented by sources from the HMXB catalogues compiled by Antoniou and Zezas [98] and Jaarsveld et al. [99] with a few parameters taken from Vasilopoulos et al. [287].
The list of (isolated) pulsars for which non-thermal emission was detected is rather short. The pulsars that are associated with HMXBs are excluded here. Except for the two pulsars PSR J0537-6910 and PSR J0540-6919, powering the two PWNe N 157B and N 158A, respectively, all other isolated pulsars detected in the LMC are comparably old ($\gtrsim 10^5$ yr) and exhibit a comparably low spin-down power ($\lesssim 10^{35}$ erg s$^{-1}$) compared to the pulsars detected at $\sim$TeV energies. So far, only pulsars with a spin-down power of $\gtrsim 10^{34}$ erg s$^{-1}$ have been detected at $\sim$TeV energies with the current generation of IACTs. However, the different environment in the LMC may result in a more efficient particle acceleration or lead to more efficient radiative losses and thus result in significant VHE $\gamma$-ray emission. Therefore, a H.E.S.S. source candidate catalogue for all LMC pulsars is compiled based on the ATNF catalogue.
The distribution of the selected sources in the H.E.S.S. source candidate catalogue over the LMC is shown in Figure 5.9.

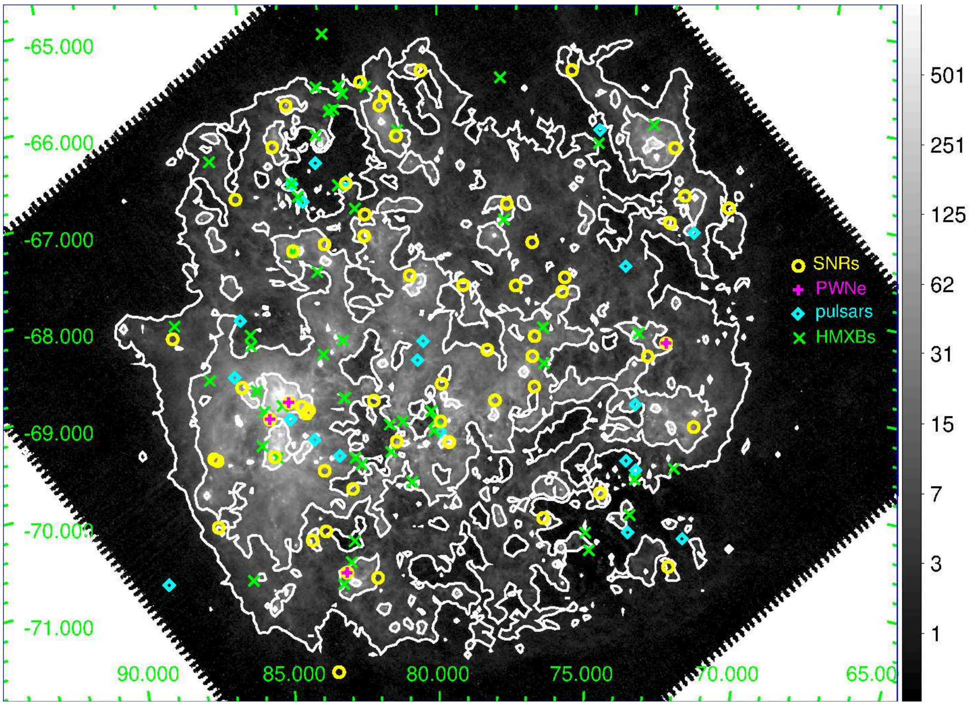

Figure 5.9: Distribution of the selected sources over the LMC, overlaid on an IR image [274]. Contours are the same as in Figure 5.3. The sky map is shown in a Cartesian projection.

### 5.2.4 Results for the LMC Sources in the H.E.S.S. Source Candidate Catalogues

Apart from the PWN N 157B, significant VHE $\gamma$-ray emission is not found for any of the LMC sources in the H.E.S.S. source candidate catalogue. The significance distributions for the source classes in the H.E.S.S. source candidate catalogue are shown in Figure 5.10. The distributions roughly follow a Gaussian distribution centred on $0$; the broadening of the distributions (width $> 1$) is most likely due to the low number of sources or due to the large survey data set. An accumulated VHE $\gamma$-ray emission in all sources of a source class is not expected.
To put constraints on the VHE $\gamma$-ray flux, integral flux upper limits are extracted from the integral flux upper limit sky map. The results for all SNRs, PWNe, HMXBs and pulsars are presented in the tables in Appendix A1. Source coordinates and additional source properties like the diameter, spin period, spin derivative, spin-down power and orbital period, are taken from the catalogues in the literature.
For a better comparison of the source populations of the SMC, the LMC and the Milky Way the integral flux upper limits are converted into upper limits on the energy flux and the luminosity in the energy range of $1 - 100\,\mathrm{TeV}$ following Equations 3.6 and 3.7 by assuming a common distance of $50\,\mathrm{kpc}$ for all LMC source candidates.
For the SNRs, PWNe, HMXBs and pulsars, additional upper limits on the power and/or energy conversion efficiencies are derived.

**Supernova Remnants** There is observational evidence that SNRs accelerate hadronic and/or leptonic cosmic rays. Under the assumption that hadronic acceleration is the dominating process causing the $\gamma$-ray emission via inelastic hadronic collisions, an upper limit on the total energy in protons can be estimated based on the upper limit on the luminosity following Equation 4.8. As protons are assumed to produce $\gamma$-rays with energies of $\sim 0.1E_{\mathrm{p}}$, the integrated $\gamma$-ray flux in the energy range of $1 - 100\,\mathrm{TeV}$ will constrain the total energy in protons in an energy range of $10\,\mathrm{TeV} - 1\,\mathrm{PeV}$. Here, a target density of the interstellar gas of $1\,\mathrm{cm}^{-3}$ and a cooling time of $4 \times 10^{15}\,\mathrm{s}$ are assumed. By comparing the upper limit on the total energy in protons with the average supernova explosion energy of $\sim 10^{51}\,\mathrm{erg\,s}^{-1}$, the efficiency of converting the energy in those protons into $\gamma$-ray emission in an energy range of $1 - 100\,\mathrm{TeV}$ can be estimated. The upper limits on the total energy in protons as well as the upper limits on the energy conversion efficiency are listed in Table A.1.
In the case that SNRs are predominantly leptonic accelerators, $\gamma$ radiation is mainly produced via the up-scattering of low energy photons through inverse Compton scattering. The energy conversion efficiency from electrons to VHE $\gamma$-rays depends on the environmental properties of the SNR such as the magnetic field or the radiation field energy density. A possible correlation with the latter will be discussed in more detail in Section 6.1.

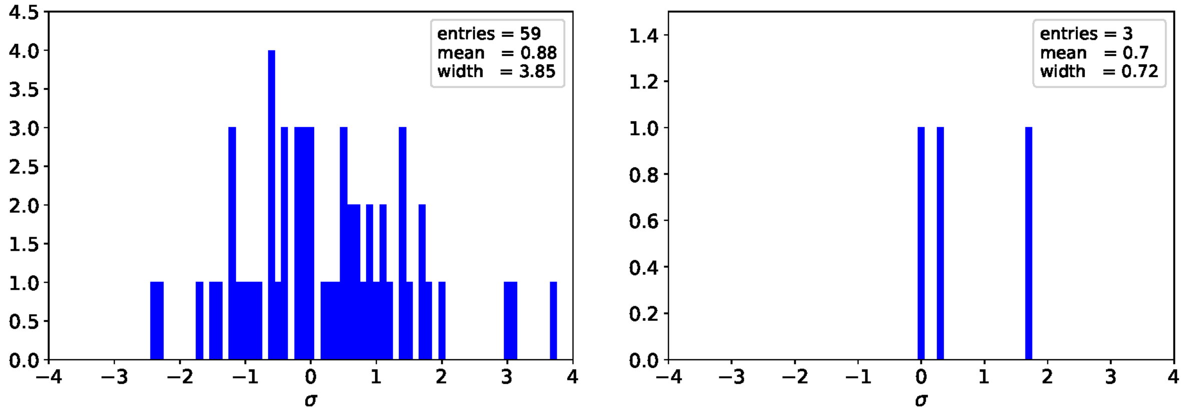

(a) SNRs

(b) PWNe

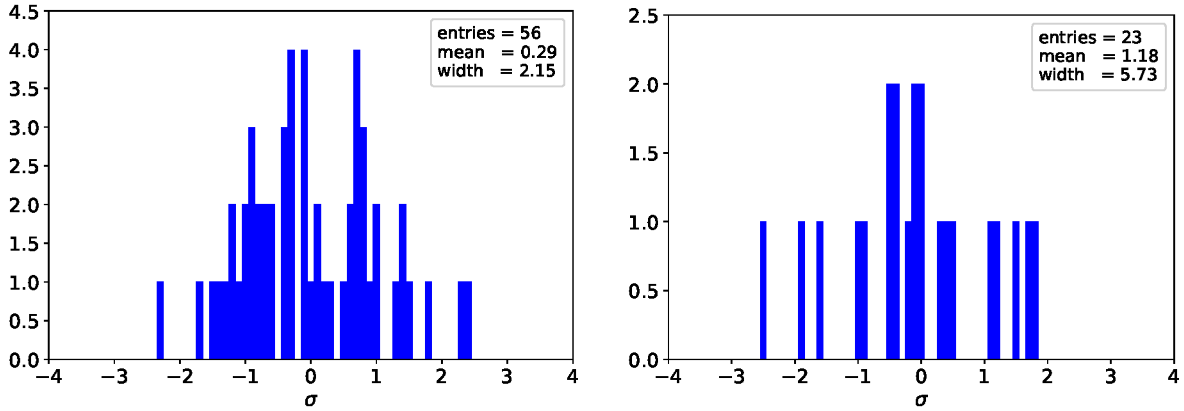

(c) HMXBs

(d) Pulsars

Figure 5.10: Significance distributions for the sources of the different source classes in the LMC H.E.S.S. source candidate catalogues.

**Pulsar Wind Nebulae** PWNe are thought to be leptonic accelerators powered by the spin-down power of their pulsars. To estimate the efficiency of converting the kinetic energy in the pulsar wind into $1-100$ TeV $\gamma$-ray emission through particle acceleration, the derived upper limits on the luminosity following Equation 4.8 are set in relation to the spin-down power of the pulsars in those PWNe where the spin-down power is known.

**High-Mass X-Ray Binaries** The VHE $\gamma$-ray emission from $\gamma$-ray binaries can be explained by either the *pulsar scenario* or the *microquasar scenario*. Two models have been developed that predict $\gamma$-ray emission in the vicinity of HMXBs. In the first scenario, the $\gamma$-ray emission is powered by the spin-down power of a pulsar. Accelerated electrons produce $\gamma$-ray emission by inverse Compton scattering the stellar photons of the companion. For 17 out of the 56 HMXBs in the LMC a spin period has been measured, indicating that the compact object is very likely a pulsar. Under the assumption that at least 10% of the spin-down power is converted into $\gamma$ rays, the lower limit on the spin-down power is given by $10 \times L_{\mathrm{UL}}$.
In the second scenario, the system is powered by accretion of the stellar wind onto the compact object. Gravitational potential energy is released as radiation. When assuming the compact object to be a neutron star with a canonical mass of $M_{\mathrm{CO}} = 1.4 M_{\odot}$, a radius of $R_{\mathrm{CO}} = 10\,\mathrm{km}$, and a mass-loss rate of $10^{-10} M_{\odot}\,\mathrm{yr}^{-1}$, the canonical accretion luminosity is given by:

$$L_{\mathrm{acc}} = \left(\frac{\dot{M}}{10^{-10} M_{\odot}/yr}\right)\left(\frac{M_{\mathrm{CO}}}{1.4 M_{\odot}}\right)\left(\frac{10\,\mathrm{km}}{R_{\mathrm{CO}}}\right) \times 1.2 \times 10^{36}\,\mathrm{erg/s}. \tag{5.1}$$

(More details are given in Section 6.6.1.) The efficiency of converting the gravitational potential energy into $\gamma$ radiation in a particular energy range is given by the ratio of the upper limit on the luminosity (following Equation 4.8) and the accretion luminosity $L_{\mathrm{acc}}$.

**Pulsars** Although the pulsars in the LMC are rather old and therefore are not expected to be radiating significant $\gamma$-ray emission, the results are still discussed for completeness. As the non-thermal emission is powered by the spin-down power of the pulsar, the upper limits on the $\gamma$-ray luminosity (following Equation 4.8) are converted into upper limits on the energy conversion efficiency by calculating the ratio of the upper limit on the $\gamma$-ray luminosity and the spin-down power of the respective pulsar.

HMXBs (and $\gamma$-ray binaries) typically show a phase modulation of their (non-)thermal emission. Therefore, an additional analysis testing for phase-modulated VHE $\gamma$-ray emission is performed.

### Phase-Modulated VHE $\gamma$-ray Emission of HMXBs

For some $\gamma$-ray binaries the on-peak luminosity is significantly higher than the full-orbit luminosity (e.g., for LMC P3 or LS I$+61^{\circ}$303). Hence, although none of the HMXBs in the LMC shows significant orbit-averaged VHE $\gamma$-ray emission, they may be detectable during their on-peak orbital phase. Therefore, a search for VHE $\gamma$-ray emission modulated with the orbital period of the HMXBs is performed. For this study all LMC HMXBs in the H.E.S.S. source candidate catalogue with a given orbital period have been reanalysed individually. As the offset between test position and camera centre is in some cases less than $0.4^{\circ}$, the acceptance profile is taken from lookups to avoid increased systematic uncertainties in the acceptance profile close to the centre of the field-of-view. The background subtraction is made by using the *reflected region background model*. The energy range is chosen analogously to the search for point-like emission in the LMC.

For each $\gamma$-ray binary candidate a folded light curve, modulated with the respective orbital period, is generated and binned in 5 and 10 phase bins. The phase binning is chosen according to the duration of the X-ray or $\gamma$-ray on-peak phase, which is typically one-tenth to one-fifth of the orbital period. Finally, the significance of the $\gamma$-ray emission is estimated in each phase bin following Equation 3.1. Figure 5.11 shows the significance distribution of all phase bins of all LMC HMXBs for a binning of 10 bins per orbital period in the energy range of $1-100$ TeV. None of the phase bins of any HMXB shows a significance of $\sigma > 5$ and the significance distribution is well defined by a Gaussian distribution with a mean of $0.15$ and a width of $0.81$ for the LMC. Thus, a cumulative weak VHE $\gamma$-ray signal at the sensitivity level that is reached by the LMC data sets can be excluded. Thus, it is unlikely that the LMC contains a second $\gamma$-ray binary as powerful as LMC P3. However, a deeper exposure, measurements of more accurate orbital periods or the addition of more measurements of orbital periods to the sample of HMXBs may shed more light on the nature of these objects.

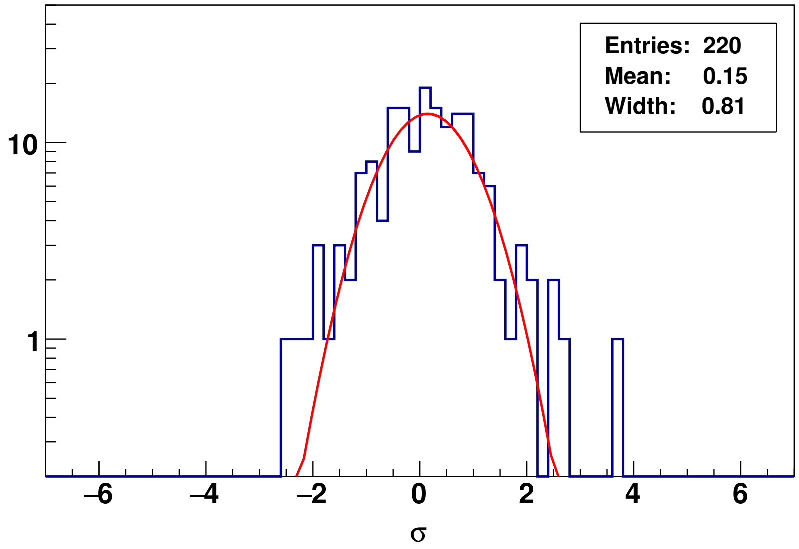

Figure 5.11: Significance distribution for the folded lightcurves in the energy range of $1-100$ TeV of all LMC HMXBs with a given orbital period with a binning of 10 bins per orbital period.

## 5.3 Analysis of the Small Magellanic Cloud

This section focusses on the analysis and results of the SMC survey data sets. Analogous to the discussion of the LMC data set the SMC data sets will be described in Section 5.3.1 followed by a description of the compilation of the SMC H.E.S.S. source candidate catalogues of potential VHE $\gamma$-ray emitters in Section 5.3.2. The description of the estimation of the integral flux upper limits as well as the description of the final flux upper limit catalogues is summarised in Section 5.3.3. The results for the SMC source population study are discussed in Chapter 6 along with the LMC results. In addition, a search for extended VHE $\gamma$-ray emission is performed for the SMC, which is described in Section 5.3.4.

### 5.3.1 Characterisation of the SMC Data Sets

As the SMC is even more distant from Earth than the LMC, all potential VHE $\gamma$-ray sources in the SMC can be assumed to appear point-like for the H.E.S.S. instrument. One exception are the star forming regions for which the analysis will be described separately in Section 5.3.4. The SMC analysis is performed analogously to the LMC analysis to guarantee a mostly unbiased population study between the SMC and LMC sources. Thus, for the search for point-like $\gamma$-ray emission, an analysis with a $\Theta^2$ cut of $0.005$ deg$^2$ ($0.016$ deg$^2$), which corresponds to a radius of the PSF of $\sim 0.07°$ ($\sim 0.13°$), is performed for the CT1-4 (CT5) data. All sky maps discussed here are correlated with the same radii. A lower energy threshold of $1$ TeV ($0.4$ TeV) is applied

to all analyses of the CT1-4 (CT5) data set. The maximum energy depends on the sensitivity limitation of the H.E.S.S. instrument (more details are given in Section 5.2.1).
A sky map of the integrated sensitivity in the energy range of $1-100\,\mathrm{TeV}$ as well as $0.4-10\,\mathrm{TeV}$ for a point-like $\gamma$-ray excess above the detection criterion is shown in Figure 5.12 for the CT1-4 and CT5 data set, respectively. In the energy range of $1-100\,\mathrm{TeV}$, a sensitivity of $\sim 2\times 10^{-9}\mathrm{m}^{-2}\mathrm{s}^{-1}$ is reached towards the centre of the *Bar* of the galaxy. This limit translates to a limit on the luminosity of $L\sim 3\times 10^{35}$ erg s$^{-1}$. The sensitivity of the CT1-4 data set degrades from the western part of the SMC towards the SMC *Wing* in the eastern part, where a sensitivity of $\sim 7\times 10^{-9}\mathrm{m}^{-2}\mathrm{s}^{-1}$ ($L\sim 1\times 10^{36}$ erg s$^{-1}$) is achieved. The best sensitivity in the energy range of $0.4-10\,\mathrm{TeV}$ is also reached towards the SMC *Bar* with $\sim 4.5\times 10^{-9}\mathrm{m}^{-2}\mathrm{s}^{-1}$, which translates to a luminosity of $L\sim 7\times 10^{35}$ erg s$^{-1}$. The sensitivity of the CT5 data set degrades towards the outskirts of the SMC (east and west) where a sensitivity of $\sim 1\times 10^{-8}\mathrm{m}^{-2}\mathrm{s}^{-1}$ ($L\sim 1.5\times 10^{36}$ erg s$^{-1}$) is reached.

The significance sky maps for the CT1-4 and CT5 data sets are shown in Figure 5.13. No $\gamma$-ray excess above the nominal $5\sigma$ criterion is seen in the entire SMC in either data set, and the significance distribution is compatible with a background-only hypothesis. This implies that the SMC does not host any source that emits VHE $\gamma$-ray emission above the sensitivity threshold of the H.E.S.S. instrument. Thus, potential VHE $\gamma$-ray sources in the SMC are less luminous than the detected $\gamma$-ray sources in the LMC.

Analogously to the LMC analysis, the measured $\gamma$-ray excess is used to estimate integral flux upper limits for selected potential $\gamma$-ray sources and the results will be compared with those of the LMC and Milky Way in Chapter 6.

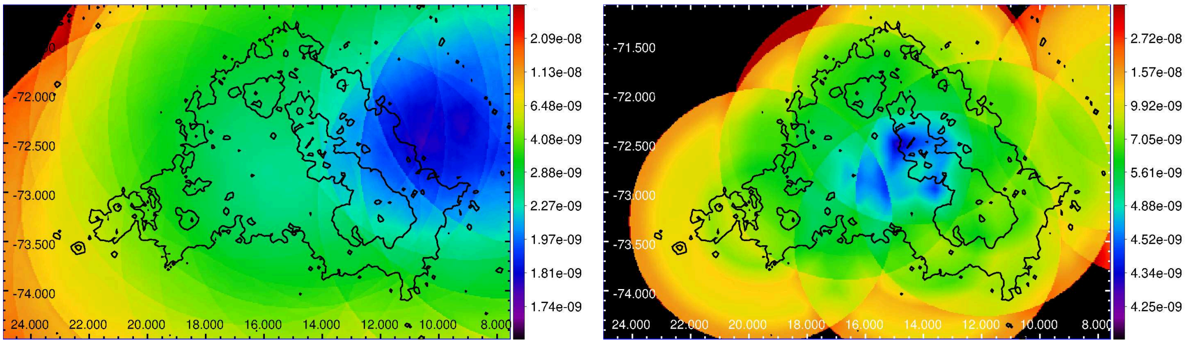

(a) (b)

Figure 5.12: Integrated sensitivity (in units of m$^{-2}$ s$^{-1}$) in the energy range of (a) $1-100\,\mathrm{TeV}$ and (b) $0.4-10\,\mathrm{TeV}$ for a point-like $\gamma$-ray excess with a significance of $>5\sigma$ for the CT1-4 and CT5 data set, respectively. The sky maps are correlated with a radius of (a) $\theta=0.07^\circ$ and (b) $\theta=0.13^\circ$ and are shown in a Cartesian projection. Contours are the same as in Figure 5.3.

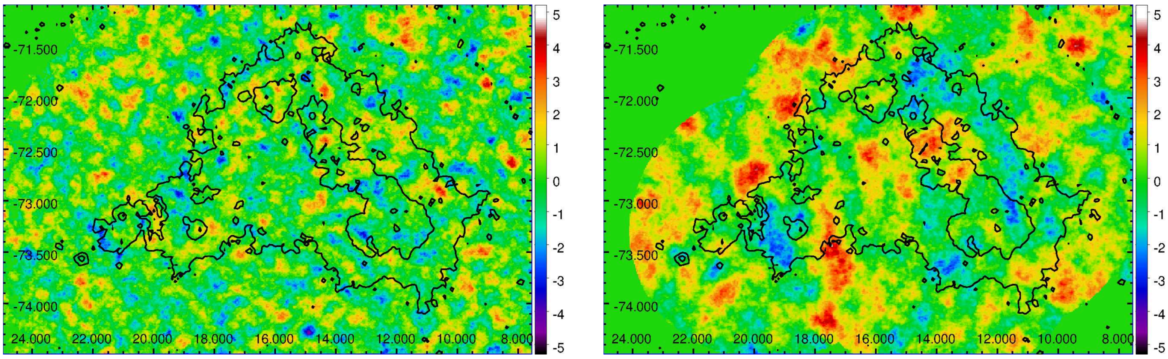

(a)

(b)

Figure 5.13: Significance sky map (in units of $\sigma$) for point-like $\gamma$-ray emission above an energy threshold of (a) $1$ TeV and (b) $0.4$ TeV for the CT1-4 and CT5 data set, respectively. Correlation radii and coordinate system are the same as for Figure 5.12. Contours are the same as in Figure 5.3.

### 5.3.2 The H.E.S.S. Source Candidate Catalogue of Potential VHE $\gamma$-Ray Sources in the SMC

Although no significant point-like VHE $\gamma$-ray emission towards the SMC is found, there are many sources that are known to emit non-thermal emission in radio or X rays. Some were expected to be powerful VHE $\gamma$-ray emitters (for example SNR E0102.2-7219 or PWN IKT 16). As in the LMC, dedicated flux upper limits in the VHE regime can help to constrain models of the acceleration and $\gamma$-ray production of these sources.

Catalogues of confirmed non-thermal sources are used to compile a H.E.S.S. source candidate catalogue, in which the H.E.S.S. results in the VHE $\gamma$-ray regime are summarised for the selected sources. The same source classes as for the LMC are considered for the SMC: SNRs, PWNe, HMXBs and pulsars. Furthermore, star-forming regions — the birth-places of stellar OB associations and clusters — are considered for the SMC. As star-forming regions cannot be considered point-like for the H.E.S.S. instrument due to their physical and angular extents, a separate analysis has to be performed, which is described in Section 5.3.4. The distribution of the sources selected over the SMC is shown in Figure 5.14.

Badenes et al. compiled the first catalogue of SNRs in the SMC that is based on multiwavelength catalogues for the SMC [104]. They study 23 SNRs that are confirmed SNRs in at least one wavelength. Two of these SNRs, IKT 16 and DEM S5, were later identified as first detected PWNe in the SMC [288, 289] and are thus added to the H.E.S.S. source candidate catalogue of PWNe as well. For SNR IKT 7, a study by Haberl et al. [290] concluded that this source is not a SNR and is thus removed from the H.E.S.S. source candidate catalogue of SNRs. Three other SNRs are not detected in the latest XMM-Newton survey [290] and are also removed from the H.E.S.S. catalogue as they do not seem to be promising candidates for VHE $\gamma$-ray emission. Thus, 18 SNRs are considered in this work.

So far, there are only two confirmed PWNe in the SMC: the powerful X-ray PWN IKT 16 [288] and the recently discovered PWN DEM S5 [289]. For both sources it is not clear which component (SNR or PWN) may be detected in the VHE regime, hence, these sources are listed in the H.E.S.S. source candidate catalogue for both SNRs and for PWNe.

No $\gamma$-ray binaries have been detected in the SMC so far. Although $\gamma$-ray binaries are thought to be the progenitors of HMXBs, some HMXBs may have been misclassified due to the large distance to the SMC as well as the lack of radio surveys providing a cross-correlation with HMXBs (e.g., [291]). Only one thermal radio source was reported to be coincident with a known X-ray binary. However, the measured radio spectral index of this source did not support the hypothesis of this object being a non-thermal emitter and hence a possible microquasar. Although no $\gamma$-ray binary has been detected in the SMC yet, the possibility is not excluded that one of the sources classified as HMXBs is indeed a $\gamma$-ray binary as is the case for LMC P3 in the LMC. The most comprehensive catalogue for HMXBs in the SMC was compiled by Haberl & Sturm 2016 [102] based on existing multiwavelengths catalogues and lists 148 confirmed and candidate HMXBs. The authors performed a systematic study showing that 102 sources of their sample are confirmed HMXBs, of which 61 are confirmed HMXBs and another 39 are most likely HMXBs or BeXBs (having a Be type star as massive star). Two of the remaining 102 sources have no H.E.S.S. exposure and are thus rejected from the H.E.S.S. source candidate catalogue. Out of the remaining sample of 100 HMXBs and BeXBs an orbital period was measured for 58 sources indicating that these binaries most likely have a neutron star as the compact object. For those sources a dedicated search for periodic VHE $\gamma$-ray emission is performed (see Section 5.3.3). For most of the HMXBs that are confirmed to have a neutron star as the compact object, the spin period derivative was added to the H.E.S.S. source candidate catalogue of HMXBs, which is taken from an extensive X-Ray Pulsar catalogue [292].

Most of the pulsars in the SMC are detected in HMXB and BeXB systems. They typically exhibit long spin periods of $\gtrsim 1$ s. VHE $\gamma$-ray emission at a detectable level is not expected from these pulsars. Thus, these pulsars are only listed once in the H.E.S.S. source candidate catalogue of HMXBs. Apart from these, only 8 additional pulsars have been detected in the SMC so far. 6 SMC pulsars are listed in the ATNF catalogue [282]. The H.E.S.S. source candidate catalogue of pulsars is complemented by two recently discovered pulsars [293].

Finally, the catalogue of Livanou et al. [105] is used as a basis for the H.E.S.S. source candidate catalogue of SFR. The following selection cuts have been applied to these SFRs to produce the final selection of SFRs that will be investigated in this work: i) all SFRs that do not host stellar associations are discarded, ii) only SFRs hosting more than 10 HII regions are kept, iii) a cut on the number density of the stellar association of $\rho_{\mathrm{SFR}} > 10^{-7}$ cm$^{-3}$ is applied and iv) a cut on the radius of the SFR of $r_{\mathrm{SFR}} < 0.4^{\circ}$ is applied. The list of SFRs investigated in this work consists of 12 SFRs (8 aggregates and 4 complexes).

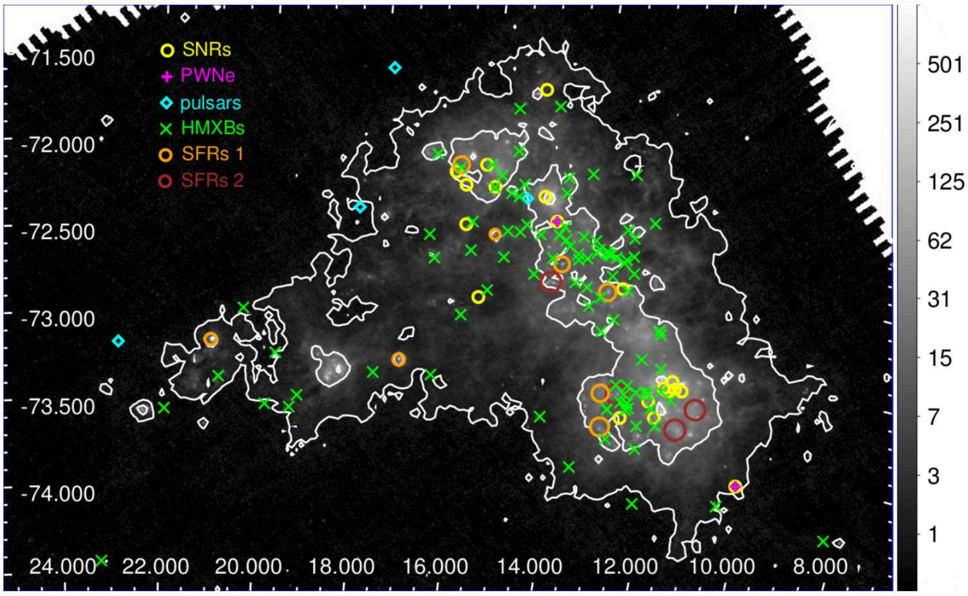

Figure 5.14: Distribution of the selected sources over the SMC, overlaid on an IR image [274]. The SFRs are split into aggregates (orange) and complexes (dark red). The size of the circle denotes the size of the SFR. Contours are the same as in Figure 5.3. The sky map is shown in a Cartesian projection.

### 5.3.3 Results for the SMC Sources in the H.E.S.S. Source Candidate Catalogues

The significance distributions for the source classes in the H.E.S.S. source candidate catalogue for the SMC are shown in Figure 5.15 and Figure 5.16 for the CT1-4 and CT5 data sets, respectively. From the figures it can be seen that the distributions roughly follow a Gaussian distribution which is centred on $0$ with a width of $\sim 1$. Thus, no accumulated VHE $\gamma$-ray emission is expected. As no significant $\gamma$-ray emission is found in either SMC data set, integral flux upper limits for the entire field of view are estimated in the energy range of $0.4 - 10$ TeV for the CT5 data set and $1 - 100$ TeV for the CT1-4 data set. The flux upper limit estimation follows the same approach as for the LMC. For the CT1-4 data set the energy range, assumed spectral parameters, confidence level and systematic uncertainties are the same as were used for the LMC CT1-4 data set. For the CT5 data set, integral flux upper limits are estimated for an energy range of $0.4 - 1$ TeV first, and then extrapolated to an energy range of $0.4 - 10$ TeV, where the spectral index and the confidence level are the same as for the CT1-4 data set. The systematic uncertainties are taken from Table 5.3. The resulting upper limit sky maps for sources that appear point-like for the H.E.S.S. instrument are shown in Figure 5.17.

The significances of the VHE $\gamma$-ray emission of all sources in the H.E.S.S. source candidate catalogue are extracted from the significance sky maps . No significant $\gamma$-ray emission is found for any of the sources in either SMC data set. Thus, integral flux upper limits at the positions of the selected sources are extracted from the integral flux upper limit sky maps and are presented

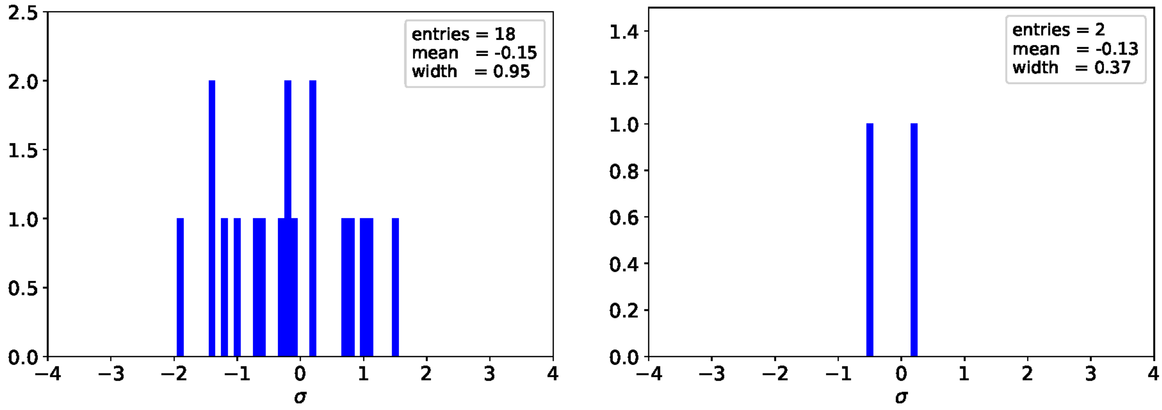

(a) SNRs (b) PWNe

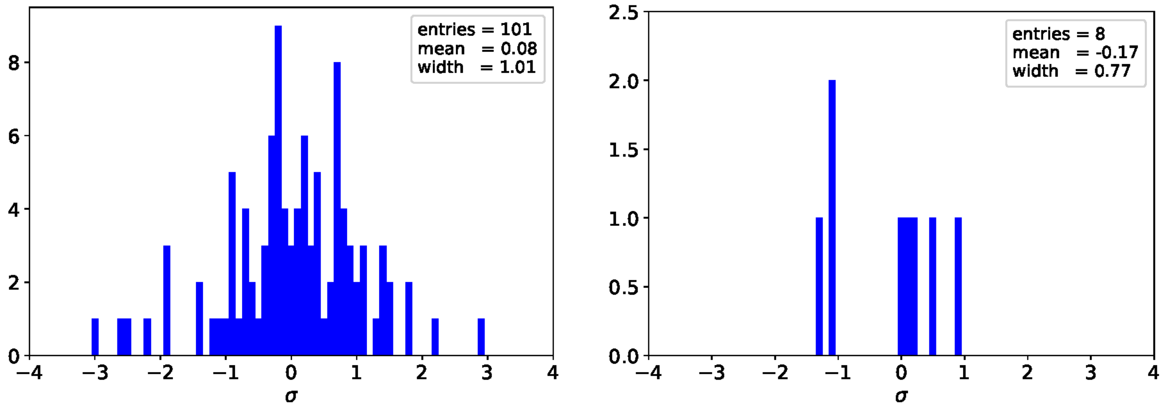

(c) HMXBs (d) Pulsars

Figure 5.15: Significance distributions for the sources of the different source classes in the SMC H.E.S.S. source candidate catalogues in the energy range of $1 - 100$ TeV.

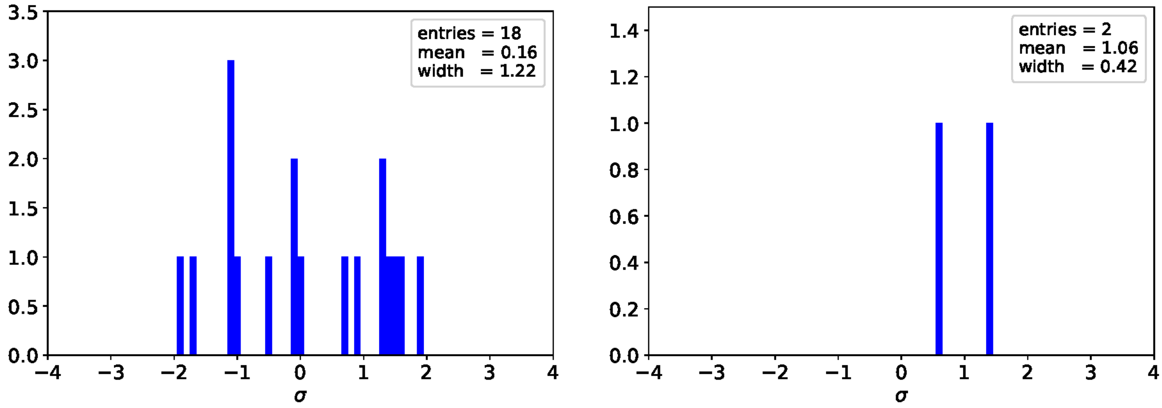

(a) SNRs

(b) PWNe

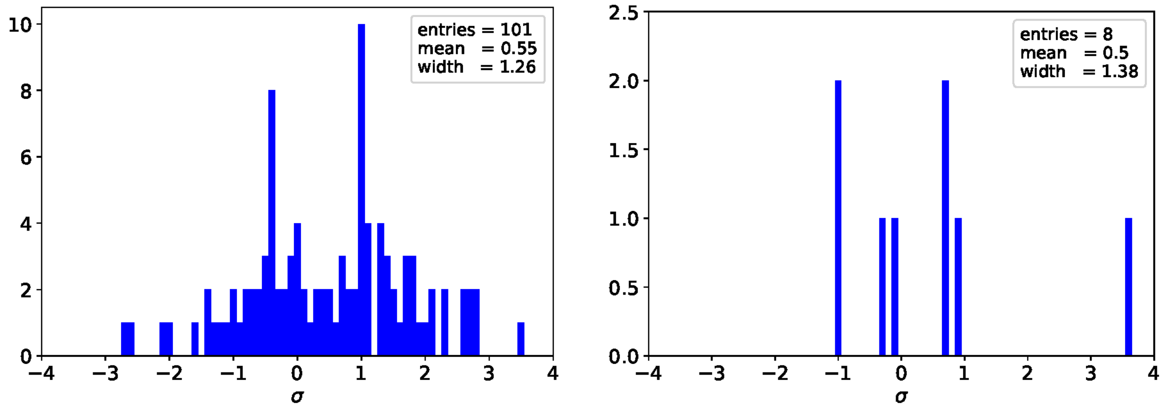

(c) HMXBs

(d) Pulsars

Figure 5.16: Significance distributions for the sources of the different source classes in the SMC H.E.S.S. source candidate catalogues in the energy range of $0.4 - 10$ TeV.

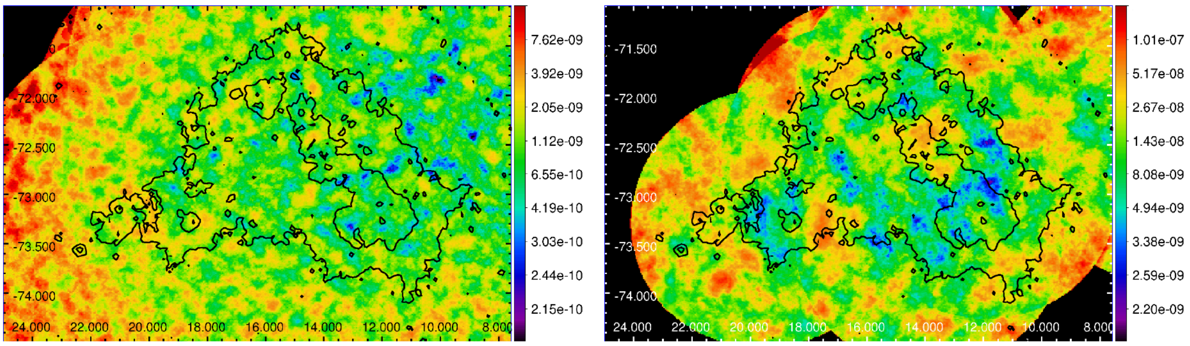

(a)

(b)

Figure 5.17: Integral flux upper limit sky maps (in units of $\mathrm{m}^{-2}\,\mathrm{s}^{-1}$) for VHE $\gamma$-ray emission of sources that appear point-like for the H.E.S.S. experiment in the energy range of (a) $1 - 100$ TeV and (b) $0.4 - 10$ TeV for the CT1-4 and CT5 data set, respectively. Upper limits are given for a $95\%$ confidence level with an assumed spectral index of $\Gamma = 2.3$. Systematic uncertainties of (a) $16\%$ and (b) $31\%$ are taken into account. Correlation radii and coordinate system are the same as for Figure 5.12. Contours are the same as in Figure 5.3.

in the tables A.5 - A.12 for the SNRs, PWNe, HMXBs and pulsars respectively.
Source coordinates and additional physical source properties like the diameter, spin period, spin period derivative, spin-down power and orbital period, are taken from the catalogues that were used to compile the H.E.S.S. source candidate catalogue.

Upper limits on the integral energy flux, luminosity, total energy in protons and/or the efficiency of converting kinetic energy into non-thermal VHE $\gamma$-rays in both energy ranges ($1 - 100$ TeV and $0.4 - 10$ TeV) are estimated according to the description in Section 5.2.4 and are presented in the tables as well.
In the case of the SNRs the total energy in protons is constrained in an energy range of $10$ TeV $- 1$ PeV and $4 - 100$ TeV for the CT1-4 and CT5 data set, respectively. More details are given in Section 4.3.1 and 5.2.4.
For the HMXBs an analysis for phase-modulated VHE $\gamma$-ray emission and a search for significant VHE $\gamma$-ray emission during X-ray outbursts is performed as well.

#### Phase-Modulated VHE $\gamma$-ray Emission of HMXBs

The analysis is performed for all SMC HMXBs in the H.E.S.S. source candidate catalogue with a given orbital period, analogously to the analysis of the LMC HMXBs as described in Section 5.2.4. The analysis is done for both data sets. The energy range is chosen analogously to the search for point-like emission in the SMC.
For each $\gamma$-ray binary candidate, a folded lightcurve — modulated with its respective orbital period — is generated and binned in 5 and 10 phase bins and the significance of the VHE $\gamma$-ray emission is estimated in each phase bin following Equation 3.1. Figure 5.18 shows the significance distribution of all phase bins of all SMC HMXBs for a binning of 10 bins per orbital period in the energy range of $1 - 100$ TeV and $0.4 - 10$ TeV for the CT1-4 and CT5 data set, respectively. None of the phase bins of any HMXB shows significant VHE $\gamma$-ray emission and the significance distributions are well defined by a Gaussian distribution with a mean of $0.03$ ($0.07$) and a width of $1.10$ ($1.05$) for the CT1-4 and CT5 data, respectively. As for the LMC HMXBs, a cumulative weak VHE $\gamma$-ray signal at the sensitivity level reached in the SMC data sets can be excluded. The analyses with a binning of 5 bins per orbital period show consistent results for both data sets. Thus, it is unlikely that the SMC hosts a $\gamma$-ray binary as powerful as the LMC $\gamma$-ray binary LMC P3. However, as for the LMC, a deeper exposure, measurements of more accurate orbital periods or adding more measurements of orbital periods to the sample of HMXBs may again reveal further insights into the nature of these objects.

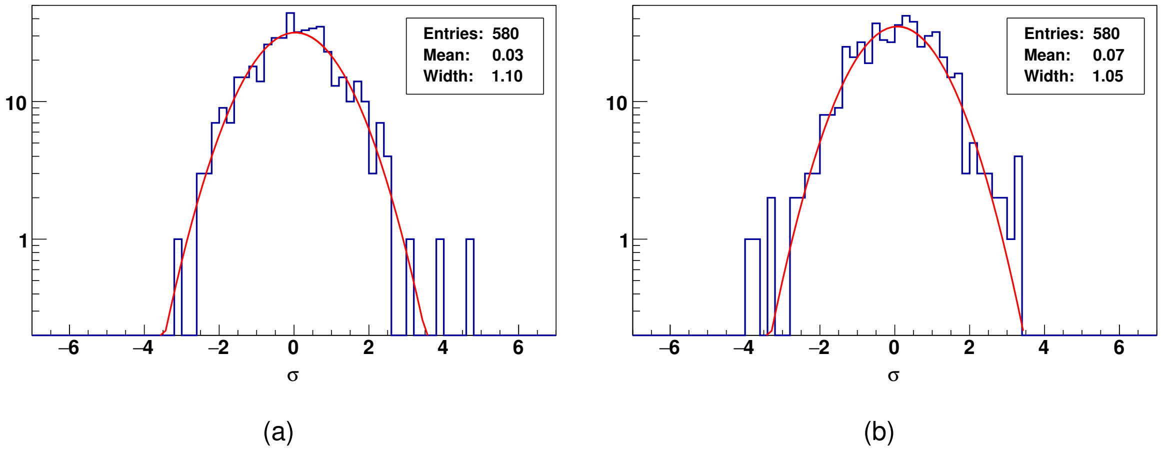

(a) (b)

Figure 5.18: Significance distribution for the folded lightcurve in the energy range of (a) $1-100$ TeV and (b) $0.4-10$ TeV of all SMC HMXBs with a given orbital period with a binning of 10 bins per orbital period.

### VHE $\gamma$-ray Emission during X-Ray Outbursts of HMXBs

Many HMXBs frequently exhibit powerful outbursts that are typically detected in X-rays. The VERITAS collaboration found that the $\gamma$-ray binary LS I$+$61$^\circ$303 also showed increased emission in the energy range of $0.3-10$ TeV contemporaneous with one of the X-ray outbursts [294], thus demonstrating that $\gamma$-ray binaries can also exhibit such powerful outbursts. A search for documented X-ray outbursts of SMC HMXBs in the literature results in four HMXBs that exhibited an outburst during the time period which are covered by the H.E.S.S. survey observations. To test if one of these HMXBs exhibited an increased VHE $\gamma$-ray emission above the sensitivity level of the SMC and LMC survey data sets, a dedicated analysis of these HMXBs is performed. As LS I$+$61$^\circ$303 was detected above an energy of $300$ GeV with a moderately steep spectral index of $\Gamma = 2.58$, a low energy threshold may be crucial for a detection of significant VHE $\gamma$-ray emission of the SMC HMXBs. Therefore, the analysis is only performed based on the SMC CT5 data set with only applying a safe energy threshold cut to the data. As the LMC survey was only performed with the HESS-I array, this analysis is only done for the SMC HMXBs.

Only those observations covering the outburst period are considered in the analysis. The emission is assumed to be point-like and the background subtraction is done by applying the *reflected region background model* while using an acceptance model from lookups. Figure 5.19 shows the significance maps for all four HMXBs during their outburst periods. None of the HMXBs shows significant VHE $\gamma$-ray emission and integral flux upper limits are derived by taking into account the systematic uncertainties derived in Section 5.1.3. Table 5.4 summarises all information and upper limits.

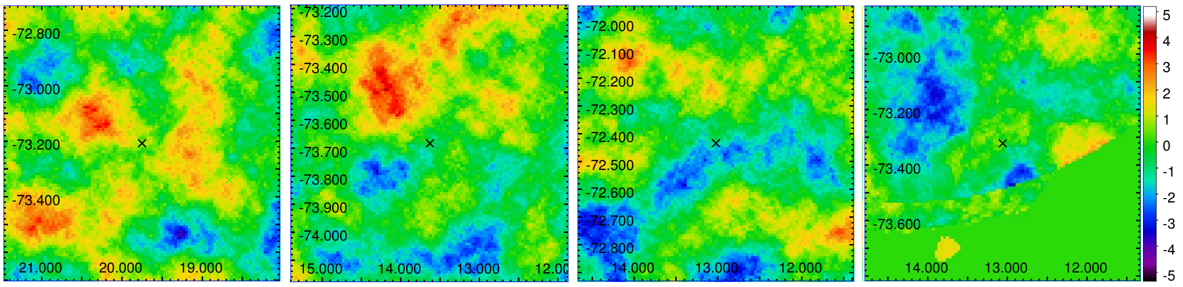

(a) HMXB 2 (b) HMXB 3 (c) HMXB 9 (d) HMXB 16

Figure 5.19: Significance sky maps (in units of $\sigma$) for the four SMC HMXBs that exhibited an outburst during the time period covered by the H.E.S.S. survey observations. The positions of the HMXBs are marked with a cross. The respective energy thresholds are (a) HMXB 2: 320 GeV (b) HMXB 3: 215 GeV (c) HMXB 9: 260 GeV and (d) HMXB 16: 900 GeV.

Table 5.4: SMC HMXBs exhibiting an outburst

| HMXB | Reference | Outburst | Observations | livetime [h] | $\sigma$ | $\mathrm{UL_F}$ [$10^{-10}\,\mathrm{m^{-2}\,s^{-1}}$] |
|---|---|---|---|---|---|---|
| 2 | Atel* [295, 296] | Oct - Nov ’15 | Oct 09 - Nov 08 | 2.8 | -0.48 | 715 |
| 3 | Atel [297–299] | Sep - Nov ’15 | Sep 06 - Nov 13 | 27.2 | -0.23 | 178 |
| 9 | T17** [300] | Aug ’16 - Jan ’17 | Nov 17 - Nov 29 | 3.2 | -1.60 | 1462 |
| 16 | Atel [301] | Oct - Dec ’17 | Nov 10 - Dec 14 | 12.6 | 1.26 | 837 |

* Atel: The Astronomer’s Telegram
** T17: Townsend et al. 2017

### 5.3.4 Search for Extended VHE $\gamma$-Ray Emission in the SMC

In addition to the search for point-like VHE $\gamma$-ray sources, a search for extended $\gamma$-ray emission on a scale $> 0.1^\circ$ is performed. Extended emission can either originate from sources with an intrinsically extended $\gamma$-ray emission region, from an accumulated diffuse signal of individual faint $\gamma$-ray sources or from a diffuse $\gamma$-ray emission caused by cosmic rays that diffused away from the acceleration sites. To account for the total VHE $\gamma$-ray emission from those extended regions, the analysis has to be adjusted. Instead of defining the *on* region by applying a $\Theta^2$ cut that equals that of the PSF of the respective analysis configuration, the $\Theta^2$ cut is adjusted according to the assumed source extension. The background estimation is adapted as follows: i) when the background is estimated based on the *reflected region background model*, the size of the individual reflected regions is adjusted according to the size of the *on* region and ii) when estimating the background based on the *ring background model* the radius and thickness of the ring have to be increased sufficiently to increase the event statistics in the background region simultaneously with the increase of event statistics in the *on* region and to avoid that a faint $\gamma$-ray emission outside the *on* region enters the estimation of the background level. The potential VHE $\gamma$-ray flux contained within a radius of $\Theta^2$ is finally integrated over the entire *on* region and the significance of the measured VHE $\gamma$-ray emission is calculated analogously to the point-like $\gamma$-ray

source analysis. Sky maps are produced in the same way as is described in Section 5.1.2, with the exception of the increased correlation radius $\Theta$ of the sky maps.
In the following two subsections the results for the analyses of SFR in the SMC and a potential diffuse VHE $\gamma$-ray emission are presented.

### Star-Forming Regions as Potential Particle Acceleration Sites

The detection of the superbubble 30 DorC in the LMC led to the question if there are other superbubbles in the star-forming Magellanic Clouds that may be as powerful as 30 DorC. As there is no superbubble catalogue available for the SMC, SFRs — which host many young massive stars and potentially host superbubbles — are analysed in this work. The sample of SFRs that is analysed in this work is described in Section 5.3.2. The described selection cuts are applied to ensure that only those SFRs that are more likely to be powerful $\gamma$-ray emitters will be investigated. For the selected 12 SFRs, a dedicated analysis for every individual SFR is performed for both SMC data sets. The background is estimated by applying the *reflected region background model* while the instrument acceptance is determined from lookups due to too small offsets $(< 0.4^\circ)$ between source location and pointing position. The significance of the VHE $\gamma$-ray emission is estimated for the whole energy range above the safe energy threshold of the respective data set of each individual SFR. No significant VHE $\gamma$-ray emission is found in either data set. The significance distribution of the SFRs for both data sets is shown in Figure 5.20. Upper limits are estimated in the energy range of $1 - 100$ TeV for the CT1-4 data set and $0.4 - 10$ TeV for the CT5 data set analogously to the flux upper limit estimation for the point-source analysis. The results are summarised in Table A.13 and A.14.

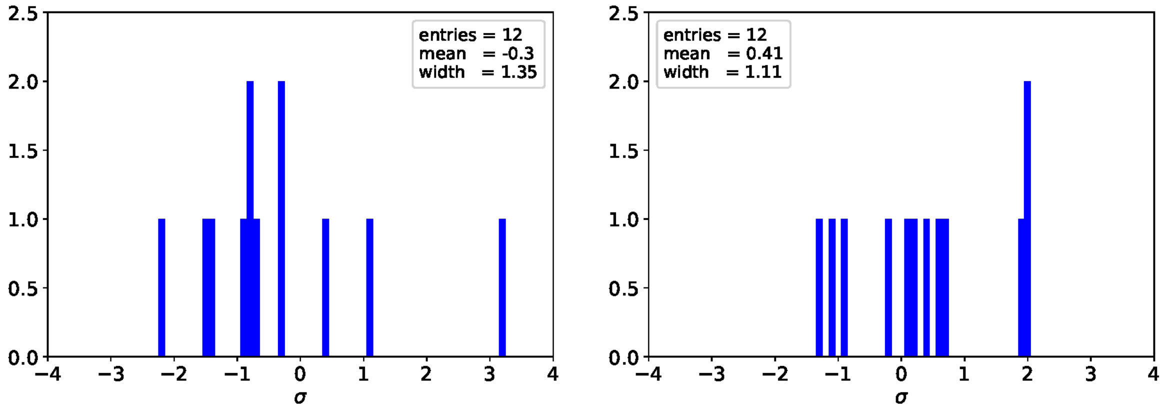

(a) (b)

Figure 5.20: Significance distribution of the VHE $\gamma$-ray emission that is contained within the extension of the SFRs inside the SMC for an energy range of (a) $1 - 100$ TeV (CT1-4 data set) and (b) $0.4 - 10$ TeV (CT5 data set).

### Diffuse Emission in the SMC

The detection of diffuse HE $\gamma$-ray emission in the Magellanic Clouds by *Fermi*-LAT [68, 69, 108] confirmed that particle diffusion on large scales also plays a role in star-forming galaxies. The question is whether the diffuse emission spectrum also extends to $\sim$ TeV energies as is the case in the Milky Way [271, 272].

The angular extent of the HE $\gamma$-ray diffuse emission in the SMC was measured to be $\sim 3^\circ$ [68, 69, 108]. An analysis of such an extended region is not possible with the existing analysis frameworks of the H.E.S.S. experiment, as the background cannot be estimated properly with the well established background methods that are described in Section 3.1.5. However, a study of the diffuse emission in energy bands shows that the extension of the diffuse emission significantly decreases with increasing energy. In the energy range between $5-10$ GeV the diffuse emission splits into substructures with scales of $\sim 0.5^\circ$ [108]. VHE $\gamma$-ray emission on these scales can be tested with the established analysis tools of the H.E.S.S. experiment. An analysis of the entire field of view of the SMC is performed analogously to the analysis for the search of point-like VHE $\gamma$-ray emission, except that the size of the *on* region is set to $\Theta^2 = 0.16$. Hence, diffuse VHE $\gamma$-ray emission contained within a circle with radius $0.4^\circ$ is studied. The analysis is only performed for the CT1-4 data set. The smaller field of view of the CT5 camera makes it impossible to find appropriate regions for the background estimation; this, in combination with the mono event reconstruction with increased uncertainties compared to the stereo event reconstruction, leads to significantly increased systematic uncertainties in the background estimation and hence to results that cannot be trusted.

The result is shown in Figure 5.21. No significant $\gamma$-ray emission above $1$ TeV on scales of radius $0.4^\circ$ is found in the SMC. Integral flux upper limits in the energy range of $1-100$ TeV are estimated for the entire field of view as described in Section 5.2.2 by taking into account a systematic uncertainty of 16%. All systematic uncertainties remain the same, except for the systematic uncertainty due to the background estimation. Although the systematic uncertainty in the background estimation is slightly increased ($\sigma_{\text{syst}} \approx 0.7\sigma_{\text{stat}}$), it is still compatible with a final systematic uncertainty of 1%. Thus, the total systematic uncertainties remain unchanged compared to the systematic uncertainties in the search for point-like $\gamma$-ray emission.

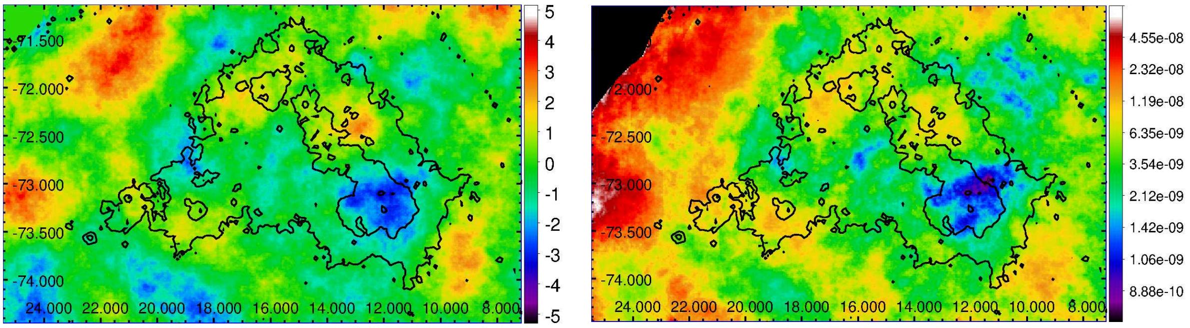

(a)

(b)

Figure 5.21: (a) Significance (in units of [$\sigma$]) and (b) integral flux upper limit (in units of [m$^{-2}$ s$^{-1}$]) sky maps in the energy range $1 - 100$ TeV for the CT1-4 data set. A correlation radius of $0.4^{\circ}$ is applied to the sky maps. Coordinate system is the same as for Figure 5.12. Contours are the same as in Figure 5.3.

# Chapter 6

# Comparison of the Source Populations between the SMC, LMC and Milky Way

Apart from the three known VHE $\gamma$-ray sources in the LMC, the systematic search for point-like $\gamma$-ray emission towards the Magellanic Clouds revealed that there are no additional powerful VHE $\gamma$-ray sources with luminosities that are detectable with the H.E.S.S. experiment. Nevertheless, the integral luminosity upper limits can be compared to the known population of VHE $\gamma$-ray sources in the Milky Way to draw conclusions on source intrinsic as well as environmental differences between the three galaxies. This chapter focusses on the comparison of the SNR (Section 6.1), PWN (Section 6.2) and $\gamma$-ray binary (Section 6.3) populations for an energy range of $1 - 100$ TeV; this means that only the results for the CT1-4 data sets are compared.

## 6.1 Supernova Remnants

Before comparing the SNR source populations of the Magellanic Clouds and the Milky Way, the completeness of the SNR samples is briefly discussed as the comparison of incomplete samples may lead to misleading conclusions.

Thanks to the high coverage fraction of the galaxy as well as observations with deep exposures by X-ray and radio instruments, the SMC sample of SNRs is most likely the most complete sample among the three galaxies. However, the depth of the SMC is still highly uncertain [82, 83] and may thus result in a less complete sample due to foreground sources masking SNRs in the background. In general, the SMC SNRs are rather old ($\gtrsim 1000$ yr to $\sim 30000$ yr) and extended ($\sim 10 - 80$ pc). Most of the SNRs are in the adiabatic or radiative phase of their evolution [302]. The star formation rate peaked $\sim 5$ Gyr ago as well as several times in the last $500$ Myr leading to a low number of type Ia supernovae, as the type Ia delay-time distribution peaks

below $1$ Gyr [303]. The increased star formation rate in the past $12$ Myr led to a higher fraction of core-collapse supernovae compared to type Ia supernovae. However, the number of young and middle-aged SNRs is very low (5 SNRs). These may result from delayed core-collapse events of massive stars due to binary interactions, rapid rotation or low metallicities [304]. The low density of the ambient medium of $n \lesssim 0.1$ cm$^{-3}$ around the SMC SNRs supports the fast growth of the SNRs shells, as there is less material slowing down the expanding ejecta.
The LMC SNR sample is less complete compared to the SMC SNR sample due to the lower coverage fraction, especially at the outskirts of the LMC, by X-ray or radio instruments [97]. The higher star formation rate in the past in the LMC compared to the SMC as well as its larger size led to a larger number of SNRs in the LMC. On average, the LMC SNRs are younger than in the SMC; this is most likely due to the peak in the star formation rate at roughly $1.5-2$ Gyr and $\sim 500$ Myr ago, leading to a larger number of type Ia SNRs in the LMC compared to the SMC, whereas the ongoing increased star formation rate in the last $12$ Myr led to the population of core-collapse supernovae in the LMC. Among the sample of the LMC SNRs are a few young ($< 1000$ yr) SNRs (e.g., N 103B or SN 1987A), which are or may become powerful VHE $\gamma$-ray emitters. Besides the increased star formation rate in the LMC compared to the SMC, the on average higher density of the ambient medium of $n \sim 0.1$ to $> 1$ cm$^{-3}$ around the LMC SNRs compared to the SMC SNRs may lead to less extended SNRs in the LMC [97, 302]. The only exception in the SMC seems to be B0102-7219 (J0104-7201 / IKT 22).
The least complete SNR sample is most likely that of the Milky Way. On the one hand, there is an observational bias. SNRs that are located in the Galactic plane are difficult to detect due to overlapping sources as well as source confusion in the highly populated region. Also, SNRs with a too large angular extension are difficult to detect, as the background estimation becomes challenging with the established background models. On the other hand, only Milky Way SNRs that are detected in TeV energies are selected for the comparison of the source populations. Out of the roughly 300 known radio detected SNRs in the Milky Way [305], only a few have been detected in VHE $\gamma$ rays so far. Most of these SNRs are young or middle-aged SNRs ($\lesssim$ a few kyr) with only two SNRs being older than $\sim 30$ kyr. Whether the age gap is an observational bias or a physical characteristic of SNRs is still not clear. Out of the Milky Way SNRs with a VHE $\gamma$-ray detection only those with luminosities $L_{1-100\mathrm{TeV}} \gtrsim 5 \times 10^{32}$ erg s$^{-1}$ will be discussed.

Figure 6.1 shows a comparison of the SNR source populations of the SMC, LMC and Milky Way as a function of the SNR diameter. Apart from SNR N 132D no other Extragalactic SNR has been detected in VHE $\gamma$ rays. By examining the integral luminosity upper limits, it can be seen that ~30% of the Magellanic Clouds SNR population have lower VHE $\gamma$-ray luminosities than that of N 132D; ~17% of the LMC SNR population and none of the SMC SNRs have VHE $\gamma$-ray luminosities less than that of HESS J1640-465; and for three LMC SNRs, a luminosity equal to HESS J1713-381 would have been detectable. None of the other Milky Way SNRs would have been detected, if they were placed at the LMC or SMC distance. The nondetection of other VHE

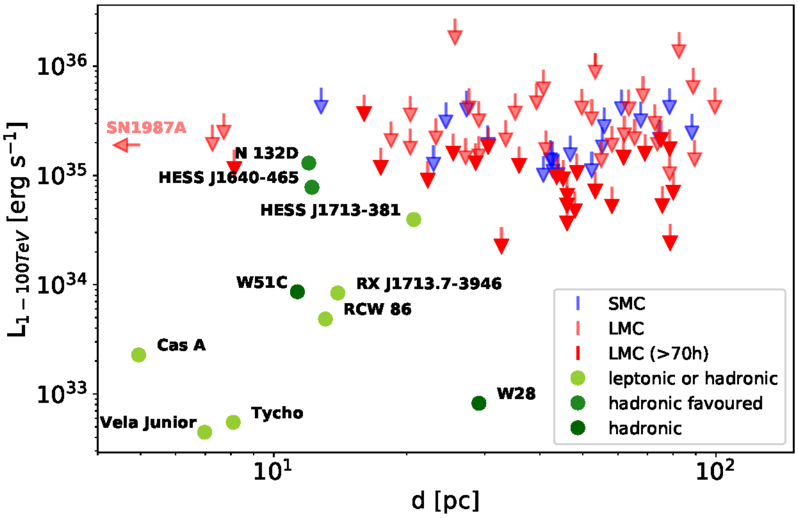

Figure 6.1: Comparison of the luminosity upper limits in the energy range of $1-100$ TeV of the SNR population in the LMC, SMC and Milky Way as a function of the SNR diameter. The diameter of SN 1987A is outside the range shown here, which is indicated with an arrow.
Results and parameters for the known SNRs are taken from the following sources (and references therein): Cas A: MAGIC collaboration 2017 [169], HESS J1640-465: H.E.S.S. collaboration 2014 [306], HESS J1713-381: H.E.S.S. collaboration 2018, Tian & Leahy 2012 [63, 307], N 132D: H.E.S.S. collaboration 2015 [23], RCW 86: H.E.S.S. collaboration 2018 [159], RX J1713.7-3946: H.E.S.S. collaboration 2018, Yang & Liu 2013 [308, 309], Tycho: VERITAS collaboration 2017, Douvion et al. 2001 [162, 310], Vela Junior: [311], W 28: H.E.S.S. collaboration 2018 [63], W 51C: MAGIC collaboration 2012, Ranasinghe et al. 2018 [152, 312].

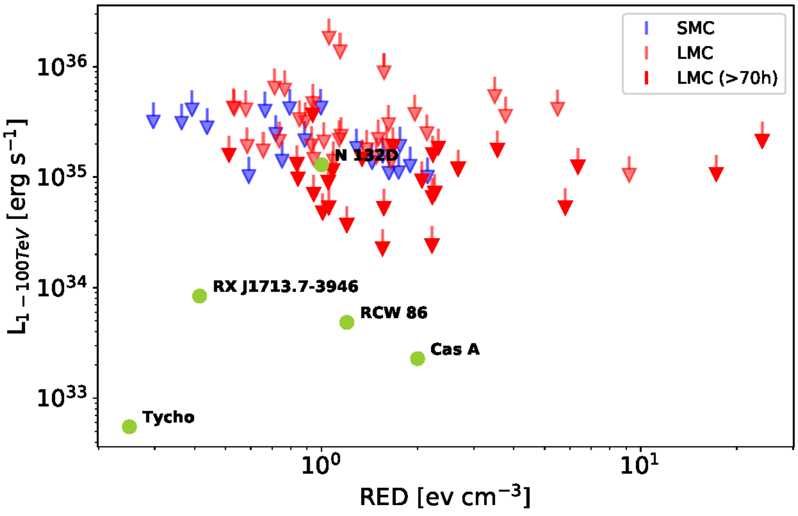

Figure 6.2: Comparison of the luminosity upper limits in the energy range of $1-100$ TeV of the SNR population in the LMC, SMC and Milky Way as a function of the radiation field energy density (RED) at the position of the SNR.
References for results and parameters for the known SNRs are the same as in Figure 6.1

$\gamma$-ray emitting SNRs in the Magellanic Clouds may be a result of i) the incompleteness of the LMC survey and the resulting inhomogeneity in the sensitivity over the field of view as well as the lower exposure for the SMC, ii) the lower total number of radio and/or X-ray detected SNRs in the Magellanic Clouds compared to the Milky Way and hence the lower probability to find more extremely powerful SNRs, iii) differences in the SNR environments between the galaxies or iv) the older age of the SMC and LMC SNR population. Concerning the first point, a more homogeneous and deeper exposure of $\sim 70$ h over the entire field of view in both Magellanic Clouds would significantly increase the fraction of SNRs for which a luminosity level of N 132D or HESS J1640-465 can be constrained (dark red arrows in Figure 6.1). The last two points are due to the described intrinsic difference of the SNR age distributions and the density of the ambient medium around the SNRs of the three galaxies.

The diameter is used as an indicator of the SNR age as ages have not been estimated for all SNRs in the Magellanic Clouds. A cross-check revealed that below an extension of $30$ pc, corresponding to an age of $\sim 7$ kyr, the correlation between age and extension can be assumed to be linear for all SMC, LMC or Milky Way SNRs[1]. Thus, the assumption that SNRs with larger extensions are older is valid for this range of extensions. SNRs with extensions of $> 30$ pc show an increased scatter in the age distribution, but are in general older than $10$ kyr. The only two SNRs, that are confirmed to be hadronic accelerators are the old ($> 30$ kyr) SNRs W 28 and W 51C in the Milky Way, which are interacting with nearby molecular clouds. Neither of these SNRs would have been detected if they were placed at the distances of the Magellanic Clouds. However, it is difficult to draw conclusions as only two representatives have been detected at VHE $\gamma$ rays so far. A deeper exposure towards the Magellanic Clouds or a study using the next generation of IACTs with improved instrument sensitivity may result in further detections of old SNRs interacting with molecular clouds that may be even more powerful than W 51C. On the other hand, an interstellar carbon monoxide (CO)[2] survey of the LMC showed an on average lower CO luminosity in the LMC compared to the Milky Way and only little spatial correlation between molecular clouds and SNRs [313], suggesting that the probability for old SNRs interacting with molecular clouds is rather low. The more powerful VHE $\gamma$ ray emitting SNRs are the young and middle-aged SNRs in the Milky Way. For most of these SNRs it is still under debate whether they are predominantly leptonic or hadron cosmic-ray accelerators. In the case of the two most luminous VHE $\gamma$-ray emitting SNRs N 132D and HESS J1640-465, a hadronic cosmic-ray acceleration scenario is favoured. This would either require a high post-shock gas density ($n_{\mathrm{H}} \gg 1\,\mathrm{cm}^{-3}$) or a high cosmic-ray energy fraction of the explosion energy ($\gg$1%). Only for two (old and extended) LMC SNRs is this fraction constrained to be $\lesssim$10%.

If the VHE $\gamma$-ray flux is predominantly caused by inverse Compton scattering of low energy pho-

---

[1] The linear relation between the age and the extension of the SNRs is certainly not the same for the SNR population of the SMC, LMC and Milky Way due to their different environments as described in the text. A more detailed study of this relation is out of the scope of this work. However, a rough agreement in the relations is sufficient for the purpose of this work.

[2] The CO emission at 2.6 mm wavelength is a tracer for molecular clouds.

tons, strong photon fields or high magnetic field strengths would be required. As magnetic field strengths of SNRs are only measured for a very limited number of SNRs, only the ambient photon field strengths can be compared to estimate the likelihood of the SNRs being leptonic cosmic-ray accelerators. The ambient radiation field energy density (RED) of the Magellanic Cloud SNRs is calculated by integrating the infrared flux that is measured by the Interface Region Imaging Spectrograph (IRIS)[3], in a wavelength range of $8.5-120\,\mu\mathrm{m}$. In the calculation it is assumed that the IR flux originates from a two-dimensional plane, which means that the resulting RED estimate should be considered as an upper limit. For the LMC which has an almost face-on orientation towards the Milky Way, the estimated RED is likely close to the real ambient RED, whereas the RED estimates for the SMC are likely more uncertain due to the unknown depth of the galaxy. Figure 6.2 shows the comparison of the integral luminosity upper limits of the Magellanic Clouds as a function of the RED with those of the Milky Way SNRs for which a leptonic cosmic-ray acceleration scenario is discussed and a measured ambient photon field density is available in the literature. All SMC SNRs and most of the LMC SNRs have ambient photon field densities of $0.2-3\,\mathrm{eV\,cm^{-3}}$ in agreement with those in the Milky Way, indicating that the Magellanic Cloud SNRs may likely be accelerators of leptonic cosmic rays or may have been in the past due to their advanced ages. Nine LMC SNRs have even higher REDs; of these, two are middle-aged SNRs (B0536-6913 at an age of $3500\,\mathrm{yr}$ and B0540-693 at an age of $1600\,\mathrm{yr}$). Although both have an exposure of $\sim 190\,\mathrm{h}$, they may be interesting candidates for observations with the next generation of IACTs.

A systematic discrepancy in the integral luminosity upper limits of the SNRs resulting from type Ia or core-collapse supernovae is not found and is thus not further discussed here.

## 6.2 Pulsar Wind Nebulae

The PWN population forms the largest class of VHE $\gamma$-ray sources with more than 30 PWNe having been detected in VHE $\gamma$ rays so far [127], which is more than 50% of the PWN population ($>$50) detected in X-rays and/or radio wavelengths [314]. In the Magellanic Clouds only 6 PWNe have been detected in X rays or radio so far, of which only one is detected in VHE $\gamma$ rays. The four known PWNe in the LMC were detected between 1993 and 2005 [280, 281, 315, 316]. Despite the deeper exposure and better resolution of later X-ray or radio surveys of the LMC, no further PWNe were firmly discovered. Maggi et al. [97] briefly discuss a few candidate PWNe based on their detection of a pulsar in the centre of the nebula. However, the authors comment that their survey is likely incomplete towards the outskirts of the LMC, and that this region may host further PWNe. The SMC PWNe were discovered recently thanks to the deep exposure of the

---

[3] Images for the LMC and SMC are downloaded from this webpage: https://skyview.gsfc.nasa.gov/current/cgi/query.pl

latest X-ray and radio surveys (by XMM-Newton, the Chandra X-ray Observatory (CHANDRA ) or the Australia Telescope Compact Array (ATCA)) [288, 289]. No further PWN candidates inside a known X-ray or radio SNR have been found in the latest study of the SMC SNR population [302]. As the SMC is well covered with a deep exposure in the latest X-ray and radio surveys, it seems unlikely that more PWNe will be found with the current generation of instruments. It is still unclear why the Magellanic Clouds seem to host significantly less PWNe than the Milky Way and why the powerful PWN N 157B is detected in VHE $\gamma$ rays with high significance but N 158A is not, even though it is very similar to N 157B. Possible explanations may be the on average older SNR / pulsar population ($\gtrsim 10$ kyr) in the Magellanic Clouds resulting in older PWNe and thus lower X-ray and radio fluxes compared to young ($< 10$ kyr) PWNe, or environmental parameters such as the density of the ISM as well as the background light at the position of the PWNe. The latter will be briefly discussed in the following.

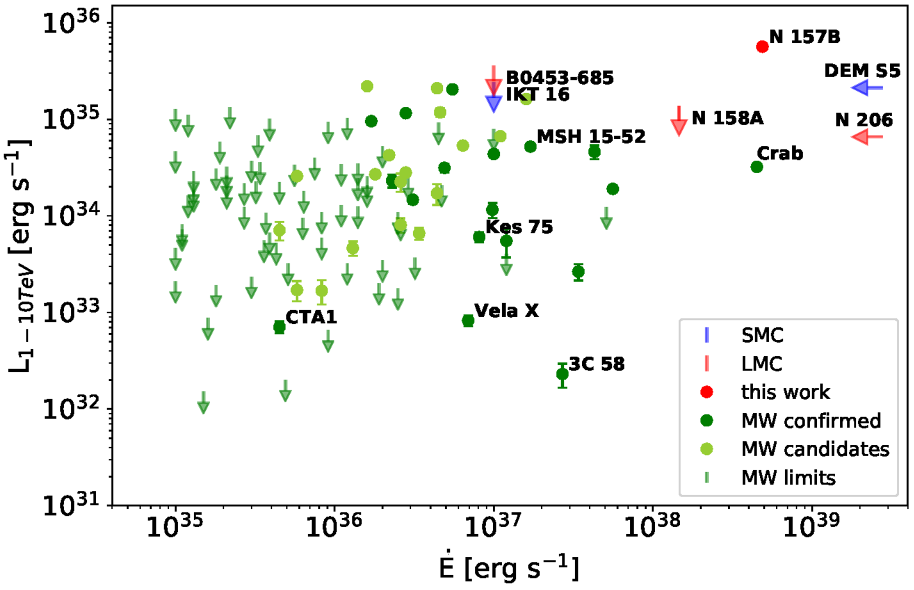

Figure 6.3: Comparison of the luminosity upper limits in the energy range of $1 - 10$ TeV of the PWN population in the LMC and SMC and the PWN population in the Milky Way as a function of the spin-down energy.
Results and parameters for the Milky Way PWN population are taken from HESS collaboration 2018 [8].

Figure 6.3 shows the comparison of the integral luminosities for the PWN populations in the Magellanic Clouds and the Milky Way as a function of their spin-down power. The two PWNe in the Magellanic Clouds without a known spin-down power are shown with an arrow to the left, indicating an upper limit in both dimensions. It can be excluded that any of the known PWNe in the Magellanic Clouds are as powerful as N 157B. Apart from the farthest outskirts in the LMC, no region in the entire field of view of either Magellanic Cloud contains a PWN at the luminosity of N 157B (see Figures 5.8 and 5.17a). On the other hand, none of the well known Milky Way PWNe (labeled in the figure) would have been detectable if they were placed at the distance of the Magellanic Clouds. Only the luminosity level of the most luminous Milky Way PWNe can be constrained by three of the five nondetected Magellanic Cloud PWNe.

As PWNe are most likely leptonic particle accelerators, their $\gamma$-ray production efficiency mainly depends on the density of the ambient photon field. The H.E.S.S. collaboration estimated the energy densities of the starlight and infrared fields to be $1.92\,\mathrm{eV\,cm^{-3}}$ and $1.194\,\mathrm{eV\,cm^{-3}}$, respectively [8]. The IR radiation field energy density, which is estimated analogously to the method used for the SNRs (see Section 6.1), lies below $1.7\,\mathrm{eV\,cm^{-3}}$ for four of the Magellanic Clouds PWNe. In the case of N 158A the IR radiation field energy density is $6.11\,\mathrm{eV\,cm^{-3}}$, and for N 157B the density is even higher at $27.65\,\mathrm{eV\,cm^{-3}}$, which may explain the extraordinary high VHE $\gamma$-ray luminosity of N 157B. The generally lower RED of the other PWNe compared to those in the Milky Way in combination with their distance makes them less likely to be VHE $\gamma$-ray source candidates, even though their spin-down power seems to be in general higher than for those of the Milky Way. However, this may well be a selection effect due to the sensitivity limitation of the current generation of instruments.

Even with a deep exposure of $> 70\,\mathrm{h}$ (i.e., for N 206 and N 158A) the $\gamma$-ray luminosities of the well known Milky Way PWNe cannot be constrained. Thus, only the next generation of IACTs may shed light on the acceleration mechanisms of the Magellanic Clouds PWNe.

## 6.3 High-Mass X-Ray Binaries as Potential $\gamma$-ray Binaries

The population of detected $\gamma$-ray binaries is very diverse in their physical parameters — e.g., they cover a wide range of orbital periods from a few days up to several years or exhibit a range of eccentricities ($\sim 0.3 - 1$) — but their VHE $\gamma$-ray emission appears to be very similar when considering their integral luminosities ($\sim 10^{33}\,\mathrm{erg\,s^{-1}}$) and their spectral indices ($2.2 - 2.7$). The only exception is the most powerful $\gamma$-ray binary detected so far. The luminosity of LMP P3, located in the LMC, is two orders of magnitude higher than the luminosities of the Milky Way $\gamma$-ray binaries. It might well be a selection effect due to the incompleteness of the Milky Way source population, as many potential $\gamma$-ray sources are hidden in the Galactic plane for the current generation of IACTs. On the other hand it may also be due to an environmental difference in the galaxies. The $\gamma$-ray binary LMC P3 will be discussed in more detail in Section 6.6.1.

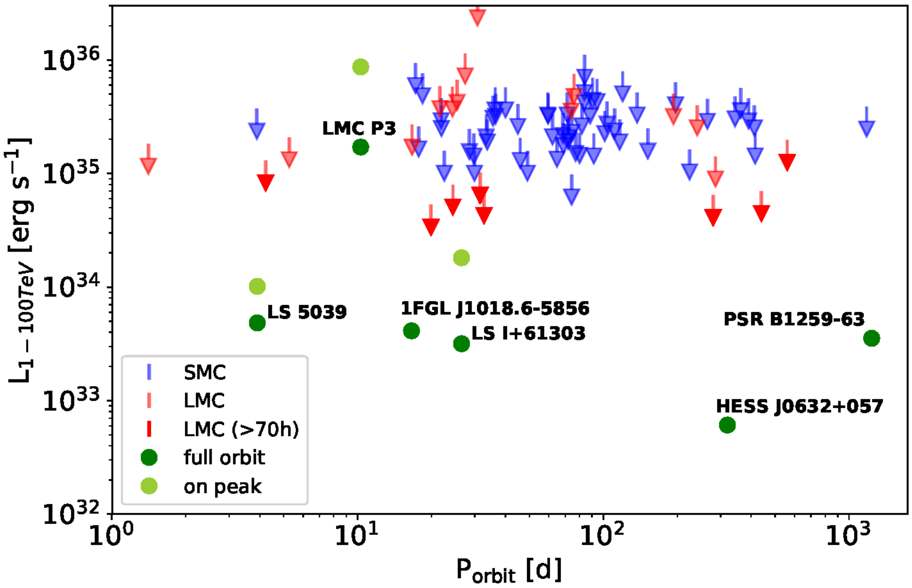

Figure 6.4: Comparison of the luminosity upper limits in the energy range of $1-100$ TeV of the HMXB population in the LMC and SMC and the $\gamma$-ray binary population in the Milky Way as a function of the orbital period.
Results and parameters for the known $\gamma$-ray binaries are taken from the following sources (and references therein): LS 5039: Mariaud et al. 2015 [317], LMC P3: HESS collaboration 2018 [100], 1FGL J1018.6-5856: HESS collaboration 2015 [318], LS I+61303: VERITAS collaboration 2016 [319], HESS J0632+057: HESS and VERITAS collaboration 2013 [320], PSR B1259-63: HESS collaboration 2005 [231].

Figure 6.4 shows the comparison of the Milky Way $\gamma$-ray binary population and the potential $\gamma$-ray binary population of the Magellanic Clouds as a function of their orbital periods. Those HMXBs without a given orbital period are not shown here. A test confirmed that there is no systematic difference in the integral luminosity upper limits between those HMXBs with and without a given orbital period, as is the case for HMXBs with a confirmed neutron star as a compact object or without. The Milky Way $\gamma$-ray binary PSR J2032+4127 is not included due to its long orbital period. For roughly 50% (30%) of the LMC (SMC) HMXBs and for all LMC HMXBs with an exposure of more than $70$ h, a VHE $\gamma$-ray emission at the level of the full-orbit (orbit averaged) luminosity of LMP P3 can be excluded. None of the Milky Way $\gamma$-ray binaries would be detectable, if they were placed at the distance of the LMC or SMC. Although some $\gamma$-ray binaries have been misclassified as HMXBs in the past (e.g., LMC P3), it is very likely that most of the objects are indeed HMXBs that have not been detected in $\gamma$ rays so far. It is assumed that $\gamma$-ray binaries are the progenitors of HMXBs. The typical lifetime of $\gamma$-ray binaries is believed to be of the order $\sim 10^5$ yr, which means that all potential $\gamma$-ray binaries resulting from the increased star formation periods $> 10^6$ yr ago have already transformed into HMXBs, which seems to be confirmed by Antoniou & Zezas [98]. Only those $\gamma$-ray binaries that may have arisen from the most recent star formation period may still be bright in VHE $\gamma$ rays. Although for many HMXBs the compact object is confirmed to be a neutron star, as is also the case for the $\gamma$-ray binaries PSR B1259-63 and PSR J2032+4127, the companion is in most of the cases a Be-type star, making them less likely VHE $\gamma$-ray candidates. Only for a few HMXBs has an O or B-type companion been confirmed (i.e., SMC X1 (HMXB 1), LMC X-1 (3A0540-697), LMC X-4 (2A0532-664), RXJ0541.5-6833 or RX J0532.5-6551), which suggests that these objects are younger, as the lifetime of an O or B-type star is of the order $10^6 - 10^7$ yr, and hence would be more promising $\gamma$-ray binary candidates. However, none of these objects show significant VHE $\gamma$-ray emission in the data set studied in this work. On the other hand, only the HMXBs LMC X1 and RXJ0541.5-6833 have a H.E.S.S. exposure of more than $70$ h and hence the upper limits of the other HMXBs may be less constraining.

A deeper and more homogeneous exposure of $\sim 70$ h can clarify if LMC P3 is the only extremely powerful $\gamma$-ray binary in the Magellanic Clouds. However, the sensitivity of the data sets does not improve significantly anymore with increasing exposure beyond $\sim 70$ h. The next generation of IACTs will most likely be able to either detect more $\gamma$-ray binaries in the Magellanic Clouds with a VHE $\gamma$-ray flux level on the order of the fluxes measured from Milky Way $\gamma$-ray binaries or will place deeper upper limits on the luminosities of these objects.

## 6.4 Star-Forming Regions Hosting Stellar Clusters

The sample of stellar clusters and SFRs that are confirmed VHE $\gamma$-ray emitters is limited to four representatives of that source class: the super stellar cluster Westerlund 1 [321], the compact stellar cluster Westerlund 2 [322], the SFR Cygnus Cocoon [323] and 30 DorC (the only massive stellar cluster outside the Milky Way [23]). All of these VHE $\gamma$-ray sources are massive, compact regions that contain a number of young massive stars with strong winds like Wolf-Rayet, O-type and B-type stars or even yellow hyper-giants and Wolf-Rayet binaries (as observed in Westerlund 1). In the case of 30 DorC also SNRs are found within the superbubble. Collisions of continuous stellar winds and shock fronts in single, binary or collective processes make these stellar clusters and SFRs to promising acceleration sites for VHE cosmic rays.

The SFRs investigated in this work seem to be dominated by early-type stars that were born $\lesssim 10^7$ yr ago [324]. Though a number of SFRs seem to reveal areas of ongoing star formation and are correlated with young luminous stars, no evidence for the formation of massive stars at high rates is found [105]. Furthermore, none of the 12 known isolated or binary Wolf-Rayet stars in the SMC [325, 326] seems to be related to SFRs. The lack of strong stellar winds inside the SMC SFRs makes these SFRs a less favourable place for efficient particle acceleration [270]. However, some of the SFRs do contain a SNR. Although, no significant VHE $\gamma$-ray emission from SNRs as point-like sources has been found, the interaction of the shock front with existing stellar winds inside the SFRs may result in more efficient particle acceleration on a larger scale.

The association of some massive SFRs in the SMC with molecular clouds [327] may then result in an efficient energy loss of the accelerated protons through hadronic interactions inside the molecular clouds and, hence, to the emission of VHE $\gamma$ rays.

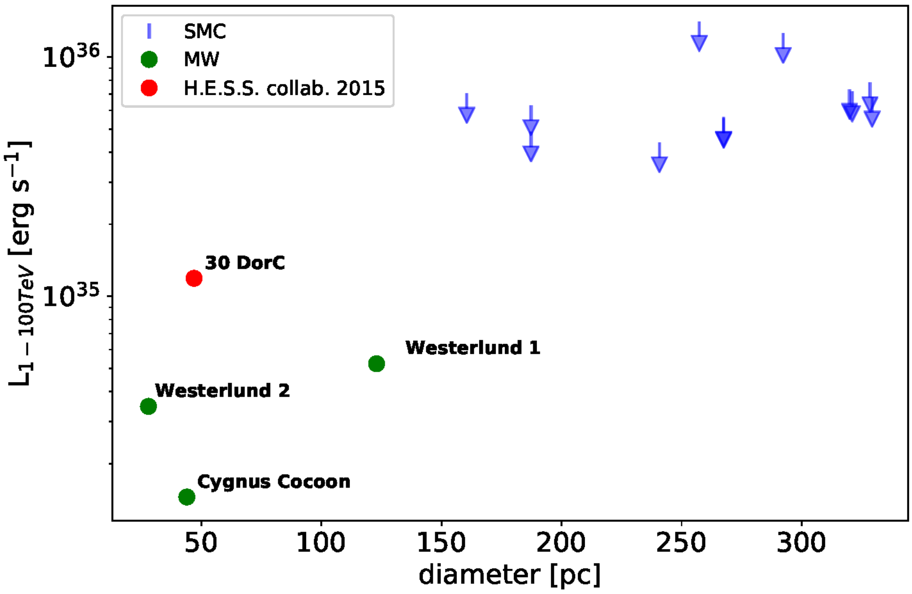

Figure 6.5: Comparison of the luminosity upper limits in the energy range of $1 - 100$ TeV of the SFRs located in the SMC and detected SFRs and stellar clusters in the Milky Way and the LMC.
Results and parameters for the confirmed SFRs / stellar clusters are taken from (and references therein): Westerlund 1: H.E.S.S. collaboration 2012 [321, 328], Westerlund 2: H.E.S.S. collaboration 2011 [322], Cygnus Cocoon: ARGO collaboration 2014 [267, 329], 30 DorC: H.E.S.S. collaboration 2015 [23].

Figure 6.5 shows the comparison of the integral luminosities of the SMC SFRs and the confirmed stellar clusters and SFRs of the Milky Way and LMC as a function of their diameter. The comparison reveals that no direct conclusion can be drawn as the luminosity upper limits are a factor $\gtrsim 4$ higher than the most luminous stellar cluster known so far.
Although it seems unlikely that the SMC SFRs are as efficient particle accelerators as the detected stellar clusters and SFRs, a final answer can probably only be given by further studies in the X-ray and $\gamma$-ray regimes. Whereas the X-ray studies may reveal whether efficient particle acceleration at a comparable level to the confirmed sources takes place at all, deeper observations in the $\gamma$-ray regime with the next generation of IACTs could clarify the origin of the non-thermal emission, which may either be leptonic or hadronic in origin. A comparison to the LMC SFR population may also be interesting, as 13 SFRs in the LMC show increased star formation rates of high mass stars.

## 6.5 Diffuse Emission

Diffuse $\gamma$-ray emission is detected at up to TeV energies for some galaxies. Besides the Milky Way [271, 272] the two starburst galaxies M 82 [330] and NGC 253 [331, 332] and M 31 [273] are detected in (V)HE $\gamma$ rays with spectra following a power law of $\Gamma \approx 2.2$ without a hint of an exponential cutoff [12, 271, 273, 332]. Diffuse HE $\gamma$-ray emission with similar spectral properties is also found for the LMC, though with a significantly lower HE $\gamma$-ray luminosity compared to NGC 253 or M 82 [331]. So far, there has been no detection of diffuse emission in VHE $\gamma$ rays in the LMC, raising the question of whether the nondetection is due to a lower cutoff in the parent cosmic-ray spectrum or due to environmental differences in the LMC. However, ongoing studies using improved analysis techniques may be able to answer this question (see discussion below). In the case of the SMC, observations in the HE $\gamma$-ray regime have already hinted at an exponential cutoff in the $\gamma$-ray spectrum at a few GeV, and the integral HE $\gamma$-ray luminosity of the SMC diffuse emission is even lower than in the LMC [68]. However, the statistics at $\gtrsim$ GeV energies are not sufficient to confirm this exponential cutoff in the $\gamma$-ray spectrum. Unfortunately, the upper limits reported in this work (see Section 5.3.4) are also not sensitive enough to confirm the existence of the exponential cutoff in the $\gamma$-ray spectrum. Figure 6.6 shows a comparison of the integral energy flux upper limit in the energy range of $1-100$ TeV to the HE $\gamma$-ray spectrum as seen by *Fermi* [108]. Assuming that the HE $\gamma$-ray emission does not show the cutoff at $\sim 12$ TeV as preferred by Lopez et al. but instead continues following a power law with index $\Gamma = 2.26$, the sensitivity of H.E.S.S. is still not sufficient to probe the diffuse VHE $\gamma$-ray emission, which has an expected energy flux of $\lesssim 10^{-12}\,\mathrm{erg\,cm^{-2}\,s^{-1}}$ at $1$ TeV. Nevertheless, VHE $\gamma$-ray emission with a luminosity at the level of the starburst galaxy NGC 253 ($L_{1-100\,\mathrm{TeV}} \sim 6.5 \times 10^{38} \left(\frac{1}{3.5\mathrm{Mpc}}\right)$ erg s$^{-1}$ [332, 333]) or M 82 ($L_{1-100\,\mathrm{TeV}} \sim 6.3 \times 10^{38} \left(\frac{1}{3.5\mathrm{Mpc}}\right)$ erg s$^{-1}$ [330]) can be ruled out. Although a detection of diffuse $\gamma$-ray emission at TeV energies seems to be unlikely, it should be noted that the diffuse emission is only tested on scales of $0.4^\circ$ radius. In the case of more extended diffuse emission a VHE $\gamma$-ray signal may not have been found due to the limitation of the background subtraction method that is applied in the analysis presented in this work. A more advanced 3D likelihood analysis, in which the background can be modelled over the entire data set without any need of *on* and *off* region in the field of view, may be more appropriate for the analysis of extended $\gamma$-ray emission. Such an analysis with tools that are currently developed [334, 335] could be the subject of a subsequent study on the diffuse VHE $\gamma$-ray emission in both Magellanic Clouds and may be able to answer questions about a possible cutoff in the parent cosmic-ray spectra of the Magellanic Clouds of $\lesssim 10$ TeV, the importance of the cosmic-ray density — which is shown to be $6-7$ times smaller than the local value in the Milky Way [68] — or about the role of the source populations and environment in the Magellanic Clouds.

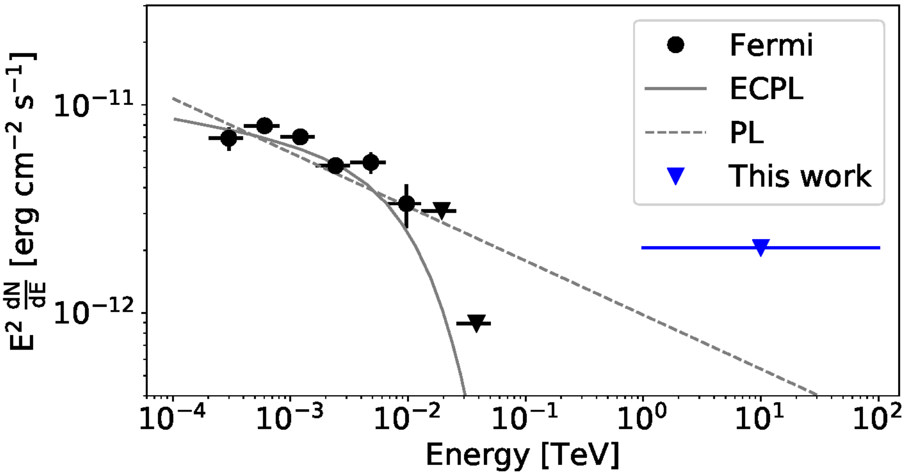

Figure 6.6: Comparison of the VHE $\gamma$-ray energy flux upper limit (average value) in the energy range of $1 - 100$ TeV and the HE $\gamma$-ray energy flux as seen by *Fermi* [108] of the diffuse emission in the SMC. The best fits to the *Fermi* data, i.e., a power law model (solid grey line) and the preferred power-law with an exponential cutoff at $\sim 12$ GeV (dashed grey line) are also shown [108].

## 6.6 Discussion of individual sources in the Magellanic Clouds

After a discussion and comparison of the entire source population of the Magellanic Clouds, this section focusses on a few individual sources that are either exceptional in their VHE $\gamma$-ray emission or were expected to be detected at TeV energies. For the three LMC sources LMC P3, N 157B and SN 1987A, the dedicated analysis that is performed is described first and is followed by a discussion of the results. In addition, the LMC PWN N 158A, SMC SNR B0102-7219 and SMC PWN IKT 16, for which a detection in TeV energies was expected, are discussed in more detail.

### 6.6.1 Increasing the Population of $\gamma$-ray Binaries — the Case of LMC P3

LMC P3 is one of seven $\gamma$-ray binaries and the first Extragalactic $\gamma$-ray binary discovered so far. The $\gamma$-ray detection by the *Fermi*-LAT satellite [276] confirmed that binaries classified as HMXBs [285] can indeed accelerate particles to $\sim$GeV energies and thus belong instead to the class of $\gamma$-ray binaries. Located in the supernova remnant SNR 0535-67.5 inside the HII region DEM L241, the compact object (neutron star or black hole) orbits the O-type companion star every $10.301 \pm 0.002$ days [276].

The LMC survey analysis was performed to provide an unbiased population study. Although it did not result in a detection ($\sigma = 1.9$), the similarity to the known $\gamma$-ray binaries LS 5039 and 1FGL 1018.6-5856 suggests that LMC P3 may also be a TeV source and hence a more in depth investigation of this source may lead to a detection of VHE $\gamma$-ray emission from the binary.

A more sensitive analysis configuration with harder cuts and increased angular resolution at large zenith angles [48, 336] is chosen for this analysis to improve the direction reconstruction and increase the signal-to-noise ratio and hence increase the chance for a detection. After the $\gamma$-hadron separation following the Multivariate Analysis technique as described in Section 3.1.5, a further cut on the image displacement inferred from Hillas parameters in the reconstruction procedure is applied as well as an additional cut on the estimated direction uncertainty. These cuts improve the angular resolution to $\lesssim 0.06^\circ$ at zenith angles of $50^\circ$, an improvement of more than 50% compared to the angular resolution of $\sim 0.14^\circ$ at zenith angles of $60^\circ$ achieved with the LMC survey analysis. However, the improvement of the angular resolution comes at the expense of lower effective area, which is decreased by up to 50% at low energies. Hence, the *hires* configuration is especially suitable for sources with hard spectra in VHEs, which are typically observed in $\gamma$-ray binaries.

A point-source analysis, based on the same data set that was used for the LMC survey, targeted at the binary LMC P3 and applying the *hires* configuration, revealed a point-like orbit-averaged emission with a significance of $\sigma = 4.1$ above an energy threshold of $1.2$ TeV. As $\gamma$-ray binaries typically show an orbital modulation of the signal, a phase resolved study is performed. As the

Table 6.1: Statistical results and spectral parameter for different orbital phase bins of LMC P3.

| Orbital phase bin | Lifetime [h] | Significance [$\sigma$] | $F_{1\,\mathrm{TeV}}$ $10^{-12}$ [TeV$^{-1}$ cm$^{-2}$ s$^{-1}$] | $\Gamma$ | $F_{1-10\,\mathrm{TeV}}$ $10^{-12}$ [cm$^{-2}$ s$^{-1}$] | $L_{1-10\,\mathrm{TeV}}$ $10^{35}$ [erg s$^{-1}$] |
|---|---|---|---|---|---|---|
| 0.0 - 0.2 | 22.9 | 1.90 | - | 2.3 (fixed) | $<$0.27 | $<$4.2 |
| 0.2 - 0.4 | 21.8 | 4.97 | 0.97 $\pm$ 0.56 | 2.9 $\pm$ 0.4 | 0.50 $\pm$ 0.20 | 4.5 $\pm$ 1.7 |
| 0.4 - 0.6 | 27.7 | 1.30 | - | 2.3 (fixed) | $<$0.18 | $<$ 2.8 |
| 0.6 - 0.8 | 28.5 | -0.13 | - | 2.3 (fixed) | $<$0.13 | $<$2.0 |
| 0.8 - 1.0 | 26.4 | 0.82 | - | 2.3 (fixed) | $<$0.12 | $<$1.8 |

If no significant VHE $\gamma$-ray emission is detected in the orbital phase bins, an integral flux upper limit in the energy range of $1-100$ TeV is derived at a 95% confidence level by assuming a power law with spectral index of $\Gamma = 2.3$.

H.E.S.S. sensitivity does not allow for a detection of significant $\gamma$-ray emission on a nightly basis (unless the source is as bright as the PWN N 157B) a phase-folded lightcurve is computed to search for potential orbital modulations. For this purpose the data set was split into five phase bins according to a 10.301 d orbit with phase bin 0.0-0.2 being centred on the HE maximum as detected by *Fermi* (MJD $57410.25 \pm 0.34$ for sinusoidal modulation) [276]. The phase bins are filled on an event-by-event basis for the whole data set based on the arrival time of the events in the camera resulting in a roughly homogeneous exposure in all phase bins (only phase bin 0.6-0.8 has a slightly higher exposure). The result is presented in Figure 6.7 and the corresponding numbers are listed in Table 6.1. The phase-folded lightcurve clearly reveals that VHE emission from LMC P3 is only detected within the second phase bin with a significance of $\sigma \approx 5.0$. To verify the significance of the orbital modulation, the folded lightcurve (in units of excess and flux) is fitted with a lightcurve of constant flux, resulting in a $\chi^2$-probability of $< 0.1$. Further tests that are typically applied to quantify the periodicity of a signal (e.g., the Rayleigh test [337] or H-test [338]), do not yield reliable results due to missing coverage of parts of the phase space as well as too low statistics in the phase bins.

With an on-peak luminosity of $4.5 \pm 1.7 \times 10^{35}$ erg s$^{-1}$ in the energy range of $1-10$ TeV, when taking the distance to the LMC to be $50$ kpc, LMC P3 is the most luminous $\gamma$-ray binary discovered so far, being more than one order of magnitude more luminous than the known Milky Way $\gamma$-ray binaries. The spectrum of the on-peak emission can be described by a power law with $F_{1\,\mathrm{TeV}} = 0.97 \pm 0.56 \times 10^{-12}$ TeV$^{-1}$ cm$^{-2}$ s$^{-1}$ and a spectral index of $\Gamma = 2.9 \pm 0.4$ without an indication of a cutoff up to at least $\sim 10$ TeV. As the observed $\gamma$-ray emission is point-like and modulated with the orbital period, the size of the emission region is at most the size of the binary system. Assuming a typical mass of $25-42 M_{\odot}$ for a companion of type O5III [285, 339] and a mass of $1.4 M_{\odot}$ for a neutron star as the compact object, Kepler's third law leads to a lower limit on the orbital semimajor axis of $0.28-0.33$ AU. Periastron and apastron are given by $a_{\mathrm{per}} = a(1-\varepsilon)$ and $a_{\mathrm{ap}} = a(1+\varepsilon)$, respectively, with $a$ being the semimajor axis and $\varepsilon$ the eccentricity. The estimated upper limit of $\varepsilon = 0.7$ [276], at which point the orbital separation at periastron would be equal to the radius of the star, yields a lower limit on periastron of

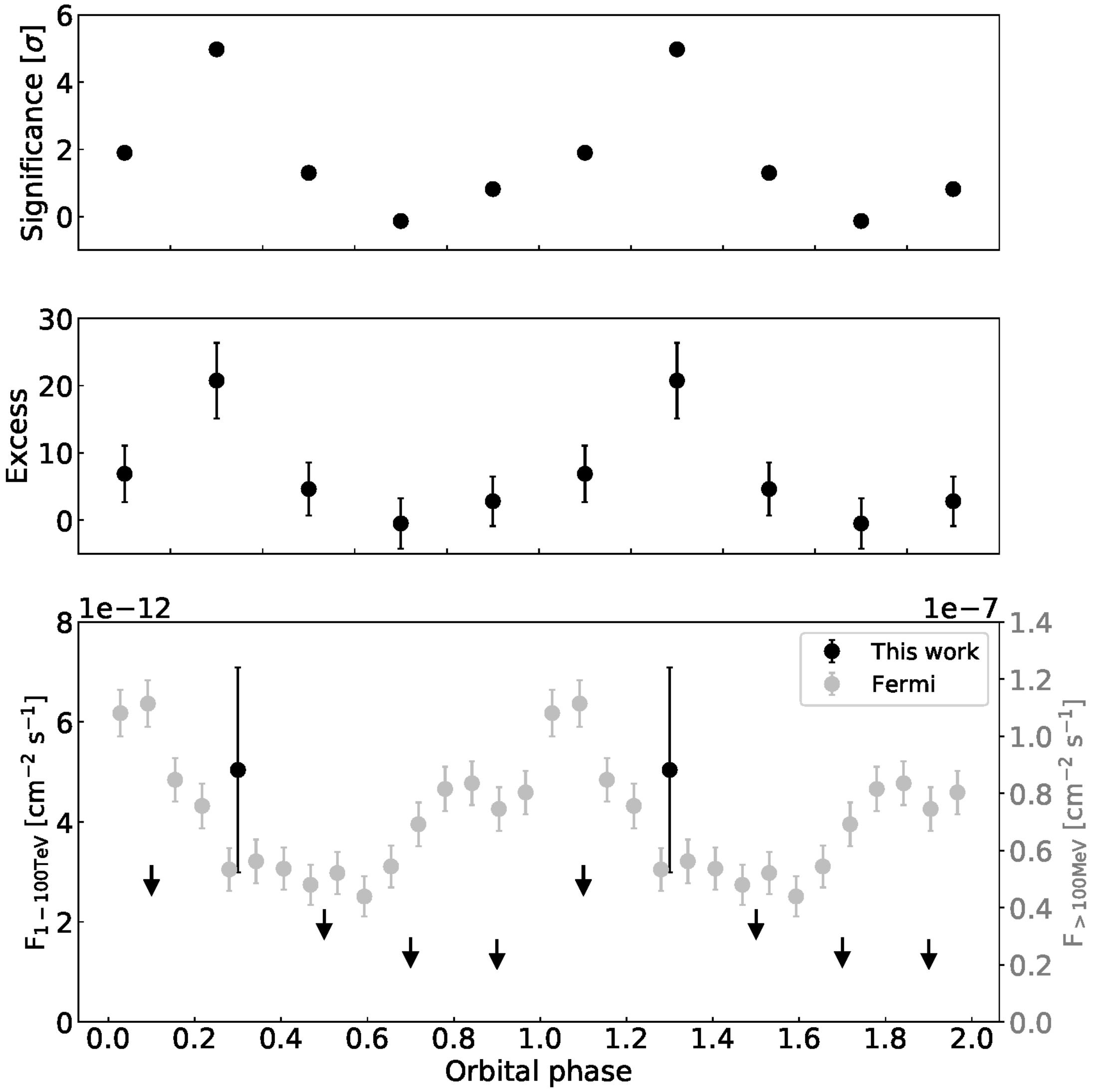

Figure 6.7: Folded $\gamma$-ray lightcurve for the $\gamma$-ray binary LMC P3. The data set is folded into 5 phase bins according to an orbital period of $10.301$ d with phase bin 0.0-0.2 centred on the HE maximum (MJD 57410.25). For the off-peak phase bins upper limits are estimated. The VHE $\gamma$-ray maximum is clearly shifted compared to the HE $\gamma$-ray maximum as seen by *Fermi*-LAT (grey) [276].

$a_{\text{per}} = 0.1$ AU and an upper limit on apastron of $a_{\text{ap}} = 0.5$ AU. When assuming a less eccentric orbit of $\varepsilon = 0.4$, the orbital separation at periastron and apastron would be $a_{\text{per}} = 0.2$ AU and $a_{\text{ap}} = 0.4$ AU, respectively.

As the nature of the compact object is unknown, the VHE $\gamma$-ray emission can be explained in either a *pulsar scenario* or a *microquasar scenario*. For more details on the theoretical background, the reader is referred to Section 4.3.3. In the *pulsar scenario* electrons are thought to be accelerated either in the vicinity of the pulsar or in the termination shock of the colliding winds of the pulsar and the stellar wind. The relativistic electrons and positrons emit $\gamma$-rays by inverse Compton scattering photons from the stellar photon field. The surface brightness of an O5III star is typically $\sim 5 \times 10^5 L_\odot$ which translates into an energy density of $\approx 2600\,\text{erg}\,\text{cm}^{-3}$ - $\approx 80\,\text{erg}\,\text{cm}^{-3}$ for the highly eccentric orbit with variations between $0.1 - 0.5$ AU. To calculate the total energy in electrons and positrons that would be required to explain the observed on-peak $\gamma$-ray emission of $L_{\text{on-peak}} = 4.5 \pm 1.7 \times 10^{35}\,\text{erg}\,\text{s}^{-1}$, the following assumptions on the physical properties of the binary system are made: i) a nominal mass of the companion of $40 M_\odot$ [339] and ii) a moderate eccentricity of $\varepsilon = 0.4$ which translates into a semimajor axis of $0.32$ AU. Thus, the photon field energy density at $0.32$ AU is $235\,\text{erg}\,\text{s}^{-3}$. The equipartition magnetic field required for this photon field energy density is $B_{\text{eq}} \sim 70$ G. In such magnetic fields, cooling of the parent electron population via synchrotron emission is negligible and it can be assumed that most of the energy is converted into $\gamma$ rays via inverse Compton emission. The inverse Compton scattering of the stellar photons is assumed to take place in the Klein-Nishina regime, where the cooling time for an electron can be estimated following Khangulyan et al. [340]

$$t_{\text{KN}} = 1.7 \times \left(\frac{u_\star}{100\,\text{erg}\,\text{cm}^{-3}}\right)^{-1} \left(\frac{E_e}{1\,\text{TeV}}\right)^{0.7} \text{s}. \tag{6.1}$$

The cooling time for an electron with an energy of $1$ TeV is of the order $10^2$ s [340], which is significantly smaller than the escape time and hence the system is assumed to be in steady state. In that case, the injection power into the electrons can be assumed to be equal to the power lost via inverse Compton photon emission. Thus, the source accelerates a population of electrons at a rate of $\sim 10^{36}\,\text{erg}\,\text{s}^{-1}$ in the energy range of $0.5 - 50$ TeV[4] with an injection index of $\Gamma_{\text{e}} = 2.9$. The total energy content of the steady-state electron population is $\sim 10^{38}$ erg. A higher eccentricity of $\varepsilon = 0.7$ would reduce the total energy by a factor of ten due to smaller distances between the two objects and hence higher photon field energy densities. As the electron cooling is dominated by inverse Compton scattering in the Klein-Nishina regime, the steady state electron spectrum in the system steepens to an index of $\Gamma_{\text{e}} \approx 2.2$. The subsequent photon spectrum observed by H.E.S.S. has an index of $\Gamma_{\text{ph}} = 2.9$, as in the Klein-Nishina regime in the steady state the photons have the same index as the injected electrons. However, the

---

[4] Here, the energy range covers two orders of magnitude, which means that the power in electrons is double the power in photons.

pulsar's spin-down power is constrained by the accelerated rate of electrons and needs to be $\dot{E} \gtrsim 10^{36}\,\mathrm{erg\,s^{-1}}$ in order to provide the energy for the observed VHE $\gamma$-ray emission alone.

In the *microquasar scenario*, in which particles are assumed to be accelerated in a jet launched through the accretion of stellar wind material onto the compact object, energy stored in the gravitational potential is channeled through accelerated particles into non-thermal radiation. The compact object can be either a black hole or a neutron star. Assuming a neutron star as the compact object gives a lower limit on the accretion luminosity that can be reached by the system. The accretion luminosity of a neutron star can be estimated via:

$$L_{\mathrm{acc}} = \frac{GM_{\mathrm{co}}\dot{M}_{\mathrm{acc}}}{R_{\mathrm{co}}} \quad = \quad \left(\frac{M_{\mathrm{co}}}{1.4M_{\odot}}\right)\left(\frac{\dot{M}_{\mathrm{acc}}}{10^{-10}M_{\odot}yr^{-1}}\right)\left(\frac{10\,\mathrm{km}}{R_{\mathrm{co}}}\right)\times 1.2\times 10^{36}\,\mathrm{erg\,s^{-1}}, \tag{6.2}$$

where $M_{\mathrm{co}}$ and $R_{\mathrm{co}}$ are the mass and radius of the compact object and $\dot{M}_{\mathrm{acc}}$ is the mass accretion rate [341]. As the accretion rate is mostly unknown, the equation can be rewritten to depend on the stellar mass-loss rate. A stellar wind particle is captured when its kinetic energy is lower than the potential energy of the compact object resulting in an accretion disc with radius $r_{\mathrm{acc}} = \frac{2GM_{\mathrm{co}}}{v_{\mathrm{w}}^2}$ surrounding the compact object. Setting the mass accretion rate of material in a disc in relation to the mass-loss rate of material ejected in a sphere:

$$\frac{\dot{M}_{\mathrm{acc}}}{\dot{M}_{\mathrm{loss}}} = \frac{\pi r_{\mathrm{acc}}^2}{4\pi a^2} = \frac{G^2M_{\mathrm{co}}^2}{a^2v_{\mathrm{w}}^4} \tag{6.3}$$

and inserting Equation 6.3 in Equation 6.2 yields:

$$L_{\mathrm{acc}} = \left(\frac{\dot{M}_{\mathrm{loss}}}{10^{-6}M_{\odot}yr^{-1}}\right)\left(\frac{0.32\,\mathrm{AU}}{a}\right)^2\left(\frac{1000\,\mathrm{km\,s^{-1}}}{v_{\mathrm{w}}}\right)^4 \tag{6.4}$$

$$\times\left(\frac{M_{\mathrm{co}}}{1.4M_{\odot}}\right)^3\left(\frac{10\,\mathrm{km}}{R_{\mathrm{co}}}\right)\times 1.8\times 10^{36}\,\mathrm{erg\,s^{-1}}. \tag{6.5}$$

Typical values for the mass-loss rate [342] and the minimum wind velocity necessary to escape the potential energy of the star are used in Equation 6.5. The high $\gamma$-ray luminosity of LMC P3 can only be produced if the binary system exhibits extreme physical parameters. High wind velocities, high mass-loss rates, a highly eccentric orbit and/or a conversion efficiency from the spin-down power through accelerated particles into non-thermal radiation close to unity are necessary to provide the accretion luminosity that would be required to explain the observed $\gamma$-ray emission within the *microquasar scenario*.

Furthermore, the orbital modulation shows that the peak of the VHE $\gamma$-ray emission is shifted with respect to the maximum of the HE $\gamma$-ray emission by one-fifth of the orbital period. The orbital modulation may be explained by $\gamma$-$\gamma$ absorption, anisotropic inverse Compton scattering and/or the eccentricity of the orbit. More details are given in Section 4.3.3. A combination of all three mechanisms can naturally explain the shift between the peak luminosities of the HE and VHE emission. Inverse Compton scattering is most efficient at superior conjunction, where collisions occur head-on, and least efficient at inferior conjunction, where only tail-on collisions are seen by the observer. Whereas the HE emission is mostly unaffected by $\gamma$-$\gamma$ absorption, pair creation with the stellar photon field leads to a shift of the emission in the VHE regime as the $\gamma$-$\gamma$ absorption is strongest at superior conjunction and lowest at inferior conjunction. Hence, superior conjunction would be at phase $0.0$ and inferior conjunction would be between phases $0.2$ and $0.4$. Furthermore, the eccentricity of the orbit may also explain the orbital modulation. To explain a VHE $\gamma$-ray modulation by a factor of $> 2.5$, corresponding to the ratio between the on-peak luminosity and the off-peak upper limit, the binary separation must vary by a factor of $> 1.6$, what would result in a lower limit on the eccentricity of $\varepsilon > 0.23$, which was indeed confirmed in a recent study [343]. Finally, the HE and VHE $\gamma$-ray emission may also arise from two different particle populations being accelerated at two different sites. Whereas the HE emission may be accelerated in the apex of the contact discontinuity between the stellar wind and the pulsar wind, the VHE component may originate from the termination shock on the opposite side [254]. Together with the geometry of the system, the phase-shift of the HE and VHE $\gamma$-ray lightcurves could be explained in this way.

LMC P3 is the most powerful $\gamma$-ray binary detected so far. With the sensitivity of current IACTs and the study of the Magellanic Clouds presented in this work the existence of similarly luminous $\gamma$-ray binaries in the LMC or SMC can be ruled out. Why there is no detection of a similarly luminous $\gamma$-ray binary in the Milky Way can have several reasons. One possibility might be that due to the orbital modulation of their $\gamma$-ray emission, they simply have not yet been identified as the orbit averaged flux may be significantly lower. They may also be hidden behind the Galactic plane. Lastly, the very luminous $\gamma$-ray binaries in the Milky Way may have evolved to HMXBs already or may simply not exist in our current time window due to the lower star formation rate in the past millions of years compared to the Magellanic Clouds.

However, more (and more accurate) measurements of orbital periods as well as better and more homogeneous coverage over the orbital period will lead to an improved phase resolution and thus may help to improve the current understanding of the particle acceleration mechanisms and the orbital modulations. In addition, a better sensitivity of the IACTs may help to increase the population of $\gamma$-ray binaries and hence may answer the question of whether there are common similarities among all $\gamma$-ray binaries or whether they are indeed all objects that need individual examination.

The results of this study were published in a paper[5] [100].

---

[5] Numbers may differ between the results that are published here and in the publication as a different software framework was used for the analysis of the published results.

### 6.6.2 The Young Supernova SN 1987A

Supernova SN 1987A, located in the LMC, was discovered on February 23, 1987. Being the first "naked-eye" supernova since 1604 (Kepler supernova) and thus offering the possibility to study the early evolutionary phase of a supernova producing a SNR, its thermal and non-thermal spectra have been intensively studied over a broad range of wavelengths from radio to $\gamma$ rays. The birth of the supernova was marked by a burst of neutrinos [344, 345], signifying the formation of a neutron star, followed by a rapid luminosity increase at optical wavelengths a few hours later [346, 347]. The multiwavelength observations indicate that SN 1987A resulted from an atypical type II-P supernova event in a complex circumstellar medium (for a review see [348, 349]). The interaction of the shock wave with the circumstellar medium results in an increase of hard X-ray and radio emission. Whereas the X-ray emission seems to have a mainly thermal origin, the detection of non-thermal radio emission confirmed the existence of electrons being accelerated and emitting photons via synchrotron radiation. Recently, a hint for an increase in X-ray and GeV flux was found [350, 351], which would confirm that cosmic-ray particles are accelerated to up to $\sim$ TeV energies. However, the authors argue that the flux increase may be due to a systematic bias (X rays) or that source confusion may play a role (GeV $\gamma$ rays).
Based on the detection of non-thermal radio emission, hydrodynamic models have been proposed suggesting efficient cosmic-ray proton acceleration at the shock front of SN 1987A which would result in VHE $\gamma$-ray emission from $\pi^0$ decay. Depending on the assumptions for the properties of the circumstellar medium the predicted flux above $1$ TeV ranges between $\sim 2.5\times10^{-13}$ cm$^{-2}$ s$^{-1}$ (in the year 2010) [352] and $\sim 8\times10^{-14}$ cm$^{-2}$ s$^{-1}$ (in 2013) [353]. Observations taken by H.E.S.S. between 2005 and 2012 resulted in an upper limit on the flux above $1$ TeV of $5\times10^{-14}$ cm$^{-2}$ s$^{-1}$, thus constraining the predicted flux level for both models. A revised model by Berezhko et al., who consider new observational results on the properties of the circumstellar medium as well as a lower mass of the outward moving equatorial ring, led to the prediction of VHE $\gamma$ rays just below the predicted flux upper limit published by H.E.S.S. The predicted maximum of the VHE $\gamma$-ray emission is expected to have occurred in 2015 followed by a gradual decrease with time. On the other hand, Martin et al. propose a two-component model considering a forward and a reverse shock, predicting a continuous increase in the VHE $\gamma$-ray flux that reaches a flux level of $\sim 4\times10^{-14}$ cm$^{-2}$ s$^{-1}$ in the energy range of $1-100$ TeV at an age of 30 years [354]. In October 2017 H.E.S.S. started a monitoring campaign of SN 1987A to test the model predictions. The results for the first two years of the monitoring campaign are presented here.

Between October 2017 and December 2019, $90$ h of observations were performed towards SN 1987A with the full HESS-II array resulting in an exposure of $87$ h. In addition, $\sim 55$ h of CT1-5 observation were taken in conjunction with the LMC survey and observations towards the Tarantula nebula between 2013 and 2016, which are also included in the analysed data that is presented here. Due to problems with the CT5 camera, roughly 40% of the runs taken with the CT5 camera do not pass the selection criteria reducing the available CT1-5 time by roughly 40%. To achieve a better sensitivity in the analysis, only data taken by CT1-4 are taken into account, resulting in an increased energy threshold in the analysis. A dedicated analysis of SN 1987A is performed by applying the *reflected region background model*. The template based $\gamma$-ray reconstruction framework is used and standard cuts are applied in the analysis. The energy threshold is defined by the minimum energy at which the energy bias is less than 10%. For a better comparison of the results with the previously published integral flux upper limit by the H.E.S.S. collaboration in 2015, the data set that was taken between 2004 and 2012 was also reanalysed with the same analysis settings that were described before. The data set of the SN 1987A monitoring campaign is also split into three sub data sets to probe the existence of a temporal flux increase.

No significant VHE $\gamma$-ray emission between 2013 and 2019 is found from the young SNR SN 1987A and upper limits on the flux in the energy range of $1-100$ TeV are derived. The results are summarised in Table 6.2. The slight increase in significance in the 2004 - 2012 as well as 2013 - 2019 data sets is most likely caused by spillover from the extremely bright PWN N 157B that becomes increasingly significant with increasing exposure. In addition, no significant increase in the integral luminosity between 2017 and 2019 is found. The higher significance and hence the higher integral flux upper limit in 2019 are likely caused by the reduced exposure. However, the results are still consistent with the results of the other data sets within the statistical uncertainties. Figure 6.8 compares the luminosity upper limits to the model predictions by Berezhko et al. and Martin et al. [352, 354]. The luminosity upper limit[6] that was published by the H.E.S.S. collaboration in 2015 is also shown. Due to the use of different analysis frameworks for the analysis presented here and the one presented by the H.E.S.S. collaboration in 2015, the probed sensitivity level is slightly better for the published flux upper limits than the results presented here. Both model predictions are well in agreement with the luminosity upper limits derived from the H.E.S.S. observations.

To probe the validity of both model predictions, either a detection of SN 1987A in VHE $\gamma$ rays or a better instrument sensitivity are required. On the one hand, a detection of SN 1987A would mean that a revision of both models is needed. On the other hand, observations with the next generation of IACTs with an improved sensitivity of roughly one order of magnitude may help to distinguish between both models. Whereas a detection of SN 1987A with a luminosity of $\sim 10^{35}$ erg s$^{-1}$ could favour the model by Martin et al., a non-detection and hence an upper limit of $\lesssim 10^{35}$ erg s$^{-1}$ would favour the model by Berezhko et al.

---

[6] Due to a mistake in the conversion of the integral flux upper limit into an integral luminosity upper limit, the published luminosity was too constraining. The correct value should be $1 \times 10^{35}$ erg s$^{-1}$.

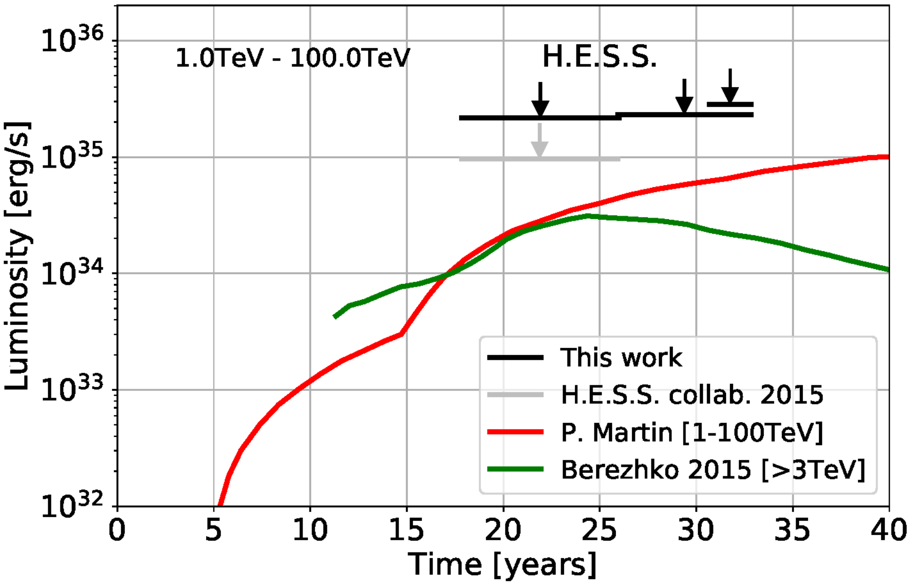

Figure 6.8: H.E.S.S. integral luminosity upper limits for SN 1987A. The luminosity upper limits are estimated in the energy range of $1 - 100$ TeV for different time periods as described in the text. The results are compared to two different model predictions for the expected VHE $\gamma$-ray emission from SN 1987A by Martin et al. (red curve) [354] and Berezhko et al. (green curve) [355].

Table 6.2: Significances and flux upper limits for the different data sets of SN 1987A.

| Period | livetime [h] | significance [$\sigma$] | $\mathrm{UL_F}$ [$10^{-10}\,\mathrm{m^{-2}\,s^{-1}}$] | $\mathrm{UL_L}$ [$10^{35}\,\mathrm{erg\,s^{-1}}$] |
|---|---|---|---|---|
| 2004 - 2012 | 209 | 3.5 | 11.21 | 2.16 |
| 2013 - 2019 | 143 | 2.6 | 11.98 | 2.31 |
| 2017 - 2019 | 87 | 2.0 | 14.60 | 2.82 |
| Oct ’17 - Apr ’18 | 42 | 0.68 | 15.65 | 3.02 |
| Sep ’18 - Dec ’18 | 24 | 0.74 | 15.72 | 3.03 |
| Aug ’19 - Dec ’19 | 21 | 2.37 | 28.78 | 5.55 |

### 6.6.3 The Exceptionally Powerful PWN N 157B

The LMC PWN N 157B is the first (and so far only) Extragalactic PWN detected in VHE $\gamma$ rays [356]. It has a pulsar spin-down power of $\dot{E} = 4.9 \times 10^{38}$ erg s$^{-1}$ and a spin period of $P = 16$ ms, comparable to those of the Crab nebula ($\dot{E} = 4.5 \times 10^{38}$ erg s$^{-1}$, $P = 33$ ms), making the two PWNe appear as twins [186]. However, their observed emission spectra are quite different. Whereas the differential non-thermal X-ray luminosities of N 157B are roughly one order of magnitude lower than those of the Crab nebula, the differential VHE $\gamma$-ray luminosity has been measured to be one order of magnitude higher [23, 45, 357]. The X-ray and $\gamma$-ray luminosities of N 157B are at a comparable level, while the X-ray luminosity of the Crab nebula is two orders of magnitude higher. These differences can hardly be explained by the marginal differences of the source properties. As PWNe are assumed to be leptonic accelerators producing non-thermal emission via synchrotron radiation and inverse Compton scattering, the level of the non-thermal emission mainly depends on environmental properties like the strengths of the magnetic field and the ambient photon field (see Section 4.3.2). Thus, the difference in the ratio of X-ray to $\gamma$-ray luminosities between the two PWNe may be explained by a combination of a weaker magnetic field of $\lesssim 45\mu\mathrm{G}$ for PWN N 157B compared to the Crab nebula ($\sim 124\mu\mathrm{G}$ [358]), which reduces the synchrotron emission from N 157B, and a strong ambient radiation field that boosts the inverse Compton emission. Several authors suggest that N 157B is associated with the star cluster LH 99 [278, 357, 359], which would naturally provide the necessary strong infrared radiation field, estimated to be $\sim 28$ eV cm$^{-3}$ (see Section 6.2). The H.E.S.S. collaboration used multiwavelength data (X-ray data from Chandra, HE flux upper limits from *Fermi*-LAT and their own results) to infer the properties of the parent electron spectrum. The favoured model to describe the multiwavelength spectrum of N 157B assumes the same injection parameters as for the Crab nebula with a minimum electron energy $E_{\mathrm{min}} = 400$ GeV, a cutoff at $E_{\mathrm{c}} = 3.5$ PeV and an index of $\Gamma_{\mathrm{e}} = 2.35$ and requires a constant injection of 11% of the current spin-down power in a magnetic field of $45\mu\mathrm{G}$ and a radiation field energy density of $\sim 20$ eV cm$^{-3}$ [23]. However, the X-ray flux is better fit when assuming a spectral index of $\Gamma_{\mathrm{e}} = 2.0$, which would require a much lower energy cutoff of $E_{\mathrm{c}} \lesssim 100$ TeV but no change in the magnetic field. Ultimately, the statistics at the highest energies were not sufficient to distinguish between the two models.

Since the publications of the VHE $\gamma$-ray results by the H.E.S.S. collaboration in 2015, further observations have been taken of the PWN N 157B, which are presented here. The total exposure on N 157B is now $235$ h. A dedicated analysis, analogous to the analysis of SN 1987A, leads to a VHE $\gamma$-ray detection at a significance level of $\sigma = 29.$ above an energy threshold of $350$ GeV. The somewhat reduced significance compared to the publication in 2015 is due to the different analysis framework that is used for the analysis presented here. A power law spectrum as well as a power law with exponential cutoff are fit to the data points (see Figure 6.9). The exponentially cutoff power law is preferred with a significance of $\sigma = 3$. The exact fit parameters

Table 6.3: Statistical results and spectral parameter for N 157B.

| | |
|---|---|
| Livetime [h] | 235 |
| Significance [$\sigma$] | 29.1 |
| Photon index $\Gamma$ | $2.2 \pm 0.1$ |
| $F_{1\,\mathrm{TeV}}$ [$10^{-12}\,\mathrm{cm}^{-2}\,\mathrm{s}^{-1}\,\mathrm{TeV}^{-1}$] | $0.84 \pm 0.04$ |
| Cutoff $E_c$ [TeV] | $9.1^{+5.1}_{-2.4}$ |
| $L_\gamma$ ($1-100$ TeV) [$10^{35}$ erg $\mathrm{s}^{-1}$] | 5.59 |

are summarised in Table 6.3. The exponential cutoff is found to be at $E_c = 9.1^{+5.1}_{-2.4}$ TeV. This result is well in agreement with the alternative model described by the H.E.S.S. collaboration, which requires a cutoff in the electron injection spectrum at $E_c \lesssim 100$ TeV, revealing an intrinsic difference in the parent electron spectra between the Crab nebula and N 157B.

To get a better estimate on the total energy in electrons and their spectral energy distribution, improved measurements of the ambient magnetic field are required to fix the ambient radiation field energy density and hence the maximum energy in electrons. In addition, position resolved X-ray observations may help to understand the magnetic field morphology as well as cosmic-ray transport in the vicinity of PWNe.

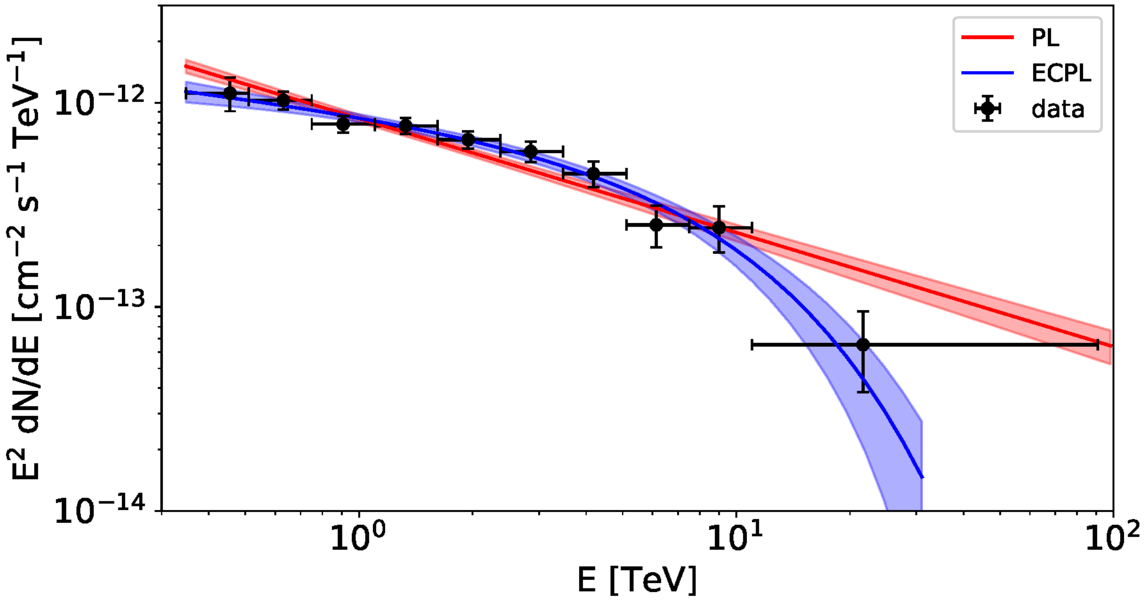

Figure 6.9: Spectrum of N 157B. The results for a fit with a power law (red) and a power law with exponential cutoff (blue) are shown. The exponentially cutoff power law is preferred with a significance of $3\sigma$.

### 6.6.4 N 158A — the Twin of N 157B

N 158A is located in the LMC and seems to be another "sibling" of the Crab nebula and N 157B. The PWN has a spin-down power of $\dot{E} = 1.5 \times 10^{38}$ erg s$^{-1}$, a spin period of $P = 50$ ms and an age of $1600$ yr [186] and is powered by the first pulsar that was detected in $\gamma$ rays outside the Milky Way, PSR J0540-6919 [360]. As it is a factor of $\sim 2$ brighter than the Crab nebula, even the ratio of its X-ray luminosity to $\gamma$-ray luminosity is comparable for the two PWNe (PSR J0540-6919: $L_X/L_\gamma \sim 1$ vs Crab: $L_X/L_\gamma \sim 5$; all others: $L_X/L_\gamma \sim 10^{-3} - 10^{-4}$) [360, 361]. Though the pulsar PSR J0540-6919 is only detected up to $\sim 10$ GeV and no $\gamma$-ray emission from an associated PWN has been detected so far, Martin et al. predicted a possible detection at up to $\sim$TeV energies within an observation time of $50$ h due to a high far infrared energy field density of $5$ eV cm$^{-3}$ [277] ($6$ eV cm$^{-3}$ in this work). However, the H.E.S.S. collaboration did not detect significant VHE $\gamma$-ray emission and published an upper limit on the flux in 2015 [23]. In Addition, the analysis presented in this work did not show any significant VHE $\gamma$-ray emission for an exposure of $\sim 190$ h for either the pulsar or the PWN. An integral flux upper limit is estimated to be $\mathrm{F}_{1-100\,\mathrm{TeV}} < 7.8 \times 10^{-14}$ cm$^{-2}$ s$^{-1}$, which translates into a luminosity of $\mathrm{L}_{1-100\,TeV} < 1.2 \times 10^{35}$ erg s$^{-1}$. The luminosity upper limit is roughly a factor $5$ below the luminosity of N 157B, and hence N 158A cannot be described as a sibling of N 157B when comparing the $\gamma$-ray spectra. On the other hand, even the Crab nebula would only be barely detectable if it were placed at the distance of the LMC. Although the three Crab-like PWNe N 158A, N 157B and the Crab nebula are very similar in their intrinsic physical properties and their X-ray luminosities are comparable, their VHE $\gamma$-ray luminosities seems to depend on other factors. A possible explanation is that the photon field energy density is in fact overestimated. The photon field energy density may not be associated with the PWN due to the line-of-sight depth of a few kpc of the LMC. A significantly lower infrared photon field energy density and hence a significantly reduced amount of target material for the inverse Compton scattering that would lead to the VHE $\gamma$-ray emission, could explain the nondetection in the VHE $\gamma$-ray regime. Another possible explanation may be the strength of the magnetic field. High magnetic fields in N 158A, exceeding those of the Crab nebula, would lead to large synchrotron losses in the magnetic field and hence the inverse Compton scattering may result in a VHE $\gamma$-ray flux below the sensitivity of the H.E.S.S. experiment.

### 6.6.5 The SMC SNR B0102-7219

B0102-7219, also known as 1E 0102.2-7219, is the brightest X-ray SNR in the SMC, being $\sim$ ten times brighter than all other SNRs in the SMC [362]. It is often compared to the LMC SNR N 132D as both are oxygen-rich, middle-aged (kinematic age between $1000$ and $3000$ yr) SNRs surrounded by a denser environment compared to other SNRs in the Magellanic Clouds

[302, 363–370], thus being also similar to the Milky Way SNR Cas A. For both SNRs in the Magellanic Clouds, a type Ib supernova event is thought to be the progenitor [363], although a more recent study favours a type IIb supernova event for B0102-7219 [371]. However, after the detection of the LMC SNR N 132D in HE [69] and VHE [23] $\gamma$ rays, a detection of the SMC SNR B0102-7219 seemed to be in reach with the current generation of IACTs. However, the results presented in this work revealed no significant VHE $\gamma$-ray emission from B0102-7219. One reason may be the significantly lower H.E.S.S. exposure of the SMC SNR ($\sim 40$ h) than the LMC SNR ($\sim 150$ h). N 132D in the LMC was only detected with a low significance by the H.E.S.S. collaboration in 2015 [23] and is not detected at all within the population study presented here with an exposure of $\sim 170$ h. The reason is again the different sensitivities of the analyses that were applied to the published data set and the one used in this work. The lower exposure combined with the larger distance of the SMC makes a detection of B0102-7219 unlikely. Furthermore, the ambient density seems to be higher in the case of N 132D [302, 370], for which there is evidence for an interaction of the progenitor star wind of N 132D with dense molecular clouds in the surrounding ISM [372]. The H.E.S.S. collaboration considers a hadronic cosmic-ray acceleration scenario for N 132D as more likely than a leptonic acceleration scenario. The high ISM densities that are required for a high $\gamma$-ray flux through hadronic interactions is thus naturally provided by these molecular clouds. In the case of a predominantly leptonic acceleration scenario, in which the $\gamma$-ray flux would be mainly caused by inverse Compton scattering of low energy photons, a high RED and a moderate ambient magnetic field (which is required to be $\sim 20\,\mu\mathrm{G}$ for N 132D) are required. The RED is estimated to be compatible for both SNRs ($\sim 1-2$ eV cm$^{-3}$, this work), while the magnetic field strength is unknown for both SNRs. Thus, the difference in the sensitivity reached due to the lower exposure towards the SMC SNR B0102-7219 might be a more plausible explanation. However, an intrinsic difference between the SNRs, such as the efficiency of converting kinetic energy into energy of cosmic rays, cannot be ruled out.

A deeper exposure of B0102-7219 with the H.E.S.S. experiment or observations with the next generation of IACTs would be required to increase the $\gamma$-ray statistics and hence to better compare the two SNRs B0102-7219 and N 132D. In addition, in order to be able to distinguish between the hadronic and leptonic acceleration scenarios, improved measurements of the non-thermal spectrum in X rays would be required to confirm or disprove a substantial synchrotron component in X rays, which would be visible in a predominantly leptonic scenario. Finally, the measurement of the magnetic field strength around both SNRs would help to better understand the acceleration mechanisms in the two sources.

### 6.6.6 IKT 16 — the Most Powerful PWN in the SMC

IKT 16 is one of two composite SNRs in the SMC with a confirmed PWN in its centre [288, 373]. The compact object is suggested to be a pulsar with a spin period of $P \sim 100$ ms and a spin-down power of $\dot{E} = 10^{37}\,\mathrm{erg\,s^{-1}}$ [288].

The non-thermal X-ray spectrum is described by a power law with index $\Gamma = 2.2$, which is comparable to the X-ray spectral index of $\Gamma = 2.3$ of the LMC PWN N 157B [277]. In contrast, the luminosity of IKT 16 is measured to be $L_{0.5-8\,\mathrm{keV}} = 1.2 \times 10^{34} (\frac{d}{61\,\mathrm{kpc}})\,\mathrm{erg\,s^{-1}}$ [288], roughly two orders of magnitude lower than the luminosity measured for N 157B [357]. However, the X-ray luminosity is comparable to the X-ray luminosity of the Milky Way PWN Vela X, which has indeed been detected in VHE $\gamma$ rays [374], suggesting that IKT 16 might also be detectable by H.E.S.S. With an age of $14.7\,\mathrm{kyr}$ it belongs to the middle-aged PWNe. For these objects, models predict a VHE $\gamma$-ray luminosity ranging between $0.1 - 10$ times the X-ray luminosity, depending on the assumptions of the initial parameters of the PWNe (e.g., the spin-down power at the birth of the PWN) and their environment (e.g., the ISM density) [8, 227, 375].

A possible VHE $\gamma$-ray flux that is a factor $5 - 10$ higher than the X-ray flux is discussed by Alsaberi et al. [289]. A luminosity of a few $\times 10^{35}\,\mathrm{erg\,s^{-1}}$ would be detectable with the current generation of IACTs. The nondetection of significant VHE $\gamma$-ray emission and the resulting luminosity upper limit of $L_{1-100\,\mathrm{TeV}} \lesssim 2 \times 10^{35}\,\mathrm{erg\,s^{-1}}$ suggest that either the VHE $\gamma$-ray luminosity is less than a factor of $\sim 10$ higher due to a lower conversion efficiency from kinetic energy in electron into VHE $\gamma$ rays or the ambient radiation field energy densities are too low, thus resulting in a VHE $\gamma$-ray flux below the sensitivity of the current generation of IACTs.

# Chapter 7

# Summary and Outlook

The increasing number and diversity of Galactic and Extragalactic VHE $\gamma$-ray sources discovered since the beginning of this century demonstrates the universality of particle acceleration to multi-TeV energies in various astrophysical environments. $\gamma$-ray astronomy started the transition from discovering new, individual objects to conducting surveys that lay the foundation for population studies in the VHE $\gamma$-ray regime. While the study of individual objects reveals information about particle acceleration mechanisms and the interplay between the relativistic cosmic rays and the environment of the source, population studies allow for a systematic study of the different source classes and deliver information about their nature and evolution. Source population studies based on the HGPS have already led to new insights into the Galactic source population and revealed the importance of the environment for the measured $\gamma$-ray emission. To find out if the VHE $\gamma$-ray source population as well as particle acceleration and interaction mechanisms in the Milky Way are unique in the universe, observations of other galaxies such as the Magellanic Clouds, the only galaxies for which individual sources can be resolved with current generation of IACTs, are required.

In this thesis the analysis of the H.E.S.S. surveys of the Magellanic Clouds is presented. The survey data sets for both galaxies are analysed in a systematic way by taking the instrument, analysis and data set dependent systematic uncertainties into account to ensure an unbiased flux estimation of the potential VHE $\gamma$-ray sources of the Magellanic Clouds. The search for point-like $\gamma$-ray emission led to the detection of the exceptionally powerful $\gamma$-ray binary LMC P3. The $\gamma$-ray flux is modulated with the orbital period of the system and reaches an on-peak luminosity of $4.5 \pm 1.7 \times 10^{35}$ erg s$^{-1}$, which is two orders of magnitude more luminous than the luminosity of known $\gamma$-ray binaries in the Milky Way. The emission can either be explained by the *pulsar scenario*, in which the pulsar's spin-down power is estimated to be $\dot{E} \gtrsim 10^{36}$ erg s$^{-1}$, or in the *microquasar scenario*, in which high wind velocities, high mass-loss rates, a highly eccentric orbit and / or a conversion efficiency from the spin-down power through accelerated particles into non-thermal radiation close to unity are necessary to provide the accretion luminosity that would be required to explain the observed $\gamma$-ray emission. The larger data set led to an increased event statistics for the PWN N 157B and allowed for an improved reconstruction of the spectrum revealing a cutoff at $E_c \approx 9$ TeV. This result is consistent with the modelled electron spectrum from the H.E.S.S. collaboration which predicts a cutoff in the electron spectrum at $\lesssim 100$ TeV [23] and thus reveals an intrinsic difference in the parent electron spectra between the Crab nebula and N 157B. Finally, the new observations taken of the young supernova remnant SN 1987A allowed for the probing of acceleration timescales of $30$ yr after the supernova explosion. The analysis revealed that a potential VHE $\gamma$-ray emission of SN 1987A is still below the sensitivity threshold of the current generation of IACTs. The estimated integral flux upper limits are about one order of magnitude above the luminosity predicted by Berezhko et al. [352] and Martin et al. [354]. Continuous monitoring (with a better instrumental sensitivity as provided by the next generation of IACTs) of SN 1987A is required to probe even longer acceleration timescales and to possibly differentiate between the two model predictions.

No further significant VHE $\gamma$-ray emission was found in the LMC and SMC data and integral flux upper limits are estimated for the entire data sets. Based on non-thermal radio and X-ray catalogues of individual sources in the Magellanic Clouds, a H.E.S.S. source candidate catalogue of potential VHE $\gamma$-ray sources is generated for both galaxies, which is used for a comparison of the source populations between the LMC, SMC and the Milky Way.

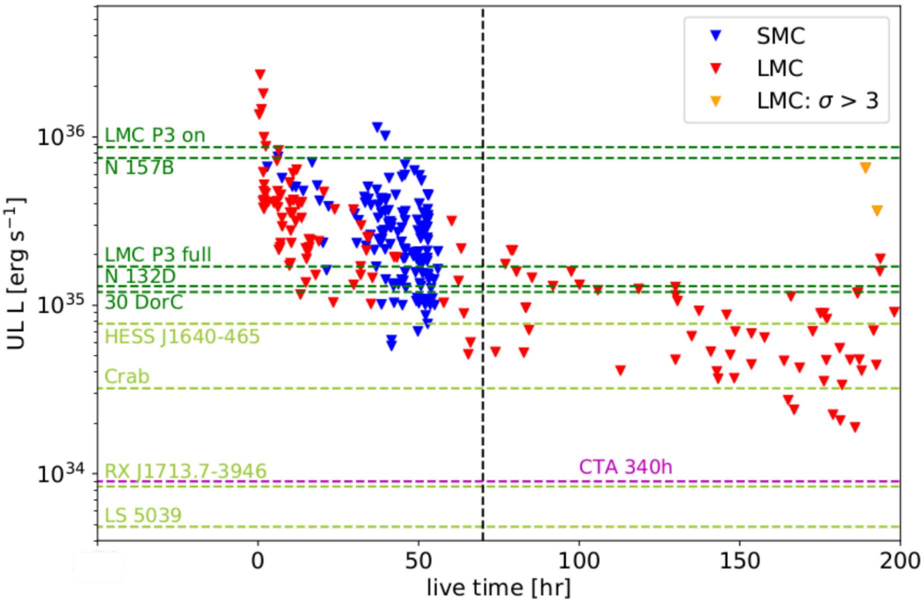

Figure 7.1: Integral luminosity upper limits as a function of acceptance corrected lifetime. The luminosities of known sources in the LMC and the Milky Way are denoted by dark and light green dashed lines, respectively. The integrated sensitivity for an exposure of $340$ h towards the LMC with CTA is shown with a magenta dashed line [376].

The comparison of the source populations of the Magellanic Clouds and the Milky Way have revealed that no other source in the Magellanic Clouds is as bright as the most powerful VHE $\gamma$-ray source known so far: the PWN N 157B, and that one-third of the source population of the Magellanic Clouds is less luminous than the other three known sources in the LMC ($L \sim 10^{35}$ erg s$^{-1}$), i.e. the SNR N 132D, the $\gamma$-ray binary LMC P3 (full-orbit luminosity) and the superbubble 30 DorC, as is shown in Figure 7.1. Thus, only 30% of the source population of the Magellanic Clouds can be probed in an unbiased way. A couple of sources are are shown to be even less luminous than the Milky Way sources HESS J1640-465 and the Crab nebula.

The reasons for the non-detections can be manyfold including the limitation of the sensitivity of the H.E.S.S. telescopes, intrinsic differences in the physical properties of the source populations of the LMC, SMC and Milky Way or differences in the different environments of all three galaxies. In general, the source populations of the Magellanic Clouds seem to be older compared to the populations of the Milky Way. Most of the binaries have already transitioned from the $\gamma$-ray phase to the HMXB phase, in which VHE $\gamma$-ray emission has not yet been observed for any of the sources, yet. The few binaries that may still be in the $\gamma$-ray phase either seem to have less extreme orbital and stellar parameters or are located in a less dense environment. The SNR population is in general older than $10^4$ yr and thus is more comparable to the old Milky Way SNRs W 28 and W 51C for which the VHE $\gamma$-ray emission is most likely caused by interactions of relativistic protons with nearby molecular clouds. As there seems to be only little spatial correlation between molecular clouds and SNRs in the LMC [313], the luminosities measured for the two Milky Way SNRs are more than one order of magnitude lower than can be constrained by the luminosity upper limits of the Magellanic Clouds SNRs and a cutoff in the $\gamma$-ray spectrum is expected at $\lesssim 1$ TeV; therefore, a detection for most of the Magellanic Cloud SNRs in VHE $\gamma$ rays is unlikely. However, both Magellanic Clouds host a couple of young SNRs like B0102-7219 in the SMC, which is often compared to the oxygen-rich LMC SNR N 132D and N 103B, which has similar properties to Kepler's SNR, B0536-6913 or B0540-693, the SNR around the most powerful X-ray pulsar, in the LMC. For B0536-6913 and B0540-693 the RED is estimated to be $9.2$ eV cm$^{-3}$ and $6.4$ eV cm$^{-3}$ (this work), respectively, indicating that they may be interesting candidates for observations with the next generation of IACTs. In Addition, the two older SNRs DEM L249 and DEM L238 with ages of $15000$ yr and $13500$ yr, respectively, may be interesting candidates for future observations as their environments are measured to be denser compared to the environments of other SNRs in the LMC [377]. In the case of the Magellanic Cloud PWNe either the spin-down power seems to be too low to produce VHE $\gamma$-ray emission at a level that is detectable with the current generation of IACTs or the RED is too low for efficient radiative energy losses, what makes the PWN N 157B exceptional in the LMC. Finally, the isolated pulsars are apparently too old to produce VHE $\gamma$-ray emission at a detectable level for H.E.S.S.

As shown in Figure 7.1 the luminosity level that can be constrained decreases with increasing exposure of the sources. For $\sim$80% of the LMC sources with a H.E.S.S. exposure of $\gtrsim 70$ h the luminosity level of all known VHE $\gamma$-ray sources in the LMC can be constrained. Thus, a homogeneous exposure of $\gtrsim 70$ h over the entire LMC and SMC would be required to detect (all) sources in the Magellanic Clouds with luminosities of $L \gtrsim 10^{35}$ erg s$^{-1}$. For the SMC another $\sim 100$ h of H.E.S.S. observations would need to be taken, which is realisable given the observation window for the SMC of $\sim 100$ h per year and an anticipated end of H.E.S.S. in three years. However, the dependence of the luminosity on the exposure seems to be less distinct than for the LMC and hence it is uncertain whether the sensitivity of H.E.S.S. is sufficient to significantly decrease the luminosity level that can be constrained by the SMC data set. In the case of the LMC another $400 - 500$ h of H.E.S.S. observations would be required, which is not realisable considering the anticipated end of H.E.S.S. A realistic possibility could be to observe selected, promising sources in the Magellanic Clouds that have a low exposure in the currently available data sets. Candidate sources may be the SMC PWN IKT 16 ($25$ h), the SNR B0102-7219 ($35$ h) or the HMXB SMC X-1 (HMXB 1, $50$ h) or the LMC HMXBs LMC X-4 (2A0532-664, $60$ h) or RX J0532.5-6551, $60$ h), which are young and have an O-type or B-type companion, and the LMC SNR N 103B ($30$ h).

Also indicated in Figure 7.1 is the integrated luminosity above $1$ TeV which can be constrained by the next generation of IACT arrays, the Cherenkov Telescope Array (CTA), after an exposure of $340$ h towards the LMC [376]. An improvement of at least one order of magnitude in integrated luminosity over the H.E.S.S. survey of the Magellanic Clouds will be achieved and hence sources with comparable luminosities to the Milky Way sources like HESS J1640-465, the Crab nebula or RX J1713-3946 will be detected if they exist in the Magellanic Clouds. Deep observations of the LMC are part of the key science projects for CTA [376]. For the SMC on the other hand, no observations with the CTA array are planned so far. To guarantee a mostly unbiased follow-up study of the source populations in the Magellanic Clouds and the Milky Way, an analogous CTA survey of the SMC has to be conducted. Due to an anticipated field-of-view radius of $\sim 4.5^\circ$ and $\sim 4.8^\circ$ for the small-size and mid-size CTA telescopes, respectively, and an extension of the SMC of $\lesssim 5^\circ$, two observation positions towards the SMC with an exposure of $250$ h each would be sufficient for a homogeneous acceptance corrected lifetime comparable to the LMC, though the luminosity level that can be detected will be slightly increased due to the larger distance to the SMC compared to the LMC. The expected number of sources that are expected to be detected can be inferred from the number of detected VHE $\gamma$-ray sources in the Milky Way and the current star formation rate in the Milky Way and SMC. So far, about 30 VHE $\gamma$-ray sources in a volume of roughly 30% of the Milky Way are known. The SMC exhibits a star formation-rate that is roughly 10% of the Milky Way star formation-rate leading to an estimated number of expected sources of 10. This number is most likely a very optimistic estimation given the rather old source population and the low-density environment compared to the Milky Way. The CTA survey of both Magellanic Clouds would thus deliver the great opportunity for an advanced study of the source populations in the Magellanic Clouds through detections of further VHE $\gamma$-ray sources or more constraining luminosity upper limits.

# Appendix A

# Tables for VHE $\gamma$-Ray Source Candidates

This appendix includes all tables for the H.E.S.S. source candidate catalogues of potential VHE $\gamma$-ray sources in the Magellanic Clouds that are described in Chapter 5 and for which the analysis results for VHE $\gamma$-ray emission are discussed in Chapter 6.

## A.1 LMC

This section lists the following tables:

Table A.1: Integral flux upper limits for the LMC SNRs in the energy range $1-100$ TeV.
Table A.2: Integral flux upper limits for the LMC PWNe in the energy range $1-100$ TeV.
Table A.3: Integral flux upper limits for the LMC HMXBs in the energy range $1-100$ TeV.
Table A.4: Integral flux upper limits for the LMC pulsars in the energy range $1-100$ TeV.

The tables include the name, the coordinates, other physical properties of the sources that are needed for the discussion of the source populations, the acceptance corrected lifetime and the analysis results: the significance, integral flux upper limits and further upper limits that are derived (for more information see Section 5.2.4).

Table A.1: Integral flux upper limits for the LMC SNRs in the energy range $1-100$ TeV.

| Type | Source Name$^a$ | Reference | RA$^a$ [°] | Dec$^a$ [°] | diameter$^a$ ["] | age$^a$ $10^3$ [yr] | SN type$^a$ | livetime [h] | $\sigma$ | UL$_{\mathrm{F}}$ $10^{-10}$ [m$^{-2}$ s$^{-1}$] | UL$_{\mathrm{EF}}$ $10^{-10}$ [erg m$^{-2}$ s$^{-1}$] | UL$_{\mathrm{L}}$ $10^{35}$ [erg s$^{-1}$] | UL$_{\mathrm{W}}$ $10^{50}$ erg] | UL$_{\mathrm{eff}}$ [%] |
|---|---|---|---|---|---|---|---|---|---|---|---|---|---|---|
| SNR | [HP99] 460 | M16 | 72.092 | -66.998 | 220 | - | - | 2.4 | 0.23 | 57.78 | 298.03 | 8.81 | 35.24 | 352 |
| SNR | J0449-6920 | M16 | 72.333 | -69.339 | 162 | - | - | 2.3 | -0.72 | 30.40 | 156.80 | 4.63 | 18.54 | 185 |
| SNR | B0450-709 | M16 | 72.612 | -70.838 | 340 | - | - | 0.4 | 0.00 | 89.26 | 460.38 | 13.61 | 54.44 | 544 |
| SNR | N4 | M16 | 73.308 | -66.920 | 256 | - | - | 7.0 | -1.33 | 15.36 | 79.24 | 2.34 | 9.37 | 94 |
| SNR | B0453-685 | M16 | 73.408 | -68.491 | 120 | $\sim$13.5 | CC | 11.7 | 0.06 | 20.81 | 107.32 | 3.17 | 12.69 | 127 |
| SNR | N9 | M16 | 73.638 | -67.220 | 216 | - | - | 7.5 | -0.33 | 21.68 | 111.83 | 3.31 | 13.22 | 132 |
| SNR | N11L | M16 | 73.704 | -66.426 | 106 | - | - | 1.6 | 1.50 | 118.80 | 612.73 | 18.11 | 72.45 | 725 |
| SNR | N86 | M16 | 73.904 | -68.646 | 366 | - | - | 12.0 | 2.01 | 41.93 | 216.27 | 6.39 | 25.57 | 256 |
| SNR | N186D | M16 | 74.979 | -70.131 | 114 | - | - | 6.1 | -0.02 | 27.29 | 140.73 | 4.16 | 16.64 | 166 |
| SNR | DEM L71 | M16 | 76.425 | -67.877 | 76 | 4.7 | Ia | 15.5 | -0.32 | 13.66 | 70.43 | 2.08 | 8.33 | 83 |
| SNR | N23 | M16 | 76.479 | -68.030 | 96 | 4.6 | CC | 15.9 | 0.10 | 14.50 | 74.78 | 2.21 | 8.84 | 88 |
| SNR | DEM L72 | M16 | 76.521 | -65.686 | 410 | - | - | 1.9 | -1.46 | 27.69 | 142.84 | 4.22 | 16.89 | 169 |
| SNR | [HP99] 1139 | M16 | 76.708 | -70.431 | 262 | 19.0 | Ia | 4.9 | -0.19 | 26.62 | 137.29 | 4.06 | 16.23 | 162 |
| SNR | [HP99] 791 | M16 | 77.154 | -69.048 | 304 | 22.5 | Ia | 42.4 | 0.59 | 12.68 | 65.41 | 1.93 | 7.73 | 77 |
| SNR | J0508-6830 | M16 | 77.208 | -68.514 | 138 | $\gtrsim$20.0 | Ia | 33.7 | 0.67 | 13.90 | 71.70 | 2.12 | 8.48 | 85 |
| SNR | N103B | M16 | 77.246 | -68.726 | 30 | 0.9 | Ia | 43.2 | 0.64 | 12.64 | 65.20 | 1.93 | 7.71 | 77 |
| SNR | B0509-67.5 | M16 | 77.379 | -67.521 | 32 | 0.4 | Ia | 15.9 | 0.53 | 16.21 | 83.61 | 2.47 | 9.89 | 99 |
| SNR | J0511-6759 | M16 | 77.796 | -67.986 | 112 | $\gtrsim$20.0 | Ia | 35.6 | -0.13 | 9.55 | 49.28 | 1.46 | 5.83 | 58 |
| SNR | [HP99] 483 | M16 | 78.112 | -67.122 | 120 | - | - | 17.9 | -0.81 | 9.94 | 51.27 | 1.52 | 6.06 | 61 |
| SNR | DEM L109 | M16 | 78.308 | -69.206 | 240 | - | - | 82.8 | -1.11 | 3.43 | 17.71 | 0.52 | 2.09 | 21 |
| SNR | J0514-6840 | M16 | 78.567 | -68.673 | 220 | - | - | 84.4 | -0.37 | 4.68 | 24.14 | 0.71 | 2.85 | 29 |
| SNR | J0517-6759 | M16 | 79.283 | -67.991 | 324 | - | - | 57.8 | -0.01 | 6.80 | 35.07 | 1.04 | 4.15 | 41 |

Table A.1: (continued)

| Type | Source Name[a] | Reference | RA[a] [°] | Dec[a] [°] | diameter[a] ["] | age[a] $10^3$ [yr] | SN type[a] | livetime [h] | $\sigma$ | UL$_\mathrm{F}$ $10^{-10}$ [m$^{-2}$ s$^{-1}$] | UL$_\mathrm{EF}$ $10^{-10}$ [erg m$^{-2}$ s$^{-1}$] | UL$_\mathrm{L}$ $10^{35}$ [erg s$^{-1}$] | UL$_\mathrm{W}$ $10^{50}$ erg] | UL$_\mathrm{eff}$ [%] |
|---|---|---|---|---|---|---|---|---|---|---|---|---|---|---|
| SNR | N120 | M16 | 79.671 | -69.653 | 148 | - | - | 105.8 | 0.96 | 8.07 | 41.64 | 1.23 | 4.92 | 49 |
| SNR | B0519-690 | M16 | 79.896 | -69.036 | 34 | 0.6 | Ia | 130.0 | 1.19 | 7.52 | 38.79 | 1.15 | 4.59 | 46 |
| SNR | B0520-694 | M16 | 79.933 | -69.436 | 190 | - | - | 135.0 | -0.13 | 4.30 | 22.17 | 0.66 | 2.62 | 26 |
| SNR | DEM 142 | M16 | 80.412 | -65.719 | 168 | - | - | 1.6 | -0.41 | 40.55 | 209.15 | 6.18 | 24.73 | 247 |
| SNR | N44 | M16 | 80.779 | -67.887 | 255 | - | - | 85.3 | 1.04 | 9.57 | 49.36 | 1.46 | 5.84 | 58 |
| SNR | DEM L175a | M16 | 81.083 | -66.406 | 240 | - | - | 15.1 | -0.53 | 12.40 | 63.96 | 1.89 | 7.56 | 76 |
| SNR | N 132D | M16 | 81.267 | -69.640 | 126 | 3.1 | CC | 169.1 | 3.15 | 12.02 | 62.02 | 1.83 | 7.33 | 73 |
| SNR | N49B | M16 | 81.354 | -65.989 | 170 | 10.0 | CC | 9.8 | -1.62 | 11.31 | 58.32 | 1.72 | 6.90 | 69 |
| SNR | N49 | M16 | 81.500 | -66.082 | 84 | 4.8 | CC | 10.1 | -1.17 | 11.67 | 60.22 | 1.78 | 7.12 | 71 |
| SNR | B0528-692 | M16 | 81.912 | -69.201 | 198 | - | - | 187.2 | -0.51 | 3.12 | 16.09 | 0.48 | 1.90 | 19 |
| SNR | DEM L204 | M16 | 81.975 | -65.827 | 282 | - | - | 9.8 | 0.59 | 35.23 | 181.72 | 5.37 | 21.49 | 215 |
| SNR | B0528-6716 | M16 | 81.983 | -67.228 | 270 | - | - | 63.3 | 1.77 | 14.27 | 73.60 | 2.18 | 8.70 | 87 |
| SNR | [HP99] 1234 | M16 | 81.987 | -71.075 | 369 | 25.0 | Ia | 62.4 | 0.75 | 9.15 | 47.19 | 1.40 | 5.58 | 56 |
| SNR | DEM L205 | M16 | 82.021 | -67.456 | 324 | - | - | 77.0 | 1.49 | 11.53 | 59.49 | 1.76 | 7.03 | 70 |
| SNR | DEM L214 | M16 | 82.463 | -66.891 | 145 | - | - | 23.8 | 1.56 | 24.40 | 125.85 | 3.72 | 14.88 | 149 |
| SNR | DEM L218 | M16 | 82.667 | -70.125 | 325 | - | - | 166.9 | -2.25 | 1.57 | 8.11 | 0.24 | 0.96 | 10 |
| SNR | N206 | M16 | 82.983 | -71.005 | 180 | 25.0 | CC | 83.4 | 0.33 | 6.34 | 32.72 | 0.97 | 3.87 | 39 |
| SNR | B0532-675 | M16 | 83.125 | -67.526 | 285 | - | - | 80.5 | 1.19 | 10.40 | 53.62 | 1.59 | 6.34 | 63 |
| SNR | J0533-7202 | M16 | 83.442 | -72.050 | 205 | - | - | 3.2 | -0.51 | 27.04 | 139.47 | 4.12 | 16.49 | 165 |
| SNR | B0534-699 | M16 | 83.508 | -69.918 | 135 | 10.0 | Ia | 179.0 | -2.32 | 1.47 | 7.59 | 0.22 | 0.90 | 9 |
| SNR | DEM L238 | M16 | 83.575 | -70.557 | 186 | 13.5 | Ia | 137.3 | 0.72 | 6.08 | 31.36 | 0.93 | 3.71 | 37 |
| SNR | SN 1987A | M16 | 83.867 | -69.270 | 2 | 0.0 | CC | 193.8 | 3.73 | 12.40 | 63.96 | 1.89 | 7.56 | 76 |

Table A.1: (continued)

| Type | Source Name[a] | Reference | RA[a] [°] | Dec[a] [°] | diameter[a] ["] | age[a] $10^3$ [yr] | SN type[a] | livetime [h] | $\sigma$ | UL$_\mathrm{F}$ $10^{-10}$ [m$^{-2}$ s$^{-1}$] | UL$_\mathrm{EF}$ $10^{-10}$ [erg m$^{-2}$ s$^{-1}$] | UL$_\mathrm{L}$ $10^{35}$ [erg s$^{-1}$] | UL$_\mathrm{W}$ $10^{50}$ erg] | UL$_\mathrm{eff}$ [%] |
|---|---|---|---|---|---|---|---|---|---|---|---|---|---|---|
| SNR | N63A | M16 | 83.933 | -66.037 | 84 | ∼3.5 | CC | 10.9 | 0.44 | 23.42 | 120.80 | 3.57 | 14.28 | 143 |
| SNR | Honeycomb | M16 | 83.942 | -69.301 | 105 | - | - | 193.6 | 3.06 | 10.45 | 53.88 | 1.59 | 6.37 | 64 |
| SNR | DEM L241 | M16 | 84.013 | -67.577 | 310 | $\gtrsim$10.0 | CC | 78.8 | 1.90 | 13.92 | 71.81 | 2.12 | 8.49 | 85 |
| SNR | DEM L249 | M16 | 84.029 | -70.644 | 200 | 15.0 | Ia | 130.6 | 1.27 | 6.96 | 35.88 | 1.06 | 4.24 | 42 |
| SNR | B0536-6914 | M16 | 84.071 | -69.224 | 66 | ∼3.5 | CC | 192.8 | 7.97 | 23.99 | 123.71 | 3.66 | 14.63 | 146 |
| SNR | DEM L256 | M16 | 84.362 | -66.464 | 227 | - | - | 14.9 | -0.91 | 8.98 | 46.29 | 1.37 | 5.47 | 55 |
| SNR | N 159 | M16 | 84.996 | -69.734 | 92 | - | - | 176.2 | 0.89 | 5.89 | 30.39 | 0.90 | 3.59 | 36 |
| SNR | B0540-693 | M16 | 85.046 | -69.332 | 72 | 1.6 | CC | 186.7 | 1.71 | 7.76 | 40.05 | 1.18 | 4.74 | 47 |
| SNR | [HP99] 456 | M16 | 85.463 | -66.984 | 300 | - | - | 32.1 | 1.49 | 19.58 | 101.00 | 2.99 | 11.94 | 119 |
| SNR | DEM L299 | M16 | 85.783 | -68.972 | 330 | - | - | 172.7 | 0.08 | 4.60 | 23.71 | 0.70 | 2.80 | 28 |
| SNR | DEM L316B | M16 | 86.746 | -69.714 | 190 | - | - | 143.3 | -1.09 | 2.40 | 12.39 | 0.37 | 1.47 | 15 |
| SNR | DEM L316A | M16 | 86.842 | -69.691 | 190 | 27.0 | Ia | 141.0 | -0.57 | 3.48 | 17.96 | 0.53 | 2.12 | 21 |
| SNR | B0548-704 | M16 | 86.954 | -70.415 | 118 | 7.1 | Ia | 91.8 | 0.93 | 8.53 | 44.00 | 1.30 | 5.20 | 52 |
| SNR | J0550-6823 | M16 | 87.625 | -68.378 | 312 | - | - | 73.9 | -1.12 | 3.47 | 17.88 | 0.53 | 2.11 | 21 |

[a] Source name, coordinates, diameter, age and SN type of the SNR are taken from M16: Maggi et al. 2016 [97].

Livetime, significance $\sigma$ and integral flux upper limits UL$_\mathrm{F}$ are extracted from the respective sky maps in the energy range of $1-100$ TeV. Upper limits on the energy flux UL$_\mathrm{EF}$, luminosity UL$_\mathrm{L}$, power UL$_\mathrm{W}$ and efficiency UL$_\mathrm{eff}$ are estimated as described in the text (Section 5.2.4). An explosion energy of $10^{51}$ erg and a number density of the ISM of 1 cm$^{-3}$ are assumed in the estimation of the luminosity upper limit.

Table A.2: Integrated upper limits for the LMC PWNe in the energy range $1 - 100$ TeV.

| Type | Source Name[a] | Reference | RA[a] | Dec[a] | age[a] | P[a] | $\dot{P}^a$ | $\dot{E}^a$ | livetime | $\sigma$ | UL$_\mathrm{F}$ | UL$_\mathrm{EF}$ | UL$_\mathrm{L}$ | UL$_\mathrm{eff}$ |
|---|---|---|---|---|---|---|---|---|---|---|---|---|---|---|
| | | | | | $10^3$ | | $10^{-15}$ | $10^{35}$ | | | $10^{-10}$ | $10^{-10}$ | $10^{35}$ | |
| | | | [°] | [°] | [yr] | [s] | [s s$^{-1}$] | [erg s$^{-1}$] | [h] | | [m$^{-2}$ s$^{-1}$] | [erg m$^{-2}$ s$^{-1}$] | [erg s$^{-1}$] | [%] |
| PWN | N 157B* | HESS15, ATNF | 84.450 | -69.170 | 4.93 | 0.016 | 51.8 | 4880 | 190.18 | 29.13 | 57.29 | 127.32 | 6.10 | 0.13 |
| PWN | N 158A | S04, ATNF | 85.050 | -69.330 | 1.67 | 0.051 | 479.0 | 1460 | 186.63 | 1.71 | 7.76 | 40.05 | 1.18 | 0.08 |
| PWN | B0453-685 | G03 | 73.408 | -68.491 | 13.50 | 100.000 | 250.0 | 100 | 11.73 | 0.06 | 20.81 | 107.32 | 3.17 | 3.17 |
| PWN | N206 | W05 | 82.983 | -71.005 | 25.00 | 0.000 | 0.0 | - | 83.37 | 0.33 | 6.34 | 32.72 | 0.97 | - |

[a] Source name, coordinates, age, period, period derivative and spin-down power are taken from the respective reference: HESS15: Hess Collaboration 2015 [23], ATNF: online version of the ATNF pulsar catalogue [282], S04: Serafimovich et al. 2004 [279], G03: Gaensler et al. 2003 [281], W05: Williams et al. 2005 [280].

Livetime, significance $\sigma$ and flux upper limits UL$_\mathrm{F}$ are extracted from the respective sky maps in the energy range of $1 - 100$ TeV. Upper limits on the energy flux UL$_\mathrm{EF}$, luminosity UL$_\mathrm{L}$ and efficiency UL$_\mathrm{eff}$ are estimated as described in the text (Section 5.2.4).

* The flux measurements are obtained in a dedicated analysis of N 157B. For more details see Section 6.6.3.

Table A.3: Integrated upper limits for the LMC HMXBs in the energy range $1-100$ TeV.

| Type | Source name$^{a}$ | Reference | RA$^{a}$ [°] | Dec$^{a}$ [°] | P$^{a}$ [s] | P$_{\mathrm{orbit}}$$^{a}$ [d] | livetime [h] | $\sigma$ | UL$_{\mathrm{F}}$ $10^{-10}$ [m$^{-2}$ s$^{-1}$] | UL$_{\mathrm{EF}}$ $10^{-10}$ [erg m$^{-2}$ s$^{-1}$] | UL$_{\mathrm{L}}$ $10^{35}$ [erg s$^{-1}$] | UL$_{\mathrm{eff,acc}}$ [%] |
|---|---|---|---|---|---|---|---|---|---|---|---|---|
| HMXB | XMMUJ054134.7-682550 | A16, J18 | 85.395 | -68.431 | 60.77 | 31.500 | 157.71 | 0.04 | 4.22 | 21.79 | 0.64 | 5.4 |
| HMXB | 2A0532-664 | AZ16 | 83.207 | -66.371 | 13.50 | 1.408 | 13.20 | -1.50 | 7.60 | 39.22 | 1.16 | 9.7 |
| HMXB | RXJ0541.5-6833 | AZ16 | 85.405 | -68.542 | - | - | 163.79 | -0.77 | 3.07 | 15.85 | 0.47 | 3.9 |
| HMXB | RXJ0546.8-6851 | AZ16 | 86.701 | -68.863 | - | - | 148.62 | 0.28 | 4.58 | 23.63 | 0.70 | 5.8 |
| HMXB | RXJ0507.6-6847 | A16, J18 | 76.908 | -68.797 | - | 5.270 | 29.78 | -0.23 | 8.69 | 44.83 | 1.33 | 11.0 |
| HMXB | RXJ0532.3-7107 | AZ16 | 83.095 | -71.126 | - | - | 66.16 | -1.05 | 3.95 | 20.36 | 0.60 | 5.0 |
| HMXB | RXJ0541.4-6936 | AZ16 | 85.343 | -69.608 | - | - | 175.13 | 0.74 | 5.89 | 30.38 | 0.90 | 7.5 |
| HMXB | RXJ0524.2-6620 | AZ16 | 81.053 | -66.347 | - | - | 14.89 | -0.34 | 14.29 | 73.73 | 2.18 | 18.2 |
| HMXB | 3A0540-697 | AZ16 | 84.912 | -69.743 | - | 4.229 | 177.09 | 0.71 | 5.44 | 28.05 | 0.83 | 6.9 |
| HMXB | RXJ0529.4-6952 | AZ16 | 82.358 | -69.870 | - | - | 176.93 | -0.61 | 3.10 | 16.00 | 0.47 | 3.9 |
| HMXB | RXJ0535.0-6700 | AZ16 | 83.775 | -67.004 | - | 241.000 | 34.10 | 0.98 | 16.59 | 85.58 | 2.53 | 21.1 |
| HMXB | H0544-665 | AZ16 | 86.065 | -66.564 | - | - | 13.63 | 0.87 | 26.92 | 138.85 | 4.10 | 34.2 |
| HMXB | XMMUJ053115.4-705350 | AZ16 | 82.814 | -70.897 | - | - | 100.12 | 1.07 | 8.69 | 44.81 | 1.32 | 11.0 |
| HMXB | RXJ0523.2-7004 | AZ16 | 80.812 | -70.070 | - | - | 142.85 | -0.89 | 2.66 | 13.70 | 0.41 | 3.4 |
| HMXB | RXJ0516.0-6916 | AZ16 | 79.000 | -69.269 | - | - | 97.54 | 1.44 | 10.41 | 53.71 | 1.59 | 13.2 |
| HMXB | RXJ0520.5-6932 | AZ16 | 80.124 | -69.532 | 8.03 | 24.430 | 147.05 | -0.55 | 3.33 | 17.17 | 0.51 | 4.2 |
| HMXB | 1SAXJ0544.1-7100 | AZ16 | 86.026 | -71.014 | 96.08 | 286.000 | 64.09 | -0.38 | 5.87 | 30.29 | 0.90 | 7.5 |
| HMXB | 1A0535-668 | AZ16 | 83.922 | -66.864 | 0.07 | 16.668 | 31.94 | -0.21 | 11.18 | 57.65 | 1.70 | 14.2 |
| HMXB | RXJ0532.5-6551 | AZ16 | 83.133 | -65.861 | - | - | 10.19 | -0.55 | 18.24 | 94.09 | 2.78 | 23.2 |
| HMXB | RXJ0502.9-6626 | AZ16 | 75.715 | -66.440 | 4.06 | - | 6.86 | -0.97 | 14.51 | 74.85 | 2.21 | 18.4 |
| HMXB | XMMUJ053011.2-655122 | A16, J18 | 82.544 | -65.858 | 271.97 | 74.000 | 9.99 | -0.05 | 23.33 | 120.33 | 3.56 | 29.6 |
| HMXB | RXJ0456.9-6824 | AZ16 | 74.225 | -68.410 | - | - | 12.67 | 0.89 | 26.06 | 134.41 | 3.97 | 33.1 |

Table A.3: - *continued*

| Type | Name | Reference | RA [°] | Dec [°] | P [s] | $P_{\mathrm{orbit}}$ [d] | livetime [h] | $\sigma$ | $UL_{\mathrm{F}}$ $10^{-10}$ [$m^{-2}$ $s^{-1}$] | $UL_{\mathrm{EF}}$ $10^{-10}$ [erg $m^{-2}$ $s^{-1}$] | $UL_{\mathrm{L}}$ $10^{35}$ [erg $s^{-1}$] | $UL_{\mathrm{eff,acc}}$ [%] |
|---|---|---|---|---|---|---|---|---|---|---|---|---|
| HMXB | RXJ0527.3-6552 | AZ16 | 81.849 | -65.876 | - | - | 9.92 | 0.11 | 26.75 | 137.97 | 4.08 | 34.0 |
| HMXB | RXJ0512.6-6717 | AZ16 | 78.174 | -67.290 | - | - | 18.94 | 0.11 | 15.75 | 81.25 | 2.40 | 20.0 |
| HMXB | RXJ0531.2-6607 | AZ16 | 82.808 | -66.118 | 13.70 | 25.400 | 10.96 | 0.62 | 27.67 | 142.72 | 4.22 | 35.2 |
| HMXB | RXJ0529.8-6556 | AZ16 | 82.448 | -65.944 | 69.23 | - | 10.35 | -0.61 | 15.40 | 79.42 | 2.35 | 19.6 |
| HMXB | RXJ0501.6-7034 | AZ16 | 75.350 | -70.559 | - | - | 1.83 | -0.08 | 65.48 | 337.72 | 9.98 | 83.2 |
| HMXB | RXJ0530.7-6606 | AZ16 | 82.698 | -66.104 | - | - | 10.91 | 1.48 | 40.01 | 206.37 | 6.10 | 50.8 |
| HMXB | RXJ0457.2-6612 | AZ16 | 74.302 | -66.203 | - | - | 1.70 | 0.00 | 24.93 | 128.58 | 3.80 | 31.7 |
| HMXB | RXJ0531.5-6518 | AZ16 | 82.900 | -65.304 | - | - | 1.07 | 0.58 | 95.90 | 494.66 | 14.62 | 121.9 |
| HMXB | 1H0538-641 | AZ16 | 84.736 | -64.084 | - | 1.705 | 0.00 | 0.00 | 0.00 | 0.00 | 0.00 | 0.0 |
| HMXB | J045106.8-694803 | AZ16 | 72.778 | -69.801 | 187.07 | 21.631 | 1.86 | -1.21 | 24.55 | 126.60 | 3.74 | 31.2 |
| HMXB | J045558.9-702001 | AZ16 | 73.995 | -70.334 | - | - | 1.88 | -0.30 | 34.17 | 176.22 | 5.21 | 43.4 |
| HMXB | J05007-7047 | AZ16 | 75.192 | -70.743 | 38.55 | 30.770 | 0.67 | 1.53 | 153.88 | 793.70 | 23.46 | 195.5 |
| HMXB | LXP169 | AZ16 | 76.981 | -68.418 | 168.78 | 24.329 | 29.73 | 2.34 | 24.30 | 125.31 | 3.70 | 30.9 |
| HMXB | J0513.4-6547 | AZ16 | 78.367 | -65.789 | 27.28 | 27.405 | 5.89 | 0.79 | 47.34 | 244.18 | 7.22 | 60.2 |
| HMXB | J052016.0-692505 | AZ16 | 80.067 | -69.418 | - | - | 148.28 | -0.97 | 2.42 | 12.50 | 0.37 | 3.1 |
| HMXB | J053041.9-665426 | AZ16 | 82.676 | -66.909 | 28.78 | - | 34.49 | 0.88 | 16.75 | 86.38 | 2.55 | 21.3 |
| HMXB | J053118.2-660730 | AZ16 | 82.826 | -66.125 | - | - | 11.00 | 0.62 | 27.67 | 142.72 | 4.22 | 35.2 |
| HMXB | J053321.3-684121 | AZ16 | 83.339 | -68.689 | - | - | 187.94 | -0.72 | 2.69 | 13.85 | 0.41 | 3.4 |
| HMXB | J05414-6858 | AZ16 | 85.361 | -69.023 | 4.42 | 19.900 | 181.84 | -1.36 | 2.21 | 11.39 | 0.34 | 2.8 |
| HMXB | J053833.9-691157 | AZ16 | 84.639 | -69.200 | - | - | 189.18 | 14.40 | 42.99 | 221.73 | 6.55 | 54.6 |
| HMXB | J0549.7-6812 | AZ16 | 87.527 | -68.249 | 6.20 | - | 65.47 | -1.65 | 3.36 | 17.31 | 0.51 | 4.3 |
| HMXB | 1 | J18 | 73.943 | -69.955 | - | 76.000 | 6.11 | 0.38 | 31.29 | 161.38 | 4.77 | 39.8 |

Table A.3: - *continued*

| Type | Name | Reference | RA [°] | Dec [°] | P [s] | $\mathrm{P_{orbit}}$ [d] | livetime [h] | $\sigma$ | $\mathrm{UL_F}$ $10^{-10}$ [m$^{-2}$ s$^{-1}$] | $\mathrm{UL_{EF}}$ $10^{-10}$ [erg m$^{-2}$ s$^{-1}$] | $\mathrm{UL_L}$ $10^{35}$ [erg s$^{-1}$] | $\mathrm{UL_{eff,acc}}$ [%] |
|---|---|---|---|---|---|---|---|---|---|---|---|---|
| HMXB | 7 | J18 | 80.205 | -69.325 | - | 440.000 | 153.62 | -0.85 | 2.93 | 15.09 | 0.45 | 3.7 |
| HMXB | 8 | J18 | 81.071 | -69.426 | - | 32.700 | 168.64 | -0.86 | 2.79 | 14.41 | 0.43 | 3.5 |
| HMXB | 9 | J18 | 81.444 | -69.748 | - | - | 165.93 | 1.34 | 7.41 | 38.23 | 1.13 | 9.4 |
| HMXB | 10 | J18 | 82.243 | -67.163 | - | 193.000 | 60.30 | 2.41 | 20.80 | 107.28 | 3.17 | 26.4 |
| HMXB | 11 | J18 | 82.545 | -69.799 | - | - | 181.28 | -2.26 | 1.36 | 7.01 | 0.21 | 1.7 |
| HMXB | 13 | J18 | 82.689 | -70.677 | - | 280.000 | 112.85 | -1.11 | 2.69 | 13.85 | 0.41 | 3.4 |
| HMXB | 14 | J18 | 82.747 | -68.548 | - | - | 181.12 | -0.27 | 3.65 | 18.83 | 0.56 | 4.6 |
| HMXB | 15 | J18, V18 | 82.785 | -69.156 | 2013.50 | - | 198.11 | 0.79 | 5.97 | 30.81 | 0.91 | 7.6 |
| HMXB | 17 | J18 | 83.368 | -67.813 | - | 560.000 | 118.53 | 1.02 | 8.21 | 42.36 | 1.25 | 10.4 |
| HMXB | 18 | J18 | 81.461 | -69.458 | - | - | 176.20 | -1.14 | 2.32 | 11.99 | 0.35 | 3.0 |
| HMXB | 19 | J18 | 85.189 | -69.248 | - | - | 184.33 | -0.36 | 3.11 | 16.05 | 0.47 | 4.0 |
| HMXB | LMCP3 | C16 | 84.000 | -67.585 | - | 10.301 | 79.35 | 1.90 | 13.92 | 71.81 | 2.12 | 17.7 |

[a] Source name, coordinates, spin and orbital periods are taken from the respective references: AZ16: Antoniou and Zezas 2016 [98], J18: Jaarsveld et al. 2018 [99], V18: Vasilopoulos 2018 [287] and C16: Corbet et al. 2016 [276].

Livetime, significance $\sigma$ and flux upper limits $\mathrm{UL_F}$ are extracted from the respective sky maps in the energy range of $1-100$ TeV. Upper limits on the energy flux $\mathrm{UL_{EF}}$, luminosity $\mathrm{UL_L}$ and efficiency $\mathrm{UL_{eff}}$ are estimated as described in the text (Section 5.2.4).

Table A.4: Integrated upper limits for the LMC pulsars in the energy range $1-100$ TeV.

| Type | Source Name$^a$ | Reference | RA$^a$ | Dec$^a$ | P$^a$ | $\dot{P}^a$ | $\dot{E}^a$ | livetime | $\sigma$ | UL$_{\mathrm{F}}$ | UL$_{\mathrm{EF}}$ | UL$_{\mathrm{L}}$ | UL$_{\mathrm{eff}}$ |
|---|---|---|---|---|---|---|---|---|---|---|---|---|---|
| | | | | | | $10^{-15}$ | $10^{35}$ | | | $10^{-10}$ | $10^{-10}$ | $10^{35}$ | |
| | | | [°] | [°] | [s] | [s s$^{-1}$] | [erg s$^{-1}$] | [h] | | [m$^{-2}$ s$^{-1}$] | [erg m$^{-2}$ s$^{-1}$] | [erg s$^{-1}$] | [%] |
| PSR | J0540-6919 | ATNF | 85.047 | -69.332 | 0.051 | 479.0 | 1460.0 | 186.68 | 1.71 | 7.76 | 40.05 | 1.18 | 0.08 |
| PSR | J0535-6935 | ATNF | 83.750 | -69.583 | 0.201 | 11.5 | 0.563 | 192.51 | -0.33 | 2.90 | 14.97 | 0.44 | 79 |
| PSR | J0455-6951 | ATNF | 73.948 | -69.859 | 0.320 | 10.2 | 0.123 | 6.20 | -0.17 | 25.06 | 129.25 | 3.82 | 3106 |
| PSR | J0456-7031 | ATNF | 74.010 | -70.519 | 0.800 | 36.7 | 0.028 | 1.79 | 0.00 | 31.22 | 161.05 | 4.76 | 16822 |
| PSR | J0534-6703 | ATNF | 83.650 | -67.064 | 1.818 | 425.0 | 0.028 | 35.16 | -0.43 | 6.69 | 34.49 | 1.02 | 3654 |
| PSR | J0502-6617 | ATNF | 75.710 | -66.300 | 0.691 | 23.1 | 0.028 | 6.47 | -0.96 | 14.02 | 72.31 | 2.14 | 7745 |
| PSR | J0522-6847 | ATNF | 80.596 | -68.784 | 0.675 | 17.7 | 0.023 | 153.64 | 0.01 | 4.47 | 23.06 | 0.68 | 2989 |
| PSR | J0519-6932 | ATNF | 79.945 | -69.540 | 0.263 | 0.7 | 0.015 | 129.97 | -0.82 | 3.12 | 16.09 | 0.48 | 3149 |
| PSR | J0449-7031 | ATNF | 72.273 | -70.525 | 0.479 | 3.4 | 0.012 | 1.52 | 0.00 | 27.28 | 140.69 | 4.16 | 34371 |
| PSR | J0532-6639 | ATNF | 83.248 | -66.660 | 0.643 | 5.3 | 0.008 | 16.46 | 0.03 | 15.97 | 82.37 | 2.43 | 30590 |
| PSR | J0529-6652 | ATNF | 82.462 | -66.877 | 0.976 | 15.5 | 0.007 | 20.47 | 1.60 | 30.95 | 159.63 | 4.72 | 71604 |
| PSR | J0543-6851 | ATNF | 85.970 | -68.857 | 0.709 | 3.9 | 0.004 | 165.08 | -1.81 | 1.79 | 9.25 | 0.27 | 6257 |
| PSR | J0555-7056 | ATNF | 88.757 | -70.946 | 0.828 | 6.0 | 0.004 | 23.43 | -1.56 | 6.82 | 35.20 | 1.04 | 25074 |
| PSR | J0451-67 | ATNF | 72.958 | -67.300 | 0.245 | - | - | 7.11 | 0.37 | 29.79 | 153.63 | 4.54 | - |
| PSR | J0456-69 | ATNF | 74.125 | -69.167 | 0.117 | - | - | 7.54 | -0.35 | 19.31 | 99.58 | 2.94 | - |
| PSR | J0457-69 | ATNF | 74.258 | -69.767 | 0.231 | - | - | 6.40 | 1.84 | 54.62 | 281.73 | 8.33 | - |
| PSR | J0458-67 | ATNF | 74.746 | -67.717 | 1.134 | - | - | 13.53 | 1.18 | 21.70 | 111.94 | 3.31 | - |
| PSR | J0521-68 | ATNF | 80.433 | -68.583 | 0.433 | - | - | 129.99 | 1.22 | 8.44 | 43.51 | 1.29 | - |
| PSR | J0532-69 | ATNF | 83.017 | -69.767 | 0.575 | - | - | 185.90 | -2.48 | 1.24 | 6.37 | 0.19 | - |
| PSR | J0535-66 | ATNF | 83.917 | -66.867 | 0.211 | - | - | 31.94 | -0.40 | 9.95 | 51.32 | 1.52 | - |
| PSR | J0537-69 | ATNF | 84.429 | -69.350 | 0.113 | - | - | 191.66 | 0.51 | 4.65 | 23.96 | 0.71 | - |
| PSR | J0542-68 | ATNF | 85.646 | -68.267 | 0.425 | - | - | 145.88 | 0.46 | 5.76 | 29.72 | 0.88 | - |

Table A.4: (continued)

| Type | Source Name | Reference | RA | Dec | P | $\dot{P}$ | $\dot{E}$ | livetime | $\sigma$ | $\mathrm{UL_F}$ | $\mathrm{UL_{EF}}$ | $\mathrm{UL_L}$ | $\mathrm{UL_{eff}}$ |
|---|---|---|---|---|---|---|---|---|---|---|---|---|---|
| | | | | | | $10^{-15}$ | $10^{35}$ | | | $10^{-10}$ | $10^{-10}$ | $10^{35}$ | |
| | | | [°] | [°] | [s] | [s $s^{-1}$] | [erg $s^{-1}$] | [h] | | [$m^{-2}$ $s^{-1}$] | [erg $m^{-2}$ $s^{-1}$] | [erg $s^{-1}$] | [%] |

[a] Coordinates, period, period derivative and spin-down power are taken from the online version of the ATNF catalogue [282].

Livetime, significance $\sigma$ and flux upper limits $\mathrm{UL_F}$ are extracted from the respective sky maps in the energy range of $1-100$ TeV. Upper limits on the energy flux $\mathrm{UL_{EF}}$, luminosity $\mathrm{UL_L}$ and efficiency $\mathrm{UL_{eff}}$ are estimated as described in the text (Section 5.2.4).

## A.2 SMC

This section lists the following tables:

Table A.5: Integral flux upper limits for the SMC SNRs in the energy range $1-100$ TeV.
Table A.6: Integral flux upper limits for the SMC SNRs in the energy range $0.4-10$ TeV.
Table A.7: Integral flux upper limits for the SMC PWNe in the energy range $1-100$ TeV.
Table A.8: Integral flux upper limits for the SMC PWNe in the energy range $0.4-10$ TeV.
Table A.9: Integral flux upper limits for the SMC HMXBs in the energy range $1-100$ TeV.
Table A.10: Integral flux upper limits for the SMC HMXBs in the energy range $0.4-10$ TeV.
Table A.11: Integral flux upper limits for the SMC pulsars in the energy range $1-100$ TeV.
Table A.12: Integral flux upper limits for the SMC SNRs in the energy range $0.4-10$ TeV.
Table A.13: Integral flux upper limits for the SMC SFRs in the energy range $1-100$ TeV.
Table A.14: Integral flux upper limits for the SMC SFRs in the energy range $0.4-10$ TeV.

The tables include the name, the coordinates, other physical properties of the sources that are needed for the discussion of the source populations, the acceptance corrected lifetime and the analysis results: the significance, integral flux upper limits and further upper limits that are derived (for more information see Section 5.2.4 and Section 5.3.3).

Table A.5: Integral flux upper limits for the SMC SNRs in the energy range $1-100$ TeV.

| Type | Source Name[a] | Reference | RA[a] [°] | Dec[a] [°] | diameter[a] ["] | livetime [h] | $\sigma$ | UL$_{\mathrm{F}}$ $10^{-10}$ [m$^{-2}$ s$^{-1}$] | UL$_{\mathrm{EF}}$ $10^{-10}$ [erg m$^{-2}$ s$^{-1}$] | UL$_{\mathrm{L}}$ $10^{35}$ [erg s$^{-1}$] | UL$_{\mathrm{W}}$ $10^{50}$ [erg] | UL$_{\mathrm{eff}}$ [%] |
|---|---|---|---|---|---|---|---|---|---|---|---|---|
| SNR | DEM-S5 | BMD 2010 | 10.229 | -73.615 | 121 | 41.1 | 0.24 | 14.21 | 73.31 | 3.16 | 12.63 | 126 |
| SNR | DEM-S32 | BMD 2010 | 11.662 | -73.144 | 136 | 52.9 | -0.25 | 6.94 | 35.81 | 1.54 | 6.17 | 62 |
| SNR | IKT2 | BMD 2010 | 11.800 | -73.141 | 66 | 52.7 | -0.09 | 8.59 | 44.31 | 1.91 | 7.64 | 76 |
| SNR | B0045-733 | BMD 2010 | 11.871 | -73.100 | 180 | 54.3 | -1.33 | 4.96 | 25.57 | 1.10 | 4.41 | 44 |
| SNR | HFPK419 | BMD 2010 | 11.921 | -73.158 | 90 | 52.5 | -1.17 | 4.89 | 25.21 | 1.09 | 4.34 | 43 |
| SNR | NS19 | BMD 2010 | 12.025 | -73.145 | 79 | 53.8 | -0.56 | 5.68 | 29.29 | 1.26 | 5.05 | 50 |
| SNR | IKT4 | BMD 2010 | 12.104 | -73.323 | 84 | 50.4 | -0.68 | 6.10 | 31.44 | 1.35 | 5.42 | 54 |
| SNR | IKT5 | BMD 2010 | 12.279 | -73.235 | 116 | 52.7 | -0.14 | 8.25 | 42.53 | 1.83 | 7.33 | 73 |
| SNR | IKT6 | BMD 2010 | 12.779 | -73.357 | 144 | 45.2 | -0.91 | 6.28 | 32.41 | 1.40 | 5.59 | 56 |
| SNR | B0050-728 | BMD 2010 | 13.137 | -72.626 | 323 | 52.9 | 0.84 | 10.98 | 56.64 | 2.44 | 9.76 | 98 |
| SNR | IKT16 | BMD 2010 | 14.570 | -72.302 | 200 | 45.80 | -0.49 | 9.68 | 49.91 | 2.15 | 8.59 | 87 |
| SNR | IKT18 | BMD 2010 | 14.854 | -72.169 | 158 | 44.9 | -1.89 | 4.51 | 23.28 | 1.00 | 4.01 | 40 |
| SNR | DEM-S108 | BMD 2010 | 15.088 | -71.561 | 149 | 33.3 | 0.77 | 18.36 | 94.69 | 4.08 | 16.32 | 163 |
| SNR | IKT21 | BMD 2010 | 15.804 | -72.150 | 62 | 39.8 | 1.54 | 18.86 | 97.26 | 4.19 | 16.76 | 168 |
| SNR | HFPK334 | BMD 2010 | 15.875 | -72.789 | 86 | 40.7 | 0.20 | 13.91 | 71.73 | 3.09 | 12.36 | 124 |
| SNR | B0102-7219 | BMD 2010 | 16.008 | -72.030 | 44 | 38.3 | 1.19 | 18.94 | 97.67 | 4.21 | 16.83 | 168 |
| SNR | IKT23 | BMD 2010 | 16.267 | -72.382 | 170 | 39.2 | -0.11 | 12.58 | 64.91 | 2.80 | 11.19 | 112 |
| SNR | DEM-S128 | BMD 2010 | 16.346 | -72.157 | 124 | 38.4 | -1.39 | 4.56 | 23.52 | 1.01 | 4.05 | 41 |
| SNR | IKT25 | BMD 2010 | 16.558 | -72.088 | 110 | 37.4 | 1.08 | 17.83 | 91.97 | 3.96 | 15.85 | 159 |

[a] Source name, coordinates and diameter of the SNR are taken from BMD 2010 [104].

Livetime, significance $\sigma$ and flux upper limits UL$_{\mathrm{F}}$ are extracted from the respective sky maps in the energy range of $1-100$ TeV. Upper limits on the energy flux UL$_{\mathrm{EF}}$, luminosity UL$_{\mathrm{L}}$, power UL$_{\mathrm{W}}$ and efficiency UL$_{\mathrm{eff}}$ are estimated as described in the text (Sections 5.2.4 and 5.3.3). An explosion energy of $10^{51}$ erg, a number density of the ISM of 1 cm$^{-3}$ and a cooling time of $4\times10^{15}$ s are assumed in the estimation of the luminosity upper limit.

Table A.6: Integral flux upper limits for the SMC SNRs in the energy range $0.4-10$ TeV.

| Type | Source Name$^{a}$ | Reference | RA$^{a}$ [°] | Dec$^{a}$ [°] | diameter$^{a}$ ["] | livetime [h] | $\sigma$ | UL$_{\mathrm{F}}$ $10^{-10}$ [m$^{-2}$ s$^{-1}$] | UL$_{\mathrm{EF}}$ $10^{-10}$ [erg m$^{-2}$ s$^{-1}$] | UL$_{\mathrm{L}}$ $10^{35}$ [erg s$^{-1}$] | UL$_{\mathrm{W}}$ $10^{50}$ [erg] | UL$_{\mathrm{eff}}$ [%] |
|---|---|---|---|---|---|---|---|---|---|---|---|---|
| SNR | DEM-S5 | BMD 2010 | 10.229 | -73.615 | 121 | 12.7 | 1.48 | 345.85 | 602.94 | 25.98 | 103.91 | 1039 |
| SNR | DEM-S32 | BMD 2010 | 11.662 | -73.144 | 136 | 25.7 | -1.69 | 43.90 | 76.53 | 3.30 | 13.19 | 132 |
| SNR | IKT2 | BMD 2010 | 11.800 | -73.141 | 66 | 26.3 | -1.07 | 46.82 | 81.63 | 3.52 | 14.07 | 141 |
| SNR | B0045-733 | BMD 2010 | 11.871 | -73.100 | 180 | 29.1 | -1.04 | 51.84 | 90.38 | 3.89 | 15.57 | 156 |
| SNR | HFPK419 | BMD 2010 | 11.921 | -73.158 | 90 | 26.7 | -0.09 | 125.36 | 218.56 | 9.42 | 37.66 | 377 |
| SNR | NS19 | BMD 2010 | 12.025 | -73.145 | 79 | 27.1 | -0.42 | 76.02 | 132.54 | 5.71 | 22.84 | 228 |
| SNR | IKT4 | BMD 2010 | 12.104 | -73.323 | 84 | 24.5 | 1.33 | 200.73 | 349.95 | 15.08 | 60.31 | 603 |
| SNR | IKT5 | BMD 2010 | 12.279 | -73.235 | 116 | 26.4 | 0.90 | 166.04 | 289.47 | 12.47 | 49.88 | 499 |
| SNR | IKT6 | BMD 2010 | 12.779 | -73.357 | 144 | 26.4 | -0.93 | 53.67 | 93.57 | 4.03 | 16.12 | 161 |
| SNR | B0050-728 | BMD 2010 | 13.137 | -72.626 | 323 | 34.4 | 1.69 | 210.10 | 366.28 | 15.78 | 63.12 | 631 |
| SNR | IKT16 | BMD 2010 | 14.570 | -72.302 | 200 | 35.86 | 0.64 | 183.49 | 319.89 | 13.78 | 55.11 | 551 |
| SNR | IKT18 | BMD 2010 | 14.854 | -72.169 | 158 | 31.5 | -1.84 | 46.68 | 81.38 | 3.51 | 14.02 | 140 |
| SNR | DEM-S108 | BMD 2010 | 15.088 | -71.561 | 149 | 17.7 | 1.94 | 442.73 | 771.84 | 33.25 | 133.01 | 1330 |
| SNR | IKT21 | BMD 2010 | 15.804 | -72.150 | 62 | 25.3 | -1.09 | 89.67 | 156.33 | 6.74 | 26.94 | 269 |
| SNR | HFPK334 | BMD 2010 | 15.875 | -72.789 | 86 | 37.7 | 1.56 | 198.48 | 346.03 | 14.91 | 59.63 | 596 |
| SNR | B0102-7219 | BMD 2010 | 16.008 | -72.030 | 44 | 23.4 | 1.38 | 287.22 | 500.74 | 21.57 | 86.29 | 863 |
| SNR | IKT23 | BMD 2010 | 16.267 | -72.382 | 170 | 29.6 | 0.08 | 84.96 | 148.11 | 6.38 | 25.52 | 255 |
| SNR | DEM-S128 | BMD 2010 | 16.346 | -72.157 | 124 | 23.4 | -0.05 | 164.41 | 286.62 | 12.35 | 49.39 | 494 |
| SNR | IKT25 | BMD 2010 | 16.558 | -72.088 | 110 | 21.6 | 0.80 | 261.57 | 456.02 | 19.65 | 78.59 | 786 |

[a] Source name, coordinates and diameter of the SNR are taken from BMD 2010 [104].

Livetime, significance $\sigma$ and flux upper limits UL$_{\mathrm{F}}$ are extracted from the respective sky maps in the energy range of $0.4-10$ TeV. Upper limits on the energy flux UL$_{\mathrm{EF}}$, luminosity UL$_{\mathrm{L}}$, power UL$_{\mathrm{W}}$ and efficiency UL$_{\mathrm{eff}}$ are estimated as described in the text (Sections 5.2.4 and 5.3.3). An explosion energy of $10^{51}$ erg, a number density of the ISM of 1 cm$^{-3}$ and a cooling time of $4 \times 10^{15}$ s are assumed in the estimation of the luminosity upper limit.

Table A.7: Integral flux upper limits for the SMC PWNe in the energy range $1 - 100$ TeV.

| Type | Source Name$^a$ | Reference | RA$^a$ [°] | Dec$^a$ [°] | diameter$^a$ (X) / (R) ["] | P$^a$ [s] | $\dot{P}^a$ $10^{-15}$ [s s$^{-1}$] | $\dot{E}^a$ $10^{35}$ [erg s$^{-1}$] | livetime [h] | $\sigma$ | UL$_\mathrm{F}$ $10^{-10}$ [m$^{-2}$ s$^{-1}$] | UL$_\mathrm{EF}$ $10^{-10}$ [m$^{-2}$ s$^{-1}$] | UL$_\mathrm{L}$ $10^{35}$ [erg s$^{-1}$] | UL$_\mathrm{eff}$ [%] |
|---|---|---|---|---|---|---|---|---|---|---|---|---|---|---|
| PWN | IKT16 | Maitra 2015 | 14.570 | -72.302 | 5.2 / 70±10 | 0.1 | 100 | 100 | 45.80 | -0.49 | 9.68 | 49.91 | 2.15 | 2 |
| PWN | DEM-S5 | Alsaberi 2019 | 10.229 | -73.615 | 120 | - | - | - | 41.11 | 0.24 | 14.21 | 73.31 | 3.16 | - |

[a] Coordinates, diameter, period, period derivative and spin-down power for IKT16 and DEM-S5 are taken from Maitra et al. [288] and Alsaberi et al. [289], respectively. The diameter of IKT16 is given for X-ray (X) and radio (R) measurements.

Livetime, significance $\sigma$ and flux upper limits UL$_\mathrm{F}$ are extracted from the respective sky maps in the energy range of $1 - 100$ TeV. Upper limits on the energy flux UL$_\mathrm{EF}$, luminosity UL$_\mathrm{L}$ and efficiency UL$_\mathrm{eff}$ are estimated as described in the text (Section 5.2.4).

Table A.8: Integral flux upper limits for the SMC PWNe in the energy range $0.4 - 10$ TeV.

| Type | Source Name$^a$ | Reference | RA$^a$ [°] | Dec$^a$ [°] | diameter$^a$ (X) / (R) ["] | P$^a$ [s] | $\dot{P}^a$ $10^{-15}$ [s s$^{-1}$] | $\dot{E}^a$ $10^{35}$ [erg s$^{-1}$] | livetime [h] | $\sigma$ | UL$_\mathrm{F}$ $10^{-10}$ [m$^{-2}$ s$^{-1}$] | UL$_\mathrm{EF}$ $10^{-10}$ [m$^{-2}$ s$^{-1}$] | UL$_\mathrm{L}$ $10^{35}$ [erg s$^{-1}$] | UL$_\mathrm{eff}$ [%] |
|---|---|---|---|---|---|---|---|---|---|---|---|---|---|---|
| PWN | IKT16 | Maitra 2015 | 14.570 | -72.302 | 5.2 / 70±10 | 0.1 | 100 | 100 | 35.86 | 0.64 | 183.49 | 319.89 | 13.78 | 14 |
| PWN | DEM-S5 | Alsaberi 2019 | 10.229 | -73.615 | 120 | - | - | - | 12.72 | 1.48 | 345.85 | 602.94 | 25.98 | - |

[a] Coordinates, diameter, period, period derivative and spin-down power for IKT16 and DEM-S5 are taken from Maitra et al. [288] and Alsaberi et al. [289], respectively. The diameter of IKT16 is given for X-ray (X) and radio (R) measurements.

Livetime, significance $\sigma$ and flux upper limits UL$_\mathrm{F}$ are extracted from the respective sky maps in the energy range of $0.4 - 10$ TeV. Upper limits on the energy flux UL$_\mathrm{EF}$, luminosity UL$_\mathrm{L}$ and efficiency UL$_\mathrm{eff}$ are estimated as described in the text (Section 5.2.4).

Table A.9: Integral flux upper limits for the SMC HMXBs in the energy range $1-100$ TeV.

| Type | Nr[a] | Reference | RA[a] | Dec[a] | P[a] | $\dot{P}$[b] | $P^{a}_{\mathrm{orbit}}$ | ecc.[c] | livetime | $\sigma$ | $\mathrm{UL_F}$ | $\mathrm{UL_{EF}}$ | $\mathrm{UL_L}$ | $\mathrm{UL_{eff,acc}}$ |
|---|---|---|---|---|---|---|---|---|---|---|---|---|---|---|
| | | | | | | $10^{-10}$ | | | | | $10^{-10}$ | $10^{-10}$ | $10^{35}$ | |
| | | | [°] | [°] | [s] | [s $s^{-1}$] | [d] | | [h] | | [$m^{-2}$ $s^{-1}$] | [erg $m^{-2}$ $s^{-1}$] | [erg $s^{-1}$] | [%] |
| HMXB | 1 | HS16, Y17 | 19.272 | -73.443 | 0.717 | - | 3.892 | - | 20.21 | -0.38 | 10.59 | 54.62 | 2.35 | 20 |
| HMXB | 2 | HS16, Y17 | 19.750 | -73.207 | 2.165 | - | 83.760 | - | 19.17 | 0.81 | 18.84 | 97.17 | 4.19 | 35 |
| HMXB | 3 | HS16, Y17, CK15 | 13.629 | -73.682 | 2.370 | -1.39 | 18.380 | 0.07 | 36.97 | 1.59 | 21.87 | 112.80 | 4.86 | 40 |
| HMXB | 4 | HS16, Y17 | 14.797 | -71.646 | 2.763 | 3.47 | 81.810 | - | 34.99 | 0.42 | 11.80 | 60.87 | 2.62 | 22 |
| HMXB | 5 | HS16, Y17 | 13.071 | -72.331 | 4.780 | -0.23 | - | - | 50.73 | 0.12 | 7.98 | 41.18 | 1.77 | 15 |
| HMXB | 6 | HS16, Y17, CK15 | 14.260 | -72.432 | 5.050 | -0.69 | 17.200 | 0.16 | 45.69 | 2.26 | 26.77 | 138.09 | 5.95 | 50 |
| HMXB | 7 | HS16, Y17, CK15 | 15.723 | -72.743 | 6.850 | -0.12 | 21.900 | 0.26 | 41.07 | -0.16 | 13.16 | 67.87 | 2.92 | 24 |
| HMXB | 8 | HS16, Y17 | 13.542 | -72.429 | 6.878 | - | - | - | 52.84 | 1.80 | 20.51 | 105.79 | 4.56 | 38 |
| HMXB | 9 | HS16, Y17 | 13.024 | -72.434 | 7.780 | 0.69 | 44.920 | - | 50.97 | 0.77 | 11.73 | 60.50 | 2.61 | 22 |
| HMXB | 10 | HS16, Y17 | 14.493 | -72.375 | 7.920 | 21.99 | 40.030 | - | 45.88 | 1.40 | 16.32 | 84.19 | 3.63 | 30 |
| HMXB | 11 | HS16, Y17, CK15 | 12.972 | -72.530 | 8.900 | 0.35 | 28.510 | 0.41 | 51.22 | 0.26 | 6.99 | 36.07 | 1.55 | 13 |
| HMXB | 12 | HS16, Y17 | 12.327 | -73.200 | 9.130 | - | 77.200 | - | 52.96 | -0.55 | 6.78 | 34.96 | 1.51 | 13 |
| HMXB | 13 | HS16, Y17, CK15 | 16.176 | -72.901 | 11.480 | 1.62 | 36.300 | 0.28 | 39.61 | 0.62 | 16.28 | 83.95 | 3.62 | 30 |
| HMXB | 15 | HS16, Y17 | 12.058 | -73.368 | 11.866 | -1.39 | - | - | 49.77 | -2.46 | 3.15 | 16.26 | 0.70 | 6 |
| HMXB | 16 | HS16, Y17 | 13.058 | -73.322 | 15.300 | -0.23 | 74.320 | - | 41.56 | -2.60 | 2.80 | 14.42 | 0.62 | 5 |
| HMXB | 17 | HS16, Y17 | 12.686 | -73.268 | 16.600 | 0.23 | 33.720 | - | 49.44 | -0.19 | 8.52 | 43.95 | 1.89 | 16 |
| HMXB | 18 | HS16, Y17, CK15 | 12.298 | -72.827 | 18.370 | 0.35 | 17.730 | 0.43 | 55.99 | -0.14 | 7.40 | 38.15 | 1.64 | 14 |
| HMXB | 19 | HS16, Y17 | 19.418 | -73.514 | 22.070 | - | 83.700 | - | 18.42 | 0.46 | 23.18 | 119.53 | 5.15 | 43 |
| HMXB | 20 | HS16, Y17 | 12.059 | -73.168 | 51.000 | - | 22.530 | - | 53.62 | -0.81 | 4.53 | 23.35 | 1.01 | 8 |
| HMXB | 21 | HS16, Y17 | 17.786 | -73.279 | 31.030 | - | 90.530 | - | 33.11 | 1.17 | 19.82 | 102.25 | 4.41 | 37 |
| HMXB | 22 | HS16, Y17 | 13.480 | -72.446 | 46.630 | -5.56 | 137.360 | - | 52.89 | 0.79 | 14.72 | 75.91 | 3.27 | 27 |
| HMXB | 23 | HS16, Y17 | 13.735 | -72.446 | 59.070 | -5.09 | 62.100 | - | 52.64 | -0.17 | 9.47 | 48.83 | 2.10 | 18 |

Table A.9: - *continued*

| Type | Nr[a] | Reference | RA[a] [°] | Dec[a] [°] | P[a] [s] | $\dot{P}$[b] $10^{-10}$ [s $s^{-1}$] | $P^{a}_{\mathrm{orbit}}$ [d] | ecc.[c] | livetime [h] | $\sigma$ | $UL_{\mathrm{F}}$ $10^{-10}$ [$m^{-2}$ $s^{-1}$] | $UL_{\mathrm{EF}}$ $10^{-10}$ [erg $m^{-2}$ $s^{-1}$] | $UL_{\mathrm{L}}$ $10^{35}$ [erg $s^{-1}$] | $UL_{\mathrm{eff,acc}}$ [%] |
|---|---|---|---|---|---|---|---|---|---|---|---|---|---|---|
| HMXB | 24 | HS16, Y17 | 16.802 | -72.593 | 65.780 | 11.57 | 111.040 | - | 38.15 | -0.09 | 10.67 | 55.05 | 2.37 | 20 |
| HMXB | 25 | HS16, Y17, CK15 | 12.264 | -72.848 | 74.670 | 8.91 | 33.380 | 0.40 | 56.01 | 0.21 | 9.42 | 48.61 | 2.09 | 17 |
| HMXB | 26 | HS16, Y17 | 13.037 | -72.634 | 82.400 | 6.13 | 362.300 | - | 51.40 | 1.19 | 16.09 | 82.99 | 3.58 | 30 |
| HMXB | 27 | HS16, Y17 | 12.738 | -72.226 | 91.120 | -132.41 | 88.370 | - | 49.60 | 0.82 | 14.50 | 74.80 | 3.22 | 27 |
| HMXB | 28 | HS16, Y17 | 13.471 | -72.445 | 95.000 | 25.46 | 71.300 | - | 52.89 | 0.79 | 14.72 | 75.91 | 3.27 | 27 |
| HMXB | 29 | HS16, Y17 | 14.363 | -73.422 | 101.160 | -18.52 | 21.949 | - | 38.58 | -0.15 | 11.18 | 57.67 | 2.48 | 21 |
| HMXB | 30 | HS16, Y17 | 13.350 | -72.454 | 138.000 | 53.24 | 103.600 | - | 51.56 | 0.17 | 12.22 | 63.00 | 2.71 | 23 |
| HMXB | 31 | HS16, Y17 | 14.024 | -72.366 | 140.100 | -12.73 | 197.000 | - | 50.22 | 0.76 | 18.11 | 93.42 | 4.02 | 34 |
| HMXB | 32 | HS16, Y17 | 13.471 | -72.445 | 144.100 | 85.65 | 59.380 | - | 52.89 | 0.79 | 14.72 | 75.91 | 3.27 | 27 |
| HMXB | 33 | HS16, Y17 | 14.460 | -72.132 | 152.340 | -12.27 | - | - | 44.67 | -0.83 | 6.41 | 33.05 | 1.42 | 12 |
| HMXB | 34 | HS16, Y17 | 16.930 | -71.998 | 153.990 | - | - | - | 34.38 | 0.49 | 19.30 | 99.53 | 4.29 | 36 |
| HMXB | 35 | HS16, Y17 | 13.230 | -71.968 | 169.300 | -72.92 | 68.540 | - | 45.62 | -0.27 | 9.77 | 50.39 | 2.17 | 18 |
| HMXB | 36 | HS16, Y17 | 12.966 | -73.176 | 172.000 | -35.07 | 68.780 | - | 50.66 | 0.10 | 7.89 | 40.70 | 1.75 | 15 |
| HMXB | 37 | HS16, Y17 | 15.468 | -72.392 | 175.400 | 28.94 | - | - | 41.44 | 0.16 | 13.07 | 67.44 | 2.91 | 24 |
| HMXB | 38 | HS16, Y17 | 14.838 | -72.388 | 201.900 | -33.56 | 71.980 | - | 45.78 | -0.42 | 8.62 | 44.45 | 1.91 | 16 |
| HMXB | 39 | HS16, Y17 | 14.870 | -72.618 | 202.520 | - | 224.600 | - | 42.35 | -2.11 | 4.66 | 24.06 | 1.04 | 9 |
| HMXB | 40 | HS16, Y17 | 12.546 | -73.007 | 214.030 | -10.30 | 29.910 | - | 55.00 | -1.81 | 4.52 | 23.32 | 1.00 | 8 |
| HMXB | 41 | HS16, Y17 | 11.847 | -73.208 | 263.000 | 16.20 | 49.120 | - | 52.05 | -1.01 | 4.53 | 23.38 | 1.01 | 8 |
| HMXB | 42 | HS16, Y17 | 23.214 | -74.429 | 264.520 | - | - | - | 2.88 | 0.14 | 29.96 | 154.53 | 6.66 | 55 |
| HMXB | 43 | HS16, Y17 | 14.456 | -72.043 | 280.400 | 115.74 | 64.800 | - | 43.71 | -0.81 | 6.00 | 30.97 | 1.33 | 11 |
| HMXB | 44 | HS16, Y17 | 14.553 | -72.513 | 291.330 | -5.79 | 59.726 | - | 45.76 | 0.34 | 14.42 | 74.38 | 3.20 | 27 |
| HMXB | 45 | HS16, Y17 | 12.700 | -73.305 | 292.700 | 31.25 | - | - | 49.04 | -0.62 | 7.07 | 36.49 | 1.57 | 13 |

Table A.9: - *continued*

| Type | Nr$^a$ | Reference | RA$^a$ [°] | Dec$^a$ [°] | P$^a$ [s] | $\dot{P}^b$ $10^{-10}$ [s s$^{-1}$] | P$^a_{\mathrm{orbit}}$ [d] | ecc.$^c$ | livetime [h] | $\sigma$ | UL$_{\mathrm{F}}$ $10^{-10}$ [m$^{-2}$ s$^{-1}$] | UL$_{\mathrm{EF}}$ $10^{-10}$ [erg m$^{-2}$ s$^{-1}$] | UL$_{\mathrm{L}}$ $10^{35}$ [erg s$^{-1}$] | UL$_{\mathrm{eff,acc}}$ [%] |
|---|---|---|---|---|---|---|---|---|---|---|---|---|---|---|
| HMXB | 46 | HS16, Y17 | 15.262 | -72.116 | 304.500 | 33.56 | 344.000 | - | 40.69 | 0.45 | 13.67 | 70.50 | 3.04 | 25 |
| HMXB | 47 | HS16, Y17 | 12.686 | -73.268 | 323.200 | -174.77 | 116.600 | - | 49.44 | -0.19 | 8.52 | 43.95 | 1.89 | 16 |
| HMXB | 48 | HS16, Y17 | 13.217 | -72.287 | 325.400 | -34.72 | 45.930 | - | 50.73 | -0.27 | 5.86 | 30.21 | 1.30 | 11 |
| HMXB | 49 | HS16, Y17 | 13.516 | -72.442 | 341.900 | 171.30 | - | - | 52.82 | 1.06 | 16.78 | 86.56 | 3.73 | 31 |
| HMXB | 50 | HS16, Y17 | 15.808 | -72.154 | 345.200 | -28.94 | 94.400 | - | 39.77 | 1.51 | 19.31 | 99.62 | 4.29 | 36 |
| HMXB | 51 | HS16, Y17 | 15.336 | -72.189 | 455.000 | -150.46 | 74.560 | - | 41.17 | -0.05 | 10.39 | 53.60 | 2.31 | 19 |
| HMXB | 52 | HS16, Y17 | 13.733 | -72.753 | 499.200 | 1.04 | 265.300 | - | 52.51 | 0.88 | 12.99 | 66.98 | 2.89 | 24 |
| HMXB | 53 | HS16, Y17 | 15.698 | -72.081 | 522.500 | -208.33 | - | - | 39.41 | 0.31 | 12.49 | 64.43 | 2.78 | 23 |
| HMXB | 54 | HS16, Y17 | 14.401 | -72.326 | 565.000 | 26.62 | 151.800 | - | 45.78 | -0.61 | 7.09 | 36.57 | 1.58 | 13 |
| HMXB | 55 | HS16, Y17 | 13.898 | -72.485 | 644.600 | 17.36 | - | - | 50.01 | 0.09 | 9.39 | 48.46 | 2.09 | 17 |
| HMXB | 56 | HS16, Y17 | 13.826 | -72.648 | 701.600 | 347.22 | 412.000 | - | 52.72 | 0.27 | 11.34 | 58.50 | 2.52 | 21 |
| HMXB | 57 | HS16, Y17 | 16.481 | -72.064 | 726.000 | 23.15 | - | - | 37.35 | 0.94 | 14.91 | 76.92 | 3.31 | 28 |
| HMXB | 58 | HS16, Y17 | 12.425 | -73.388 | 755.500 | -474.54 | 389.900 | - | 44.76 | 0.61 | 13.04 | 67.26 | 2.90 | 24 |
| HMXB | 59 | HS16, Y17 | 12.374 | -73.183 | 894.000 | -78.70 | 91.500 | - | 53.21 | -0.70 | 6.42 | 33.12 | 1.43 | 12 |
| HMXB | 60 | HS16, Y17 | 15.528 | -71.688 | 967.000 | -72.92 | 101.400 | - | 33.63 | -0.28 | 10.17 | 52.48 | 2.26 | 19 |
| HMXB | 61 | HS16, Y17 | 21.942 | -73.549 | 1062.000 | 821.76 | - | - | 7.46 | -0.10 | 25.68 | 132.44 | 5.71 | 48 |
| HMXB | 62 | HS16, Y17 | 15.906 | -72.026 | 1323.000 | -752.31 | - | - | 38.60 | 1.34 | 19.51 | 100.62 | 4.34 | 36 |
| HMXB | 63 | HS16, Y17 | 13.693 | -72.423 | 4693.000 | - | - | - | 52.71 | 0.74 | 13.18 | 67.96 | 2.93 | 24 |
| HMXB | 64 | HS16, Y17 | 8.234 | -73.806 | - | - | - | - | 30.06 | 0.35 | 15.76 | 81.30 | 3.50 | 29 |
| HMXB | 65 | HS16, Y17 | 10.533 | -73.751 | - | - | - | - | 34.22 | 1.41 | 22.80 | 117.60 | 5.07 | 42 |
| HMXB | 70 | HS16, Y17 | 12.142 | -73.042 | - | - | 414.913 | - | 54.83 | -0.83 | 6.41 | 33.06 | 1.42 | 12 |
| HMXB | 71 | HS16, Y17 | 12.204 | -73.274 | - | - | - | - | 51.00 | -0.56 | 8.46 | 43.65 | 1.88 | 16 |

Table A.9: - *continued*

| Type | Nr[a] | Reference | RA[a] [°] | Dec[a] [°] | P[a] [s] | $\dot{P}^b$ $10^{-10}$ [s $s^{-1}$] | $P^a_{\mathrm{orbit}}$ [d] | ecc.[c] | livetime [h] | $\sigma$ | $UL_{\mathrm{F}}$ $10^{-10}$ [$m^{-2}$ $s^{-1}$] | $UL_{\mathrm{EF}}$ $10^{-10}$ [erg $m^{-2}$ $s^{-1}$] | $UL_{\mathrm{L}}$ $10^{35}$ [erg $s^{-1}$] | $UL_{\mathrm{eff,acc}}$ [%] |
|---|---|---|---|---|---|---|---|---|---|---|---|---|---|---|
| HMXB | 72 | HS16, Y17 | 12.232 | -73.829 | 15.640 | - | 36.432 | - | 31.26 | 0.40 | 14.42 | 74.38 | 3.20 | 27 |
| HMXB | 74 | HS16, Y17 | 12.307 | -73.194 | - | - | 80.100 | - | 53.11 | -0.65 | 6.50 | 33.55 | 1.45 | 12 |
| HMXB | 76 | HS16, Y17 | 12.377 | -73.519 | - | - | - | - | 36.78 | -0.06 | 7.63 | 39.37 | 1.70 | 14 |
| HMXB | 79 | HS16, Y17 | 12.551 | -73.199 | - | - | - | - | 48.35 | -0.28 | 8.85 | 45.65 | 1.97 | 16 |
| HMXB | 81 | HS16, Y17 | 12.650 | -73.294 | - | - | - | - | 49.28 | -0.18 | 9.32 | 48.06 | 2.07 | 17 |
| HMXB | 84 | HS16, Y17 | 12.739 | -73.169 | - | - | - | - | 50.75 | -0.31 | 7.71 | 39.77 | 1.71 | 14 |
| HMXB | 85 | HS16, Y17 | 12.774 | -73.220 | - | - | - | - | 50.08 | -1.33 | 4.63 | 23.88 | 1.03 | 9 |
| HMXB | 86 | HS16, Y17 | 12.821 | -73.268 | - | - | - | - | 49.59 | -0.95 | 4.97 | 25.64 | 1.10 | 9 |
| HMXB | 91 | HS16, Y17 | 12.998 | -73.491 | - | - | - | - | 38.43 | 0.30 | 12.36 | 63.76 | 2.75 | 23 |
| HMXB | 93 | HS16, Y17 | 13.064 | -73.321 | - | - | - | - | 41.56 | -2.98 | 2.58 | 13.31 | 0.57 | 5 |
| HMXB | 95 | HS16, Y17 | 13.155 | -72.459 | - | - | - | - | 51.08 | 1.00 | 13.44 | 69.31 | 2.99 | 25 |
| HMXB | 96 | HS16, Y17 | 13.188 | -72.479 | - | - | - | - | 51.13 | 0.88 | 13.07 | 67.40 | 2.90 | 24 |
| HMXB | 97 | HS16, Y17 | 13.217 | -72.808 | - | - | - | - | 52.81 | -1.83 | 3.49 | 18.01 | 0.78 | 6 |
| HMXB | 101 | HS16, Y17 | 13.372 | -72.563 | - | - | - | - | 52.96 | 1.45 | 15.46 | 79.71 | 3.43 | 29 |
| HMXB | 104 | HS16, Y17 | 13.424 | -72.886 | - | - | - | - | 52.20 | -1.85 | 3.92 | 20.23 | 0.87 | 7 |
| HMXB | 105 | HS16, Y17 | 13.469 | -72.444 | - | - | - | - | 52.91 | 0.79 | 14.72 | 75.91 | 3.27 | 27 |
| HMXB | 107 | HS16, Y17 | 13.539 | -72.695 | - | - | - | - | 52.64 | 0.98 | 14.17 | 73.06 | 3.15 | 26 |
| HMXB | 111 | HS16, Y17 | 13.782 | -72.378 | - | - | - | - | 49.77 | 0.21 | 12.54 | 64.69 | 2.79 | 23 |
| HMXB | 114 | HS16, Y17 | 14.023 | -72.003 | - | - | - | - | 46.02 | -0.69 | 5.72 | 29.49 | 1.27 | 11 |
| HMXB | 115 | HS16, Y17 | 14.058 | -72.500 | - | - | 72.231 | - | 47.97 | -0.07 | 9.29 | 47.94 | 2.07 | 17 |
| HMXB | 116 | HS16, Y17 | 14.061 | -72.632 | - | - | - | - | 45.24 | -0.34 | 8.57 | 44.21 | 1.90 | 16 |
| HMXB | 117 | HS16, Y17 | 14.079 | -72.468 | - | - | - | - | 50.63 | 0.29 | 11.28 | 58.20 | 2.51 | 21 |

Table A.9: - *continued*

| Type | Nr[a] | Reference | RA[a] [°] | Dec[a] [°] | P[a] [s] | $\dot{P}^b$ $10^{-10}$ [s s$^{-1}$] | P$^a_{\mathrm{orbit}}$ [d] | ecc.[c] | livetime [h] | $\sigma$ | UL$_{\mathrm{F}}$ $10^{-10}$ [m$^{-2}$ s$^{-1}$] | UL$_{\mathrm{EF}}$ $10^{-10}$ [erg m$^{-2}$ s$^{-1}$] | UL$_{\mathrm{L}}$ $10^{35}$ [erg s$^{-1}$] | UL$_{\mathrm{eff,acc}}$ [%] |
|---|---|---|---|---|---|---|---|---|---|---|---|---|---|---|
| HMXB | 119 | HS16, Y17 | 14.349 | -72.399 | - | - | - | - | 45.75 | 2.98 | 30.84 | 159.08 | 6.85 | 57 |
| HMXB | 121 | HS16, Y17 | 15.126 | -72.343 | - | - | - | - | 42.19 | -1.36 | 5.85 | 30.17 | 1.30 | 11 |
| HMXB | 123 | HS16, Y17 | 15.232 | -72.389 | - | - | - | - | 42.08 | -1.13 | 6.07 | 31.30 | 1.35 | 11 |
| HMXB | 124 | HS16, Y17 | 15.448 | -71.931 | - | - | - | - | 38.42 | 1.11 | 15.93 | 82.15 | 3.54 | 29 |
| HMXB | 125 | HS16, Y17 | 15.482 | -72.544 | - | - | 35.610 | - | 41.58 | 1.00 | 13.84 | 71.40 | 3.08 | 26 |
| HMXB | 126 | HS16, Y17 | 15.483 | -72.174 | - | - | - | - | 40.60 | 0.59 | 16.53 | 85.26 | 3.67 | 31 |
| HMXB | 132 | HS16, Y17 | 16.122 | -72.527 | - | - | 29.750 | - | 39.74 | -0.84 | 6.41 | 33.06 | 1.42 | 12 |
| HMXB | 133 | HS16, Y17 | 16.148 | -72.363 | - | - | - | - | 39.58 | -0.11 | 9.68 | 49.94 | 2.15 | 18 |
| HMXB | 136 | HS16, Y17 | 16.637 | -73.262 | - | - | - | - | 36.18 | -0.30 | 9.60 | 49.52 | 2.13 | 18 |
| HMXB | 137 | HS16, Y17 | 16.935 | -72.462 | - | - | 1180.000 | - | 37.52 | -0.22 | 11.13 | 57.41 | 2.47 | 21 |
| HMXB | 141 | HS16, Y17 | 19.912 | -73.503 | - | - | - | - | 14.04 | 0.09 | 21.54 | 111.08 | 4.79 | 40 |
| HMXB | 142 | HS16, Y17 | 20.421 | -72.959 | - | - | 84.000 | - | 16.83 | 1.82 | 31.85 | 164.25 | 7.08 | 59 |
| HMXB | 143 | HS16, Y17 | 20.865 | -73.356 | - | - | 119.900 | - | 11.78 | 0.73 | 22.73 | 117.22 | 5.05 | 42 |

[a] The numbering, coordinates, spin and orbital periods are taken from HS16 [102].

[b] The spin down derivative, if available, is taken from Y17 [292].

[c] Eccentricities are taken from CK15 [378].

Livetime, significance $\sigma$ and flux upper limits UL$_{\mathrm{F}}$ are extracted from the respective sky maps in the energy range of $1-100$ TeV. Upper limits on the energy flux UL$_{\mathrm{EF}}$, luminosity UL$_{\mathrm{L}}$ and efficiency UL$_{\mathrm{eff}}$ are estimated as described in the text (Section 5.2.4).

Table A.10: Integral flux upper limits for the SMC HMXBs in the energy range $0.4 - 10$ TeV.

| Type | Nr[a] | Reference | RA[a] | Dec[a] | P[a] | $\dot{P}^b$ | $P^a_{\mathrm{orbit}}$ | ecc.[c] | livetime | $\sigma$ | $\mathrm{UL}_{\mathrm{F}}$ | $\mathrm{UL}_{\mathrm{EF}}$ | $\mathrm{UL}_{\mathrm{L}}$ | $\mathrm{UL}_{\mathrm{eff,acc}}$ |
|---|---|---|---|---|---|---|---|---|---|---|---|---|---|---|
| | | | | | | $10^{-10}$ | | | | | $10^{-10}$ | $10^{-10}$ | $10^{35}$ | |
| | | | [°] | [°] | [s] | [s $s^{-1}$] | [d] | | [h] | | [$m^{-2}$ $s^{-1}$] | [erg $m^{-2}$ $s^{-1}$] | [erg $s^{-1}$] | [%] |
| HMXB | 1 | HS16, Y17 | 19.272 | -73.443 | 0.717 | - | 3.892 | - | 18.52 | -2.55 | 55.38 | 96.54 | 4.16 | 35 |
| HMXB | 2 | HS16, Y17 | 19.750 | -73.207 | 2.165 | - | 83.760 | - | 19.65 | -1.59 | 31.39 | 54.73 | 2.36 | 20 |
| HMXB | 3 | HS16, Y17 CK15 | 13.629 | -73.682 | 2.370 | -1.39 | 18.380 | 0.07 | 22.65 | -2.67 | 38.52 | 67.15 | 2.89 | 24 |
| HMXB | 4 | HS16, Y17 | 14.797 | -71.646 | 2.763 | 3.47 | 81.810 | - | 18.89 | -1.90 | 92.01 | 160.41 | 6.91 | 58 |
| HMXB | 5 | HS16, Y17 | 13.071 | -72.331 | 4.780 | -0.23 | - | - | 31.95 | 1.39 | 303.87 | 529.76 | 22.82 | 190 |
| HMXB | 6 | HS16, Y17 CK15 | 14.260 | -72.432 | 5.050 | -0.69 | 17.200 | 0.16 | 34.75 | 2.90 | 450.84 | 785.99 | 33.86 | 282 |
| HMXB | 7 | HS16, Y17 CK15 | 15.723 | -72.743 | 6.850 | -0.12 | 21.900 | 0.26 | 38.44 | 1.14 | 141.15 | 246.08 | 10.60 | 88 |
| HMXB | 8 | HS16, Y17 | 13.542 | -72.429 | 6.878 | - | - | - | 33.99 | 0.99 | 291.02 | 507.35 | 21.86 | 182 |
| HMXB | 9 | HS16, Y17 | 13.024 | -72.434 | 7.780 | 0.69 | 44.920 | - | 32.14 | 1.58 | 305.86 | 533.23 | 22.97 | 191 |
| HMXB | 10 | HS16, Y17 | 14.493 | -72.375 | 7.920 | 21.99 | 40.030 | - | 35.18 | 2.84 | 488.32 | 851.32 | 36.68 | 306 |
| HMXB | 11 | HS16, Y17 CK15 | 12.972 | -72.530 | 8.900 | 0.35 | 28.510 | 0.41 | 32.45 | 1.12 | 193.36 | 337.09 | 14.52 | 121 |
| HMXB | 12 | HS16, Y17 | 12.327 | -73.200 | 9.130 | - | 77.200 | - | 26.91 | 1.44 | 198.18 | 345.51 | 14.89 | 124 |
| HMXB | 13 | HS16, Y17 CK15 | 16.176 | -72.901 | 11.480 | 1.62 | 36.300 | 0.28 | 36.42 | 1.70 | 67.63 | 117.91 | 5.08 | 42 |
| HMXB | 15 | HS16, Y17 | 12.058 | -73.368 | 11.866 | -1.39 | - | - | 23.81 | 1.06 | 147.81 | 257.69 | 11.10 | 93 |
| HMXB | 16 | HS16, Y17 | 13.058 | -73.322 | 15.300 | -0.23 | 74.320 | - | 31.19 | -0.34 | 69.25 | 120.73 | 5.20 | 43 |
| HMXB | 17 | HS16, Y17 | 12.686 | -73.268 | 16.600 | 0.23 | 33.720 | - | 26.42 | -0.40 | 43.66 | 76.12 | 3.28 | 27 |
| HMXB | 18 | HS16, Y17 CK15 | 12.298 | -72.827 | 18.370 | 0.35 | 17.730 | 0.43 | 30.72 | 0.31 | 72.22 | 125.91 | 5.42 | 45 |
| HMXB | 19 | HS16, Y17 | 19.418 | -73.514 | 22.070 | - | 83.700 | - | 17.57 | -2.03 | 49.74 | 86.72 | 3.74 | 31 |
| HMXB | 20 | HS16, Y17 | 12.059 | -73.168 | 51.000 | - | 22.530 | - | 27.19 | 0.08 | 123.62 | 215.51 | 9.28 | 77 |
| HMXB | 21 | HS16, Y17 | 17.786 | -73.279 | 31.030 | - | 90.530 | - | 22.59 | 1.62 | 451.88 | 787.79 | 33.94 | 283 |
| HMXB | 22 | HS16, Y17 | 13.480 | -72.446 | 46.630 | -5.56 | 137.360 | - | 34.19 | 1.06 | 279.48 | 487.24 | 20.99 | 175 |
| HMXB | 23 | HS16, Y17 | 13.735 | -72.446 | 59.070 | -5.09 | 62.100 | - | 34.56 | 2.19 | 407.79 | 710.94 | 30.63 | 255 |

Table A.10: *- continued*

| Type | Nr$^a$ | Reference | RA$^a$ [°] | Dec$^a$ [°] | P$^a$ [s] | $\dot{P}^b$ $10^{-10}$ [s s$^{-1}$] | P$^a_{\rm orbit}$ [d] | ecc.$^c$ | livetime [h] | $\sigma$ | UL$_{\rm F}$ $10^{-10}$ [m$^{-2}$ s$^{-1}$] | UL$_{\rm EF}$ $10^{-10}$ [erg m$^{-2}$ s$^{-1}$] | UL$_{\rm L}$ $10^{35}$ [erg s$^{-1}$] | UL$_{\rm eff,acc}$ [%] |
|---|---|---|---|---|---|---|---|---|---|---|---|---|---|---|
| HMXB | 24 | HS16, Y17 | 16.802 | -72.593 | 65.780 | 11.57 | 111.040 | - | 32.86 | -0.35 | 47.04 | 82.02 | 3.53 | 29 |
| HMXB | 25 | HS16, Y17 CK15 | 12.264 | -72.848 | 74.670 | 8.91 | 33.380 | 0.40 | 30.61 | 0.45 | 62.85 | 109.57 | 4.72 | 39 |
| HMXB | 26 | HS16, Y17 | 13.037 | -72.634 | 82.400 | 6.13 | 362.300 | - | 34.16 | 2.18 | 252.20 | 439.68 | 18.94 | 158 |
| HMXB | 27 | HS16, Y17 | 12.738 | -72.226 | 91.120 | -132.41 | 88.370 | - | 29.51 | -1.36 | 60.06 | 104.71 | 4.51 | 38 |
| HMXB | 28 | HS16, Y17 | 13.471 | -72.445 | 95.000 | 25.46 | 71.300 | - | 34.19 | 1.06 | 279.48 | 487.24 | 20.99 | 175 |
| HMXB | 29 | HS16, Y17 | 14.363 | -73.422 | 101.160 | -18.52 | 21.949 | - | 30.04 | -0.28 | 71.97 | 125.48 | 5.41 | 45 |
| HMXB | 30 | HS16, Y17 | 13.350 | -72.454 | 138.000 | 53.24 | 103.600 | - | 33.90 | 0.19 | 165.88 | 289.19 | 12.46 | 104 |
| HMXB | 31 | HS16, Y17 | 14.024 | -72.366 | 140.100 | -12.73 | 197.000 | - | 34.90 | 1.86 | 416.37 | 725.89 | 31.27 | 261 |
| HMXB | 32 | HS16, Y17 | 13.471 | -72.445 | 144.100 | 85.65 | 59.380 | - | 34.19 | 1.06 | 279.48 | 487.24 | 20.99 | 175 |
| HMXB | 33 | HS16, Y17 | 14.460 | -72.132 | 152.340 | -12.27 | - | - | 31.04 | -1.23 | 44.64 | 77.82 | 3.35 | 28 |
| HMXB | 34 | HS16, Y17 | 16.930 | -71.998 | 153.990 | - | - | - | 18.70 | 0.06 | 160.50 | 279.81 | 12.06 | 100 |
| HMXB | 35 | HS16, Y17 | 13.230 | -71.968 | 169.300 | -72.92 | 68.540 | - | 25.19 | -0.92 | 97.32 | 169.66 | 7.31 | 61 |
| HMXB | 36 | HS16, Y17 | 12.966 | -73.176 | 172.000 | -35.07 | 68.780 | - | 35.49 | -0.26 | 39.39 | 68.66 | 2.96 | 25 |
| HMXB | 37 | HS16, Y17 | 15.468 | -72.392 | 175.400 | 28.94 | - | - | 35.72 | 1.02 | 342.60 | 597.28 | 25.73 | 214 |
| HMXB | 38 | HS16, Y17 | 14.838 | -72.388 | 201.900 | -33.56 | 71.980 | - | 34.97 | 1.75 | 309.00 | 538.71 | 23.21 | 193 |
| HMXB | 39 | HS16, Y17 | 14.870 | -72.618 | 202.520 | - | 224.600 | - | 35.08 | 1.06 | 162.26 | 282.88 | 12.19 | 102 |
| HMXB | 40 | HS16, Y17 | 12.546 | -73.007 | 214.030 | -10.30 | 29.910 | - | 37.22 | -0.47 | 43.13 | 75.19 | 3.24 | 27 |
| HMXB | 41 | HS16, Y17 | 11.847 | -73.208 | 263.000 | 16.20 | 49.120 | - | 25.82 | -0.49 | 98.40 | 171.55 | 7.39 | 62 |
| HMXB | 42 | HS16, Y17 | 23.214 | -74.429 | 264.520 | - | - | - | 0.00 | 0.00 | 0.00 | 0.00 | 0.00 | 0 |
| HMXB | 43 | HS16, Y17 | 14.456 | -72.043 | 280.400 | 115.74 | 64.800 | - | 29.66 | -0.62 | 72.99 | 127.24 | 5.48 | 46 |
| HMXB | 44 | HS16, Y17 | 14.553 | -72.513 | 291.330 | -5.79 | 59.726 | - | 35.01 | 2.34 | 329.69 | 574.77 | 24.76 | 206 |
| HMXB | 45 | HS16, Y17 | 12.700 | -73.305 | 292.700 | 31.25 | - | - | 26.40 | -0.56 | 43.26 | 75.42 | 3.25 | 27 |

Table A.10: *- continued*

| Type | Nr$^a$ | Reference | RA$^a$ [°] | Dec$^a$ [°] | P$^a$ [s] | $\dot{P}^b$ $10^{-10}$ [s s$^{-1}$] | P$^a_{\rm orbit}$ [d] | ecc.$^c$ | livetime [h] | $\sigma$ | UL$_{\rm F}$ $10^{-10}$ [m$^{-2}$ s$^{-1}$] | UL$_{\rm EF}$ $10^{-10}$ [erg m$^{-2}$ s$^{-1}$] | UL$_{\rm L}$ $10^{35}$ [erg s$^{-1}$] | UL$_{\rm eff,acc}$ [%] |
|---|---|---|---|---|---|---|---|---|---|---|---|---|---|---|
| HMXB | 46 | HS16, Y17 | 15.262 | -72.116 | 304.500 | 33.56 | 344.000 | - | 26.14 | -1.33 | 78.37 | 136.63 | 5.89 | 49 |
| HMXB | 47 | HS16, Y17 | 12.686 | -73.268 | 323.200 | -174.77 | 116.600 | - | 26.42 | -0.40 | 43.66 | 76.12 | 3.28 | 27 |
| HMXB | 48 | HS16, Y17 | 13.217 | -72.287 | 325.400 | -34.72 | 45.930 | - | 31.28 | 1.97 | 362.38 | 631.77 | 27.22 | 227 |
| HMXB | 49 | HS16, Y17 | 13.516 | -72.442 | 341.900 | 171.30 | - | - | 34.00 | 0.78 | 273.86 | 477.44 | 20.57 | 171 |
| HMXB | 50 | HS16, Y17 | 15.808 | -72.154 | 345.200 | -28.94 | 94.400 | - | 25.28 | -0.60 | 101.64 | 177.20 | 7.63 | 64 |
| HMXB | 51 | HS16, Y17 | 15.336 | -72.189 | 455.000 | -150.46 | 74.560 | - | 30.11 | -0.98 | 52.28 | 91.15 | 3.93 | 33 |
| HMXB | 52 | HS16, Y17 | 13.733 | -72.753 | 499.200 | 1.04 | 265.300 | - | 35.28 | 0.83 | 302.81 | 527.90 | 22.74 | 190 |
| HMXB | 53 | HS16, Y17 | 15.698 | -72.081 | 522.500 | -208.33 | - | - | 23.94 | -0.50 | 111.81 | 194.92 | 8.40 | 70 |
| HMXB | 54 | HS16, Y17 | 14.401 | -72.326 | 565.000 | 26.62 | 151.800 | - | 35.44 | 1.33 | 364.85 | 636.07 | 27.40 | 228 |
| HMXB | 55 | HS16, Y17 | 13.898 | -72.485 | 644.600 | 17.36 | - | - | 34.96 | 2.68 | 454.21 | 791.87 | 34.12 | 284 |
| HMXB | 56 | HS16, Y17 | 13.826 | -72.648 | 701.600 | 347.22 | 412.000 | - | 34.51 | 0.64 | 250.83 | 437.30 | 18.84 | 157 |
| HMXB | 57 | HS16, Y17 | 16.481 | -72.064 | 726.000 | 23.15 | - | - | 21.64 | 0.99 | 300.80 | 524.41 | 22.59 | 188 |
| HMXB | 58 | HS16, Y17 | 12.425 | -73.388 | 755.500 | -474.54 | 389.900 | - | 25.10 | -0.16 | 47.31 | 82.48 | 3.55 | 30 |
| HMXB | 59 | HS16, Y17 | 12.374 | -73.183 | 894.000 | -78.70 | 91.500 | - | 30.56 | 0.81 | 167.43 | 291.90 | 12.58 | 105 |
| HMXB | 60 | HS16, Y17 | 15.528 | -71.688 | 967.000 | -72.92 | 101.400 | - | 19.32 | -0.17 | 186.93 | 325.88 | 14.04 | 117 |
| HMXB | 61 | HS16, Y17 | 21.942 | -73.549 | 1062.000 | 821.76 | - | - | 6.86 | 0.09 | 151.39 | 263.93 | 11.37 | 95 |
| HMXB | 62 | HS16, Y17 | 15.906 | -72.026 | 1323.000 | -752.31 | - | - | 23.45 | 1.16 | 228.95 | 399.15 | 17.20 | 143 |
| HMXB | 63 | HS16, Y17 | 13.693 | -72.423 | 4693.000 | - | - | - | 34.00 | 2.05 | 484.46 | 844.60 | 36.39 | 303 |
| HMXB | 64 | HS16, Y17 | 8.234 | -73.806 | - | - | - | - | 0.00 | 0.00 | 0.00 | 0.00 | 0.00 | 0 |
| HMXB | 65 | HS16, Y17 | 10.533 | -73.751 | - | - | - | - | 12.59 | 1.48 | 306.84 | 534.93 | 23.05 | 192 |
| HMXB | 70 | HS16, Y17 | 12.142 | -73.042 | - | - | 414.913 | - | 31.34 | -0.79 | 72.67 | 126.69 | 5.46 | 45 |
| HMXB | 71 | HS16, Y17 | 12.204 | -73.274 | - | - | - | - | 25.67 | 1.35 | 219.60 | 382.85 | 16.49 | 137 |

Table A.10: *- continued*

| Type | Nr$^a$ | Reference | RA$^a$ [°] | Dec$^a$ [°] | P$^a$ [s] | $\dot{P}^b$ $10^{-10}$ [s s$^{-1}$] | P$^a_{\mathrm{orbit}}$ [d] | ecc.$^c$ | livetime [h] | $\sigma$ | UL$_{\mathrm{F}}$ $10^{-10}$ [m$^{-2}$ s$^{-1}$] | UL$_{\mathrm{EF}}$ $10^{-10}$ [erg m$^{-2}$ s$^{-1}$] | UL$_{\mathrm{L}}$ $10^{35}$ [erg s$^{-1}$] | UL$_{\mathrm{eff,acc}}$ [%] |
|---|---|---|---|---|---|---|---|---|---|---|---|---|---|---|
| HMXB | 72 | HS16, Y17 | 12.232 | -73.829 | 15.640 | - | 36.432 | - | 17.07 | 0.73 | 162.25 | 282.86 | 12.19 | 102 |
| HMXB | 74 | HS16, Y17 | 12.307 | -73.194 | - | - | 80.100 | - | 27.05 | 1.03 | 172.50 | 300.74 | 12.96 | 108 |
| HMXB | 76 | HS16, Y17 | 12.377 | -73.519 | - | - | - | - | 23.01 | -0.39 | 80.32 | 140.02 | 6.03 | 50 |
| HMXB | 79 | HS16, Y17 | 12.551 | -73.199 | - | - | - | - | 30.60 | 0.56 | 137.26 | 239.29 | 10.31 | 86 |
| HMXB | 81 | HS16, Y17 | 12.650 | -73.294 | - | - | - | - | 26.33 | -0.79 | 38.90 | 67.82 | 2.92 | 24 |
| HMXB | 84 | HS16, Y17 | 12.739 | -73.169 | - | - | - | - | 36.21 | -0.39 | 56.34 | 98.22 | 4.23 | 35 |
| HMXB | 85 | HS16, Y17 | 12.774 | -73.220 | - | - | - | - | 31.37 | 0.29 | 68.00 | 118.55 | 5.11 | 43 |
| HMXB | 86 | HS16, Y17 | 12.821 | -73.268 | - | - | - | - | 26.84 | -0.52 | 46.12 | 80.41 | 3.46 | 29 |
| HMXB | 91 | HS16, Y17 | 12.998 | -73.491 | - | - | - | - | 25.16 | -1.13 | 80.98 | 141.18 | 6.08 | 51 |
| HMXB | 93 | HS16, Y17 | 13.064 | -73.321 | - | - | - | - | 31.19 | -0.38 | 61.68 | 107.53 | 4.63 | 39 |
| HMXB | 95 | HS16, Y17 | 13.155 | -72.459 | - | - | - | - | 33.31 | 1.38 | 257.49 | 448.91 | 19.34 | 161 |
| HMXB | 96 | HS16, Y17 | 13.188 | -72.479 | - | - | - | - | 33.48 | 1.08 | 188.20 | 328.11 | 14.14 | 118 |
| HMXB | 97 | HS16, Y17 | 13.217 | -72.808 | - | - | - | - | 36.29 | 1.53 | 277.31 | 483.45 | 20.83 | 174 |
| HMXB | 101 | HS16, Y17 | 13.372 | -72.563 | - | - | - | - | 33.90 | 0.51 | 93.43 | 162.89 | 7.02 | 58 |
| HMXB | 104 | HS16, Y17 | 13.424 | -72.886 | - | - | - | - | 36.34 | 1.41 | 152.95 | 266.65 | 11.49 | 96 |
| HMXB | 105 | HS16, Y17 | 13.469 | -72.444 | - | - | - | - | 34.09 | 1.06 | 279.48 | 487.24 | 20.99 | 175 |
| HMXB | 107 | HS16, Y17 | 13.539 | -72.695 | - | - | - | - | 34.25 | 1.89 | 325.72 | 567.86 | 24.46 | 204 |
| HMXB | 111 | HS16, Y17 | 13.782 | -72.378 | - | - | - | - | 33.73 | 2.66 | 607.75 | 1059.53 | 45.65 | 380 |
| HMXB | 114 | HS16, Y17 | 14.023 | -72.003 | - | - | - | - | 28.80 | -1.02 | 70.17 | 122.33 | 5.27 | 44 |
| HMXB | 115 | HS16, Y17 | 14.058 | -72.500 | - | - | 72.231 | - | 34.98 | 2.70 | 434.73 | 757.90 | 32.65 | 272 |
| HMXB | 116 | HS16, Y17 | 14.061 | -72.632 | - | - | - | - | 34.96 | 0.72 | 250.87 | 437.36 | 18.84 | 157 |
| HMXB | 117 | HS16, Y17 | 14.079 | -72.468 | - | - | - | - | 34.66 | 3.57 | 497.96 | 868.14 | 37.40 | 312 |

Table A.10: *- continued*

| Type | Nr$^a$ | Reference | RA$^a$ [°] | Dec$^a$ [°] | P$^a$ [s] | $\dot{P}^b$ $10^{-10}$ [s s$^{-1}$] | P$^a_{\mathrm{orbit}}$ [d] | ecc.$^c$ | livetime [h] | $\sigma$ | UL$_{\mathrm{F}}$ $10^{-10}$ [m$^{-2}$ s$^{-1}$] | UL$_{\mathrm{EF}}$ $10^{-10}$ [erg m$^{-2}$ s$^{-1}$] | UL$_{\mathrm{L}}$ $10^{35}$ [erg s$^{-1}$] | UL$_{\mathrm{eff,acc}}$ [%] |
|---|---|---|---|---|---|---|---|---|---|---|---|---|---|---|
| HMXB | 119 | HS16, Y17 | 14.349 | -72.399 | - | - | - | - | 34.67 | 2.34 | 413.12 | 720.22 | 31.03 | 259 |
| HMXB | 121 | HS16, Y17 | 15.126 | -72.343 | - | - | - | - | 35.14 | 1.79 | 352.52 | 614.57 | 26.48 | 221 |
| HMXB | 123 | HS16, Y17 | 15.232 | -72.389 | - | - | - | - | 35.30 | 1.06 | 322.29 | 561.87 | 24.21 | 202 |
| HMXB | 124 | HS16, Y17 | 15.448 | -71.931 | - | - | - | - | 23.02 | 1.18 | 231.18 | 403.03 | 17.36 | 145 |
| HMXB | 125 | HS16, Y17 | 15.482 | -72.544 | - | - | 35.610 | - | 35.45 | 0.48 | 145.60 | 253.83 | 10.94 | 91 |
| HMXB | 126 | HS16, Y17 | 15.483 | -72.174 | - | - | - | - | 25.72 | -0.81 | 59.12 | 103.07 | 4.44 | 37 |
| HMXB | 132 | HS16, Y17 | 16.122 | -72.527 | - | - | 29.750 | - | 34.30 | 2.75 | 221.58 | 386.30 | 16.64 | 139 |
| HMXB | 133 | HS16, Y17 | 16.148 | -72.363 | - | - | - | - | 29.73 | 0.39 | 117.26 | 204.42 | 8.81 | 73 |
| HMXB | 136 | HS16, Y17 | 16.637 | -73.262 | - | - | - | - | 22.95 | 0.12 | 320.74 | 559.17 | 24.09 | 201 |
| HMXB | 137 | HS16, Y17 | 16.935 | -72.462 | - | - | 1180.000 | - | 28.66 | -0.31 | 90.69 | 158.11 | 6.81 | 57 |
| HMXB | 141 | HS16, Y17 | 19.912 | -73.503 | - | - | - | - | 13.00 | -0.03 | 144.98 | 252.76 | 10.89 | 91 |
| HMXB | 142 | HS16, Y17 | 20.421 | -72.959 | - | - | 84.000 | - | 15.12 | 1.90 | 170.66 | 297.53 | 12.82 | 107 |
| HMXB | 143 | HS16, Y17 | 20.865 | -73.356 | - | - | 119.900 | - | 10.57 | 0.00 | 299.65 | 522.40 | 22.51 | 188 |

[a] The numbering, coordinates, spin and orbital periods are taken from HS16 [102].

[b] The spin down derivative, if available, is taken from Y17 [292].

[c] Eccentricities are taken from CK15 [378].

Livetime, significance $\sigma$ and flux upper limits UL$_{\mathrm{F}}$ are extracted from the respective sky maps in the energy range of $0.4-10$ TeV. Upper limits on the energy flux UL$_{\mathrm{EF}}$, luminosity UL$_{\mathrm{L}}$ and efficiency UL$_{\mathrm{eff}}$ are estimated as described in the text (Section 5.2.4).

Table A.11: Integral flux upper limits for the SMC PSRs in the energy range $1-100\,$TeV.

| Type | Source Name | Reference | RA$^a$ [°] | Dec$^a$ [°] | P$^a$ [s] | $\dot{P}^a$ $10^{-15}$ [s s$^{-1}$] | $\dot{E}^a$ $10^{35}$ [erg s$^{-1}$] | livetime [h] | $\sigma$ | UL$_{\mathrm{F}}$ $10^{-10}$ [m$^{-2}$ s$^{-1}$] | UL$_{\mathrm{EF}}$ $10^{-10}$ [erg m$^{-2}$ s$^{-1}$] | UL$_{\mathrm{L}}$ $10^{35}$ [erg s$^{-1}$] | UL$_{\mathrm{eff}}$ [%] |
|---|---|---|---|---|---|---|---|---|---|---|---|---|---|
| PSR | J0043-7300 | Titus et al 2019 | 10.858 | -73.189 | 0.94 | - | - | 50.90 | -1.26 | 4.91 | 25.34 | 1.09 | - |
| PSR | J0045-7042 | ATNF | 11.357 | -70.702 | 0.63 | 2.49 | 0.0039 | 21.95 | 0.27 | 17.44 | 89.94 | 3.87 | 99356 |
| PSR | J0057-7201 | ATNF | 14.433 | -72.022 | 0.74 | 0.10 | 0.0001 | 43.53 | 0.91 | 12.26 | 63.22 | 2.72 | 2779235 |
| PSR | J0100-7211 | ATNF | 15.179 | -72.193 | 8.02 | 18800.00 | 0.0140 | 44.67 | 0.19 | 10.74 | 55.39 | 2.39 | 17046 |
| PSR | J0111-7131 | ATNF | 17.870 | -71.530 | 0.69 | 7.09 | 0.0086 | 21.34 | -1.06 | 7.28 | 37.54 | 1.62 | 18806 |
| PSR | J0113-7220 | ATNF | 18.296 | -72.342 | 0.33 | 4.86 | 0.0550 | 30.73 | 0.06 | 10.55 | 54.39 | 2.34 | 4261 |
| PSR | J0131-7310 | ATNF | 22.869 | -73.169 | 0.35 | 1.76 | 0.0160 | 6.18 | 0.53 | 34.34 | 177.13 | 7.63 | 47697 |
| PSR | J0052-72 | Titus et al 2019 | 13.119 | -72.087 | 0.19 | - | - | 49.27 | -1.00 | 4.77 | 24.63 | 1.06 | - |

[a] Coordinates, period, period derivative and spin-down power are taken from the online version of the ATNF catalogue [282].

Livetime, significance $\sigma$ and flux upper limits UL$_{\mathrm{F}}$ are extracted from the respective sky maps in the energy range of $1-100\,$TeV. Upper limits on the energy flux UL$_{\mathrm{EF}}$, luminosity UL$_{\mathrm{L}}$ and efficiency UL$_{\mathrm{eff}}$ are estimated as described in the text (Section 5.2.4).

Table A.12: Integral flux upper limits for the SMC PSRs in the energy range $0.4-10\,$TeV.

| Type | Source Name | Reference | RA$^a$ [°] | Dec$^a$ [°] | P$^a$ [s] | $\dot{P}^a$ $10^{-15}$ [s s$^{-1}$] | $\dot{E}^a$ $10^{35}$ [erg s$^{-1}$] | livetime [h] | $\sigma$ | UL$_\mathrm{F}$ $10^{-10}$ [m$^{-2}$ s$^{-1}$] | UL$_\mathrm{EF}$ $10^{-10}$ [erg m$^{-2}$ s$^{-1}$] | UL$_\mathrm{L}$ $10^{35}$ [erg s$^{-1}$] | UL$_\mathrm{eff}$ [%] |
|---|---|---|---|---|---|---|---|---|---|---|---|---|---|
| PSR | J0043-7300 | Titus et al 2019 | 10.858 | -73.189 | 0.94 | - | - | 20.22 | 0.77 | 211.24 | 368.27 | 15.87 | - |
| PSR | J0045-7042 | ATNF | 11.357 | -70.702 | 0.63 | 2.49 | 0.0039 | - | - | - | - | - | - |
| PSR | J0057-7201 | ATNF | 14.433 | -72.022 | 0.74 | 0.10 | 0.0001 | 29.75 | -0.90 | 68.42 | 119.28 | 5.14 | 5243949 |
| PSR | J0100-7211 | ATNF | 15.179 | -72.193 | 8.02 | 18800.00 | 0.0140 | 30.51 | -0.27 | 94.15 | 164.14 | 7.07 | 50511 |
| PSR | J0111-7131 | ATNF | 17.870 | -71.530 | 0.69 | 7.09 | 0.0086 | 10.42 | 3.65 | 419.73 | 731.75 | 31.53 | 366580 |
| PSR | J0113-7220 | ATNF | 18.296 | -72.342 | 0.33 | 4.86 | 0.0550 | 21.12 | 0.80 | 210.47 | 366.93 | 15.81 | 28743 |
| PSR | J0131-7310 | ATNF | 22.869 | -73.169 | 0.35 | 1.76 | 0.0160 | 5.54 | 0.91 | 125.85 | 219.40 | 9.45 | 59078 |
| PSR | J0052-72 | Titus et al 2019 | 13.119 | -72.087 | 0.19 | - | - | 25.52 | -0.98 | 77.25 | 134.67 | 5.80 | - |

[a] Coordinates, period, period derivative and spin-down power are taken from the online version of the ATNF catalogue [282].

Livetime, significance $\sigma$ and flux upper limits UL$_\mathrm{F}$ are extracted from the respective sky maps in the energy range of $0.4-10\,$TeV. Upper limits on the energy flux UL$_\mathrm{EF}$, luminosity UL$_\mathrm{L}$ and efficiency UL$_\mathrm{eff}$ are estimated as described in the text (Section 5.2.4).

Table A.13: Integral flux upper limits for the SMC SFRs in the energy range $1-100$ TeV.

| Type | Source Name | Reference | RA [°] | Dec [°] | diameter [pc] | $\rho_{ass}$ $10^{-6}$ [pc$^{-2}$] | livetime [h] | $\sigma$ | UL$_{\mathrm{F}}$ $10^{-10}$ [m$^{-2}$ s$^{-1}$] | UL$_{\mathrm{EF}}$ $10^{-10}$ [erg m$^{-2}$ s$^{-1}$] | UL$_{\mathrm{L}}$ $10^{35}$ [erg s$^{-1}$] |
|---|---|---|---|---|---|---|---|---|---|---|---|
| SFR | A2 | L07 | 21.038 | -73.148 | 187 | 9.08 | 10.70 | -0.87 | 22.84 | 117.81 | 5.08 |
| SFR | A5 | L07 | 17.296 | -73.194 | 187 | 9.08 | 35.18 | -1.32 | 17.72 | 91.40 | 3.94 |
| SFR | A7 | L07 | 16.479 | -72.046 | 257 | 4.81 | 37.13 | 3.22 | 51.31 | 264.65 | 11.40 |
| SFR | A9 | L07 | 15.704 | -72.420 | 161 | 12.35 | 40.81 | 1.17 | 25.70 | 132.55 | 5.71 |
| SFR | A13 | L07 | 14.363 | -72.540 | 241 | 10.98 | 44.95 | -0.79 | 15.99 | 82.47 | 3.55 |
| SFR | A15 | L07 | 13.417 | -72.658 | 268 | 8.89 | 53.03 | -0.25 | 20.25 | 104.46 | 4.50 |
| SFR | A16 | L07 | 13.242 | -73.236 | 268 | 8.89 | 42.87 | -0.20 | 20.40 | 105.24 | 4.53 |
| SFR | A17 | L07 | 13.146 | -73.427 | 292 | 3.73 | 39.61 | 0.48 | 45.75 | 235.96 | 10.17 |
| SFR | C9 | L07 | 14.525 | -72.649 | 321 | 3.09 | 44.83 | -0.64 | 26.10 | 134.62 | 5.80 |
| SFR | C14 | L07 | 12.925 | -73.224 | 329 | 2.93 | 50.88 | -0.78 | 24.77 | 127.77 | 5.50 |
| SFR | C22 | L07 | 11.650 | -73.369 | 328 | 2.95 | 48.69 | -2.16 | 28.50 | 146.98 | 6.33 |
| SFR | C23 | L07 | 11.333 | -73.234 | 320 | 12.44 | 50.25 | -1.48 | 26.67 | 137.57 | 5.93 |

[a] Coordinates, diameter and density of associations ($\rho_{\mathrm{ass}}$) are taken from L07 [105].

The livetime is extracted from the acceptance corrected livetime sky map, significance $\sigma$ and flux upper limits UL$_{\mathrm{F}}$ are estimated based on the spatially integrated VHE $\gamma$-ray emission within the extension of the respective SFR in the energy range of $1-100$ TeV as explained in Section 5.3.4. Upper limits on the energy flux UL$_{\mathrm{EF}}$ and luminosity UL$_{\mathrm{L}}$ are estimated as described in section (Section 3.1.8).

Table A.14: Integral flux upper limits for the SMC SFRs in the energy range $0.4-10$ TeV.

| Type | Source Name | Reference | RA [°] | Dec [°] | diameter [pc] | $\rho_{ass}$ $10^{-6}$ [pc$^{-2}$] | livetime [h] | $\sigma$ | UL$_{\mathrm{F}}$ $10^{-10}$ [m$^{-2}$ s$^{-1}$] | UL$_{\mathrm{EF}}$ $10^{-10}$ [erg m$^{-2}$ s$^{-1}$] | UL$_{\mathrm{L}}$ $10^{35}$ [erg s$^{-1}$] |
|---|---|---|---|---|---|---|---|---|---|---|---|
| SFR | A2 | L07 | 21.038 | -73.148 | 187 | 9.08 | 10.24 | 0.44 | 134.46 | 234.41 | 10.10 |
| SFR | A5 | L07 | 17.296 | -73.194 | 187 | 9.08 | 23.61 | 2.01 | 164.44 | 286.68 | 12.35 |
| SFR | A7 | L07 | 16.479 | -72.046 | 257 | 4.81 | 21.55 | -0.87 | 103.66 | 180.71 | 7.79 |
| SFR | A9 | L07 | 15.704 | -72.420 | 161 | 12.35 | 35.61 | -1.29 | 62.63 | 109.19 | 4.70 |
| SFR | A13 | L07 | 14.363 | -72.540 | 241 | 10.98 | 35.24 | 0.62 | 81.57 | 142.21 | 6.13 |
| SFR | A15 | L07 | 13.417 | -72.658 | 268 | 8.89 | 33.78 | 0.14 | 192.77 | 336.07 | 14.48 |
| SFR | A16 | L07 | 13.242 | -73.236 | 268 | 8.89 | 34.47 | 2.06 | 134.38 | 234.27 | 10.09 |
| SFR | A17 | L07 | 13.146 | -73.427 | 292 | 3.73 | 25.40 | 0.74 | 86.79 | 151.31 | 6.52 |
| SFR | C9 | L07 | 14.525 | -72.649 | 321 | 3.09 | 33.91 | 0.27 | 140.90 | 245.64 | 10.58 |
| SFR | C14 | L07 | 12.925 | -73.224 | 329 | 2.93 | 33.56 | 1.94 | 214.27 | 373.56 | 16.09 |
| SFR | C22 | L07 | 11.650 | -73.369 | 328 | 2.95 | 21.38 | -0.13 | 161.67 | 281.85 | 12.14 |
| SFR | C23 | L07 | 11.333 | -73.234 | 320 | 12.44 | 21.57 | -1.04 | 121.61 | 212.02 | 9.13 |

[a] Coordinates, diameter and density of associations ($\rho_{\mathrm{ass}}$) are taken from L07 [105].

The livetime is extracted from the acceptance corrected livetime sky map, significance $\sigma$ and flux upper limits UL$_{\mathrm{F}}$ are estimated based on the spatially integrated VHE $\gamma$-ray emission within the extension of the respective SFR in the energy range of $0.4-10$ TeV as explained in Section 5.3.4. Upper limits on the energy flux UL$_{\mathrm{EF}}$ and luminosity UL$_{\mathrm{L}}$ are estimated as described in section (Section 3.1.8).

# Appendix B

# Bow shocks of runaway stars

Stars with strong winds that move supersonically through the ISM can produce a bow shock while compressing matter ahead of the star. These shocks were proposed to be acceleration sites for cosmic rays up to multi-TeV energies [60]. As runaway stars are typically isolated objects moving through a low density ISM, the bow-shaped shocks are also mostly isolated systems. A continuous injection of material through the stellar wind results in a system, which is in steady-state leading to an equilibrium of continuous particle acceleration and radiative losses in a self-contained system. Thus, the study of $\gamma$ rays originating from bow shocks of runaway stars is particularly interesting to understand cosmic-ray acceleration mechanisms in astrophysical shocks.

This chapter describes the VHE $\gamma$-ray analysis of bow shocks of runaway stars, which got serendipitously observed within the HGPS [63] and other targeted H.E.S.S. observations. The chapter starts with a short introduction to the theoretical background in Section B.1, followed by an overview of existing studies of bow shocks of runaway stars. The VHE $\gamma$-ray analysis is described in Section B.4. Due to the diverse observational parameter space, the systematic uncertainties, described in Section B.4.2 have to be considered to guarantee a mostly unbiased population study, which is described in Section B.4.4.

## B.1 Formation and Structure of Bow Shocks of Runaway Stars

Stars, that are born at the same time out of the same molecular cloud, are referred to as stellar clusters, if they are gravitationally bound, or as stellar associations moving around a central black hole with an orbital speed given by the galaxy's rotation curve. Due to gravitational interactions or energetic events such as supernova explosions a star can be ejected from its birth association [379–381]. With typical peculiar velocities of $v \sim 30$ km/s [382, 383], those *runaway stars* move supersonically through the ISM. Between 10% and 30% of those runaway stars exhibit strong winds (e.g. OB stars or Wolf-Rayet stars), a continuous flow of material ejected from the surface of the star, which leads to a bow shock, an arc-shaped structure, ahead of the star by compressing the surrounding gas [384, 385]. The collision of the supersonic stellar wind with the ISM results in a system of two shocks.

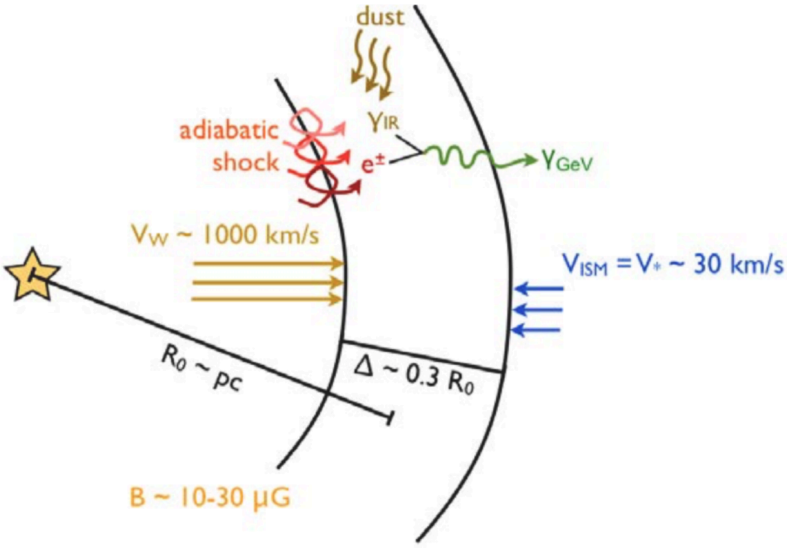

Figure B.1: Schematic structure of a bow shock at its rest frame. Image Credit: S. Klepser.

Figure B.1 schematically shows the structure of a bow shock and environmental parameters in the bow shock's rest frame. The arc-shaped shock forms at a typical distance $R_0$ (also called the stand-off radius) ahead of the star and consists of a slow forward shock and a reverse shock, which are separated by the contact discontinuity. Under the assumption that the stellar wind can be considered as a constant power source, the ram pressure of the wind $P_{\mathrm{w}} = \rho_{\mathrm{w}} \times v_{\mathrm{w}}^2$, with the wind density $\rho_{\mathrm{w}}$ and the wind velocity $v_{\mathrm{w}}$, and the ram pressure of the ISM $P_{\mathrm{ISM}} = \rho_{\mathrm{ISM}} \times v_{\mathrm{ISM}}^2$, with the ISM density $\rho_{\mathrm{ISM}}$ and the ISM velocity $v_{\mathrm{ISM}}$, can be assumed to be in equilibrium in the bow shock region. The stand-off radius is then given by:

$$R_0 = \sqrt{\frac{\dot{M}_* v_{\mathrm{w}}}{4\pi \rho_{\mathrm{ISM}} v_*^2}}$$

where $\dot{M}_*$ is the mass-loss rate of the star.

The forward shock moves approximately with the same speed as the runaway star $v_*$. As the cooling length of the shock is much smaller than the stand-off radius, the gas inside the shock is cooling rapidly and the shock is hence called radiative shock. The rebounded material causes a second shock, also called reverse shock, moving towards the star with the speed of the wind $v_{\mathrm{w}}$. As the reverse shock is moving much faster it can be considered to be adiabatic [386, 387]. The stellar wind continuously injects material into the stellar shock region thus providing the system continuously with target material, which is required for thermal as well as non-thermal emission. Via radiative heating of the swept up ISM by the stellar radiation field or via Bremsstrahlung caused by decelerated electrons in the ISM, bow shocks can produce thermal emission at infrared wavelengths, where they are typically detected. Figure B.2 shows an infra-red image of the bow shock of the B-type supergiant star Kappa Cassiopeiae.

Figure B.2: Infra-red image of the bow shock of the runaway star Kappa Cassiopeiae taken by Spitzer. Image Credit: NASA/JPL-Caltech

## B.2 Observations of Stellar Bow Shocks

Van Buren and McCray were the first reporting on thermal emission of bow-shaped structures around OB and Wolf-Rayet stars, seen by InfraRed Astronomical Satellite (IRAS) in the infra-red wavelength regime [388]. The first survey of stellar bow shocks of runaway stars was performed in 1995 based on IRAS data with the conclusion that the bow shape structures are a result of the radiatively heated swept up dust near the fast moving stars [384]. Other surveys have been performed by e.g. Noriega & Crespo [389] with a follow-up survey based on archival IRAS data [390], searching for bow shape structure in data from the Midcourse Space Experiment (MSX) satellite, the Spitzer Space Telescope and the preliminary data release of the Wide-Field Infrared Survey Explorer (WISE); or by Peri et al. [385], who compiled the first catalogue of bow shocks of runaway stars based on available IRAS data for catalogued runaway stars - the Extensive stellar BOw Shock Survey catalogue (E-BOSS), that was updated in 2015 to the most comprehensive catalogue of bow shocks of runaway stars - the second E-BOSS catalogue release [65]. The catalogue comprises 73 bow shock candidates that were selected based on existing catalogues and recent publications of bow shocks of runaway stars, mainly observed with the Wide-Field Infrared Survey Explorer (WISE), as well as serendipitously discovered bow shock for completion. All of the above listed surveys confirm the presence of thermal emission of supersonically moving stars.

In 2010, the first bow shock emitting non-thermal radio emission was detected [59]. Follow-up observations of Suzaku, searching for a non-thermal X-ray counterpart of the bow shock of BD 43°3654, revealed no significant emission towards the bow shock. However, the resulting upper limits constrained the emission model from Benaglia et al. [59], implying that either the efficiency of the shock-heating process was overestimated, leading to maximum electron energies of less than 10 TeV, or the magnetic field turbulences in the shock acceleration regions are smaller than assumed. All other searches for non-thermal X-ray emission from bow shocks resulted in upper limits (i.e. [391, 392]) or could not firmly identify the nature and origin of the emission (i.e. [61, 393]), leading to the conclusion, that the emitted synchrotron radiation of accelerated electrons seems to be below the sensitivity of the current generation of X-ray instruments.

A systematic search for $\gamma$-ray emission in the HE regime based on *Fermi* data, that would constrain the non-thermal emission due to inverse Compton radiation or due to proton-proton interactions as predicted by several studies [59, 60, 393], was performed by Schulz et al. [394], resulting in upper limits for 27 bow shock candidates. The upper limit for the most promising candidate $\zeta$ Ophiuchi was found to be a factor of $\sim 5$ below the predicted emission [60]. Recently, Sánchez-Ayaso et al. [395] discussed a possible association of two unidentified *Fermi* sources with stellar bow shocks and came to the conclusion, that an association is very likely but can not be fully confirmed. In the VHE regime the H.E.S.S. collaboration performed the first systematic search of bow shocks based on archival H.E.S.S. data [10]. (The results are presented in Section B.4.) In the following the relevant processes for non-thermal VHE $\gamma$-ray emission of bow shocks of runaway stars will be explained.

## B.3 Bow Shocks of Runaway Stars as Non-Thermal Emitters

Shocks provide perfect conditions for particle acceleration up to $> 10^{15}$ eV resulting in $\gamma$-ray emission up to TeV energies as has been shown for SNRs or PWNe [7, 63, 110]. Provided that the shock produced by the runaway star is strong and dense enough, particles are assumed to be accelerated via diffusive shock acceleration and radiate non-thermal emission through interactions of the relativistic particles with the swept-up material, radiation fields and magnetic fields. The kinetic energy that is transferred to non-thermal particles through diffusive shock acceleration is released via $\gamma$-rays. The resulting spectral energy distribution depends on the dominating radiative losses. Depending on the bow shock system, either the hadronic or the leptonic energy losses dominate [60], whereby the acceleration efficiency and maximum energy depend on the acceleration timescales. The different processes are described in more detail in the following. A more detailed description on the relevant non-thermal radiative losses can be found here [60].

### Synchrotron Radiation

Synchrotron radiation is released, when the relativistic cosmic rays inside bow shocks are deflected while gyrating in the magnetic field. The average energy-loss rate of relativistic electrons is given by Equation 4.1 and the cooling time is proportional to $E^{-1}$ assuming a fixed magnetic field. The radiated non-thermal emission can be observed at $\sim 10^{-10} - 10^{5}$ eV.
So far, only from the bow shock of the runaway star BD 43°3654 non-thermal emission is detected, that is attributed to synchrotron emission of relativistic electrons. Under the assumption, that the acceleration mechanisms are the same in all bow shocks of runaway stars, the radio detection of BD 43°3654 constrains the magnetic field in these systems.

### Inverse Compton Scattering

The cooled electrons (via synchrotron radiation) can up-scatter low-energy photons of the stellar radiation field or the infra-red photon field from heated dust thus leading to non-thermal inverse Compton radiation. The cooling time is given by Equation 4.2.
The target photon fields in bow shocks of runaway stars are dominated by the stellar radiation field at the distance $R_0$ from the star and the infra-red radiation field from heated dust cooling by radiating infra-red photons [60]. The incident photon energies are given by the temperature spectrum of the photon field. Both photon fields are assumed to follow a black-body spectrum with temperature $T_\star$, in case of the stellar photon field, and

$$T_{\mathrm{IR}} = 27 \left(\frac{a}{1\mu\mathrm{m}}\right)^{-1/6} \left(\frac{L_\star}{10^{38}\,\mathrm{erg/s}}\right)^{1/6} \left(\frac{R_0}{1\mathrm{pc}}\right)^{-1/3} \mathrm{K}$$

for the temperature of the infra-red photon field, following Draine & Lee [396]. $a$ depicts the dust grain size, that is assumed to be $a \sim 0.2\,\mu\mathrm{m}$.

### Relativistic Bremsstrahlung

Relativistic Bremsstrahlung is released, when electrons get deflected in the Coulomb field of protons and ionised nuclei. For estimating the cooling time caused by Bremsstrahlung in bow shocks of runaway stars, del Valle & Romero [60] assume a complete ionised plasma leading to

$$t_{\mathrm{Br}}^{-1} \propto n \ln E,$$

where $n$ is the density of the target ions in the shocked stellar wind, which is directly proportional to the stellar wind density, that mainly defines the flux level of the emitted spectrum. Due to the logarithmic dependence on the energy, the cooling time is almost independent of the energies of the electron population.

### Proton-Proton Inelastic Collisions

Protons mainly lose energy through inelastic proton-proton collisions with material provided by the ambient matter. The cooling time for proton-proton collisions is defined in Equation 4.4. The dependence of the energy of the non-thermal emission is rather weak for the energy range considered in this work (see Figure B.3).

### Non-Thermal Contribution from the shocked ISM

Relativistic particles escaping from the acceleration region to the denser shocked ISM continue cooling via proton-proton inelastic collisions and relativistic Bremsstrahlung. Particle diffusion is expected in systems with highly turbulent stellar winds colliding with the incoming ISM. The characteristic timescale for particle diffusion can be approximated by [387]:

$$t_{\mathrm{diff}} \sim \frac{R_0^2}{D_{10\,\mathrm{GeV}}},$$

where $D_{10\,\mathrm{GeV}}$ is the diffusion coefficient at $E = 10\,\mathrm{GeV}$. The diffusion coefficient is assumed to be only dependent on the particles energy, but it also depends on the diffusion regime (slow Bohm diffusion or fast diffusion). In the fast diffusion regime, particle diffusion is more relevant than in the Bohm regime. As well, the diffusion timescale depends on the physical properties of the star.

Particle advection can be caused by the velocity field of the stellar wind and the ISM. The characteristic timescale for particle advection can be estimated via [387]:

$$t_{\mathrm{adv}} \sim \frac{R_0}{v},$$

with $v$ being either the stellar wind velocity or the ISM velocity. Thus, the characteristic timescale for particle advection is energy independent and only depends on the stellar properties.

The $\gamma$ rays produced via non-thermal radiative losses of those escaped particles contribute to

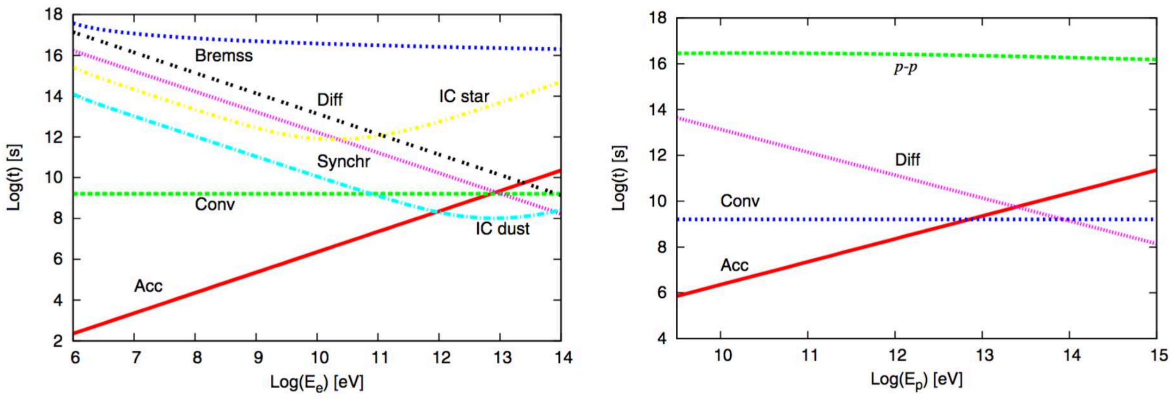

(a) (b)

Figure B.3: Acceleration and cooling timescales for electrons (left) and protons (right) for the bow shock of the runaway star $\eta$ Ophiuchi. Shown are the timescales for the acceleration (Acc) and cooling via synchrotron radiation (Synchr), inverse Compton on the stellar photon field (IC star) and the infra-red photon field from heated dust (IC dust), Bremsstrahlung (Brems), proton-proton inelastic collision (p-p), diffusion (Diff) and convection (Conv). Figure taken from [60].

the resulting spectral energy distribution emitted by the bow shock.

Figure B.3 shows the timescales for the particle acceleration together with the timescales for different energy loss processes for the bow shock of the runaway star $\eta$ Ophiuchi [60]. In this specific bow shock, the inverse Compton scattering of infra-red photons emitted from the dust dominates the non-thermal radiation losses. Bremsstrahlung, inverse Compton scattering of stellar photons and proton-proton inelastic collisions are subdominant processes in this system. del Valle & Romero conclude, that the non-thermal emission radiated by electrons or protons that diffused or advected into the dense ISM is negligible compared to the other energy losses.

### Absorption through $\gamma$-$\gamma$ Annihilation via Pair Creation

The $\gamma$ rays emitted via radiative losses of relativistic particles can be absorbed in the acceleration region immediately after being created due to photon-photon annihilation via pair production with thermal and non-thermal photons available in the acceleration region. The absorption depends on the line-of-sight [397] and hence on the orientation and dimension of the system. The $\gamma$-ray absorption varies strongly, being highest, if the bow shock is located behind the runaway star with respect to the observer. If the bow shock is located behind the star with respect to the observers perspective, the emitted $\gamma$ rays strongly interact with the ambient photon field, whereas the $\gamma$-ray absorption is lowest, if the bow shock is placed in front of the star in the line-of sight between observer and star. The threshold energy is given by

$$E\varepsilon = \frac{2(m_\mathrm{e}c^2)^2}{1 - e_\gamma e_\mathrm{ph}},$$

with $e_\gamma$ and $e_\mathrm{ph}$ being the directions of the travelling $\gamma$ ray and photon.

The $\gamma$-ray absorption leads to a reduction of the $\gamma$-ray flux finally reaching Earth.

#### Estimation of Maximum Particle Energy

Particles start to cool via non-thermal radiative losses as soon as the accelerated relativistic particles exceed a minimum energy $E_\mathrm{min} \gtrsim m_\mathrm{e}c^2$. The maximum energy of the electrons and protons is reached as soon as the energy losses dominate over the particle acceleration. Thus, the maximum energy can be estimated, by equating the acceleration timescale $t_\mathrm{acc}$ with the smallest cooling rate $t_\mathrm{cool,min}$. As the gyroradius of the particles increases with increasing energy, particles will only stay in the acceleration region, when in addition the Hillas criterion (Equation 4.6) is fulfilled.

Figure B.3 shows, that the maximum energy for both particle populations, electrons and protons, is of the order of $\sim 1$ TeV. When assuming an acceleration region with a size of $\sim 1$ pc and a magnetic field in the shock region of $\sim 10^{-6}$ G [387], the Hillas criterium is fulfilled with $E_\mathrm{max} \sim 1$ TeV.

### B.3.1 Power Considerations

The only source for the available power in the bow-shock system is the kinetic energy injected by the stellar wind:

$$P_\mathrm{wind} = \frac{1}{2}\dot{M}_\mathrm{w}v_\mathrm{w}^2.$$

As the wind is emitted isotropically in a volume of a sphere, whereas the bow shock covers only a limited solid angle of the sphere, only a fraction of the wind power is available in the bow shock system $P_\mathrm{bs} = fP_\mathrm{wind}$. Furthermore, only a small fraction $f_\mathrm{rp}$ of this kinetic energy is transferred to relativistic particles. This fraction is generally assumed to be $\sim 10\%$ [398]. In Section B.5 the results will be discussed in connection with a more recent paper, where the authors assume a fraction of $f_\mathrm{rp} \sim 0.05$.

Due to the simplistic structure of these systems, observations of bow shocks of runaway stars can prove or constrain these assumptions in a straight-forward manner.

### B.3.2 Particle Distribution

Under the assumption that particle injection into the acceleration region, particle acceleration, and radiative losses are in steady state, the particle distribution $N(E)$ for electrons and protons can be estimated by solving the transport equation in steady state [145]:

$$\frac{\partial}{\partial E}\left[\left.\frac{\mathrm{d}E}{\mathrm{d}t}\right|_{\mathrm{loss}} N(E)\right]+\frac{N(E)}{t_{\mathrm{esc}}}=Q(E), \tag{B.1}$$

where $t_{\mathrm{esc}}$ is the convection time. The injection function $Q(E)$ follows a power-law distribution $Q(E)=Q_0E^{-\alpha}$ with normalisation $Q_0$, which results from the diffusive shock acceleration. Solving Equation B.1 shows, that the particle distribution also follows a power law. Using the result for the particle distribution and the cooling times for each energy-loss process and taking into account the ratio of the power injected in electrons and positrons and the $\gamma$-ray absorption level, the luminosity of the respective non-thermal radiation process and hence the final spectral energy distribution due to non-thermal radiation can be estimated (more details can be found in del Valle & Romero [60]).

## B.4 VHE Analysis of selected Bow Shocks of Runaway Stars

Already in the 1980s massive stars with strong winds have been discussed to be $\gamma$-ray sources [399–401]. With the detection of non-thermal emission from the bow shock of BD 43°3654 [59] it is confirmed, that electrons can be accelerated to relativistic energies in the bow shocks of massive stars. More recent models by del Valle and Romero [60] predict non-thermal emission of bow shocks of runaway stars even up to TeV energies under the assumption, that the rich infrared photon fields, locally generated by the heated dust in the shock front, provide sufficient target material for inverse Compton interactions resulting in detectable $\gamma$-ray fluxes. Figure B.4 shows a spectral energy distribution (SED) for the most promising candidate $\zeta$ Ophiuchi, indicating that this source might be detectable with the current generation of IACTs.

The key energy ranges to constrain possible acceleration mechanisms in bow shocks of runaway stars are the high-energy (HE) and very-high-energy (VHE) regimes. A systematic search for HE $\gamma$-ray emission based on *Fermi*-LAT data resulted in an upper limit catalogue [394]. Although no HE $\gamma$-ray emission originating from those bow shocks was found, a systematic search for VHE $\gamma$-ray emission might be successful as the HE photons could be absorbed in the photon fields.

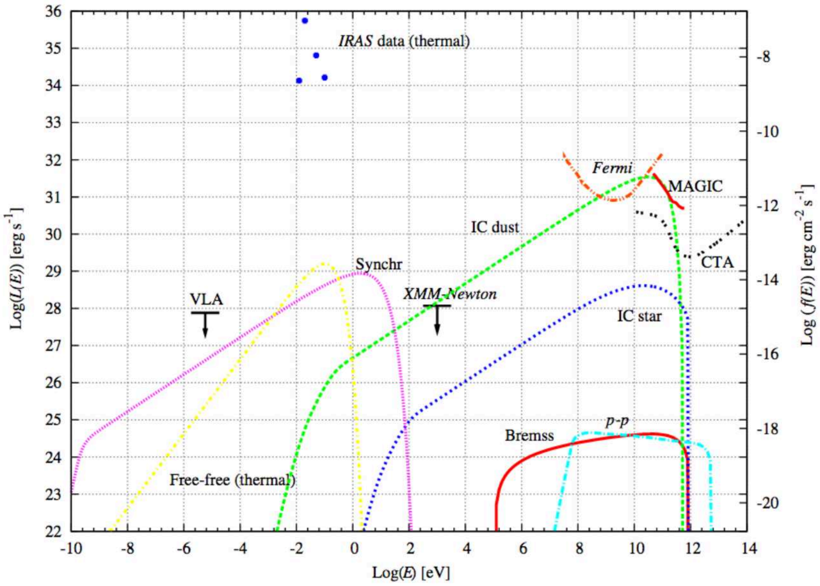

Figure B.4: Predicted spectral energy distribution for the O9.5V star $\zeta$ Ophiuchi, assuming a distance of $222$ pc, along with thermal data points from IRAS, non-thermal upper limits from VLA (Very Large Array) and XMM-Newton and sensitivity curves of the current (red) and future (black) $\gamma$-ray instruments *Fermi*, MAGIC (Major Atmospheric Gamma-Ray Imaging Cherenkov Telescopes) and CTA. Figure taken from [60].

### B.4.1 Selection of Bow Shocks

The bow shocks presented in this work, are selected based on available H.E.S.S. observations of those bow shock candidates listed in the second E-BOSS catalogue release. As most of the bow shock candidates are located towards the Galactic plane (see Figure B.5), many of them got observed serendipitously during the observations of the HGPS thus profiting from large exposure times. In total 26 bow shock candidates got observed by H.E.S.S. between 2003 and 2014, for which the analysis is presented in this work. The coordinates, distances, wind velocities and mass-loss rates for the selected sample are listed in Table B.1.

All bow shocks are analysed analogous to the subsample of bow shocks that were used to study the systematic uncertainties of a diverse data set (see Section 3.3.1 for more details). Due to larger distances than $0.07°$ between the bow shock and the star, the bow shocks HIP 32067, HIP 88652, HIP 92865, Star 1 and G 2 are analysed at the position of the bow shock. The positions are visually estimated based on publicly available WISE (Wide-field Infrared Survey Explorer) data, and the *on* region was increased to $\Theta_{cut} = 0.1°$. For HIP 32067, with a tabulated bow shock length of $13'$, the test region is increased to $\Theta_{cut} = 0.12°$.
The significance of the $\gamma$-ray emission for each bow shock is estimated using Equation 3.1.

Figure B.6 shows the significance distribution of all analysed bow shocks. None of the bow shocks shows significant VHE $\gamma$-ray emission in the energy range of $\sim 300$ GeV to $\sim 50$ TeV

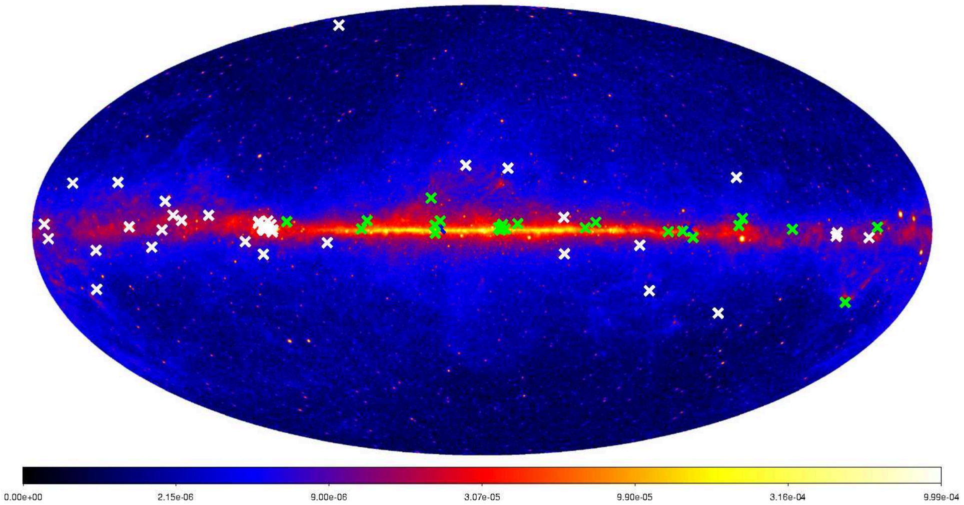

Figure B.5: Spatial distribution of all bow-shock candidates of runaway stars listed in the second E-BOSS catalogue release. Bow-shock candidates with H.E.S.S. exposure are highlighted in green. Bow shocks marked in blue are included in the publication by the H.E.S.S. collaboration [10] but are not included in this work (see text for more details). Sky map: Credit: NASA/DOE/*Fermi*-LAT Collaboration.

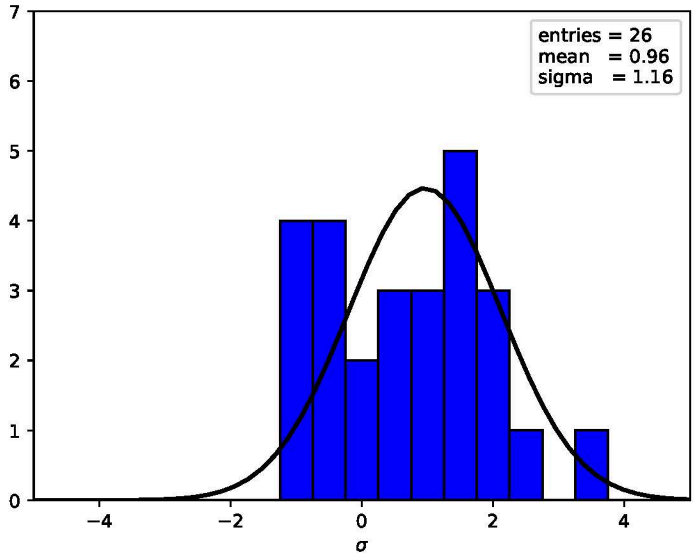

Figure B.6: Significance distribution for all analysed bow shocks. The distribution is following a gaussian distribution with a sigma of $\sim 1.2$ and a mean of $\sim 1$.

Table B.1: Selected bow shocks of runaway stars from the second E-BOSS catalogue release. ID, name of Star, distance $d$, wind velocity $v_{\mathrm{wind}}$ and mass-loss rate $\dot{M}$ are given as listed in the second E-BOSS catalogue release. The coordinates of the positions l and b denote the ones used for the analysis, which is not in all cases equal to the coordinates listed in table 3 of the E-BOSS catalogue and Table 6 of the second E-BOSS catalogue release [65, 385] (see text for details). The wind velocity is taken from Peri et al. [385, 385]; brackets indicate values adopted from stars with the same spectral type.

| ID | Star | l [°] | b [°] | $d$ [pc] | $v_{\mathrm{wind}}$ [km/s] | $\dot{M}$ $10^{-6} M_{\odot}$/yr |
|---|---|---|---|---|---|---|
| EB8 | HIP 25923 | 210.44 | $-20.98$ | 900 | [1000] | 0.06 |
| EB13 | HIP 32067* | 206.20 | 0.85 | 2117±367 | 2960 | 0.13 |
| EB15 | HIP 38430 | 243.16 | 0.36 | 900 | [2570] | 0.70 |
| EB17 | HIP 72510 | 318.77 | 2.77 | 350 | [2545] | 0.27 |
| EB18 | HIP 75095 | 322.68 | 0.91 | 800 | [1065] | 0.14 |
| EB23 | HIP 88652* | 15.11 | 3.36 | 650 | [1535] | 0.50 |
| EB24 | HIP 92865* | 41.75 | 3.41 | 350 | [1755] | 0.04 |
| EB32 | SER1** | 264.78 | 1.54 | - | 250 | 0.03 |
| EB33 | HIP 44368 | 263.10 | 3.90 | $1900\pm200^{a}$ | 1100 | 0.80 |
| EB36 | SER2** | 282.48 | $-2.46$ | - | - | - |
| EB40 | SER3** | 286.46 | $-0.34$ | - | 250 | 0.03 |
| EB41 | J1117-6120 | 291.88 | $-0.50$ | 7600 | 2600 | 0.60 |
| EB42 | SER7** | 347.15 | 2.36 | - | - | - |
| EB43 | G4 | 352.57 | 2.11 | 1700 | 2550 | 0.50 |
| EB44 | G2** | 352.81 | 1.34 | 1700 | 2250 | 0.40 |
| EB45 | G5 | 351.65 | 0.51 | 1700 | 2000 | 0.10 |
| EB46 | G6 | 353.06 | 1.29 | 1700 | [1000] | 0.10 |
| EB47 | G8 | 353.16 | 1.05 | 1700 | [1500] | 0.04 |
| EB48 | G1 | 353.42 | 0.45 | 1700 | 2100 | 0.20 |
| EB49 | G7 | 354.03 | 0.85 | 1700 | [1000] | 0.10 |
| EB50 | G3 | 353.30 | 0.08 | 1700 | 2000 | 0.40 |
| EB51 | HIP 86768 | 18.70 | 11.60 | 737 | [550] | 0.03 |
| EB52 | Star 1* | 16.99 | 1.77 | 1800 | 2200 | 0.63 |
| EB56 | BD -14 5040 | 16.89 | $-1.12$ | 1800 | 400 | 0.03 |
| EB57 | 4U 1907+09 | 43.74 | 0.47 | 4000 | 2900 | 0.70 |
| EB58 | HIP 98418 | 71.60 | 2.90 | 529.1 | 2545 | 0.24 |

[*] The analysis was performed at the bow shock coordinates, see text for more details.

[**] Coordinates listed in the second E-BOSS catalogue release are the apex coordinates of the bow shock and not from the star.

[a] The distance uncertainty (listed here) is wrong in the second E-BOSS catalogue release (1900±$0.1$ pc), correct value listed here [66]: $1.9\pm0.2$ kpc.

and the distribution is approximately following a standard gaussian distribution. An analysis of the sample with different selection cuts yields comparable result but with less constraining upper limits due to higher energy thresholds and slightly worse sensitivities of the respective selection cut. Upper limits are estimated and will be presented in Section B.4.3.

#### Mismatch of Coordinates in the second E-BOSS catalogue release

While writing this thesis, a mismatch in the coordinates listed in the second E-BOSS catalogue release was found. The published coordinates in the second E-BOSS catalogue release are inconsistent between Table 6 in the pdf version [65] and the corresponding online material[1]. The authors of the second E-BOSS catalogue release are informed but the problem of the mismatch has not yet been resolved during the time of writing the thesis. To make sure, that the conclusions drawn in this work are not affected by supposedly wrong results due to analyses at wrong coordinates, the affected bow shocks are discarded in this work. In total, six bow shocks are affected (marked with a blue cross in Figure B.5, partly overlapping due to small distances).
As this mismatch in the coordinates was only detected after the H.E.S.S. publication on the VHE $\gamma$-ray analysis of bow shocks of runaway stars, these bow shock candidates are included in the H.E.S.S. publication [10], for which the analysis was performed based on the coordinates listed in Table 6 of the pdf version of the second E-BOSS catalogue release.

### B.4.2 Investigation of the Systematic Uncertainties

Due to the fact that the bow shocks of runaway stars were observed serendipitously, the data sets cover a broad range of the observational parameter space. To ensure an unbiased estimation of the flux upper limits, the systematic uncertainties of the H.E.S.S. experiment are evaluated. This evaluation is done based on a subsample of bow shocks covering the most extreme values of the observational parameter space. A detailed description is given in Section 3.3. The resulting systematic uncertainties of 20% are adopted for all bow shocks of runaway stars.
However, the systematic population study can still be biased due to selection effects. First, the catalogued candidates of bow shocks of runaway stars are selected based on the IR surveys (mainly WISE, for further details see Section B.2). A selection bias in the IR surveys would translate into a selection bias in the E-BOSS catalogue and hence into a selection bias in the selected H.E.S.S. sample. Second, all bow shocks of runaway stars were only serendipitously observed by H.E.S.S. with the deepest exposure towards the Galactic plane. The coverage with H.E.S.S. exposure may introduce another selection bias in the selected sample. These selection effects can only be reduced by an improved sky coverage and are not further considered here.

---

[1] *http://vizier.u-strasbg.fr/viz-bin/VizieR-4*

### B.4.3 Estimation of Upper Limits

As no $\gamma$-ray emission towards the analysed bow shock candidates of runaway stars is detected, upper limits are estimated and compared to model predictions. The upper limits are estimated following the description in Section 3.1.8. Table B.2 lists the estimated upper limits for the selected sample of bow shocks of runaway stars. The upper limits are estimated at a confidence level of 95% by assuming a spectrum following a power law with spectral index $\Gamma = 2.5$ and taking into account the estimated systematic uncertainty of 20% for all bow shocks. Differential upper limits are estimated in five logarithmically equally spaced energy bins between $0.14$ and $17.92$ TeV, to have a connection between the lowest VHE $\gamma$-ray upper limits to the HE $\gamma$-ray model predictions. An integral upper limit is estimated in the energy range of $0.1 - 10$ TeV, to constrain the total power transferred to TeV $\gamma$-rays. For a better comparison of the upper limits relative to each other, the live-time (the observation time of H.E.S.S.) as well as the acceptance corrected live-time (the observation time corrected for non-uniform acceptance profiles across the camera field of view) in parentheses are also listed in the table.
Assuming different indices of $\Gamma = 2.0$ and $\Gamma = 3.0$ leads to marginal changes in the upper limits of the order of 10% or less.

### B.4.4 Constraining Model Predictions for Bow Shocks of Runaway Stars

A comparison of the upper limits to existing model predictions can either prove or constrain the predictions. As there are no model predictions available for the bow shocks presented in this work, the results are compared to four existing model predictions [59–62], including the radio detected source BD 43°3654. The models are motivated based on dedicated studies of the non-thermal emission for the four objects BD 43°3654, $\zeta$ Ophiuchi, HIP 101186 and AE Aurigae. As the bow shocks, investigated in this work, are spread over a large range of distances and do not necessarily match the distance of the sources for which model predictions exist, the flux upper limits are translated into luminosity upper limits using the listed distances from Table B.1 via Equation 3.7.

Figure B.7 shows the comparison between the estimated luminosity upper limits of all bow shocks with a given distance and the model predictions for the four bow shocks $\zeta$ Ophiuchi, BD 43°3654, AE Aurigae and HIP 101186. For three bow shocks of runaway stars investigated in this work the VHE ($\gtrsim 400$ GeV) $\gamma$-ray luminosity is lower than the predicted non-thermal emission from BD 43°3654. All other bow shocks of runaway stars have estimated luminosity upper limits for which none of the model predictions can be constrained.

To furthermore constrain the assumption of 10% of the kinetic energy being converted into non-

Table B.2: Flux upper limits ($95\%$ confidence-level) for the selected sample of bow shocks of runaway stars. Differential upper limits are estimated in 5 energy bands and an integrated upper limit is estimated in the energy range of $0.1-10$ TeV. ID, Star, (acceptance corrected) live-time and significance are listed as well.

| ID | Star | Live-time (acc.-corr.) | significance | Upper limits dN /dE [$10^{-12}$ TeV$^{-1}$ cm$^{-2}$ s$^{-1}$] | | | | | Upper limits E$^2$ dN /dE [$10^{-12}$ TeV cm$^{-2}$ s$^{-1}$] |
|---|---|---|---|---|---|---|---|---|---|
| | | | | Energy bins [TeV] | | | | | Energy range [TeV] |
| | | [h] | [$\sigma$] | $0.14-0.37$ | $0.37-0.97$ | $0.97-2.57$ | $2.57-6.78$ | $6.78-17.92$ | $0.1-10$ |
| EB8 | HIP 25923 | 3.9 (2.2) | 1.06 | 1.84 | 0.88 | 0.74 | 0.71 | 2.39 | 10.05 |
| EB13 | HIP 32067* | 21.7 (9.4) | -0.52 | 1.73 | 0.40 | 0.31 | 0.52 | 0.37 | 4.95 |
| EB15 | HIP 38430 | 1.8 (0.1) | -0.03 | 86.84 | 5.73 | 3.46 | 9.45 | 90.38 | 37.65 |
| EB17 | HIP 72510 | 12.8 (2.4) | 2.13 | 11.75 | 1.16 | 1.17 | 1.58 | 1.04 | 24.94 |
| EB18 | HIP 75095 | 22.5 (13.9) | 1.02 | 1.98 | 0.25 | 0.17 | 0.32 | 0.39 | 4.39 |
| EB23 | HIP 88652* | 9.2 (2.5) | 1.99 | 2.29 | 2.32 | 1.16 | 0.54 | 2.17 | 21.80 |
| EB24 | HIP 92865* | 3.9 (2.3) | 0.56 | 7.26 | 0.77 | 0.63 | 1.72 | 1.01 | 12.67 |
| EB32 | SER1** | 3.0 (2.0) | 1.88 | 2.94 | 1.10 | 0.61 | 0.44 | 1.14 | 12.95 |
| EB33 | HIP 44368 | 7.9 (6.1) | 1.92 | 2.43 | 0.93 | 0.35 | 0.30 | 0.83 | 10.41 |
| EB36 | SER2** | 15.7 (7.9) | 1.97 | 2.57 | 0.86 | 0.25 | 0.20 | 0.37 | 8.52 |
| EB40 | SER3** | 62.2 (29.0) | 1.65 | 1.48 | 0.35 | 0.31 | 0.28 | 0.17 | 5.13 |
| EB41 | J1117-6120 | 52.9 (32.3) | -0.23 | 1.48 | 0.38 | 0.13 | 0.19 | 0.13 | 2.64 |
| EB42 | SER7** | 13.2 (7.7) | -0.54 | 1.02 | 0.28 | 0.29 | 0.31 | 0.59 | 3.43 |
| EB43 | G4 | 4.8 (1.5) | 0.53 | 2.60 | 0.49 | 0.33 | 0.35 | 1.17 | 6.39 |
| EB44 | G2* | 20.9 (8.7) | 0.01 | 0.86 | 0.34 | 0.25 | 0.30 | 0.69 | 3.88 |
| EB45 | G5 | 28.0 (11.9) | 1.25 | 0.70 | 0.33 | 0.17 | 0.19 | 0.31 | 4.07 |
| EB46 | G6 | 30.1 (11.6) | -0.12 | 0.51 | 0.20 | 0.16 | 0.21 | 0.36 | 2.23 |
| EB47 | G8 | 34.9 (16.6) | 3.5 | 0.72 | 0.49 | 0.36 | 0.26 | 0.18 | 6.75 |
| EB48 | G1 | 56.4 (31.1) | 2.10 | 0.71 | 0.35 | 0.09 | 0.12 | 0.14 | 3.71 |
| EB49 | G7 | 38.0 (20.5) | 0.09 | 0.40 | 0.16 | 0.11 | 0.13 | 0.28 | 1.74 |
| EB50 | G3 | 48.3 (29.9) | 2.45 | 0.90 | 0.29 | 0.09 | 0.12 | 0.09 | 3.88 |
| EB51 | HIP 86768 | 1.3 (0.4) | -0.52 | 20.00 | 1.60 | 1.06 | 2.62 | 6.71 | 17.78 |
| EB52 | Star 1* | 20.6 (13.9) | -0.06 | 0.85 | 0.20 | 0.20 | 0.17 | 0.32 | 2.53 |
| EB56 | BD -14 5040 | 111.3 (73.2) | 2.71 | 0.37 | 0.12 | 0.15 | 0.15 | 0.09 | 2.99 |
| EB57 | 4U 1907+09 | 94.2 (63.1) | -0.76 | 0.72 | 0.12 | 0.08 | 0.09 | 0.19 | 1.38 |
| EB58 | HIP 98418 | 4.1 (3.0) | 0.93 | - | 22.73 | 1.23 | 1.21 | 1.18 | 37.15 |

[*] The analysis was performed at the position of the bow shock, see text for more details.

[**] The adopted coordinates from the second E-BOSS catalogue release are given at the position of the bow shock.

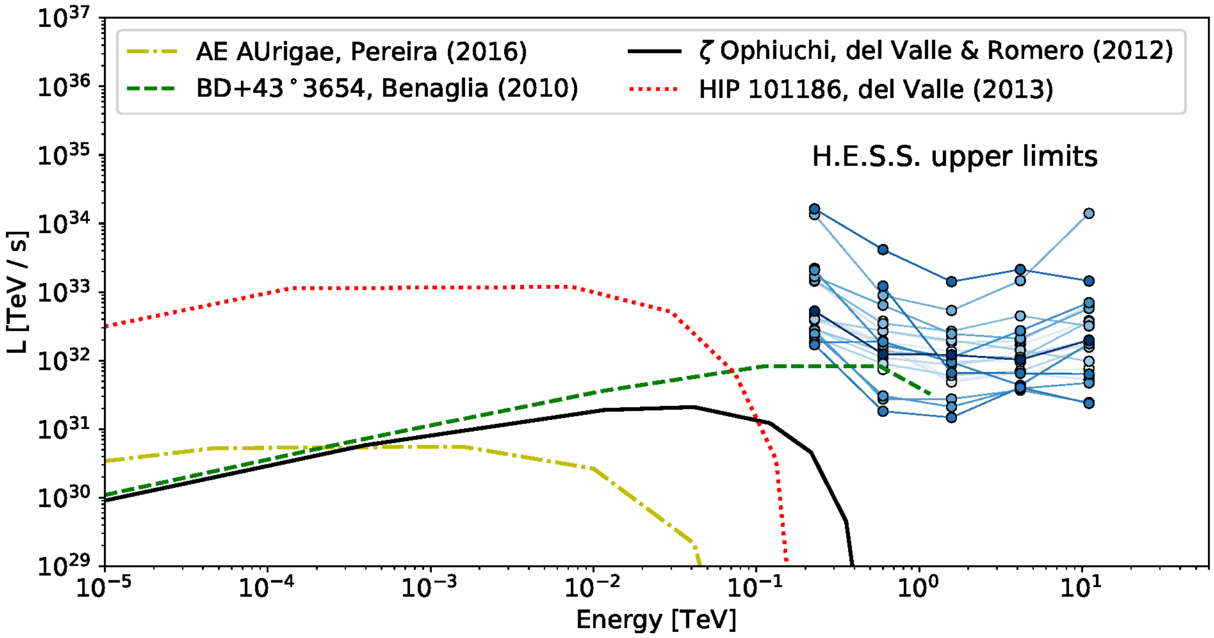

Figure B.7: VHE $\gamma$-ray luminosity upper limits for 22 bow shocks of runaway stars with known distances. The upper limits are compared to model predictions for four bow shocks (not part of the analysed sample).

thermal emission, the integral flux upper limits are compared to the available power in the bow shock system. The upper limit on the power, that is transferred to VHE $\gamma$ rays is estimated via Equation 3.7 after translating the integral flux upper limits in the energy range of $0.1 - 10$ TeV into integral energy flux upper limits via Equation 3.6.

The result is shown in Figure B.8 as the ratio of $P_{\mathrm{ul}}/P_{\mathrm{w}}$ as a function of the wind power. The red horizontal line depicts 0.1% of the kinetic wind energy. All bow shock candidates constrain the fraction of wind power converted into VHE $\gamma$-rays. For three bow shocks of runaway stars (4U 1907+09, HIP 72510 and Star 1) of the sample it is shown, that less than 0.1% of the wind power is converted into VHE $\gamma$-rays. The majority of the sample constrains the fraction of the wind power to be between 0.1-1%.

It should be noted, that the estimated wind power depicts the total power released in the wind and does not consider the solid angle covered by the bow shock. Assuming the wind power to be emitted isotropically, only a fraction of the total wind power given by $\frac{\Omega_{\mathrm{bs}}}{4\pi}$, with $\Omega_{\mathrm{bs}}$ being the solid angle covered by the bow shock, is available for particle acceleration in the vicinity of the bow shock. The solid angles of the bow-shock sample range from $\sim 0.25$ sr to $\sim 0.75$ sr. The solid angle estimation is based on the morphologies of the bow shocks, that are extracted from the published infra-red images by Peri et al. [65] and hence is just a rough estimation. Also no density variation within the bow shocks is taken into account. After correcting the wind power for the solid angle covered by the bow shocks, the fraction of wind energy being converted into VHE

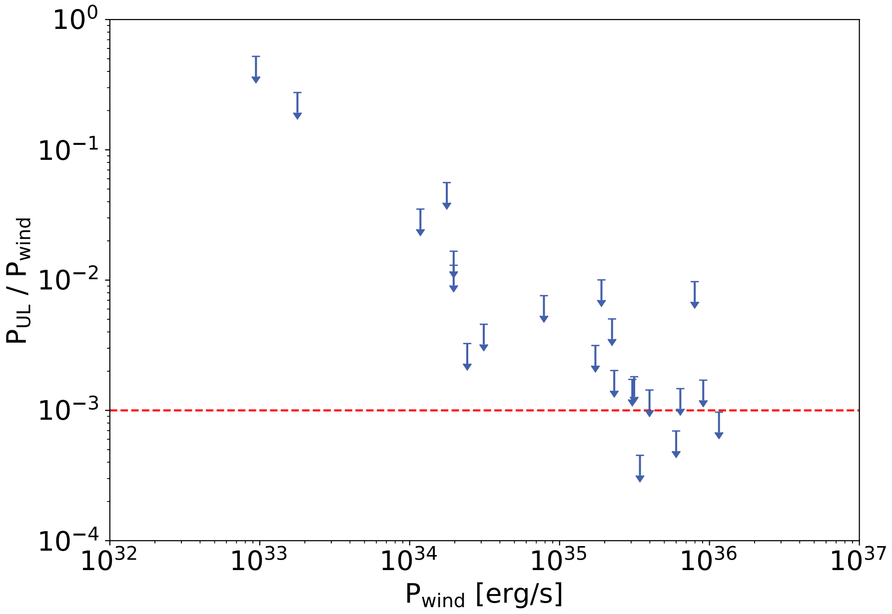

Figure B.8: Fraction of wind power, that is converted into VHE $\gamma$-rays as a function of the wind power for 22 bow shock candidates with identified runaway stars. The red dotted line depicts the fraction of 0.1% of the wind power being converted into VHE $\gamma$-rays.

$\gamma$ rays is still constrained to be $< 0.1\%$ by those three bow shocks of runaway stars.

## B.5 Conclusion

In this thesis, the most comprehensive study of bow shocks of runaway stars in VHE $\gamma$ rays is presented. By considering the systematic uncertainties of the experiment, a mostly unbiased estimation of the VHE $\gamma$-ray fluxes for the diverse data sets is achieved. The study reveals no evidence for VHE $\gamma$-ray emission for all bow shocks in the sample and suggests that the VHE $\gamma$-ray emission is below the flux level detectable by the current generation of IACTs. In combination with the HE $\gamma$-ray upper limits [394] and X-ray upper limits (i.e. [391, 392, 402]) the theoretical models published by the time of writing this thesis (see Figure B.7 and references therein) can be constrained.

There are several possible reasons for the overprediction of the VHE $\gamma$-ray flux levels in the models:

- Benaglia et al. [59] assumed for BD 43°3654 a mass-loss rate of $1.6 \times 10^{-4}\,\mathrm{M}_\odot$/yr [403]. A detailed study on the mass-loss rate of O-type and early B-type runaway stars by Kobulnicky et al. [404] resulted in a mass-loss rate of $\sim 2 \times 10^{-5}\,\mathrm{M}_\odot$/yr for BD 43°3654, almost one order of magnitude lower compared to the assumed mass-loss rate by Benaglia et al. As the density of the wind at the bow shock is proportional to the mass-loss rate, an overestimation directly translates into an overestimation of the wind density at the bow shock and hence into an overestimation of the density of accelerated particles producing $\gamma$ radiation.

- The particle acceleration in the bow shocks may be less efficient as assumed in the models. Toalá et al. [392] discuss, that the injection efficiency of energy from the thermal plasma to accelerate particles may be reduced due to the open morphology of the bow shock unlike e.g. in SNRs [405].
- Terada et al. [406] discuss, that the magnetic field in the bow shocks of runaway stars might be less turbulent as in PWNe or in SNRs as assumed in their model. If furthermore the magnetic-field turbulence is generated by the accelerated protons themselves (as is the case in SNRs), they conclude that the proton injection rate has to be smaller than in SNRs.
- The maximum energy of the accelerated particles might be lower than assumed in the model predictions leading to a lower maximum energy in the emitted $\gamma$-ray spectrum.
- BD 43°3654 might be an exceptional bow shock of its runaway star exhibiting more extreme physical properties as the other bow shocks of runaway stars. VHE $\gamma$-ray observations of BD 43°3654 would be required to confirm or disprove BD 43°3654 to be indeed a powerful VHE $\gamma$-ray emitter.

The fraction of kinetic energy of the stellar wind power translated into VHE $\gamma$-rays is constrained to be less than 0.1% for three bow shocks of runaway stars of the sample.

After publishing the VHE $\gamma$-ray results by the H.E.S.S. collaboration [10] del Valle & Pohl published a revised model by taking the X-ray, HE and VHE $\gamma$-ray flux upper limits into account [387]. The model is based on the assumption of electrons being accelerated through diffusive shock acceleration leading to non-thermal emission via synchrotron radiation at radio and X-ray energies and to $\gamma$-ray emission via inverse Compton up-scattering. This assumption is motivated by the detection of non-thermal radio emission from the bow shock of the runaway star BD 43°3654, that is expected to originate from synchrotron emission of relativistic electrons. For the calculations they consider a typical runaway star with typical stellar parameters. The model reveals that a fraction of the wind energy of about $\sim 10^{-4}$ is converted into inverse Compton emission with a peak emission at $\sim 100$ GeV and a maximum energy of $\sim 1$ TeV.

To compare the VHE upper limits presented in this work with the results from del Valle & Pohl, the fraction of kinetic energy converted into $\gamma$-rays with energies $> 100$ GeV (results of this work) compared to the total energy radiated through inverse Compton has to be estimated. The estimation of the total energy in $\gamma$ rays is done based on the spectral energy distribution published by del Valle & Pohl (see Figure 11 of the paper [387]). The fraction of kinetic energy converted into $\gamma$ rays with energies $> 100\,\mathrm{GeV}$ is estimated to be $\lesssim 2\%$. Furthermore, the presented VHE $\gamma$-ray flux upper limits are translated into upper limits on the fraction of wind energy converted into inverse Compton radiation, which are of the order of $\sim 5 \times 10^{-2}$ - $\sim 5 \times 10^{-1}$. This is about three orders of magnitude higher than the results published by del Valle & Pohl. Other $\gamma$-ray sources like PWNe are shown to exhibit TeV $\gamma$-ray conversion efficiencies over a large range of a few percent down to $\sim 0.01\%$ [407–409].

To compare the acceleration efficiencies of bow shocks of runaway stars to other astrophysical systems, the upper limits on the fraction of wind power being converted into inverse Compton radiation are translated into upper limits on the conversion efficiency of the wind power into electrons. del Valle & Pohl conclude (based on their model), that only $\lesssim 0.4\%$ of the injected power in electrons is radiated with a roughly equal distribution to synchrotron and inverse Compton emission. This leads to a conversion efficiency for kinetic energy in electrons into VHE $\gamma$ rays of the order of a few percent. Under the assumption, that all bow shocks analysed in this work can be described by the same model, the upper limits on the fraction of wind power converted into inverse Compton radiation result in non-constraining upper limits on the conversion efficiencies for electrons of the order of $\sim 1000\%$. For novae, for example, where particles are expected to be accelerated via diffusive shock acceleration [410] in a bow shock driven by the ejecta in the ISM, *Fermi* observations revealed conversion efficiencies of $\lesssim$0.1% in case of a leptonic scenario [411, 412].

Assuming the model predictions by del Valle & Pohl apply to all bow shocks of runaway stars, IACTs with improved sensitivities of two to three orders of magnitude would be required for either detecting VHE $\gamma$-ray emission from bow shocks of runaway stars or constraining their latest model predictions. With an improved sensitivity by a factor of ten compared to the current generation of IACTs, even CTA [413] might not be able to detect VHE $\gamma$-ray emission towards bow shocks of runaway stars. However, the authors discuss scenarios of higher stellar velocities and higher magnetic fields with the conclusion, that both factors would increase either the inverse Compton emission or the maximum energy of the $\gamma$-rays, respectively, leading to an increased VHE $\gamma$-ray flux. Furthermore, the model by del Valle & Pohl is not able to reproduce the detected non-thermal radio flux from the bow shock of the runaway star BD 43°3654, which seems to be an exceptional bow shock, giving rise to the speculation, that CTA may indeed play an important role for the understanding of the physical mechanisms in bow shocks of runaway stars.

# Bibliography

[1] V. F. Hess. Über die beobachtung der durchdringenden strahlung bei sieben freiballonfahrten. *Physikalische Zeitschrift*, Band 13:1084–1091, 1912.

[2] Padeli P. Papadopoulos, Wing-Fai Thi, Francesco Miniati, and Serena Viti. Extreme cosmic ray dominated regions: a new paradigm for high star formation density events in the Universe. *Monthly Notices of the Royal Astronomical Society*, 414(2):1705–1714, June 2011.

[3] Munier Salem, Greg L. Bryan, and Cameron Hummels. Cosmological Simulations of Galaxy Formation with Cosmic Rays. *The Astrophysical Journal Letters*, 797(2):L18, December 2014.

[4] Fermi-LAT Collaboration. The Large Area Telescope on the Fermi Gamma-Ray Space Telescope Mission. *The Astrophysical Journal*, 697(2):1071–1102, June 2009.

[5] Fermi-GBM Collaboration. The Fermi Gamma-ray Burst Monitor. *The Astrophysical Journal*, 702(1):791–804, September 2009.

[6] AGILE collaboration. The agile mission. *Astronomy & Astrophysics*, 502(3):995–1013, Jan 2009.

[7] T. C. Weekes, M. F. Cawley, D. J. Fegan, K. G. Gibbs, A. M. Hillas, P. W. Kowk, R. C. Lamb, D. A. Lewis, D. Macomb, N. A. Porter, and et al. Observation of tev gamma rays from the crab nebula using the atmospheric cerenkov imaging technique. *The Astrophysical Journal*, 342:379, Jul 1989.

[8] H. Abdalla, A. Abramowski, F. Aharonian, F. Ait Benkhali, A. G. Akhperjanian, T. Andersson, E. O. Angüner, M. Arrieta, P. Aubert, and et al. The population of tev pulsar wind nebulae in the h.e.s.s. galactic plane survey. *Astronomy & Astrophysics*, 612:A2, Apr 2018.

[9] H. Abdalla, A. Abramowski, F. Aharonian, F. Ait Benkhali, E. O. Angüner, M. Arakawa, M. Arrieta, P. Aubert, M. Backes, and et al. Population study of galactic supernova remnants at very high $\gamma$-ray energies with h.e.s.s. *Astronomy & Astrophysics*, 612:A3, Apr 2018.

[10] H.E.S.S. Collaboration. Systematic search for very-high-energy gamma-ray emission from bow shocks of runaway stars. *Astronomy & Astrophysics*, 612:A12, Apr 2018.

[11] S. Carrigan, F. Brun, R. C. G. Chaves, C. Deil, A. Donath, H. Gast, V. Marandon, and M. Renaud. The H.E.S.S. Galactic Plane SurveyMaps, Source Catalog and Source Population. In *International Cosmic Ray Conference*, volume 33 of *International Cosmic Ray Conference*, page 952, January 2013.

[12] Fermi Collaboration. GeV Observations of Star-forming Galaxies with the Fermi Large Area Telescope. *The Astrophysical Journal*, 755(2):164, August 2012.

[13] H. E. S. S. Collaboration. Detection of Gamma Rays from a Starburst Galaxy. *Science*, 326(5956):1080, November 2009.

[14] Jason Harris and Dennis Zaritsky. The star formation history of the small magellanic cloud. *The Astronomical Journal*, 127(3):1531–1544, Mar 2004.

[15] Jason Harris and Dennis Zaritsky. The star formation history of the large magellanic cloud. *The Astronomical Journal*, 138(5):1243–1260, Sep 2009.

[16] G. Indu and A. Subramaniam. The recent star-formation history of the large and small magellanic clouds. *Astronomy & Astrophysics*, 535:A115, Nov 2011.

[17] Stefano Rubele, Léo Girardi, Leandro Kerber, Maria-Rosa L. Cioni, Andrés E. Piatti, Simone Zaggia, Kenji Bekki, Alessandro Bressan, Gisella Clementini, Richard de Grijs, and et al. The vmc survey - xiv. first results on the look-back time star formation rate tomography of the small magellanic cloud. *Monthly Notices of the Royal Astronomical Society*, 449(1):639–661, Mar 2015.

[18] Stefano Rubele, Giada Pastorelli, Léo Girardi, Maria-Rosa L Cioni, Simone Zaggia, Paola Marigo, Kenji Bekki, Alessandro Bressan, Gisella Clementini, Richard de Grijs, and et al. The vmc survey – xxxi: The spatially resolved star formation history of the main body of the small magellanic cloud. *Monthly Notices of the Royal Astronomical Society*, 478(4):5017–5036, Jun 2018.

[19] M. D. Filipovic, R. F. Haynes, G. L. White, and P. A. Jones. A radio continuum study of the Magellanic Clouds. VII. Discrete radio sources in the Magellanic Clouds. *Astronomy & Astrophysics, Supplement*, 130:421–440, June 1998.

[20] T. D. Joseph, Filipović, M. D. , E. J. Crawford, Bojičić, I. , E. L. Alexander, G. F. Wong, H. Andernach, H. Leverenz, R. P. Norris, R. Z. E. Alsaberi, C. Anderson, L. A. Barnes, L. M. Bozzetto, F. Bufano, J. D. Bunton, F. Cavallaro, J. D. Collier, H. Dénes, Y. Fukui, T. Galvin, F. Haberl, A. Ingallinera, A. D. Kapinska, B. S. Koribalski, R. Kothes, D. Li, P. Maggi, C. Maitra, Manojlović, P. , J. Marvil, N. I. Maxted, A. N. O'Brien, J. M. Oliveira, C. M. Pennock, S. Riggi, G. Rowell, L. Rudnick, H. Sano, M. Sasaki, N. Seymour, R. Soria, M. Stupar, N. F. H. Tothill, C. Trigilio, K. Tsuge, G. Umana, Urošević, D. , J. Th van Loon, E. Vardoulaki, Velović, V. , M. Yew, D. Leahy, Y. H. Chu, M. J. Michałowski, P. J. Kavanagh, and K. R. Grieve. The ASKAP EMU Early Science Project: radio continuum survey of the Small Magellanic Cloud. *Monthly Notices of the Royal Astronomical Society*, 490(1):1202–1219, November 2019.

[21] F. Haberl. The XMM-Newton survey of the Large (and Small) Magellanic Cloud. In *The X-ray Universe 2014*, page 4, July 2014.

[22] F. Haberl, R. Sturm, J. Ballet, D. J. Bomans, D. A. H. Buckley, M. J. Coe, R. Corbet, M. Ehle, M. D. Filipovic, M. Gilfanov, D. Hatzidimitriou, N. La Palombara, S. Mereghetti, W. Pietsch, S. Snowden, and A. Tiengo. The XMM-Newton survey of the Small Magellanic Cloud. *Astronomy & Astrophysics*, 545:A128, September 2012.

[23] H. E. S. S. Collaboration, A. Abramowski, F. Aharonian, F. Ait Benkhali, A. G. Akhperjanian, E. O. Angüner, M. Backes, S. Balenderan, A. Balzer, A. Barnacka, and et al. The exceptionally powerful TeV $\gamma$-ray emitters in the Large Magellanic Cloud. *Science*, 347(6220):406–412, Jan 2015.

[24] J. Schmidt, F.; Knapp. Corsika shower images, 2005.

[25] P. A. Cherenkov. Visible emission of clean liquids by action of $\gamma$ radiation. *Doklady Akademii Nauk SSSR*, 2:451, 1934.

[26] Stefan Hoppe. *Emitters of VHE $\gamma$-radiation as revealed by the H.E.S.S. Galactic plane survey*. PhD thesis, Ruperto-Carola University of Heidelberg, http://archiv.ub.uni-heidelberg.de/volltextserver/8893/1/Dissertation_Stefan_Hoppe.pdf, Dec 2008.

[27] Konrad Bernlöhr. Simulation of imaging atmospheric Cherenkov telescopes with CORSIKA and sim_telarray. *Astroparticle Physics*, 30(3):149–158, October 2008.

[28] Mathieu de Naurois. Blue light in the desert night. *Nature Astronomy*, 2:593–593, July 2018.

[29] K. Bernlöhr, O. Carrol, R. Cornils, S. Elfahem, P. Espigat, S. Gillessen, G. Heinzelmann, G. Hermann, W. Hofmann, D. Horns, I. Jung, R. Kankanyan, A. Katona, B. Khelifi, H. Krawczynski, M. Panter, M. Punch, S. Rayner, G. Rowell, M. Tluczykont, and R. van Staa. The optical system of the H.E.S.S. imaging atmospheric Cherenkov telescopes. Part I: layout and components of the system. *Astroparticle Physics*, 20(2):111–128, November 2003.

[30] R. Cornils, S. Gillessen, I. Jung, W. Hofmann, M. Beilicke, K. Bernlöhr, O. Carrol, S. Elfahem, G. Heinzelmann, G. Hermann, D. Horns, R. Kankanyan, A. Katona, H. Krawczynski, M. Panter, S. Rayner, G. Rowell, M. Tluczykont, and R. van Staa. The optical system of the H.E.S.S. imaging atmospheric Cherenkov telescopes. Part II: mirror alignment and point spread function. *Astroparticle Physics*, 20(2):129–143, November 2003.

[31] A. Bouvier, L. Gebremedhin, C. Johnson, A. Kuznetsov, D. A. Williams, N. Otte, R. Strausbaugh, N. Hidaka, H. Tajima, J. Hinton, R. White, M. Errando, and R. Mukherjee. Photosensor characterization for the Cherenkov Telescope Array: silicon photomultiplier versus multi-anode photomultiplier tube. In *Hard X-Ray, Gamma-Ray, and Neutron Detector Physics XV*, volume 8852 of *Proceedings of the SPIE*, page 88520K, September 2013.

[32] S. Funk, G. Hermann, J. Hinton, D. Berge, K. Bernlöhr, W. Hofmann, P. Nayman, F. Toussenel, and P. Vincent. The trigger system of the h.e.s.s. telescope array. *Astroparticle Physics*, 22(3-4):285–296, Nov 2004.

[33] J. Bolmont, P. Corona, P. Gauron, P. Ghislain, C. Goffin, L. Guevara Riveros, J.-F. Huppert, O. Martineau-Huynh, P. Nayman, J.-M. Parraud, and et al. The camera of the fifth h.e.s.s. telescope. part i: System description. *Nuclear Instruments and Methods in Physics Research Section A: Accelerators, Spectrometers, Detectors and Associated Equipment*, 761:46–57, Oct 2014.

[34] M. Schandri. Investigation of observation quality parameters for h.e.s.s.-ii. Master's thesis, Friedrich-Alexander-University, March 2018.

[35] T. Ashton. A nectar-based upgrade for the cherenkov cameras of the h.e.s.s. 12-meter telescopes. *submitted to Astroparticle Physics*.

[36] V. P. Fomin, A. A. Stepanian, R. C. Lamb, D. A. Lewis, M. Punch, and T. C. Weekes. New methods of atmospheric Cherenkov imaging for gamma-ray astronomy. I. The false source method. *Astroparticle Physics*, 2:137–150, May 1994.

[37] A. Daum, G. Hermann, M. Heß, W. Hofmann, H. Lampeitl, G. Pühlhofer, F. Aharonian, A.G. Akhperjanian, J.A. Barrio, A.S. Beglarian, and et al. First results on the performance of the hegra iact array. *Astroparticle Physics*, 8(1-2):1–11, Dec 1997.

[38] N. Leroy, O. Bolz, J. Guy, I. Jung, I. Redondo, L. Rolland, J.-P. Tavernet, K.-M. Aye, P. Berghaus, K. Bernleohr, K. Bernlöhr, P. M. Chadwick, V. Chitnis, M. de Naurois, A. Djannati-Ataì, P. Espigat, G. Hermann, J. Hinton, B. Khelifi, A. Kohnle, R. Le Gallou, C. Masterson, S. Pita, T. Saito, C. Théoret, P. Vincent, and H.E.S.S. Collaboration. Calibration Results for the First Two H.E.S.S. Array Telescopes. *International Cosmic Ray Conference*, 5:2895, July 2003.

[39] F. Aharonian, A.G. Akhperjanian, K.-M. Aye, A.R. Bazer-Bachi, M. Beilicke, W. Benbow, D. Berge, P. Berghaus, K. Bernlöhr, O. Bolz, and et al. Calibration of cameras of the h.e.s.s. detector. *Astroparticle Physics*, 22(2):109–125, Nov 2004.

[40] O. Bolz. *Absolute energy calibration of the imaging Cherenkov telescopesof the H.E.S.S. experiment and results of first observations of the supernovaremnant RX J1713.7-3946*. PhD thesis, Karl-Ruprecht University, 2004.

[41] W. Hofmann and H.E.S.S. Collaboration. Status of the H.E.S.S. Project. *International Cosmic Ray Conference*, 5:2811, July 2003.

[42] J. Hahn, R. de los Reyes, K. Bernlöhr, P. Krüger, Y. T. E. Lo, P. M. Chadwick, M. K. Daniel, C. Deil, H. Gast, K. Kosack, and V. Marand on. Impact of aerosols and adverse atmospheric conditions on the data quality for spectral analysis of the H.E.S.S. telescopes. *Astroparticle Physics*, 54:25–32, February 2014.

[43] A. M. Hillas. Cerenkov light images of EAS produced by primary gamma. *International Cosmic Ray Conference*, 3, August 1985.

[44] M. de Naurois. Analysis methods for Atmospheric Cerenkov Telescopes. *arXiv Astrophysics e-prints*, July 2006.

[45] F. Aharonian, A. G. Akhperjanian, A. R. Bazer-Bachi, M. Beilicke, W. Benbow, D. Berge, K. Bernlöhr, C. Boisson, O. Bolz, V. Borrel, and et al. Observations of the crab nebula with hess. *Astronomy & Astrophysics*, 457(3):899–915, Sep 2006.

[46] R. D. Parsons and J. A. Hinton. A Monte Carlo template based analysis for air-Cherenkov arrays. *Astroparticle Physics*, 56:26–34, April 2014.

[47] R. Parsons, T. Murach, and M. Gajdus. H.E.S.S. II Data Analysis with ImPACT. In A. S. Borisov, V. G. Denisova, Z. M. Guseva, E. A. Kanevskaya, M. G. Kogan, A. E. Morozov, V. S. Puchkov, S. E. Pyatovsky, G. P. Shoziyoev, M. D. Smirnova, A. V. Vargasov, V. I. Galkin, S. I. Nazarov, and R. A. Mukhamedshin, editors, *34th International Cosmic Ray Conference (ICRC2015)*, volume 34 of *International Cosmic Ray Conference*, page 826, July 2015.

[48] Stefan Ohm, Christopher van Eldik, and Kathrin Egberts. Gamma-hadron separation in very-high-energy gamma-ray astronomy using a multivariate analysis method. *Astroparticle Physics*, 31:pp., 2009.

[49] S. Ohm. *Development of an Advanced $\gamma$/hadron separation technique and application to particular $\gamma$-ray sources with H.E.S.S.* PhD thesis, Ruperto-Carola University of Heidelberg, May 2010.

[50] D. Berge, S. Funk, and J. Hinton. Background modelling in very-high-energy $\gamma$-ray astronomy. *Astronomy & Astrophysics*, 466(3):1219–1229, Apr 2007.

[51] T.-P. Li and Y.-Q. Ma. Analysis methods for results in gamma-ray astronomy. *The Astrophysical Journal*, 272:317, Sep 1983.

[52] Y. I. Crewther and J. R. Protheroe. Calculation of Effective Areas of Air Shower Arrays used for Ultra High Energy Gamma Ray Astronomy. *International Cosmic Ray Conference*, 4:351, 1990.

[53] Mathieu De Naurois. *Very High Energy astronomy from H.E.S.S. to CTA. Opening of a new astronomical window on the non-thermal Universe*. Habilitation à diriger des recherches, Université Pierre et Marie Curie - Paris VI, March 2012.

[54] Wolfgang A. Rolke, Angel M. López, and Jan Conrad. Limits and confidence intervals in the presence of nuisance parameters. *Nuclear Instruments and Methods in Physics Research Section A: Accelerators, Spectrometers, Detectors and Associated Equipment*, 551(2-3):493–503, Oct 2005.

[55] K. Bernlöhr. Simulations of detector arrays and the impact of atmospheric parameters. *arXiv e-prints*, February 2014.

[56] K. Bernloehr. Atmospheric effects on the Cherenkov technique. *International Cosmic Ray Conference*, 5:276, 1999.

[57] H. Abdalla, A. Abramowski, F. Aharonian, F. Ait Benkhali, A.G. Akhperjanian, T. Andersson, E.O. Angüner, M. Arrieta, P. Aubert, and et al. Gamma-ray blazar spectra with h.e.s.s. ii mono analysis: The case of pks 2155-304 and pg 1553+113. *Astronomy & Astrophysics*, 600:A89, Apr 2017.

[58] S. Gillessen. *Sub-Bogenminuten-genaue Positionen von TeV-Quellen mit H.E.S.S.* PhD thesis, Ruprecht-Karls-Universitat Heidelberg, https://www.bsz-bw.de/cgi-bin/xvms.cgi?SWB11244050, 2004.

[59] P. Benaglia, G. E. Romero, J. Martí, C. S. Peri, and A. T. Araudo. Detection of nonthermal emission from the bow shock of a massive runaway star. *Astronomy and Astrophysics*, 517:L10, Jul 2010.

[60] M. V. del Valle and G. E. Romero. Non-thermal processes in bowshocks of runaway stars. *Astronomy & Astrophysics*, 543:A56, Jun 2012.

[61] M. V. del Valle, G. E. Romero, and M. De Becker. Is the bowshock of the runaway massive star hd 195592 afermisource? *Astronomy & Astrophysics*, 550:A112, Feb 2013.

[62] V. Pereira, J. López-Santiago, M. Miceli, R. Bonito, and E. de Castro. Modeling nonthermal emission from stellar bow shocks. *Astronomy & Astrophysics*, 588:A36, Mar 2016.

[63] H.E.S.S. Collaboration. The h.e.s.s. galactic plane survey. *Astronomy & Astrophysics*, 612:A1, 2018.

[64] Wolfgang A. Rolke and Angel M. López. Confidence intervals and upper bounds for small signals in the presence of background noise. *Nuclear Instruments and Methods in Physics Research A*, 458(3):745–758, February 2001.

[65] C. S. Peri, P. Benaglia, and N. L. Isequilla. E-boss: An extensive stellar bow shock survey. ii. catalogue second release. *Astronomy & Astrophysics*, 04 2015.

[66] K. Sadakane, R. Hirata, J. Jugaku, Y. Kondo, M. Matsuoka, Y. Tanaka, and G. Hammerschlag-Hensberge. Ultraviolet spectroscopic observations of HD 77581 (Vela X-1 = 4U 0900-40). *The Astrophysical Journal*, 288:284–291, January 1985.

[67] P. Sreekumar, D. L. Bertsch, B. L. Dingus, C. E. Fichtel, R. C. Hartman, S. D. Hunter, G. Kanbach, D. A. Kniffen, Y. C. Lin, J. R. Mattox, H. A. Mayer-Hasselwander, P. F. Michelson, C. von Montigny, P. L. Nolan, K. Pinkau, E. J. Schneid, and D. J. Thompson. Observations of the Large Magellanic Cloud in High-Energy Gamma Rays. *The Astrophysical Journal Letters*, 400:L67, Dec 1992.

[68] A. A. Abdo, M. Ackermann, M. Ajello, L. Baldini, J. Ballet, G. Barbiellini, D. Bastieri, K. Bechtol, R. Bellazzini, B. Berenji, and et al. Detection of the small magellanic cloud in gamma-rays with fermi/lat. *Astronomy & Astrophysics*, 523:A46, Nov 2010.

[69] Fermi Collaboration. Deep view of the Large Magellanic Cloud with six years of Fermi-LAT observations. *Astronomy & Astrophysics*, 586:A71, Feb 2016.

[70] *Stations of the Moon in pre-Islamic Arabian culture*. 889 CE.

[71] *Book of Fixed Stars*. 964 CE.

[72] Edward Arber, Richard Eden, Pietro Martire d' Anghiera, and Sebastian Münster. *The first three English books on America*. Birmingham : [Printed by Turnbull & Spears, Edinburgh], 1885.

[73] with Lord Stanley of Alderley Pigafetta et al. *The First Voyage Round the World, by Magellan*. London, England: The Hakluyt Society,, 1874.

[74] James Dunlop. A Catalogue of Nebulae and Clusters of Stars in the Southern Hemisphere, Observed at Paramatta in New South Wales. *Philosophical Transactions of the Royal Society of London Series I*, 118:113–151, Jan 1828.

[75] John Frederick William Herschel. A General Catalogue of Nebulae and Clusters of Stars. *Philosophical Transactions of the Royal Society of London Series I*, 154:1–137, Jan 1864.

[76] J. L. E. Dreyer. A New General Catalogue of Nebulæ and Clusters of Stars, being the Catalogue of the late Sir John F. W. Herschel, Bart, revised, corrected, and enlarged. *Memoirs of the Royal Astronomical Society*, 49:1, Jan 1888.

[77] Henrietta S. Leavitt. 1777 variables in the Magellanic Clouds. *Annals of Harvard College Observatory*, 60:87–108.3, Jan 1908.

[78] Henrietta S. Leavitt and Edward C. Pickering. Periods of 25 Variable Stars in the Small Magellanic Cloud. *Harvard College Observatory Circular*, 173:1–3, Mar 1912.

[79] Ejnar Hertzsprung. Über die räumliche Verteilung der Veränderlichen vom $\delta$ Cephei-Typus. *Astronomische Nachrichten*, 196:201, Nov 1913.

[80] E. P. Hubble. Cepheids in spiral nebulae. *The Observatory*, 48:139–142, May 1925.

[81] D. S. Mathewson, V. L. Ford, and N. Visvanathan. The Structure of the Small Magellanic Cloud. *The Astrophysical Journal*, 301:664, Feb 1986.

[82] Hugh H. Crowl, Ata Sarajedini, Andrés E. Piatti, Doug Geisler, Eduardo Bica, Juan J. Clariá, and Jr. Santos, João F. C. The Line-of-Sight Depth of Populous Clusters in the Small Magellanic Cloud. *The Astronomical Journal*, 122(1):220–231, Jul 2001.

[83] S. Subramanian and A. Subramaniam. Depth estimation of the Large and Small Magellanic Clouds. *Astronomy & Astrophysics*, 496(2):399–412, Mar 2009.

[84] J. V. Hindman, F. J. Kerr, and R. X. McGee. A Low Resolution Hydrogen-line Survey of the Magellanic System. II. Interpretation of Results. *Australian Journal of Physics*, 16:570, Jan 1963.

[85] D. S. Mathewson, M. N. Cleary, and J. D. Murray. The Magellanic Stream. *The Astrophysical Journal*, 190:291–296, Jun 1974.

[86] Jonathan Diaz and Kenji Bekki. Constraining the orbital history of the Magellanic Clouds: a new bound scenario suggested by the tidal origin of the Magellanic Stream. *Monthly Notices of the Royal Astronomical Society*, 413(3):2015–2020, May 2011.

[87] Gurtina Besla, David Martínez-Delgado, Roeland P. van der Marel, Yuri Beletsky, Mark Seibert, Edward F. Schlafly, Eva K. Grebel, and Fabian Neyer. Low Surface Brightness Imaging of the Magellanic System: Imprints of Tidal Interactions between the Clouds in the Stellar Periphery. *The Astrophysical Journal*, 825(1):20, Jul 2016.

[88] M. S. Oey, J. Dorigo Jones, N. Castro, P. Zivick, G. Besla, H. C. Januszewski, M. Moe, N. Kallivayalil, and D. J. Lennon. Resolved Kinematics of Runaway and Field OB Stars in the Small Magellanic Cloud. *The Astrophysical Journal Letters*, 867(1):L8, Nov 2018.

[89] Sara Rezaei kh., Atefeh Javadi, Habib Khosroshahi, and Jacco Th. van Loon. The star formation history of the magellanic clouds derived from long-period variable star counts. *Monthly Notices of the Royal Astronomical Society*, 445(3):2214–2222, Oct 2014.

[90] G. Pietrzyński, D. Graczyk, A. Gallenne, W. Gieren, I. B. Thompson, B. Pilecki, P. Karczmarek, M. Górski, K. Suchomska, M. Taormina, and et al. A distance to the large magellanic cloud that is precise to one per cent. *Nature*, 567(7747):200–203, Mar 2019.

[91] Paul J. McMillan. Mass models of the milky way. *Monthly Notices of the Royal Astronomical Society*, 414(3):2446–2457, Apr 2011.

[92] Gurtina Besla. The Orbits and Total Mass of the Magellanic Clouds. *arXiv e-prints*, page arXiv:1511.03346, Nov 2015.

[93] Thomas P. Robitaille and Barbara A. Whitney. The present-day star formation rate of the milky way determined fromspitzer-detected young stellar objects. *The Astrophysical Journal*, 710(1):L11–L15, Jan 2010.

[94] Karl G. Henize. Catalogues of H$\alpha$-emission Stars and Nebulae in the Magellanic Clouds. *The Astrophysical Journal, Supplement*, 2:315, Sep 1956.

[95] R. D. Davies, K. H. Elliott, and J. Meaburn. The nebular complexes of the Large and Small Magellanic Clouds. *Memoirs of the Royal Astronomical Society*, 81:89, Jan 1976.

[96] H. Baumgardt, G. Parmentier, P. Anders, and E. K. Grebel. VizieR Online Data Catalog: Massive clusters in the LMC (Baumgardt+, 2013). *VizieR Online Data Catalog*, page J/MNRAS/430/676, Mar 2014.

[97] P. Maggi, F. Haberl, P. J. Kavanagh, M. Sasaki, L. M. Bozzetto, M. D. Filipović, G. Vasilopoulos, W. Pietsch, S. D. Points, Y.-H. Chu, and et al. The population of x-ray supernova remnants in the large magellanic cloud. *Astronomy & Astrophysics*, 585:A162, Jan 2016.

[98] V. Antoniou and A. Zezas. Star formation history and X-ray binary populations: the case of the Large Magellanic Cloud. *Monthly Notices of the Royal Astronomical Society*, 459(1):528–553, Jun 2016.

[99] N. van Jaarsveld, D. A. H. Buckley, V. A. McBride, F. Haberl, G. Vasilopoulos, C. Maitra, A. Udalski, and B. Miszalski. Identification of high-mass X-ray binaries selected from XMM-Newton observations of the LMC. *Monthly Notices of the Royal Astronomical Society*, 475(3):3253–3261, Apr 2018.

[100] HESS Collaboration, H. Abdalla, A. Abramowski, F. Aharonian, F. Ait Benkhali, E. O. Angüner, M. Arakawa, C. Armand, M. Arrieta, M. Backes, and et al. Detection of variable VHE $\gamma$-ray emission from the extra-galactic $\gamma$-ray binary LMC P3. *Astronomy & Astrophysics*, 610:L17, Mar 2018.

[101] Dariusz Graczyk, Grzegorz Pietrzyński, Ian B. Thompson, Wolfgang Gieren, Bogumił Pilecki, Piotr Konorski, Andrzej Udalski, Igor Soszyński, Sandro Villanova, Marek Górski, and et al. The araucaria project. the distance to the small magellanic cloud from late-type eclipsing binaries. *The Astrophysical Journal*, 780(1):59, Dec 2013.

[102] F. Haberl and R. Sturm. High-mass X-ray binaries in the Small Magellanic Cloud. *Astronomy & Astrophysics*, 586:A81, February 2016.

[103] Grigoris Maravelias, Andreas Zezas, Vallia Antoniou, Despina Hatzidimitriou, and Frank Haberl. Clarifying the population of HMXBs in the Small Magellanic Cloud. *arXiv e-prints*, page arXiv:1811.10933, Nov 2018.

[104] C. Badenes, D. Maoz, and B. T. Draine. On the size distribution of supernova remnants in the Magellanic Clouds. *Monthly Notices of the Royal Astronomical Society*, 407:1301–1313, September 2010.

[105] E. Livanou, I. Gonidakis, E. Kontizas, U. Klein, M. Kontizas, D. Kester, Y. Fukui, N. Mizuno, and P. Tsalmantza. Star-forming Regions in the Small Magellanic Cloud: Multiwavelength Properties of Stellar Complexes. *The Astronomical Journal*, 133:2179–2186, May 2007.

[106] Stephen C. Russell and Michael A. Dopita. Abundances of the heavy elements in the magellanic clouds. iii - interpretation of results. *The Astrophysical Journal*, 384:508, Jan 1992.

[107] Andrew Schenck, Sangwook Park, and Seth Post. A chandra study of the interstellar metallicity in the large magellanic cloud using supernova remnants. *The Astronomical Journal*, 151(6):161, May 2016.

[108] Laura A. Lopez, Katie Auchettl, Tim Linden, Alberto D. Bolatto, Todd A. Thompson, and Enrico Ramirez-Ruiz. Evidence for cosmic-ray escape in the small magellanic cloud using fermi gamma rays. *The Astrophysical Journal*, 867(1):44, Oct 2018.

[109] M. Ackermann, M. Ajello, A. Allafort, L. Baldini, J. Ballet, D. Bastieri, K. Bechtol, R. Bellazzini, B. Berenji, E. D. Bloom, and et al. Gev observations of star-forming galaxies with thefermilarge area telescope. *The Astrophysical Journal*, 755(2):164, Aug 2012.

[110] F. Aharonian, A. Akhperjanian, J. Barrio, K. Bernlöhr, H. Börst, H. Bojahr, O. Bolz, J. Contreras, J. Cortina, S. Denninghoff, and et al. Evidence for tev gamma ray emission from cassiopeia a. *Astronomy & Astrophysics*, 370(1):112–120, Apr 2001.

[111] ENRICO Fermi. On the origin of the cosmic radiation. *Physical Review*, 75(8):1169–1174, Apr 1949.

[112] A. Sandroos, G. Li, and L. Zhao. First- and Second-order Fermi Acceleration at Parallel Shocks. *arXiv e-prints*, August 2014.

[113] A. R. Bell. The acceleration of cosmic rays in shock fronts - i. *Monthly Notices of the Royal Astronomical Society*, 182(2):147–156, Feb 1978.

[114] L O'C Drury. An introduction to the theory of diffusive shock acceleration of energetic particles in tenuous plasmas. *Reports on Progress in Physics*, 46(8):973–1027, Aug 1983.

[115] Roger Blandford and David Eichler. Particle acceleration at astrophysical shocks: A theory of cosmic ray origin. *Physics Reports*, 154(1):1–75, Oct 1987.

[116] M A Malkov and L O'C Drury. Nonlinear theory of diffusive acceleration of particles by shock waves. *Reports on Progress in Physics*, 64(4):429–481, Mar 2001.

[117] A. Kis. Multi-spacecraft observations of diffuse ions upstream of earth's bow shock. *Geophysical Research Letters*, 31(20), 2004.

[118] E. M. de Gouveia Dal Pino and A. Lazarian. Production of the large scale superluminal ejections of the microquasar grs 1915+105 by violent magnetic reconnection. *Astronomy & Astrophysics*, 441(3):845–853, Sep 2005.

[119] J. F. Drake, M. Swisdak, K. M. Schoeffler, B. N. Rogers, and S. Kobayashi. Formation of secondary islands during magnetic reconnection. *Geophysical Research Letters*, 33(13):L13105, July 2006.

[120] Elisabete M. de Gouveia Dal Pino and Grzegorz Kowal. *Particle Acceleration by Magnetic Reconnection*, volume 407 of *Astrophysics and Space Science Library*, page 373. Springer-Verlag Berlin Heidelberg, 2015.

[121] V. L. Ginzburg and S. I. Syrovatskii. Cosmic magnetobremsstrahlung (synchrotron radiation). *Annual Review of Astronomy and Astrophysics*, 3(1):297–350, Sep 1965.

[122] Arthur H. Compton. A quantum theory of the scattering of x-rays by light elements. *Physical Review*, 21(5):483–502, May 1923.

[123] GEORGE R. BLUMENTHAL and ROBERT J. GOULD. Bremsstrahlung, synchrotron radiation, and compton scattering of high-energy electrons traversing dilute gases. *Reviews of Modern Physics*, 42(2):237–270, Apr 1970.

[124] J. J. Thomson. *Conduction of Electricity Through Gases*. Cambridge University Press, 1906.

[125] O. Klein and Y. Nishina. Über die streuung von strahlung durch freie elektronen nach der neuen relativistischen quantendynamik von dirac. *Zeitschrift für Physik*, 52(11-12):853–868, Nov 1929.

[126] S. R. Kelner, F. A. Aharonian, and V. V. Bugayov. Energy spectra of gamma rays, electrons, and neutrinos produced at proton-proton interactions in the very high energy regime. *Physical Review D*, 74(3), Aug 2006.

[127] S. P. Wakely and D. Horan. Tevcat: An online catalog for very high energy gamma-ray astronomy. *International Cosmic Ray Conference*, 3:1341–1344, 2008.

[128] D. A. Green. A revised catalogue of 294 galactic supernova remnants. *Journal of Astrophysics and Astronomy*, 40(4):36, Aug 2019.

[129] Jacco Vink. Supernova remnants: the x-ray perspective. *The Astronomy and Astrophysics Review*, 20(1):49, Dec 2012.

[130] Wolfgang Hillebrandt and Jens C. Niemeyer. Type ia supernova explosion models. *Annual Review of Astronomy and Astrophysics*, 38(1):191–230, Sep 2000.

[131] Bruno Leibundgut. Type ia supernovae. *Astronomy and Astrophysics Review*, 10(3):179–209, Sep 2000.

[132] Adam Burrows. Supernova explosions in the universe. *Nature*, 403(6771):727–733, Feb 2000.

[133] Stan Woosley and Thomas Janka. The physics of core-collapse supernovae. *Nature Physics*, 1(3):147–154, Dec 2005.

[134] E. R. Micelotta, M. Matsuura, and A. Sarangi. Dust in supernovae and supernova remnants ii: Processing and survival. *Space Science Reviews*, 214(2):53, Mar 2018.

[135] A. Wongwathanarat, E. Müller, and H. Th. Janka. Three-dimensional simulations of core-collapse supernovae: from shock revival to shock breakout. *Astronomy & Astrophysics*, 577:A48, May 2015.

[136] R. A. Chevalier. Self-similar solutions for the interaction of stellar ejecta with an external medium. *The Astrophysical Journal*, 258:790, Jul 1982.

[137] Denis F. Cioffi, Christopher F. McKee, and Edmund Bertschinger. Dynamics of radiative supernova remnants. *The Astrophysical Journal*, 334:252, Nov 1988.

[138] J. Kelly Truelove and Christopher F. McKee. Evolution of nonradiative supernova remnants. *The Astrophysical Journal Supplement Series*, 120(2):299–326, Feb 1999.

[139] J. Kelly Truelove and Christopher F. McKee. Errata: Evolution of nonradiative supernova remnants. *The Astrophysical Journal Supplement Series*, 128(1):403–403, May 2000.

[140] J. Vink, J. S. Kaastra, and J. A. M. Bleeker. X-ray spectroscopy of the supernova remnant RCW 86. A new challenge for modeling the emission from supernova remnants. *Astronomy & Astrophysics*, 328:628–633, December 1997.

[141] A. R. Bell. The acceleration of cosmic rays in shock fronts - ii. *Monthly Notices of the Royal Astronomical Society*, 182(3):443–455, Mar 1978.

[142] R. D. Blandford and J. P. Ostriker. Particle acceleration by astrophysical shocks. *The Astrophysical Journal Letters*, 221:L29–L32, April 1978.

[143] A M Hillas. Can diffusive shock acceleration in supernova remnants account for high-energy galactic cosmic rays? *Journal of Physics G: Nuclear and Particle Physics*, 31(5):R95–R131, Apr 2005.

[144] W. Baade and F. Zwicky. Cosmic rays from super-novae. *Proceedings of the National Academy of Sciences*, 20(5):259–263, May 1934.

[145] V. L. Ginzburg and S. I. Syrovatskii. *The Origin of Cosmic Rays*. Macmillan, 1964.

[146] W. R. Webber. A new estimate of the local interstellar energy density and ionization rate of galactic cosmic cosmic rays. *The Astrophysical Journal*, 506(1):329–334, Oct 1998.

[147] T. K. Gaisser. *Cosmic rays and particle physics*. 1990.

[148] P. Lipari. The lifetime of cosmic rays in the Milky Way. *arXiv e-prints*, July 2014.

[149] Masaki Mori. The galactic diffuse gamma-ray spectrum from cosmic-ray proton interactions. *The Astrophysical Journal*, 478(1):225–232, Mar 1997.

[150] F. A. Aharonian and A. M. Atoyan. Broad-band diffuse gamma ray emission of the galactic disk. *Astronomy & Astrophysics*, 362:937–952, October 2000.

[151] William T. Reach, Jeonghee Rho, and T. H. Jarrett. Shocked Molecular Gas in the Supernova Remnants W28 and W44: Near-Infrared and Millimeter-Wave Observations. *The Astrophysical Journal*, 618(1):297–320, January 2005.

[152] MAGIC collaboration. Morphological and spectral properties of the W51 region measured with the MAGIC telescopes. *Astronomy & Astrophysics*, 541:A13, May 2012.

[153] A. A. Abdo, M. Ackermann, M. Ajello, A. Allafort, L. Baldini, J. Ballet, G. Barbiellini, D. Bastieri, K. Bechtol, R. Bellazzini, and et al. Fermilarge area telescope observations of the supernova remnant w28 (g6.4–0.1). *The Astrophysical Journal*, 718(1):348–356, Jun 2010.

[154] A. Giuliani, M. Tavani, A. Bulgarelli, E. Striani, S. Sabatini, M. Cardillo, Y. Fukui, A. Kawamura, A. Ohama, N. Furukawa, and et al. Agile detection of gev $\gamma$-ray emission from the snr w28. *Astronomy and Astrophysics*, 516:L11, Jun 2010.

[155] A. A. Abdo, M. Ackermann, M. Ajello, L. Baldini, J. Ballet, G. Barbiellini, M. G. Baring, D. Bastieri, B. M. Baughman, K. Bechtol, and et al. Gamma-ray emission from the shell of supernova remnant w44 revealed by the fermi lat. *Science*, 327(5969):1103–1106, Jan 2010.

[156] A. Giuliani, M. Cardillo, M. Tavani, Y. Fukui, S. Yoshiike, K. Torii, G. Dubner, G. Castelletti, G. Barbiellini, A. Bulgarelli, and et al. Neutral pion emission from accelerated protons in the supernova remnant w44. *The Astrophysical Journal*, 742(2):L30, Nov 2011.

[157] M. Tavani, A. Giuliani, A. W. Chen, A. Argan, G. Barbiellini, A. Bulgarelli, P. Caraveo, P. W. Cattaneo, V. Cocco, T. Contessi, and et al. Direct evidence for hadronic cosmic-ray acceleration in the supernova remnant ic 443. *The Astrophysical Journal*, 710(2):L151–L155, Feb 2010.

[158] M. Ackermann, M. Ajello, A. Allafort, L. Baldini, J. Ballet, G. Barbiellini, M. G. Baring, D. Bastieri, K. Bechtol, R. Bellazzini, and et al. Detection of the characteristic pion-decay signature in supernova remnants. *Science*, 339(6121):807–811, Feb 2013.

[159] A. Abramowski, F. Aharonian, F. Ait Benkhali, A. G. Akhperjanian, E. O. Angüner, M. Backes, A. Balzer, Y. Becherini, J. Becker Tjus, and et al. Detailed spectral and morphological analysis of the shell type supernova remnant rcw 86. *Astronomy & Astrophysics*, 612:A4, Apr 2018.

[160] F. Giordano, M. Naumann-Godo, J. Ballet, K. Bechtol, S. Funk, J. Lande, M. N. Mazziotta, S. Rainò, T. Tanaka, O. Tibolla, and et al. Fermilarge area telescope detection of the young supernova remnant tycho. *The Astrophysical Journal*, 744(1):L2, Dec 2011.

[161] V. A. Acciari, E. Aliu, T. Arlen, T. Aune, M. Beilicke, W. Benbow, S. M. Bradbury, J. H. Buckley, V. Bugaev, K. Byrum, and et al. Discovery of tev gamma-ray emission fromtycho's supernova remnant. *The Astrophysical Journal*, 730(2):L20, Mar 2011.

[162] S. Archambault, A. Archer, W. Benbow, R. Bird, E. Bourbeau, M. Buchovecky, J. H. Buckley, V. Bugaev, M. Cerruti, M. P. Connolly, and et al. Gamma-ray observations of tycho's supernova remnant with veritas andfermi. *The Astrophysical Journal*, 836(1):23, Feb 2017.

[163] G. Morlino and D. Caprioli. Strong evidence for hadron acceleration in tycho's supernova remnant. *Astronomy & Astrophysics*, 538:A81, Feb 2012.

[164] F. Acero, F. Aharonian, A. G. Akhperjanian, G. Anton, U. Barres de Almeida, A. R. Bazer-Bachi, Y. Becherini, B. Behera, M. Beilicke, K. Bernlöhr, and et al. First detection of vhe $\gamma$-rays from sn 1006 by hess. *Astronomy and Astrophysics*, 516:A62, Jun 2010.

[165] A. A. Abdo, M. Ackermann, M. Ajello, L. Baldini, J. Ballet, G. Barbiellini, D. Bastieri, B. M. Baughman, K. Bechtol, R. Bellazzini, and et al. Fermiobservations of cassiopeia and cepheus: Diffuse gamma-ray emission in the outer galaxy. *The Astrophysical Journal*, 710(1):133–149, Jan 2010.

[166] J. Albert, E. Aliu, H. Anderhub, P. Antoranz, A. Armada, C. Baixeras, J. A. Barrio, H. Bartko, D. Bastieri, J. K. Becker, and et al. Observation of vhe $\gamma$-rays from cassiopeia a with the magic telescope. *Astronomy & Astrophysics*, 474(3):937–940, Oct 2007.

[167] Yajie Yuan, Stefan Funk, Gülauger Jóhannesson, Joshua Lande, Luigi Tibaldo, and Yasunobu Uchiyama. Fermilarge area telescope detection of a break in the gamma-ray spectrum of the supernova remnant cassiopeia a. *The Astrophysical Journal*, 779(2):117, Dec 2013.

[168] V. A. Acciari, E. Aliu, T. Arlen, T. Aune, M. Bautista, M. Beilicke, W. Benbow, D. Boltuch, S. M. Bradbury, J. H. Buckley, and et al. Observations of the shell-type supernova remnant cassiopeia a at tev energies with veritas. *The Astrophysical Journal*, 714(1):163–169, Apr 2010.

[169] M. L. Ahnen, S. Ansoldi, L. A. Antonelli, C. Arcaro, A. Babić, B. Banerjee, P. Bangale, U. Barres de Almeida, J. A. Barrio, J. Becerra González, and et al. A cut-off in the tev gamma-ray spectrum of the snr cassiopeia a. *Monthly Notices of the Royal Astronomical Society*, 472(3):2956–2962, Aug 2017.

[170] F. A. Aharonian, A. G. Akhperjanian, K.-M. Aye, A. R. Bazer-Bachi, M. Beilicke, W. Benbow, D. Berge, P. Berghaus, K. Bernlöhr, O. Bolz, and et al. High-energy particle acceleration in the shell of a supernova remnant. *Nature*, 432(7013):75–77, Nov 2004.

[171] F. Aharonian, A. G. Akhperjanian, A. R. Bazer-Bachi, M. Beilicke, W. Benbow, D. Berge, K. Bernlöhr, C. Boisson, O. Bolz, V. Borrel, and et al. Primary particle acceleration above 100 tev in the shell-type supernova remnant rx j1713.7-3946 with deep hess observations. *Astronomy & Astrophysics*, 464(1):235–243, Nov 2006.

[172] A. A. Abdo, M. Ackermann, M. Ajello, A. Allafort, L. Baldini, J. Ballet, G. Barbiellini, M. G. Baring, D. Bastieri, R. Bellazzini, and et al. Observations of the young supernova remnant rx j1713.7–3946 with thefermilarge area telescope. *The Astrophysical Journal*, 734(1):28, May 2011.

[173] G. Morlino, E. Amato, and P. Blasi. Gamma-ray emission from snr rx j1713.7-3946 and the origin of galactic cosmic rays. *Monthly Notices of the Royal Astronomical Society*, 392(1):240–250, Jan 2009.

[174] Brian W. Grefenstette, Stephen P. Reynolds, Fiona A. Harrison, T. Brian Humensky, Steven E. Boggs, Chris L. Fryer, Tracey DeLaney, Kristin K. Madsen, Hiromasa Miyasaka, Daniel R. Wik, and et al. Locating the most energetic electrons in cassiopeia a. *The Astrophysical Journal*, 802(1):15, Mar 2015.

[175] V. N. Zirakashvili and F. A. Aharonian. Nonthermal radiation of young supernova remnants: The case of rx j1713.7-3946. *The Astrophysical Journal*, 708(2):965–980, Dec 2009.

[176] Donald C. Ellison, Daniel J. Patnaude, Patrick Slane, and John Raymond. Efficient cosmic ray acceleration, hydrodynamics, and self-consistent thermal x-ray emission applied to supernova remnant rx j1713.7-3946. *The Astrophysical Journal*, 712(1):287–293, Feb 2010.

[177] S. Gabici and F. A. Aharonian. Hadronic gamma-rays from rx j1713.7-3946? *Monthly Notices of the Royal Astronomical Society: Letters*, 445(1):L70–L73, Sep 2014.

[178] Stefan Funk. Ground- and space-based gamma-ray astronomy. *Annual Review of Nuclear and Particle Science*, 65(1):245–277, Oct 2015.

[179] Heinrich J. Voelk and Peter L. Biermann. Maximum energy of cosmic-ray particles accelerated by supernova remnant shocks in stellar wind cavities. *The Astrophysical Journal*, 333:L65, Oct 1988.

[180] Martina Cardillo, Elena Amato, and Pasquale Blasi. On the cosmic ray spectrum from type ii supernovae expanding in their red giant presupernova wind. *Astroparticle Physics*, 69:1–10, Sep 2015.

[181] Alexandre Marcowith, Vikram V Dwarkadas, Matthieu Renaud, Vincent Tatischeff, and Gwenael Giacinti. Core-collapse supernovae as cosmic ray sources. *Monthly Notices of the Royal Astronomical Society*, 479(4):4470–4485, Jul 2018.

[182] A. R. Bell, K. M. Schure, B. Reville, and G. Giacinti. Cosmic-ray acceleration and escape from supernova remnants. *Monthly Notices of the Royal Astronomical Society*, 431(1):415–429, Feb 2013.

[183] K. M. Schure and A. R. Bell. Magnetic field amplification by cosmic rays in supernova remnants. In G. Pugliese, A. de Koter, and M. Wijburg, editors, *370 Years of Astronomy in Utrecht*, volume 470 of *Astronomical Society of the Pacific Conference Series*, page 209, January 2013.

[184] Roger A. Chevalier and Claes Fransson. Thermal and non-thermal emission from circumstellar interaction. *Handbook of Supernovae*, pages 875–937, 2017.

[185] M. Ackermann, I. Arcavi, L. Baldini, J. Ballet, G. Barbiellini, D. Bastieri, R. Bellazzini, E. Bissaldi, R. D. Blandford, R. Bonino, and et al. Search for early gamma-ray production in supernovae located in a dense circumstellar medium with thefermilat. *The Astrophysical Journal*, 807(2):169, Jul 2015.

[186] R. N. Manchester, G. B. Hobbs, A. Teoh, and M. Hobbs. VizieR Online Data Catalog: ATNF Pulsar Catalog (Manchester+, 2005). *VizieR Online Data Catalog*, page VII/245, Aug 2005.

[187] Chengmin Zhang, Yuanyue Pan, and Ali Taani. Pulsar Distributions in the Magnetic and Spin Period Diagram. In *International Journal of Modern Physics Conference Series*, volume 23, pages 165–169, Jan 2013.

[188] E. Ergma and E. P. J. van den Heuvel. On the initial progenitor masses of stellar mass black holes and neutron stars. *Astronomy & Astrophysics*, 331:L29–L32, Mar 1998.

[189] Michael P. Muno. Which stars form black holes and neutron stars? Aug 2007.

[190] S. Ansoldi, L. A. Antonelli, P. Antoranz, A. Babic, P. Bangale, U. Barres de Almeida, J. A. Barrio, J. Becerra González, W. Bednarek, E. Bernardini, and et al. Teraelectronvolt pulsed emission from the crab pulsar detected by magic. *Astronomy & Astrophysics*, 585:A133, Jan 2016.

[191] A. Djannati-Ataï, G. Giavitto, M. Holler, B. Rudak, C. Venter, and H. E. S. S. Collaboration. Probing Vela pulsar down to 20 GeV with H.E.S.S. II observations. In *6th International Symposium on High Energy Gamma-Ray Astronomy*, volume 1792 of *American Institute of Physics Conference Series*, page 040028, Jan 2017.

[192] M. et al. (MAGIC Collaboration) Lopez. Astrophysics $+$ MAGIC conference, 2018.

[193] F. A. Aharonian, S. V. Bogovalov, and D. Khangulyan. Abrupt acceleration of a 'cold' ultrarelativistic wind from the Crab pulsar. *Nature*, 482(7386):507–509, Feb 2012.

[194] Alex G. Muslimov and Alice K. Harding. Extended Acceleration in Slot Gaps and Pulsar High-Energy Emission. *The Astrophysical Journal*, 588(1):430–440, May 2003.

[195] Alex G. Muslimov and Alice K. Harding. High-Altitude Particle Acceleration and Radiation in Pulsar Slot Gaps. *The Astrophysical Journal*, 606(2):1143–1153, May 2004.

[196] K. S. Cheng, M. Ruderman, and L. Zhang. A Three-dimensional Outer Magnetospheric Gap Model for Gamma-Ray Pulsars: Geometry, Pair Production, Emission Morphologies, and Phase-resolved Spectra. *The Astrophysical Journal*, 537(2):964–976, Jul 2000.

[197] J. G. Kirk. Particle Acceleration in Relativistic Current Sheets. *Physical Review Letters*, 92(18):181101, May 2004.

[198] Anatoly Spitkovsky. Time-dependent Force-free Pulsar Magnetospheres: Axisymmetric and Oblique Rotators. *The Astrophysical Journal*, 648(1):L51–L54, Sep 2006.

[199] Iwona Mochol. Pulsar Striped Winds. In Diego F. Torres, editor, *Modelling Pulsar Wind Nebulae*, volume 446 of *Astrophysics and Space Science Library*, page 135, Jan 2017.

[200] S. S. Komissarov. Time-dependent, force-free, degenerate electrodynamics. *Monthly Notices of the Royal Astronomical Society*, 336(3):759–766, Nov 2002.

[201] Samuel E. Gralla and Nabil Iqbal. Effective field theory of force-free electrodynamics. *Physical Review D*, 99(10):105004, May 2019.

[202] Vasily Beskin. Pulsar magnetospheres and pulsar winds. In *6th International Symposium on High Energy Gamma-Ray Astronomy*, volume 1792 of *American Institute of Physics Conference Series*, page 020001, Jan 2017.

[203] Benoît Cerutti and Andrei M. Beloborodov. Electrodynamics of Pulsar Magnetospheres. *Space Science Reviews*, 207(1-4):111–136, Jul 2017.

[204] Alice K. Harding. Pulsar Emission Physics: The First Fifty Years. In P. Weltevrede, B. B. P. Perera, L. L. Preston, and S. Sanidas, editors, *Pulsar Astrophysics the Next Fifty Years*, volume 337 of *IAU Symposium*, pages 52–57, Aug 2018.

[205] Benoît Cerutti. Gamma-ray pulsars: What have we learned from ab-initio kinetic simulations? *arXiv e-prints*, page arXiv:1811.09215, Nov 2018.

[206] James J. Condon and Scott M. Ransom. *Essential Radio Astronomy*. ISBN: 978-0-691-13779-7. Princeton, NJ: Princeton University Press, 2016.

[207] A. A. Abdo, M. Ackermann, M. Ajello, W. B. Atwood, M. Axelsson, L. Baldini, J. Ballet, G. Barbiellini, M. G. Baring, D. Bastieri, and et al. The First Fermi Large Area Telescope Catalog of Gamma-ray Pulsars. *The Astrophysical Journal, Supplement*, 187(2):460–494, Apr 2010.

[208] F. A. Aharonian, A. M. Atoyan, and T. Kifune. Inverse Compton gamma radiation of faint synchrotron X-ray nebulae around pulsars. *Monthly Notices of the Royal Astronomical Society*, 291(1):162–176, Oct 1997.

[209] E. de O*ñ*a-Wilhelmi, B. Rudak, J. A. Barrio, J. L. Contreras, Y. Gallant, D. Hadasch, T. Hassan, M. Lopez, D. Mazin, N. Mirabal, G. Pedaletti, M. Renaud, R. de los Reyes, D. F. Torres, and CTA Consortium. Prospects for observations of pulsars and pulsar wind nebulae with CTA. *Astroparticle Physics*, 43:287–300, Mar 2013.

[210] L. Zhang, S. B. Chen, and J. Fang. Nonthermal radiation from pulsar wind nebulae. *The Astrophysical Journal*, 676(2):1210–1217, Apr 2008.

[211] A. A. Abdo, M. Ackermann, M. Ajello, A. Allafort, L. Baldini, J. Ballet, G. Barbiellini, D. Bastieri, K. Bechtol, R. Bellazzini, and et al. Gamma-ray flares from the crab nebula. *Science*, 331(6018):739–742, Jan 2011.

[212] HESS Collaboration, A. Abramowski, F. Aharonian, F. Ait Benkhali, A. G. Akhperjanian, E. O. Angüner, M. Backes, A. Balzer, Y. Becherini, J. Becker Tjus, and et al. Acceleration of petaelectronvolt protons in the Galactic Centre. *Nature*, 531(7595):476–479, Mar 2016.

[213] D. F. Torres, A. Cillis, J. Martín, and E. de Oña Wilhelmi. Time-dependent modeling of TeV-detected, young pulsar wind nebulae. *Journal of High Energy Astrophysics*, 1:31–62, May 2014.

[214] Fermi-LAT Collaboration. Fermi Large Area Telescope Observations of the Crab Pulsar And Nebula. *The Astrophysical Journal*, 708(2):1254–1267, Jan 2010.

[215] Lorenzo Sironi and Anatoly Spitkovsky. Particle Acceleration in Relativistic Magnetized Collisionless Pair Shocks: Dependence of Shock Acceleration on Magnetic Obliquity. *The Astrophysical Journal*, 698(2):1523–1549, Jun 2009.

[216] Y. E. Lyubarsky. The termination shock in a striped pulsar wind. *Monthly Notices of the Royal Astronomical Society*, 345(1):153–160, Oct 2003.

[217] Lorenzo Sironi and Benoît Cerutti. Particle Acceleration in Pulsar Wind Nebulae: PIC Modelling. In Diego F. Torres, editor, *Modelling Pulsar Wind Nebulae*, volume 446 of *Astrophysics and Space Science Library*, page 247, Jan 2017.

[218] Lorenzo Sironi and Anatoly Spitkovsky. Particle Acceleration in Relativistic Magnetized Collisionless Electron-Ion Shocks. *The Astrophysical Journal*, 726(2):75, Jan 2011.

[219] Elena Amato. Particle acceleration and radiation in Pulsar Wind Nebulae. *arXiv e-prints*, page arXiv:1503.02402, Mar 2015.

[220] L. Sironi, U. Keshet, and M. Lemoine. Relativistic Shocks: Particle Acceleration and Magnetization. *Space Science Reviews*, 191(1-4):519–544, Oct 2015.

[221] A. Mignone. MhD Modeling: Aims, Usage, Scales assessd, Caveats, Codes. In Diego F. Torres, editor, *Modelling Pulsar Wind Nebulae*, volume 446 of *Astrophysics and Space Science Library*, page 187, Jan 2017.

[222] A. Mignone. Multidimensional Relativistic MhD Simulations of Pulsar Wind Nebulae: Dynamics and Emission. In Diego F. Torres, editor, *Modelling Pulsar Wind Nebulae*, volume 446 of *Astrophysics and Space Science Library*, page 215, Jan 2017.

[223] A. M. Atoyan and F. A. Aharonian. On the mechanisms of gamma radiation in the Crab Nebula. *Monthly Notices of the Royal Astronomical Society*, 278(2):525–541, Jan 1996.

[224] J. J. Hester. The Crab Nebula : an astrophysical chimera. *Annual Review of Astronomy and Astrophysics*, 46:127–155, Sep 2008.

[225] R. J. Gould and G. R. Burbidge. High energy cosmic photons. *Annales d'Astrophysique*, 28:171, Feb 1965.

[226] O. C. de Jager and A. K. Harding. The Expected High-Energy to Ultra–High-Energy Gamma-Ray Spectrum of the Crab Nebula. *The Astrophysical Journal*, 396:161, Sep 1992.

[227] Jonatan Martín, Diego F. Torres, and Nanda Rea. Time-dependent modelling of pulsar wind nebulae: study on the impact of the diffusion-loss approximations. *Monthly Notices of the Royal Astronomical Society*, 427(1):415–427, Nov 2012.

[228] Amir Levinson and Roger Blandford. On the Jets Associated with Galactic Superluminal Sources. *The Astrophysical Journal Letters*, 456:L29, Jan 1996.

[229] K. Reitberger, A. Reimer, O. Reimer, and H. Takahashi. The first full orbit of $\eta$ Carinae seen by Fermi. *Astronomy & Astrophysics*, 577:A100, May 2015.

[230] E. Leser, S. Ohm, M. Füßling, M. de Naurois, K. Egberts, P. Bordas, S. Klepser, O. Reimer, A. Reimer, J. Hinton, and H. E. S. S. Collaboration. First Results of Eta Carinae Observations with H.E.S.S. II. In *35th International Cosmic Ray Conference (ICRC2017)*, volume 301 of *International Cosmic Ray Conference*, page 717, Jan 2017.

[231] H. E. S. S. Collaboration. Discovery of the binary pulsar PSR B1259-63 in very-high-energy gamma rays around periastron with HESS. *Astronomy & Astrophysics*, 442(1):1–10, Oct 2005.

[232] H. E. S. S. Collaboration. Discovery of Very High Energy Gamma Rays Associated with an X-ray Binary. *Science*, 309(5735):746–749, Jul 2005.

[233] MAGIC collaboration. Variable Very-High-Energy Gamma-Ray Emission from the Microquasar LS I +61 303. *Science*, 312(5781):1771–1773, Jun 2006.

[234] H. E. S. S. Collaboration. Discovery of a point-like very-high-energy $\gamma$-ray source in Monoceros. *Astronomy & Astrophysics*, 469(1):L1–L4, Jul 2007.

[235] H. E. S. S. Collaboration. Discovery of VHE emission towards the Carina arm region with the H.E.S.S. telescope array: HESS J1018-589. *Astronomy & Astrophysics*, 541:A5, May 2012.

[236] MAGIC and VERITAS Collaboration. Periastron observations of tev gamma-ray emission from a binary system with a 50-year period. *The Astrophysical Journal*, 867(1):L19, Oct 2018.

[237] Guillaume Dubus. Gamma-ray emission from binaries in context. *Comptes Rendus Physique*, 16(6-7):661–673, Aug 2015.

[238] Lorenzo Sironi and Anatoly Spitkovsky. Acceleration of Particles at the Termination Shock of a Relativistic Striped Wind. *The Astrophysical Journal*, 741(1):39, Nov 2011.

[239] V. F. Shvartsman. Neutron Stars in Binary Systems Should Not Be Pulsars. *Soviet Astronomy*, 15:342, Oct 1971.

[240] A. F. Illarionov and R. A. Sunyaev. Why the Number of Galactic X-ray Stars Is so Small? *Astronomy and Astrophysics*, 39:185, Feb 1975.

[241] Marco Tavani, Jonathan Arons, and Victoria M. Kaspi. Regimes of High-Energy Shock Emission from the Be Star/Pulsar System PSR 1259-63. *The Astrophysical Journal Letters*, 433:L37, Sep 1994.

[242] Roger Blandford, David Meier, and Anthony Readhead. Relativistic Jets from Active Galactic Nuclei. *Annual Review of Astronomy and Astrophysics*, 57:467–509, Aug 2019.

[243] I. F. Mirabel and L. F. Rodríguez. Sources of Relativistic Jets in the Galaxy. *Annual Review of Astronomy and Astrophysics*, 37:409–443, Jan 1999.

[244] David L. Meier. The theory and simulation of relativistic jet formation: towards a unified model for micro- and macroquasars. *New Astronomy Reviews*, 47(6-7):667–672, Oct 2003.

[245] Josep M. Paredes, Josep Martí, Marc Ribó, and Maria Massi. Discovery of a High-Energy Gamma-Ray-Emitting Persistent Microquasar. *Science*, 288(5475):2340–2342, Jun 2000.

[246] M. Massi, M. Ribó, J. M. Paredes, M. Peracaula, and R. Estalella. One-sided jet at milliarcsecond scales in LS I $+61^{\circ}303$. *Astronomy & Astrophysics*, 376:217–223, Sep 2001.

[247] G. Dubus. Gamma-ray binaries: pulsars in disguise? *Astronomy & Astrophysics*, 456(3):801–817, Sep 2006.

[248] I. F. Mirabel. Astronomy: Very energetic gamma-rays from microquasars and binary pulsars. *Science*, 312(5781):1759–1760, Jun 2006.

[249] Guillaume Dubus. Gamma-ray binaries and related systems. *Astronomy and Astrophysics Review*, 21:64, Aug 2013.

[250] F. Aharonian, A. G. Akhperjanian, A. R. Bazer-Bachi, M. Beilicke, W. Benbow, D. Berge, K. Bernlöhr, C. Boisson, O. Bolz, V. Borrel, and et al. 3.9 day orbital modulation in the tev $\gamma$-ray flux and spectrum from the x-ray binary ls 5039. *Astronomy & Astrophysics*, 460(3):743–749, Sep 2006.

[251] A. Sierpowska and W. Bednarek. $\gamma$-rays from cascades in close massive binaries containing energetic pulsars. *Monthly Notices of the Royal Astronomical Society*, 356(2):711–726, Jan 2005.

[252] F. Aharonian, L. Anchordoqui, D. Khangulyan, and T. Montaruli. Microquasar LS 5039: a TeV gamma-ray emitter and a potential TeV neutrino source. In *Journal of Physics Conference Series*, volume 39 of *Journal of Physics Conference Series*, pages 408–415, May 2006.

[253] G. Dubus, B. Cerutti, and G. Henri. The modulation of the gamma-ray emission from the binary LS 5039. *Astronomy & Astrophysics*, 477(3):691–700, Jan 2008.

[254] V. Zabalza, V. Bosch-Ramon, F. Aharonian, and D. Khangulyan. Unraveling the high-energy emission components of gamma-ray binaries. *Astronomy & Astrophysics*, 551:A17, Mar 2013.

[255] V. Bosch-Ramon, D. Khangulyan, and F. A. Aharonian. The magnetic field and the location of the TeV emitter in Cygnus ;X-1 and LS ;5039. *Astronomy & Astrophysics*, 489(2):L21–L24, Oct 2008.

[256] V. Bosch-Ramon, M. V. Barkov, D. Khangulyan, and M. Perucho. Simulations of stellar/pulsar-wind interaction along one full orbit. *Astronomy & Astrophysics*, 544:A59, Aug 2012.

[257] Guillaume Dubus, Nicolas Guillard, Pierre-Olivier Petrucci, and Pierrick Martin. Sizing up the population of gamma-ray binaries. *Astronomy & Astrophysics*, 608:A59, Dec 2017.

[258] C. De Loore. The evolution of massive stars. *Space Science Reviews*, 26(2):113–155, June 1980.

[259] E. Parizot, A. Marcowith, E. van der Swaluw, A. M. Bykov, and V. Tatischeff. Superbubbles and energetic particles in the Galaxy. I. Collective effects of particle acceleration. *Astronomy & Astrophysics*, 424:747–760, September 2004.

[260] P. J. Kavanagh, M. Sasaki, L. M. Bozzetto, M. D. Filipović, S. D. Points, P. Maggi, and F. Haberl. XMM-Newton study of 30 Doradus C and a newly identified MCSNR J0536-6913 in the Large Magellanic Cloud⋆. *Astronomy & Astrophysics*, 573:A73, January 2015.

[261] Laura A. Lopez, Brian W. Grefenstette, Katie Auchettl, Kristin K. Madsen, and Daniel Castro. Evidence of Particle Acceleration in the Superbubble 30 Doradus C with NuSTAR. *arXiv e-prints*, page arXiv:1811.12416, November 2018.

[262] Bryan C. Dunne, Sean D. Points, and You-Hua Chu. X-Rays from Superbubbles in the Large Magellanic Cloud. VI. A Sample of Thirteen Superbubbles. *The Astrophysical Journal Supplement Series*, 136(1):119–135, Sep 2001.

[263] A. M. Bykov and I. N. Toptygin. A Model of Particle Acceleration to High Energies by Multiple Supernova Explosions in OB Associations. *Astronomy Letters*, 27(10):625–633, October 2001.

[264] F. A. Aharonian, A. M. Atoyan, and H. J. Voelk. High energy electrons and positrons in cosmic rays as an indicator of the existence of a nearby cosmic tevatron. *Astronomy & Astrophysics*, 294:L41–L44, February 1995.

[265] Felix Aharonian, Ruizhi Yang, and Emma de O˜na Wilhelmi. Massive stars as major factories of Galactic cosmic rays. *Nature Astronomy*, 3:561–567, March 2019.

[266] Patrick J. Kavanagh. Thermal and non-thermal X-ray emission from stellar clusters and superbubbles. *Astrophysics and Space Science*, 365(1):6, January 2020.

[267] The ARGO-YBJ Collaboration. Identification of the TeV Gamma-Ray Source ARGO J2031+4157 with the Cygnus Cocoon. *The Astrophysical Journal*, 790(2):152, August 2014.

[268] Rui-zhi Yang, Emma de Oña Wilhelmi, and Felix Aharonian. Diffuse $\gamma$-ray emission in the vicinity of young star cluster Westerlund 2. *Astronomy & Astrophysics*, 611:A77, April 2018.

[269] Patrick J. Kavanagh, Jacco Vink, Manami Sasaki, You-Hua Chu, Miroslav D. Filipović, Stefan Ohm, Frank Haberl, Perica Manojlovic, and Pierre Maggi. Magnetic field estimates from the X-ray synchrotron emitting rims of the 30 Dor C superbubble and the implications for the nature of 30 Dor C's TeV emission. *Astronomy & Astrophysics*, 621:A138, January 2019.

[270] C. J. Cesarsky and T. Montmerle. Gamma-Rays from Active Regions in the Galaxy - the Possible Contribution of Stellar Winds. *Space Science Reviews*, 36(2):173–193, October 1983.

[271] A. Abramowski, F. Aharonian, F. Ait Benkhali, A. G. Akhperjanian, E. O. Angüner, M. Backes, S. Balenderan, A. Balzer, A. Barnacka, Y. Becherini, and et al. Diffuse Galactic gamma-ray emission with H.E.S.S. *Physical Review D*, 90(12):122007, December 2014.

[272] A. Neronov and D. Semikoz. Galactic diffuse gamma-ray emission at TeV energy. *Astronomy & Astrophysics*, 633:A94, January 2020.

[273] Fermi Collaboration. Fermi Large Area Telescope observations of Local Group galaxies: detection of M 31 and search for M 33. *Astronomy & Astrophysics*, 523:L2, November 2010.

[274] K. D. Gordon, M. Meixner, M. R. Meade, B. Whitney, C. Engelbracht, C. Bot, M. L. Boyer, B. Lawton, M. Sewiło, B. Babler, and et al. Surveying the agents of galaxy evolution in the tidally stripped, low metallicity small magellanic cloud (sage-smc). i. overview. *The Astronomical Journal*, 142(4):102, Aug 2011.

[275] F. Aharonian, A. G. Akhperjanian, A. R. Bazer-Bachi, M. Beilicke, W. Benbow, D. Berge, K. Bernlohr, C. Boisson, O. Bolz, V. Borrel, and et al. The h.e.s.s. survey of the inner galaxy in very high energy gamma rays. *The Astrophysical Journal*, 636(2):777–797, Jan 2006.

[276] R. H. D. Corbet, L. Chomiuk, M. J. Coe, J. B. Coley, G. Dubus, P. G. Edwards, P. Martin, V. A. McBride, J. Stevens, J. Strader, L. J. Townsend, and A. Udalski. A luminous gamma-ray binary in the large magellanic cloud. *The Astrophysical Journal*, 829(2):105, Oct 2016.

[277] J. Martin, D. F. Torres, A. Cillis, and E. de Oña Wilhelmi. Is there room for highly magnetized pulsar wind nebulae among those non-detected at TeV? *Monthly Notices of the Royal Astronomical Society*, 443(1):138–145, Sep 2014.

[278] Q. Daniel Wang and Eric V. Gotthelf. ROSAT and ASCA Observations of the Crab-like Supernova Remnant N157B in the Large Magellanic Cloud. *The Astrophysical Journal*, 494(2):623–635, Feb 1998.

[279] N. I. Serafimovich, Yu. A. Shibanov, P. Lundqvist, and J. Sollerman. The young pulsar PSR B0540-69.3 and its synchrotron nebula in the optical and X-rays. *Astronomy & Astrophysics*, 425:1041–1060, Oct 2004.

[280] R. M. Williams, Y. H. Chu, J. R. Dickel, R. A. Gruendl, F. D. Seward, M. A. Guerrero, and G. Hobbs. Supernova Remnants in the Magellanic Clouds. V. The Complex Interior Structure of the N206 Supernova Remnant. *The Astrophysical Journal*, 628(2):704–720, Aug 2005.

[281] B. M. Gaensler, S. P. Hendrick, S. P. Reynolds, and K. J. Borkowski. Discovery of a New Pulsar Wind Nebula in the Large Magellanic Cloud. *The Astrophysical Journal Letters*, 594(2):L111–L114, Sep 2003.

[282] R. N. Manchester, G. Fan, A. G. Lyne, V. M. Kaspi, and F. Crawford. Discovery of 14 Radio Pulsars in a Survey of the Magellanic Clouds. *The Astrophysical Journal*, 649:235–242, September 2006.

[283] R. Chris Smith, You-Hua Chu, Mordecai-Mark Mac Low, M. S. Oey, and Uli Klein. The New Supernova Remnants in OB Associations in the Large Magellanic Cloud. *The Astronomical Journal*, 108:1266, Oct 1994.

[284] F. D. Seward, R. M. Williams, Y. H. Chu, J. R. Dickel, R. C. Smith, and S. D. Points. Chandra Observation of the Magellanic Cloud Supernova Remnant 0454-67.2 in N9. *The Astrophysical Journal*, 640(1):327–334, Mar 2006.

[285] F. D. Seward, P. A. Charles, D. L. Foster, J. R. Dickel, P. S. Romero, Z. I. Edwards, M. Perry, and R. M. Williams. DEM L241, a Supernova Remnant Containing a High-mass X-Ray Binary. *The Astrophysical Journal*, 759(2):123, Nov 2012.

[286] J. P. Ridley, F. Crawford, D. R. Lorimer, S. R. Bailey, J. H. Madden, R. Anella, and J. Chennamangalam. Eight new radio pulsars in the Large Magellanic Cloud. *Monthly Notices of the Royal Astronomical Society*, 433(1):138–146, July 2013.

[287] G. Vasilopoulos, C. Maitra, F. Haberl, D. Hatzidimitriou, and M. Petropoulou. Identification of two new HMXBs in the LMC: an $\sim$2013 s pulsar and a probable SFXT. *Monthly Notices of the Royal Astronomical Society*, 475(1):220–231, Mar 2018.

[288] C. Maitra, J. Ballet, M. D. Filipović, F. Haberl, A. Tiengo, K. Grieve, and Q. Roper. IKT 16: the first X-ray confirmed composite SNR in the SMC. *Astronomy & Astrophysics*, 584:A41, December 2015.

[289] Rami Z E Alsaberi, C Maitra, M D Filipović, L M Bozzetto, F Haberl, P Maggi, M Sasaki, P Manjolović, V Velović, P Kavanagh, and et al. Discovery of a pulsar-powered bow shock nebula in the small magellanic cloud supernova remnant dem s5. *Monthly Notices of the Royal Astronomical Society*, 486(2):2507–2524, Apr 2019.

[290] F. Haberl, R. Sturm, J. Ballet, D. J. Bomans, D. A. H. Buckley, M. J. Coe, R. Corbet, M. Ehle, M. D. Filipovic, M. Gilfanov, and et al. Thexmm-newtonsurvey of the small magellanic cloud. *Astronomy & Astrophysics*, 545:A128, Sep 2012.

[291] T. D. Joseph, M. D. Filipović, E. J. Crawford, Bojičić, I. , E. L. Alexander, G. F. Wong, H. Andernach, H. Leverenz, R. P. Norris, R. Z. E. Alsaberi, C. Anderson, L. A. Barnes, L. M. Bozzetto, F. Bufano, J. D. Bunton, F. Cavallaro, J. D. Collier, H. Dénes, Y. Fukui, T. Galvin, F. Haberl, A. Ingallinera, A. D. Kapinska, B. S. Koribalski, R. Kothes, D. Li, P. Maggi, C. Maitra, Manojlović, P. , J. Marvil, N. I. Maxted, A. N. O'Brien, J. M. Oliveira, C. M. Pennock, S. Riggi, G. Rowell, L. Rudnick, H. Sano, M. Sasaki, N. Seymour, R. Soria, M. Stupar, N. F. H. Tothill, C. Trigilio, K. Tsuge, G. Umana, Urošević, D. , J. Th van Loon, E. Vardoulaki, Velović, V. , M. Yew, D. Leahy, Y. H. Chu, M. J. Michałowski, P. J. Kavanagh, and K. R. Grieve. The ASKAP EMU Early Science Project: radio continuum survey of the Small Magellanic Cloud. *Monthly Notices of the Royal Astronomical Society*, 490(1):1202–1219, Nov 2019.

[292] J. Yang, S. G. T. Laycock, D. M. Christodoulou, S. Fingerman, M. J. Coe, and J. J. Drake. A comprehensive library of x-ray pulsars in the small magellanic cloud: Time evolution of their luminosities and spin periods. *The Astrophysical Journal*, 839(2):119, Apr 2017.

[293] Titus, N. and Stappers, B. W. and Morello, V. and Caleb, M. and Filipović and , M. D. and McBride, V. A. and Ho, W. C. G. and Buckley, D. A. H. Targeted search for young radio pulsars in the SMC: Discovery of two new pulsars. *Monthly Notices of the Royal Astronomical Society*, page 1513, Jun 2019.

[294] P. Kar and VERITAS Collaboration. Long-term VERITAS monitoring of LS I 61 $+$303 in conjunction with X-ray, and GeV observation campaigns. In *34th International Cosmic Ray Conference (ICRC2015)*, volume 34 of *International Cosmic Ray Conference*, page 818, Jul 2015.

[295] M. J. Coe, A. J. Bird, C. M. Boon, V. A. McBride, E. S. Bartlett, J. Kennea, and C. Ferrigno. SMC transient X-ray source IGR J01217-7257 detected by INTEGRAL. *The Astronomer's Telegram*, 8246:1, Nov 2015.

[296] F. Haberl, G. Vasilopoulos, R. Sturm, and P. Maggi. Identification of IGR J01217-7257 with the transient pulsar XTE J0119-731 (SXP2.16) using XMM-Newton. *The Astronomer's Telegram*, 8305:1, Nov 2015.

[297] J. A. Kennea, D. N. Burrows, M. J. Coe, A. J. Bird G. Vasilopoulos, F. Haberl, P. A. Evans, A. P. Beardmore, H. A. Krimm, P. Romano, P. Curran, K. Yamaoka, M. Serino, and H. Negoro. Swift observations show MAXI J0051-736 is a new outburst of SMC X-2. *The Astronomer's Telegram*, 8091:1, Sep 2015.

[298] V. Lipunov, E. Gorbovskoy, D. Buckley, E. O. Gress, P. Balanutsa, V. Kornilov, N. Tiurina, A. Kuznetsov, I. Gorbunov, E. Popova, D. Vlasenko, O. Gress, N. Budnev, K. Ivanov, A. Tlatov, V. Senik D. Dormidontov, Yu. Sergienko, A. Gabovich, V. Yurkov, V. Krushinskiy, R. Rebolo, M. Serra-Ricart, N. Lodieu, and G. Israelian. MASTER-SAAO Follow Up observations of the X-ray Transient MAXI J0051-736/SMC X-2. *The Astronomer's Telegram*, 8093:1, Sep 2015.

[299] S. Fotopoulou, M. J. Coe, A. J. Bird, V. McBride, and E. Bozzo. INTEGRAL detection of SMC X-2 in outburst. *The Astronomer's Telegram*, 8207:1, Oct 2015.

[300] L. J. Townsend, J. A. Kennea, M. J. Coe, V. A. McBride, D. A. H. Buckley, P. A. Evans, and A. Udalski. The 2016 super-Eddington outburst of SMC X-3: X-ray and optical properties and system parameters. *Monthly Notices of the Royal Astronomical Society*, 471(4):3878–3887, Nov 2017.

[301] L. Ducci, P. Romano, J. A. Kennea, C. Malacaria, S. Covino, A. Santangelo, P. A. Evans, M. J. Coe, and L. J. Townsend. Swift/XRT detection of an outburst from SXP 15.3. *The Astronomer's Telegram*, 11030:1, Dec 2017.

[302] Pierre Maggi, Miroslav D. Filipović, Branislav Vukotić, Jean Ballet, Frank Haberl, Chandreyee Maitra, Patrick Kavanagh, Manami Sasaki, and Milorad Stupar. The supernova remnant population of the Small Magellanic Cloud. *Astronomy & Astrophysics*, 631:A127, Nov 2019.

[303] D. Maoz and F. Mannucci. Type-Ia Supernova Rates and the Progenitor Problem: A Review. *Publications of the Astronomical Society of Australia*, 29(4):447–465, Jan 2012.

[304] Katie Auchettl, Laura A. Lopez, Carles Badenes, Enrico Ramirez-Ruiz, John F. Beacom, and Tyler Holland -Ashford. Measurement of the Core-collapse Progenitor Mass Distribution of the Small Magellanic Cloud. *The Astrophysical Journal*, 871(1):64, January 2019.

[305] D. A. Green. A catalogue of 294 Galactic supernova remnants. *Bulletin of the Astronomical Society of India*, 42(2):47–58, Jun 2014.

[306] H. E. S. S. Collaboration. HESS J1640-465 - an exceptionally luminous TeV $\gamma$-ray supernova remnant. *Monthly Notices of the Royal Astronomical Society*, 439(3):2828–2836, Apr 2014.

[307] W. W. Tian and D. A. Leahy. Distances of the TeV supernova remnant complex CTB 37 towards the Galactic bar. *Monthly Notices of the Royal Astronomical Society*, 421(3):2593–2597, Apr 2012.

[308] H. E. S. S. Collaboration. H.E.S.S. observations of RX J1713.7-3946 with improved angular and spectral resolution: Evidence for gamma-ray emission extending beyond the X-ray emitting shell. *Astronomy & Astrophysics*, 612:A6, Apr 2018.

[309] Chuyuan Yang and Siming Liu. Energy Partition between Energetic Electrons and Turbulent Magnetic Field in Supernova Remnant RX J1713.7-3946. *The Astrophysical Journal*, 773(2):138, Aug 2013.

[310] T. Douvion, P. O. Lagage, C. J. Cesarsky, and E. Dwek. Dust in the tycho, kepler and crab supernova remnants. *Astronomy & Astrophysics*, 373(1):281–291, Jul 2001.

[311] H. E. S. S. Collaboration. Deeper H.E.S.S. observations of Vela Junior (RX J0852.0-4622): Morphology studies and resolved spectroscopy. *Astronomy & Astrophysics*, 612:A7, Apr 2018.

[312] S. Ranasinghe and D. A. Leahy. Revised Distances to 21 Supernova Remnants. *The Astronomical Journal*, 155(5):204, May 2018.

[313] Yasuo Fukui, Norikazu Mizuno, Reiko Yamaguchi, Akira Mizuno, Toshikazu Onishi, Hideo Ogawa, Yoshinori Yonekura, Akiko Kawamura, Kengo Tachihara, Kecheng Xiao, Nobuyuki Yamaguchi, Atsushi Hara, Takahiro Hayakawa, Sigeo Kato, Rihei Abe, Hiro Saito, Satoru Mano, Ken'ichi Matsunaga, Yoshihiro Mine, Yoshiaki Moriguchi, Hiroko Aoyama, Shin-ichiro Asayama, Nao Yoshikawa, and Monica Rubio. First Results of a CO Survey of the Large Magellanic Cloud with NANTEN; Giant Molecular Clouds as Formation Sites of Populous Clusters. *Publications of the Astronomical Society of Japan*, 51:745–749, Dec 1999.

[314] M.S.E. Roberts. The pulsar wind nebula catalog (march 2005 version). *(available on the World-Wide-Web at "http://www.physics.mcgill.ca/ pulsar/pwncat.html")*, 2004.

[315] R. N. Manchester, L. Staveley-Smith, and M. J. Kesteven. The Radio Structure of Supernova Remnant 0540-693. *The Astrophysical Journal*, 411:756, Jul 1993.

[316] E. V. Gotthelf and Q. D. Wang. N157B: X-ray evidence for a Crab-like supernova remnant. In H. U. Zimmermann, J. Trümper, and H. Yorke, editors, *Roentgenstrahlung from the Universe*, pages 255–256, Feb 1996.

[317] C. Mariaud, P. Bordas, F. Aharonian, M. Boettcher, G. Dubus, M. de Naurois, C. Romoli, and V. Zabalza. VHE observations of the gamma-ray binary system LS 5039 with H.E.S.S. *arXiv e-prints*, page arXiv:1509.05791, Sep 2015.

[318] H. E. S. S. Collaboration. Discovery of variable VHE $\gamma$-ray emission from the binary system 1FGL J1018.6-5856. *Astronomy & Astrophysics*, 577:A131, May 2015.

[319] VERITAS Collaboration. Exceptionally Bright TeV Flares from the Binary LS I +61 303. *The Astrophysical Journal Letters*, 817(1):L7, Jan 2016.

[320] VERITAS Collaboration and H.E.S.S. Collaboration. Long-term TeV and X-Ray Observations of the Gamma-Ray Binary HESS J0632+057. *The Astrophysical Journal*, 780(2):168, Jan 2014.

[321] A. Abramowski, F. Acero, F. Aharonian, A. G. Akhperjanian, G. Anton, A. Balzer, A. Barnacka, U. Barres de Almeida, Y. Becherini, J. Becker, and et al. Discovery of extended vhe $\gamma$-ray emission from the vicinity of the young massive stellar cluster westerlund 1. *Astronomy & Astrophysics*, 537:A114, Jan 2012.

[322] H. E. S. S. Collaboration. Revisiting the Westerlund 2 field with the HESS telescope array. *Astronomy & Astrophysics*, 525:A46, January 2011.

[323] J. Katsuta, Y. Uchiyama, and S. Funk. Extended Gamma-Ray Emission from the G25.0+0.0 Region: A Star-forming Region Powered by the Newly Found OB Association? *The Astrophysical Journal*, 839(2):129, April 2017.

[324] F. Maragoudaki, M. Kontizas, D. H. Morgan, E. Kontizas, A. Dapergolas, and E. Livanou. The recent structural evolution of the SMC. *Astronomy & Astrophysics*, 379:864–869, December 2001.

[325] R. Hainich, D. Pasemann, H. Todt, T. Shenar, A. Sander, and W. R. Hamann. Wolf-Rayet stars in the Small Magellanic Cloud. I. Analysis of the single WN stars. *Astronomy & Astrophysics*, 581:A21, September 2015.

[326] T. Shenar, R. Hainich, H. Todt, A. Sander, W. R. Hamann, A. F. J. Moffat, J. J. Eldridge, H. Pablo, L. M. Oskinova, and N. D. Richardson. Wolf-Rayet stars in the Small Magellanic Cloud. II. Analysis of the binaries. *Astronomy & Astrophysics*, 591:A22, June 2016.

[327] Mónica Rubio. Properties of star forming regions in the Magellanic Clouds. In Jacco Th. Van Loon and Joana M. Oliveira, editors, *The Magellanic System: Stars, Gas, and Galaxies*, volume 256 of *IAU Symposium*, pages 215–226, March 2009.

[328] Mojgan Aghakhanloo, Jeremiah W. Murphy, Nathan Smith, John Parejko, Mariangelly Díaz-Rodríguez, Maria R. Drout, Jose H. Groh, Joseph Guzman, and Keivan G. Stassun. Inferring the parallax of Westerlund 1 from Gaia DR2. *Monthly Notices of the Royal Astronomical Society*, 492(2):2497–2509, February 2020.

[329] M. M. Hanson. A Study of Cygnus OB2: Pointing the Way toward Finding Our Galaxy's Super-Star Clusters. *The Astronomical Journal*, 597(2):957–969, November 2003.

[330] VERITAS Collaboration. A connection between star formation activity and cosmic rays in the starburst galaxy M82. *Nature*, 462(7274):770–772, December 2009.

[331] H. E. S. S. Collaboration. Spectral Analysis and Interpretation of the $\gamma$-Ray Emission from the Starburst Galaxy NGC 253. *The Astrophysical Journal*, 757(2):158, October 2012.

[332] H. E. S. S. Collaboration. The starburst galaxy NGC 253 revisited by H.E.S.S. and Fermi-LAT. *Astronomy & Astrophysics*, 617:A73, September 2018.

[333] R. Rekola, M. G. Richer, Marshall L. McCall, M. J. Valtonen, J. K. Kotilainen, and Chris Flynn. Distance to NGC 253 based on the planetary nebula luminosity function. *Monthly Notices of the Royal Astronomical Society*, 361(1):330–336, July 2005.

[334] Jürgen Knödlseder, Michael Mayer, Christoph Deil, Rolf Buehler, Johan Bregeon, and Pierrick Martin. ctools: Cherenkov Telescope Science Analysis Software, January 2016.

[335] A. Donath, C. Deil, M. Paz Arribas, J. King, E. Owen, R. Terrier, I. Reichardt, J. Harris, R. Buehler, and S. Klepser. Gammapy: An open-source Python package for gamma-ray astronomy. In *34th International Cosmic Ray Conference (ICRC2015)*, volume 34 of *International Cosmic Ray Conference*, page 789, July 2015.

[336] C. C. Lu. Improving the H.E.S.S. angular resolution using the Disp method. *arXiv e-prints*, page arXiv:1310.1200, Oct 2013.

[337] K. V. Mardia. *Statistics of Directional data*. Academic Press, New York, 1972.

[338] O. C. de Jager, B. C. Raubenheimer, and J. W. H. Swanepoel. A powerful test for weak periodic signals with unknown light curve shape in sparse data. *Astronomy & Astrophysics*, 221:180–190, Aug 1989.

[339] F. Martins, D. Schaerer, and D. J. Hillier. A new calibration of stellar parameters of Galactic O stars. *Astronomy & Astrophysics*, 436(3):1049–1065, Jun 2005.

[340] D. Khangulyan, F. Aharonian, and V. Bosch-Ramon. On the formation of TeV radiation in LS 5039. *Monthly Notices of the Royal Astronomical Society*, 383(2):467–478, Jan 2008.

[341] J. Frank, A. King, and D. Raine. Book-Review - Accretion Power in Astrophysics - ED.2. *Science*, 258:1015, November 1992.

[342] Jorick S. Vink, A. de Koter, and H. J. G. L. M. Lamers. Mass-loss predictions for O and B stars as a function of metallicity. *Astronomy & Astrophysics*, 369:574–588, Apr 2001.

[343] B. van Soelen, N. Komin, A. Kniazev, and P. Väisänen. The orbital parameters of the gamma-ray binary LMC P3†. *Monthly Notices of the Royal Astronomical Society*, 484(3):4347–4351, Apr 2019.

[344] K. Hirata, T. Kajita, M. Koshiba, M. Nakahata, Y. Oyama, N. Sato, A. Suzuki, M. Takita, Y. Totsuka, T. Kifune, T. Suda, K. Takahashi, T. Tanimori, K. Miyano, M. Yamada, E. W. Beier, L. R. Feldscher, S. B. Kim, A. K. Mann, F. M. Newcomer, R. van, W. Zhang, and B. G. Cortez. Observation of a neutrino burst from the supernova SN1987A. *Physical Review Letters*, 58(14):1490–1493, April 1987.

[345] R. M. Bionta, G. Blewitt, C. B. Bratton, D. Casper, A. Ciocio, R. Claus, B. Cortez, M. Crouch, S. T. Dye, S. Errede, G. W. Foster, W. Gajewski, K. S. Ganezer, M. Goldhaber, T. J. Haines, T. W. Jones, D. Kielczewska, W. R. Kropp, J. G. Learned, J. M. Losecco, J. Matthews, R. Miller, M. S. Mudan, H. S. Park, L. R. Price, F. Reines, J. Schultz, S. Seidel, E. Shumard, D. Sinclair, H. W. Sobel, J. L. Stone, L. R. Sulak, R. Svoboda, G. Thornton, J. C. van der Velde, and C. Wuest. Observation of a neutrino burst in coincidence with supernova 1987A in the Large Magellanic Cloud. *Physical Review Letters*, 58(14):1494–1496, April 1987.

[346] B. Marsden. Supernova 1987a in the large magellanic cloud. *International Astronomical Union Circular*, 4316, Feb 1987.

[347] Ian K. Shelton. Supernova 1987A: Photometry of the Discovery and Pre-Discovery Plates. *The Astronomical Journal*, 105:1886, May 1993.

[348] W. David Arnett, John N. Bahcall, Robert P. Kirshner, and Stanford E. Woosley. Supernova 1987A. *Annual Review of Astronomy and Astrophysics*, 27:629–700, January 1989.

[349] Richard McCray and Claes Fransson. The Remnant of Supernova 1987A. *Annual Review of Astronomy and Astrophysics*, 54:19–52, September 2016.

[350] Denys Malyshev, Gerd Pühlhofer, Andrea Santangelo, and Jacco Vink. Evidence for recent GeV brightening of the SN 1987A region. *arXiv e-prints*, page arXiv:1903.03045, March 2019.

[351] O. Petruk, V. Beshley, V. Marchenko, and M. Patrii. GeV light curves of young supernova remnants. *arXiv e-prints*, page arXiv:1912.06452, December 2019.

[352] E. G. Berezhko, L. T. Ksenofontov, and H. J. Völk. Expected Gamma-Ray Emission of Supernova Remnant SN 1987A. *The Astrophysical Journal*, 732(1):58, May 2011.

[353] V. V. Dwarkadas. Exploring the $\gamma$-ray emissivity of young supernova remnants - I. Hadronic emission. *Monthly Notices of the Royal Astronomical Society*, 434(4):3368–3377, October 2013.

[354] Pierrick Martin. Particleaccelerators in the lmc. In *IAU S331 Supernova 1987A: 30 Years Later - Cosmic Rays and Nuclei From Supernovae and their aftermaths*, https://indico.in2p3.fr/event/14344/attachments/14823/18176/PierrickMartin.pdf, Feb 2017.

[355] E. G. Berezhko, L. T. Ksenofontov, and H. J. Völk. Re-examination of the Expected Gamma-Ray Emission of Supernova Remnant SN 1987A. *The Astrophysical Journal*, 810(1):63, Sep 2015.

[356] H. E. S. S. Collaboration. Discovery of gamma-ray emission from the extragalactic pulsar wind nebula N 157B with H.E.S.S. *Astronomy & Astrophysics*, 545:L2, September 2012.

[357] Yang Chen, Q. Daniel Wang, E. V. Gotthelf, Bing Jiang, You-Hua Chu, and Robert Gruendl. Chandra ACIS Spectroscopy of N157B: A Young Composite Supernova Remnant in a Superbubble. *The Astrophysical Journal*, 651(1):237–249, November 2006.

[358] M. Meyer, D. Horns, and H. S. Zechlin. The Crab Nebula as a standard candle in very high-energy astrophysics. *Astronomy & Astrophysics*, 523:A2, November 2010.

[359] You-Hua Chu, Jr. Kennicutt, Robert C., Robert A. Schommer, and Joshua Laff. 30 DOR B: a supernova remnant in a star formation region. *The Astronomical Journal*, 103:1545–1551, May 1992.

[360] Fermi Collaboration. An extremely bright gamma-ray pulsar in the large magellanic cloud. *Science*, 350:801–805, 11 2015.

[361] A. A. Abdo, M. Ajello, A. Allafort, L. Baldini, J. Ballet, G. Barbiellini, M. G. Baring, D. Bastieri, A. Belfiore, R. Bellazzini, and et al. The secondfermilarge area telescope catalog of gamma-ray pulsars. *The Astrophysical Journal Supplement Series*, 208(2):17, Sep 2013.

[362] H. Inoue, K. Koyama, and Y. Tanaka. Soft X-ray observation of Supernova Remnants in the Small Magellanic Cloud. In J. Danziger and P. Gorenstein, editors, *Supernova Remnants and their X-ray Emission*, volume 101 of *IAU Symposium*, pages 535–540, January 1983.

[363] William P. Blair, Jon A. Morse, John C. Raymond, Robert P. Kirshner, John P. Hughes, Michael A. Dopita, Ralph S. Sutherland, Knox S. Long, and P. Frank Winkler. Hubble Space Telescope Observations of Oxygen-rich Supernova Remnants in the Magellanic Clouds. II. Elemental Abundances in N132D and 1E 0102.2-7219. *The Astrophysical Journal*, 537(2):667–689, July 2000.

[364] I. R. Tuohy and M. A. Dopita. Ring ejection in type II supernovae : 1E 0102.2-7219 in the Small Magellanic Cloud. *The Astrophysical Journal Letters*, 268:L11–L15, May 1983.

[365] William P. Blair, John C. Raymond, John Danziger, and Francesca Matteucci. The Ultraviolet Spectrum of an Oxygen-rich Supernova Remnant in the Small Magellanic Cloud. *The Astrophysical Journal*, 338:812, March 1989.

[366] Steven L. Finkelstein, Jon A. Morse, James C. Green, Jeffrey L. Linsky, J. Michael Shull, Theodore P. Snow, John T. Stocke, Kenneth R. Brownsberger, Dennis C. Ebbets, Erik Wilkinson, Sara R. Heap, Claus Leitherer, Blair D. Savage, Oswald H. Siegmund, and Alan Stern. Optical Structure and Proper-Motion Age of the Oxygen-rich Supernova Remnant 1E 0102-7219 in the Small Magellanic Cloud. *The Astrophysical Journal*, 641(2):919–929, Apr 2006.

[367] Long Xi, Terrance J. Gaetz, Paul P. Plucinsky, John P. Hughes, and Daniel J. Patnaude. The Expansion of the Forward Shock of 1E 0102.2-7219 in X-Rays. *The Astrophysical Journal*, 874(1):14, March 2019.

[368] Frédéric Vogt and Michael A. Dopita. The 3D structure of N132D in the LMC: a late-stage young supernova remnant. *Astrophysics and Space Science*, 331(2):521–535, Feb 2011.

[369] Frédéric P. A. Vogt, Ivo R. Seitenzahl, Michael A. Dopita, and Parviz Ghavamian. [Fe XIV] and [Fe XI] reveal the forward shock in SNR 1E 0102.2-7219. *Astronomy & Astrophysics*, 602:L4, June 2017.

[370] John P. Hughes, Ichizo Hayashi, and Katsuji Koyama. ASCA X-Ray Spectroscopy of Large Magellanic Cloud Supernova Remnants and the Metal Abundances of the Large Magellanic Cloud. *The Astrophysical Journal*, 505(2):732–748, October 1998.

[371] Ivo R. Seitenzahl, Frédéric P. A. Vogt, Jason P. Terry, Parviz Ghavamian, Michael A. Dopita, Ashley J. Ruiter, and Tuguldur Sukhbold. Integral Field Spectroscopy of Supernova Remnant 1E0102-7219 Reveals Fast-moving Hydrogen and Sulfur-rich Ejecta. *The Astrophysical Journal Letters*, 853(2):L32, February 2018.

[372] Frédéric Vogt and Michael A. Dopita. The 3D structure of N132D in the LMC: a late-stage young supernova remnant. *Astrophysics and Space Science*, 331(2):521–535, February 2011.

[373] R. A. Owen, M. D. Filipović, J. Ballet, F. Haberl, E. J. Crawford, J. L. Payne, R. Sturm, W. Pietsch, S. Mereghetti, M. Ehle, A. Tiengo, M. J. Coe, D. Hatzidimitriou, and D. A. H. Buckley. IKT 16: a composite supernova remnant in the Small Magellanic Cloud. *Astronomy & Astrophysics*, 530:A132, June 2011.

[374] H. E. S. S. Collaboration. First detection of a VHE gamma-ray spectral maximum from a cosmic source: HESS discovery of the Vela X nebula. *Astronomy & Astrophysics*, 448(2):L43–L47, March 2006.

[375] M. Mayer, J. Brucker, M. Holler, I. Jung, K. Valerius, and C. Stegmann. Predicting the X-ray flux of evolved pulsar wind nebulae based on VHE gamma-ray observations. *arXiv e-prints*, page arXiv:1202.1455, February 2012.

[376] Cherenkov Telescope Array Consortium. *Science with the Cherenkov Telescope Array*. World Scientific Publishing Co. Pte. Ltd., ISBN #9789813270091, Mar 2019.

[377] Kazimierz J. Borkowski, Sean P. Hendrick, and Stephen P. Reynolds. Dense, Fe-rich Ejecta in Supernova Remnants DEM L238 and DEM L249: A New Class of Type Ia Supernova? *The Astrophysical Journal*, 652(2):1259–1267, December 2006.

[378] M. J. Coe and J. Kirk. Catalogue of Be/X-ray binary systems in the Small Magellanic Cloud: X-ray, optical and IR properties. *Monthly Notices of the Royal Astronomical Society*, 452(1):969–977, Sep 2015.

[379] A. Poveda, J. Ruiz, and C. Allen. Run-away Stars as the Result of the Gravitational Collapse of Proto-stellar Clusters. *Boletin de los Observatorios Tonantzintla y Tacubaya*, 4:86–90, April 1967.

[380] F. Zwicky. *Morphological astronomy*. Springer, 1957.

[381] M. S. Fujii and S. P. Zwart. The origin of ob runaway stars. *Science*, 334(6061):1380–1383, Nov 2011.

[382] D. R. Gies and C. T. Bolton. The binary frequency and origin of the ob runaway stars. *The Astrophysical Journal Supplement Series*, 61:419, Jun 1986.

[383] N. Tetzlaff, R. Neuhäuser, and M. M. Hohle. A catalogue of young runaway hipparcos stars within 3 kpc from the sun. *Monthly Notices of the Royal Astronomical Society*, 410(1):190–200, Oct 2010.

[384] Dave van Buren, Alberto Noriega-Crespo, and Ruth Dgani. An iras/issa survey of bow shocks around runaway stars. *The Astronomical Journal*, 110:2914, Dec 1995.

[385] C. S. Peri, P. Benaglia, D. P. Brookes, I. R. Stevens, and N. Isequilla. E-boss: an extensive stellar bow shock survey. i: Methods and first catalogue. *Astronomy & Astrophysics*, 09 2011.

[386] D. van Buren. Stellar Wind Bow Shocks. In J. P. Cassinelli and E. B. Churchwell, editors, *Massive Stars: Their Lives in the Interstellar Medium*, volume 35 of *Astronomical Society of the Pacific Conference Series*, page 315, January 1993.

[387] M. V. del Valle and M. Pohl. Nonthermal emission from stellar bow shocks. *The Astrophysical Journal*, 864(1):19, Aug 2018.

[388] Dave van Buren and Richard McCray. Bow shocks and bubbles are seen around hot stars by iras. *The Astrophysical Journal*, 329:L93, Jun 1988.

[389] Alberto Noriega-Crespo, Dave van Buren, and Ruth Dgani. Bow shocks around runaway stars.iii.the high resolution maps. *The Astronomical Journal*, 113:780, Feb 1997.

[390] V. V. Gvaramadze, A. Y. Kniazev, P. Kroupa, and S. Oh. Search for ob stars running away from young star clusters. *Astronomy & Astrophysics*, 535:A29, Oct 2011.

[391] Toalá, J. A. and Oskinova, L. M. and González-Galán, A. and Guerrero, M. A. and Ignace, R. and Pohl, M. X-ray observations of bow shocks around runaway o stars. the case of $zeta$ oph and bd+43°3654. *The Astrophysical Journal*, 821(2):79, May 2016.

[392] Toalá, J. A. and Oskinova, L. M. and Ignace, R. On the absence of non-thermal x-ray emission around runaway o stars. *The Astrophysical Journal*, 838(2):L19, Mar 2017.

[393] López-Santiago, J. and Miceli, M. and del Valle, M. V. and Romero, G. E. and Bonito, R. and Albacete-Colombo, J. F. and Pereira, V. and de Castro, E. and Damiani, F. Ae aurigae: First detection of non-thermal x-ray emission from a bow shock produced by a runaway star. *The Astrophysical Journal*, 757(1):L6, Aug 2012.

[394] A. Schulz, M. Ackermann, R. Buehler, M. Mayer, and S.Klepser. Systematic search for high-energy gamma-ray emission from bow shocks of runaway stars. *Astronomy & Astrophysics*, 04 2014.

[395] E. Sánchez-Ayaso, María V. del Valle, J. Martí, G. E. Romero, and P. L. Luque-Escamilla. Possible association of two stellar bowshocks with unidentified fermi sources. *The Astrophysical Journal*, 861(1):32, Jun 2018.

[396] B. T. Draine and H. M. Lee. Optical properties of interstellar graphite and silicate grains. *The Astrophysical Journal*, 285:89, Oct 1984.

[397] G. E. Romero, M. V. del Valle, and M. Orellana. Gamma-ray absorption and the origin of the gamma-ray flare in cygnus x-1. *Astronomy and Astrophysics*, 518:A12, Jul 2010.

[398] R. D. Blandford and J. P. Ostriker. Particle acceleration by astrophysical shocks. *The Astrophysical Journal*, 221:L29, Apr 1978.

[399] M. Casse and J. A. Paul. Local gamma rays and cosmic-ray acceleration by supersonic stellar winds. *The Astrophysical Journal*, 237:236, Apr 1980.

[400] H. J. Voelk and M. Forman. Cosmic rays and gamma-rays from ob stars. *The Astrophysical Journal*, 253:188, Feb 1982.

[401] R. L. White. Synchrotron emission from chaotic stellar winds. *The Astrophysical Journal*, 289:698, Feb 1985.

[402] M. De Becker, M. V. del Valle, G. E. Romero, C. S. Peri, and P. Benaglia. X-ray study of bow shocks in runaway stars. *Monthly Notices of the Royal Astronomical Society*, 471(4):4452–4464, Jul 2017.

[403] Henry A. Kobulnicky, Ian J. Gilbert, and Daniel C. Kiminki. Ob stars and stellar bow shocks in cygnus-x: A novel laboratory estimating stellar mass loss rates. *The Astrophysical Journal*, 710(1):549–566, Jan 2010.

[404] Henry A. Kobulnicky, William T. Chick, and Matthew S. Povich. Mass-loss rates for o and early b stars powering bow shock nebulae: Evidence for bistability behavior. *The Astronomical Journal*, 158(2):73, Jul 2019.

[405] Aya Bamba, Ryo Yamazaki, Tatsuo Yoshida, Toshio Terasawa, and Katsuji Koyama. A spatial and spectral study of nonthermal filaments in historical supernova remnants: Observational results withchandra. *The Astrophysical Journal*, 621(2):793–802, Mar 2005.

[406] Yukikatsu Terada, Makoto S. Tashiro, Aya Bamba, Ryo Yamazaki, Tomomi Kouzu, Shu Koyama, and Hiromi Seta. Search for diffuse x-rays from the bow shock region of runaway star bd +43 3654 with suzaku. *Publications of the Astronomical Society of Japan*, 64(6):138, Dec 2012.

[407] M. Ackermann, M. Ajello, L. Baldini, J. Ballet, G. Barbiellini, D. Bastieri, K. Bechtol, R. Bellazzini, B. Berenji, E. D. Bloom, and et al. Fermi-lat search for pulsar wind nebulae around gamma-ray pulsars. *The Astrophysical Journal*, 726(1):35, Dec 2010.

[408] H. Gast F. Sheldaei, A. Djannati-Atai and H.E.S.S. Collaboration. Disc aovery of vhe emission near psr j1831-0952 with hess: A new gamma-ray discovered pulsar wind nebula? In *Fermi Symposium, Rome*, 2011.

[409] H. Gast F. Sheldaei, A. Djannati-Atai and H.E.S.S. Collaboration. Hess j1831-098, a new gamma-ray discovered pulsar wind nebula? https://www.mpi-hd.mpg.de/hfm/HESS/pages/home/som/2011/06/, 2011.

[410] B. D. Metzger, T. Finzell, I. Vurm, R. Hascoët, A. M. Beloborodov, and L. Chomiuk. Gamma-ray novae as probes of relativistic particle acceleration at non-relativistic shocks. *Monthly Notices of the Royal Astronomical Society*, 450(3):2739–2748, May 2015.

[411] Fermi Collaboration. Fermi establishes classical novae as a distinct class of gamma-ray sources. *Science*, 345(6196):554–558, Jul 2014.

[412] C. C. Cheung, P. Jean, S. N. Shore, L. Stawarz, R. H. D. Corbet, J. Knödlseder, S. Starrfield, D. L. Wood, R. Desiante, F. Longo, and et al. Fermi-lat gamma-ray detections of classical novae v1369 centauri 2013 and v5668 sagittarii 2015. *The Astrophysical Journal*, 826(2):142, Jul 2016.

[413] Jim Hinton, Subir Sarkar, Diego Torres, and Johannes Knapp. A new era in gamma-ray astronomy with the cherenkov telescope array. *Astroparticle Physics*, 43:1–2, Mar 2013.

# Acknowledgements / Danksagung

Die Anfertigung dieser Arbeit war nur möglich durch die Unterstützung von vielen Seiten. Die motivierende, unterstützende und familiäre Umgebung am DESY und insbesondere in der H.E.S.S. Gruppe hat eine ideale Atmosphäre für die Anfertigung einer solchen Arbeit geschaffen. Eine gute Einbindung in das wissenschaftliche Umfeld durch die H.E.S.S. Kollaboration war dabei genauso wichtig wie die wissenschaftliche sowie karrieretechnische Förderung durch die H.E.S.S. Gruppe am DESY. Aber auch die Unterstützung vieler einzelner Personen und die soziale Struktur waren grundlegend für die Fertigstellung dieser Arbeit. Ein besonderer Dank geht dabei an:

- Meinen Doktorvater Christian Stegmann, der meine Begeisterung für die Astroteilchenphysik geweckt hat und dem ich meine Zeit am DESY zu verdanken habe.
- die Gutachter dieser Arbeit sowie die Mitglieder des Prüfungskomitees für ihre Geduld bei der Begutachtung dieser Arbeit.
- Meine Betreuer Stefan Ohm und Stefan Klepser, die mir täglich mit ihrem Rat zur Seite standen und maßgeblich dazu beigetragen haben, diese Arbeit in ihre finale Version zu bringen. Danke für eure Geduld in den letzten Jahren und die Unterstützung (all) meiner Entscheidungen.
- Heike und Sylvia, die dieser Arbeit mehr als den nötigen Feinschliff verpasst haben und sie vermutlich mittlerweile auswendig kennen. Danke für all die Zeit und Geduld, die ihr in die Verbesserung dieser Arbeit investiert habt!
- Jhilik und der H.E.S.S. crew in Namibia für die unvergessliche Zeit auf Schicht. Danke lieber Volker für die tollen Gespräche und Ausflugstipps, die uns gezeigt haben, dass Namibia aus mehr als nur dem H.E.S.S. Gelände besteht und uns die Kultur ein wenig näher gebracht haben.
- Jeden einzelnen der H.E.S.S. Gruppe für all die aufbauenden, interessanten, erleuchtenden, Ideen bringenden und lustigen Bürogespräche.

- Meine Familie, die mir in jeder Situation unterstützend in jeder Hinsicht zur Seite stand. Danke mein Schatz für die großartige Unterstützung in unserem stressigen Alltag, auf die ich mich immer verlassen konnte.
- Mein kleines "E-Team" und *, das mir jeden Tag aufs Neue gezeigt hat, dass es im Leben um mehr als Abgabefristen geht, dass Scheitern und aus Fehlern lernen Grundvoraussetzung für eine Weiterentwicklung ist, dass die Welt so viel unkomplizierter ist als wir sie sehen, man nur manchmal den Blickwinkel ändern muss, mich immer wieder herausgefordert hat komplexe wissenschaftliche Zusammenhänge einfach zu erklären, und vor allem, mir selbst in schweren Zeiten immer wieder ein Lächeln ins Gesicht gezaubert hat.

Nicht unerwähnt sollten all diejenigen bleiben, die meinen Alltag, von dessen Qualität die tägliche Motivation abhängt, mitgestaltet haben und ein offenes Ohr für mich hatten.

# Selbstständigkeitserklärung

Ich versichere, dass ich die vorliegende Arbeit selbständig und nur mit den angegeben Quellen und Hilfsmitteln angefertigt habe. Alle Stellen der Arbeit, die ich aus diesen Quellen und Hilfsmitteln dem Wortlaut oder dem Sinne nach entnommen habe, sind kenntlich gemacht und im Literaturverzeichnis aufgeführt. Weiterhin versichere ich, dass ich die vorliegende Arbeit, weder in der vorliegenden, noch in einer mehr oder weniger abgewandelten Form, als Dissertation an einer anderen Hochschule eingereicht habe.

Potsdam, den 28.04.2020 Maria Haupt